# INTRINSIC AND EXTRINSIC REGULATORY MECHANISMS OF THE DYNAMIN-RELATED G PROTEIN ATLASTIN: IMPLICATIONS IN CELLULAR FUNCTION AND HUMAN HEALTH

A Dissertation

Presented to the Faculty of the Graduate School

Of Cornell University

In Partial Fulfillment of the Requirements for the Degree of

Doctor of Philosophy

by

Carolyn McCartney Kelly

May 2021

# INTRINSIC AND EXTRINSIC REGULATORY MECHANISMS OF THE DYNAMIN-RELATED G PROTEIN ATLASTIN: IMPLICATIONS IN CELLULAR FUNCTION AND HUMAN HEALTH

Carolyn McCartney Kelly, Ph.D.

Cornell University 2021

The complex and diverse biochemical processes that support life require both the physical separation and dynamic communication that membranes provide. Critical membrane dynamics are achieved through fusion and fission events that are regulated and catalyzed by various classes of proteins, including dynamins. Here we present studies of the dynamin-related GTPase, atlastin (ATL), which catalyzes homotypic fusion of peripheral ER tubules to form and maintain its distinctive reticular structure. Humans have three isoforms (ATL1-3), all localizing to and functioning in the ER. Mutations in *atl1* and *atl3* are causative in two hereditary neuropathies, hereditary spastic paraplegia (HSP) and hereditary sensory neuropathy (HSN), caused by length-dependent axonal degeneration. Previous structural and biochemical studies have converged on a mechanistic model of how ATLs undergo GTP binding- and hydrolysis-dependent conformational changes coupled with dimerization in a manner that supports membrane fusion. However, questions remain regarding how this model translates to ATL's mechanism in a complex biological environment, including what mechanisms dictate how ATL favors GTP hydrolysis-dependent dimerization across *trans* membranes rather than *cis* membrane dimerization, which is a futile cycle in regards to membrane fusion, and the modes of ATL regulation that result in re-structuring of ER morphology in response to various cell signals, especially cell division.

Here, we present two novel modes of ATL1 regulation, both intrinsically through an uncharacterized N-terminal hypervariable region (HVR) and extrinsically through phosphorylation of several conserved serine resides within this motif. Our evidence reveals that the structured

ATL1 HVR provides a novel intermolecular contact that supports innate aspects of its membrane tethering activity. We also establish that ATL1 HVR-dependent phosphorylation has effects on both its kinetic behavior and cellular function, and using a kinase screen, have identified a list of candidate ATL1 modifiers. We have also structurally and biochemically characterized a novel HSP-associated ATL1 mutation, resulting in a whole codon insertion. We have uncovered a gain-of-function pathogenic mechanism yielding increased membrane tethering activity and altered ER sub-localization, while GTP hydrolysis remains unaffected. We propose the causative mechanism lies in the disruption of a pre-hydrolysis conformational state, leaving the mutant protein primed for faster nucleotide-dependent dimerization. These studies expand our current understanding of ATL's functional mechanisms in the cell and our appreciation of how this translates to human neuronal health.

## BIOGRAPHICAL SKETCH

Carolyn was born in Boston, Massachusetts but spent her formative years living in its suburb of Burlington, where she attended Burlington High School, graduating in the top 2% of her class. In the fall of 2010, she matriculated at the University of Massachusetts Amherst where she majored in Biochemistry and Molecular Biology and was a member of the Commonwealth Honors College. In addition to her coursework, Carolyn applied for a position in Dr. Scott Garman's research lab, where she spent two years developing her honors thesis on the structural characterization of the lysosomal enzyme NPC2. Outside of the classroom, Carolyn established herself as an active member of the UMass community through participation in the UMass Minuteman Marching Band, in which she was selected as both Field Staff and Section Leader in her junior and senior year, respectively; membership in the Honor Fraternity Phi Sigma Pi, in which she served as the Chair of the Education Committee for a semester; and through work with fellow students and department staff to establish a departmental Peer Advisor program. She was recognized by her department for her academic achievement and pursuit of non-traditional challenges with the Jessica Hayes Memorial Scholarship her junior year. After graduation in June of 2014, Carolyn enrolled in the graduate field of Biochemistry, Molecular and Cell Biology at Cornell University, where she joined the research group of Dr. Holger Sondermann for her dissertation research. Here she has been working to address how current mechanistic models of the dynamin-related G protein atlastin translate to its native activity in the cellular environment of the endoplasmic reticulum, with implications in both basic cell biology as well as human health.

To my parents,

Paula McCartney and James Kelly

“Regrets, I've had a few
But then again, too few to mention
I did what I had to do
And saw it through without exemption
I planned each chartered course
Each careful step along the byway
But more, much more than this
I did it my way

Yes, there were times, I'm sure you knew
When I bit off more than I could chew
But through it all, when there was doubt
I ate it up and spit it out
I faced it all and I stood tall
And did it my way”

-Paul Anka

## ACKNOWLEDGEMENTS

I would like to first thank my doctoral advisor, Dr. Holger Sondermann, for his thoughtful guidance through my graduate school journey. While in the Sondermann lab, I have learned an incredible amount, not just about the science, but about myself. I have learned how to challenge and better motivate myself, how to face and overcome unexpected obstacles, and how to just figure things out. Most importantly, I've gained an incredible amount of confidence in myself and my abilities that I did not have when I came to Cornell. I attribute much of this growth to Holger's mentorship, with the independence he affords us, the high standards he maintains, and the support and encouragement he provides.

Next, I would like to thank all my fellow lab members, past and present. When I first joined the Sondermann lab, I had the great privilege of working with and being trained by Rick Cooley and John O'Donnell, for whom I have endless respect. John also worked on the atlastin project, and so we worked together during my rotation and after I officially joined the lab. I attribute much of how I approach my work and how I think about science in general to his guidance. Rick, too, helped provide a great learning environment toward the beginning of my graduate research. He is one of the most knowledgeable, intentional scientists I have ever known, but he was also a patient and kind teacher. I am so grateful I had the opportunity to work alongside both of them. A majority of my time in the Sondermann lab has also been spent with Justin Lormand, who joined the year after I did. Although we both tend to keep to ourselves, we are also of a similar mind in many ways. I have endless respect for Justin and his work, and I am really glad I had the chance to work alongside him. We have had many other great students come and go over the years whom I'd also like to acknowledge, including Zoey Prokopiak, Maria Font, Maithili Deshpande, and Charlie Savelle. I would also like to thank Peter Zeiger, who was the undergraduate researcher helping with my project for the last couple years of my research. Peter is a very bright and hard-working student who made a crucial contribution to the research presented in Chapter 3 and who taught me what it takes to be a better mentor.

A number of people from both the Molecular Medicine and the Molecular Biology and Genetics Departments have also made it possible for me to make it to this point, including Deb Crane, Wendy Sweeney, Kevin Lyon, Greg Mitchell, and the MBG GFAs, Vicki Shaff and Casey Moore. I would also like to thank Maurine Linder, who has always been a great source of support to me through graduate school, but especially in the chaotic, final months of my research. I also am very thankful for the other members of my thesis committee: Carolyn Sevier and Bill Brown. They have both helped guide me and my research over the years and I am so grateful for their contributions.

I could not have made it through grad school without a number of amazing friendships. When I came to Ithaca for the first time for my interview in February of 2014, I met Lina Bagepalli. We clicked immediately, and we've been inseparable ever since. We have each been there for each other through exams, seminars, frustrations in lab, and every up and down life had to throw at us. Whenever I needed a friend, she was there with a glass of wine, a cup of tea, or both (depending on the day). Through her I also got to meet two other incredible friends: Egi Tentori and Sarah Then Bergh. They have both been great friends to me over the years. Sarah, in particular, has become a close confidant and an extension of my family, as she has celebrated Thanksgiving with us for several years now. Our friendship is one that came into my life at a moment when it was exactly what I needed; there are no pretenses and so much love.

Another Cornell friend I am so thankful to have met is James Chon. While I have known James since my interview at Cornell and we have been friends since I started here, we have become much closer in the last few years. James has provided a safe space for me in difficult times with kindness, compassion, and a complete lack of judgement. I can only hope to emulate the love and support he has given me.

Two other BMCB classmates who have become my great friends during graduate school are Erin Price and Wendy Beck. Erin and I worked across the hall from each other, which ended up being a true blessing. Whenever I needed help with an experiment, or, more often, someone

to chat with or vent with, Erin was there. Erin is also one of the most intelligent and strongest people I know. Watching her journey since I met her has inspired me and I'm grateful to have her in my life. Although Wendy and I didn't see each other frequently during most of our time at Cornell, we spent most of our first year together, as we did two of our lab rotations together. In that time, we established a really important bond. Even though we don't talk often, when we do it's as though no time has passed, and I'm so glad that I had her friendship over the years.

Although I met and befriended so many great people during my time at UMass, none have been so important to me as the ladies of the The Coop: Katie Mutrie, Bridget Eng, and Tierney Bocsi. Since meeting freshman year (except Katie…we go back 20 years), these three have become my sisters. I have never met another human who gets me more on such a fundamental level than Tierney. She is my soulmate-best-friend. We have been through so much together and have so much love for each other, no matter how long between our talks and visits. Bridget, too, has been there for me in so many ways. I have felt so grateful for our ever-growing friendship, knowing that we can talk for hours about nothing or everything, any time of the day or night. Katie and I met in elementary school and we have been best friends ever since. We have grown up together, with all the happy, tough, exciting, and tumultuous events that go along with that. It is such a rare gift to find a true sister in this world, especially one living down the street.

I also feel very lucky to count among my current best friends the friends I grew up with, especially Katie, Kevin, and Eric. Kevin and I became friends freshman year of high school and over the years have bonded over our shared love of marching band, music, academics, and laughter. I love our thoughtful conversations and fun ski adventures with Katie. I am so excited for the next chapter of our lives where we're all back in MA together. Although Eric is all the way in LA, our friendship has remained one of my most cherished. Eric has continuously inspired my appreciation and love of music, art, and all things beautiful. I'm so grateful to have each of you in my life.

The last year and a half of my graduate school experience was pretty chaotic, and not just because I was trying to finish experiments and write several papers and my thesis. My lab moved to Germany, there was a global pandemic that shut down research for months, and my mom has been battling cancer. But through all of this, my boyfriend, Zac Zaremba, has been there to keep me (relatively) sane. I have told him this many times but having him in my life has made everything else feel more manageable. Knowing that I have him by my side has allowed me to look at the world differently. With our love and support, we have both been able to grow so much.

And lastly, I have to thank my family. I've had the great fortune of becoming closer with my aunt and uncle, Anne and Mark, over the last six years as their home in Troy was the perfect halfway stop between Boston and Ithaca when I was traveling between home and school, and they have always welcomed me with open arms. My Pascucci family in California has also always been a great source of love and support. And I am especially thankful for my godparents, my Aunt Tish and Uncle Bill, and my cousins Kevin and Keara, for being my second family my whole life. Lasty, I am so grateful for my immediate family. My brother, Chris, and his girlfriend, Vada, are such kind and loving people who are always there to make me laugh and keep me centered. But most important are my parents. Of course, I would not be here without them, but I also know I would not be at Cornell graduating with my PhD without them. So many times in my life when I've felt stifled by self-doubt or fear of failure, they've lift me up and built me back up to continue pushing forward. So much of my identity comes from them and the examples they have set with regard to friendships and relationships, work ethic, their selflessness, and so much more. When I am lost, I know I need only look their way.

## TABLE OF CONTENTS

## LIST OF FIGURES

## LIST OF TABLES

# CHAPTER ONE

# INTRODUCTION

## Membrane fusion

Cellular membranes exist to establish physical barriers to create favorable environments for disparate biochemical reactions that must co-exist and coordinate to maintain homeostasis in a single cell. However, in order for these compartments to work together they must be able to communicate and transport biological molecules, which inherently involves dynamic changes in these membranes. Additionally, as cells divide, proper inheritance of organelles into daughter cells requires highly regulated and dynamic membrane fusion and fission processes (Lowe and Barr, 2007). Biological membranes require a protein catalyst to overcome the energy barrier of fusion and scission (McNew, 2008; McNew *et al*., 2013). The fusion of two phospholipid bilayers progresses in several distinct steps, starting in a state of two physically separate membranes (Figure 1.1A) that must first create close contact, overcoming a highly favorable hydration layer for each membrane (Figure 1.1B). This is followed by the coming together of the outer leaflets into a hemi-fusion state consisting of a connected stalk, which expands to allow formation of a pseudo-bilayer involving the inner leaflet of each bilayer (Figure 1.1C). The last step is the formation of a fusion pore after disruption of inner leaflet pseudo-bilayer, allowing mixing of aqueous solutions of either compartment (Figure 1.1D) (Kuzmin *et al*., 2001; McNew, 2008, Jahn and Grubmüller, 2002).

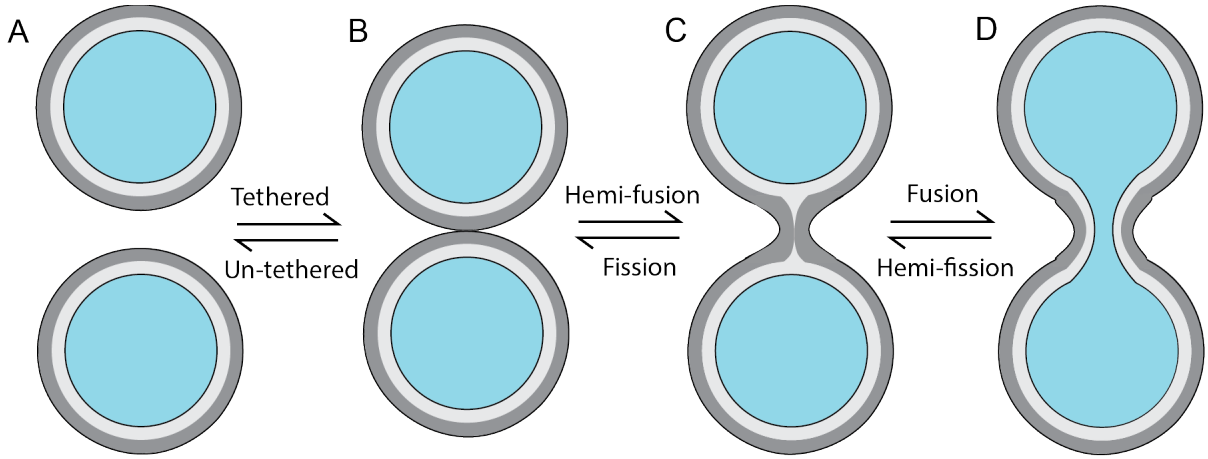


**Figure 1.1 Intermediate steps of membrane fusion and fission.** Aqueous solution contents shown in blue with each leaflet of the bilayer in grey (outer in dark grey and inner in light grey). **(A)** Two membranes begin the fusion process physically separate. **(B)** Membranes are brought into close proximity through tethering, overcoming a highly favorable hydration layer. **(C)** Hemi-fusion intermediate with the outer leaflets creating a stalk-like pseudo-bilayer. **(D)** Complete fusion after inner leaflets have fused and a fusion pore allows mixing of aqueous content.

In order to overcome the activation energy of these transition states, curvature must be introduced into the membranes, which can be achieved through local perturbations by fusion proteins (Jahn and Grubmüller, 2002). Several mechanisms for overcoming the activation energy have been characterized in canonical classes of membrane fusion proteins including the viral fusion protein hemagglutinin (HA), and the soluble N-ethylmaleimide-sensitive factor attachment protein receptors (SNAREs), which act in the eukaryotic secretory pathway. Entry of enveloped virus particles, such as the influenza virus, into host cells is initiated when the surface-exposed, proteolytically processed HA undergoes pH-triggered conformational changes in host endosomes. This results in the insertion of HA's hydrophobic fusion peptide into the host membrane, leaving viral and host membranes tethered by an extended HA intermediate. Energy from refolding of HA, aided by membrane perturbations by the fusion peptide and transmembrane region, catalyzes fusion of viral and host membrane (Bullough *et al*., 1994; Harrison, 2015). SNAREs have the dual function of directed membrane recognition and catalysis of membrane

fusion, largely in transport of vesicles within the secretory pathway. Similar to HA-mediated fusion, SNAREs rely on folding energy to initiate membrane fusion through the formation of a coiled-coil zipper-like complex composed of one α-helix from a vesicular membrane SNARE (v- or R-SNARE) and three α-helices from a target membrane SNARE (t- or Q-SNARE), with transmembrane regions in both membranes providing local membrane perturbations to promote lipid mixing (Poirier *et al*., 1998; McNew, 2008; Blumenthal *et al*., 2003).

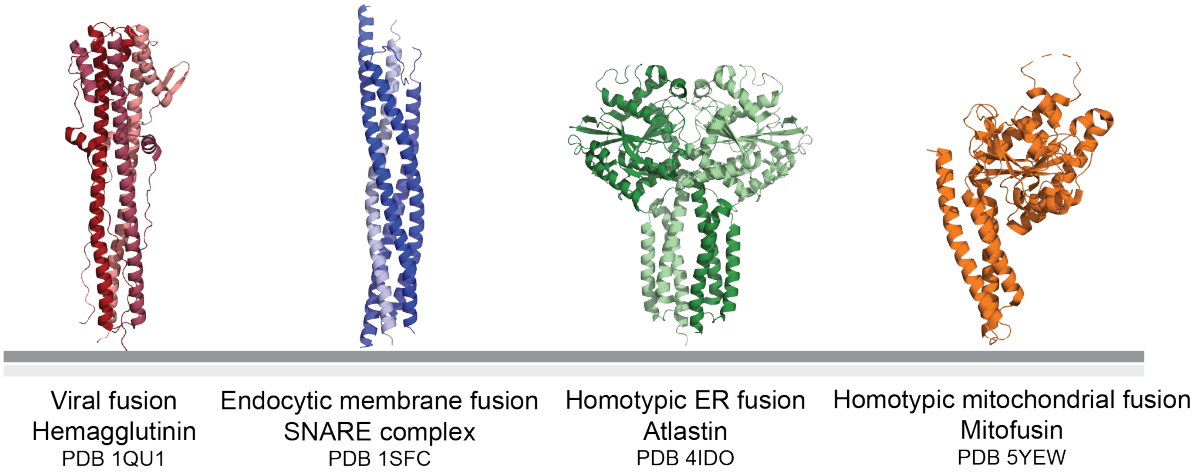


**Figure 1.2 Proteins responsible for different modes of membrane fusion.** Cartoon representations of membrane fusion proteins displayed with relative membrane insertion orientation (membrane as the grey lines). **(A)** Hemagglutinin homotrimer (HA2) (PDB 1QU1; Chen *et al*., 1999). **(B)** Structure of the SNARE complex involved in synaptic exocytosis, composed of syntaxin-1A, synaptobrevin-II and SNAP-25B (PDB 1SFC; Sutton *et al*., 1998). **(C)** Homodimer of human atlastin 1 bound to GDP•$AlF_4^-$ (PDB 4IDO; Byrnes *et al*., 2013). **(D)** Human mitofusin 1 minimal GTPase domain bound to GDP•$BeF_3^-$ (PDB 5YEW; Yan *et al*., 2018).

These well-studied systems delineate how membrane fusion is catalyzed using the energy of favorable protein folding events. However, another mechanism relies on mechanochemical energy of GTP hydrolysis and is carried out by members of the dynamin-related protein (DRP) family. While several DRP members, including the namesake, dynamin, function in membrane

fission, several members catalyze membrane fusion. Given the fundamental differences in how these enzymes approach overcoming the energy barrier in membrane fusion, numerous questions arise surrounding the mechanisms of action, regulation, and consequences for cellular health.

**The dynamin superfamily**

Most dynamin superfamily members play a role in membrane remodeling in various organelles using mechanochemical force fueled by GTP hydrolysis (Ford and Chappie, 2019). Dynamin and Drp1 catalyze membrane fission at the plasma membrane (PM) and mitochondria, respectively. Conversely, mitofusins (Mfn1 and Mfn2) and optic atrophy 1 (OPA1) catalyze homotypic fusion of the outer and inner mitochondrial membrane, respectively, while atlastins (ATL1-3) fuse endoplasmic reticulum (ER) tubules to establish a peripheral, reticular tubule network (Praefcke and McMahon, 2004; Daumke and Praefcke, 2016; Jimah and Hinshaw, 2019). Other members function in processes such as interferon-induced pathogen resistance, such as MxA and MxB (Gao *et al.*, 2011) and guanylate binding proteins (GBP1-7) (Prakash *et al.*, 2011; Daumke and Praefcke, 2016), or regulation of endocytic recycling via EHD1-4 (Naslavsky and Caplan, 2011), (Figure 1.3A-B).

Dynamin superfamily members are composed of several conserved domains including a large, N-terminal G domain, a stalk-like middle domain, and a membrane association domain (Figure 1.3C). Dynamin's large G domain is a member of the GAD family (G proteins activated by dimerization) and is responsible for hydrolysis of GTP to GDP and inorganic phosphate ($P_i$) (Gasper *et al.*, 2009). The large G domain is composed of a conserved core, characteristic of all G proteins, with protein-specific insertions throughout (Praefcke and McMahon, 2004). These G domains differ from small, regulatory G proteins not only in size, but in intrinsic GTP binding and hydrolysis rates, with dynamins retaining a low binding affinity and high intrinsic turnover efficiency. In contrast, small G proteins have higher binding affinities for GTP but require external

stimulation of hydrolysis from a GTPase-activating protein (GAP) and release of GDP by a guanine exchange factor (GEF) (Ferguson and De Camilli, 2012; Praefcke and McMahon, 2004; Jimah and Hinshaw, 2019).

Following the G domain is an α-helical stalk domain (middle domain), which varies both in length and structure amongst family members. A significant rigid body rotation occurs between the G and middle domains through the GTP hydrolysis cycle (Daumke and Praefcke, 2016). The C terminus contains protein-specific features, including either a transmembrane domain, pleckstrin homology (PH) domain, or lipid modification for insertion/association with cognate membranes; a GTPase effector domain (GED) for regulation of GTPase activity; and/or proline-rich domain for binding Src-homology 3 domain (SH3) containing proteins (Ferguson and De Camilli, 2012; Praefcke and McMahon, 2004).

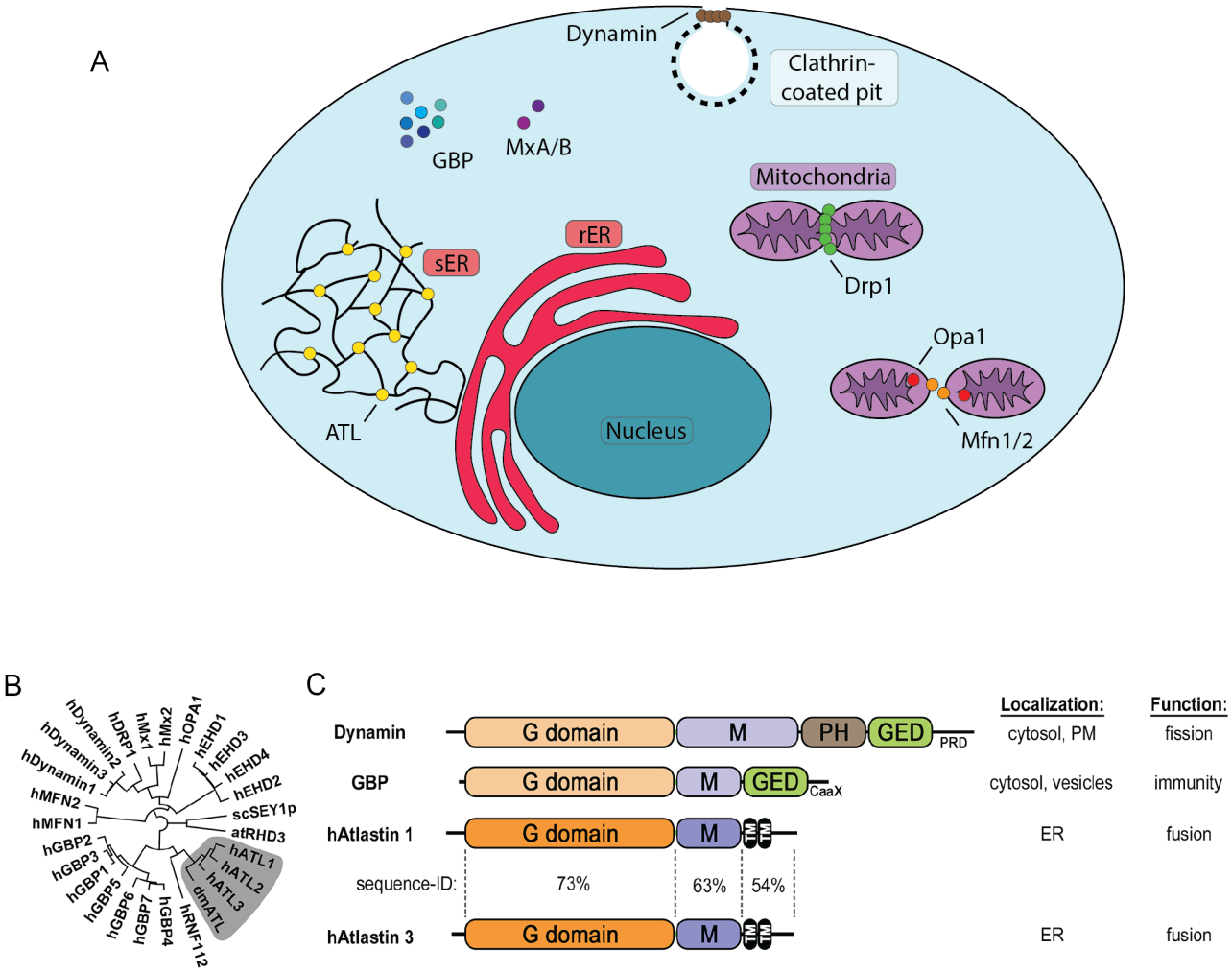


**Figure 1.3. Dynamin superfamily members. (A)** Localization of dynamin superfamily members in the cell. Dynamin (brown circles) is recruited to the stalks of developing clathrin-coated pits and catalyzes fission upon polymerization-dependent GTPase stimulation. Drp1 (green circles) promotes mitochondrial fission in a similar manner, while Mfn (orange circles) catalyzes fusion of the outer mitochondrial membrane and Opa1 (red circles) of the inner mitochondrial membrane. ATL (yellow circles) fuses tubules of the smooth ER tubules (sER) to create 3-way junctions. GBP and MxA and MxB act primarily in the cytosol in pathogen resistance in an interferon-dependent manner. **(B)** Phylogeny tree of dynamin related proteins representing the evolutionary relationship. **(C)** Domain architecture of dynamin and the closely related GBP with ATL. ATL1 and ATL3 are shown here with sequence identity as they are the least similar of the ATL isoforms. G domains are in orange at the N-terminus (left), middle domains are in purple, and distinct features are at the C-terminus (left): PH domain in brown, GED in green, and TM domains in black.

Although many structural components are conserved, the mechanisms of action amongst these proteins varies depending on their function. In membrane fission by dynamin or DRP1, GTP-bound protomers are recruited to target membranes and oligomerize in helical rings, which stimulates GTP hydrolysis-dependent conformational changes yielding a "pinching off" action that leads to fission of the membrane (Kalia *et al*., 2018; Chappie *et al.*, 2011). Homotypic membrane fusion by ATL and MFN is triggered by homo-dimerization across *trans* membranes, bringing the membranes in close proximity for fusion (Bian *et al*., 2011; Byrnes and Sondermann, 2011; Yan *et al*., 2018). Details of these mechanisms will be explored below.

**Human atlastins**

*The endoplasmic reticulum*

The ER is a complex organelle consisting of multiple domains, each of which has crucial and distinct functions, morphologies, and protein compositions, while retaining connectivity through a single lumen. At its center, the nucleus is encompassed by the nuclear envelope (NE) composed of two phospholipid bilayers, surrounded by the rough ER (rER), which is characteristically formed by sheets studded by ribosomes and translocation complexes (e.g., SEC61β) that promote transfer into the rER lumen of newly synthesized proteins requiring post-translational processing and/or membrane targeting and trafficking (Voeltz *et al*., 2002; Park and Blackstone, 2010).

At the periphery of the cell, the ER is no longer decorated by ribosomes and translocons as its sheets transition into smooth tubules that extend to the PM, forming a reticular network as tubule ends throughout the cell tether and fuse to create ubiquitous three-way junctions. The smooth ER (sER) is critical in release and restoration of ER $Ca^{2+}$ levels as a function of myriad signaling pathways, as well as lipid and sterol metabolism and their subsequent distribution to organelles through membrane contact sites (MCS). The high-curvature of ER tubules is stabilized by a class of positive curvature-inducing proteins including reticulons and DP1/REEPs (Yop1 in

yeast) that contain hairpin-like transmembrane domains, acting as a wedge in the phospholipid layer (Zurek *et al*., 2011; Voeltz *et al*., 2006). Several of these membrane-shaping proteins interact with and/or modify microtubules as a means to structurally coordinate the ER to the cytoskeleton (Park *et al*., 2010; Lumb *et al*., 2012). Microtubules are intricately intertwined in maintenance of ER morphology by actively distributing ER structures, specifically tubules, throughout the cell (Terasaki *et al*., 1986). However, formation of a polygonal ER tubule network is not dependent on the presence of microtubules (Dreier and Rapoport, 2000).

Adding to the complexity of the ER is its dynamic nature. The ratios of rER to sER varies depending on cell type, developmental stage, species, phase of the cell cycle, and environmental stimuli. For example, cells with high secretory loads require more rER to support protein synthesis and processing, while mitotic cells must completely disassemble their nuclear envelopes then coordinate their reformation in two daughter cells (Terasaki *et al*., 2001; McCullough and Lucocq, 2005; English *et al*., 2009). It has been shown that overexpression or knockdown of ER structural proteins will push the ratio of sheets to tubules in one direction or the other (Voeltz *et al*., 2006), but further study is required to understand how cells regulate these morphological dynamics on an organelle-level.

*Atlastin in the ER*

Atlastin (ATL) was first identified as a mutational hotspot in the neurodegenerative disease hereditary spastic paraplegia (HSP) (Zhao *et al.*, 2001). In subsequent studies, ATL was renamed to ATL1 as two other human isoforms were identified (ATL2 and ATL3), all of which localized primarily to the ER, with minimal localization of the *cis* Golgi cisternae (Zhu *et al*., 2003; Rismanchi *et al*., 2008). All mammals retain these three isoforms while other eukaryotes (such as yeast and invertebrates) encode only one isoform. This may indicate divergent functions for the mammalian isoforms, which have high sequence similarity with the highest identity in the GTPase domain and greater divergence at the N- and C- termini (Zhu *et al.*, 2003). The three human ATL isoforms are

differentially expressed in human tissues, with ATL1 primarily in the brain, especially the pyramidal cells of the cerebral cortex and hippocampus (Zhu *et al.*, 2003), while ATL2 and ATL3 are more ubiquitously expressed (Rismanchi *et al*., 2008). At the cellular level, while all three isoforms localize to the tubular ER, ATL1 and ATL2 are more evenly distributed along the tubules while ATL3 is also observed at small puncta at 3-way junctions (Rismanchi *et al*., 2008).

It was first suggested that ATL plays a role in controlling ER morphology when it was observed that expression of catalytically dead mutant protein in mammalian cells resulted in long, unbranched ER tubules (Rismanchi *et al*., 2008), which has been corroborated by subsequent studies (Zhao *et al.*, 2016; Hu *et al*., 2009; Hu *et al*., 2015). This function was confirmed by several pivotal reports the next year. The first report identified that ATL was the minimal machinery necessary for membrane fusion *in vitro* using the *D. melanogaster* ATL homolog (dmATL) reconstituted in proteoliposomes (Orso *et al*., 2009). Fusion was dependent on ATL-catalyzed GTP hydrolysis. The second report demonstrated that a reticular structure could be created *in vitro* using the microsomal fraction from *X. laevis* eggs upon the addition of GTP (Hu *et al*., 2009). This process was inhibited with the addition of ATL-specific antibodies or ATL's cytosolic domain. A more recent study has now demonstrated that ATL is the minimal machinery necessary in the formation of an *in vitro* reticular ER-like structure using only proteoliposomes, purified dmATL, and GTP (Powers *et al*., 2017).

The G and middle domains of ATL constitute its catalytic core, conferring nucleotide binding and hydrolysis comparable to that of full length (FL) ATL (Wu *et al*., 2015; Moss *et al*., 2011), as well as nucleotide-dependent dimerization. ATL dimerizes in the presence of non-hydrolyzable GTP analogs and the transition state analog, GDP•$AlF_4^-$, while remaining monomeric in GDP-bound or apo states (Byrnes *et al*., 2013; O'Donnell *et al*., 2017). Critically, the catalytic core can functionally interact with the FL ATL in a nucleotide- and hydrolysis-dependent manner, demonstrated by its ability to act as a concentration-dependent inhibitor of *in vitro* membrane fusion (Bian *et al*., 2011; Moss *et al*., 2011), *in vitro* reticular ER network formation (Wang *et al*.,

2013), and its dominant negative effect on reticular ER formation in mammalian cells (Moss *et al*., 2011).

Curvature-inducing membrane proteins of the ER's tubules have been shown to interact directly through their membrane domains as a means of coordinating morphology and dynamics of the sER (Park and Blackstone, 2010; Hu *et al.,* 2009, Rismanchi *et al*., 2008, Sanderson *et al.,* 2006; Chang *et al.,* 2013; Shibata *et al.,* 2008). These proteins include members of the DP1/Yop1 family, of which humans have six (REEP1-6) and yeast have one (Yop1), as well as the reticulon family, of which humans have four (Rtn1-4) and yeast have two (Rtn1-2). While DP1/Yop1 and reticulon proteins function primarily in establishing positive curvature of tubules through the action of their wedge-like hairpin transmembrane domains, REEP1-4 are also known to bind microtubules through their C terminus (Park *et al.,* 2010). Other proteins known to interact with ATLs in this manner are spastin, a HSP-associated protein that functions in microtubule binding and severing (Rismanchi *et al*., 2008; Sanderson *et al.,* 2006; Evans *et al*., 2006; Park *et al*., 2010; Lee *et al*., 2009), as well as protrudin, which is also an SGP mutant (Chang *et al.,* 2013). Lunapark works in opposition to ATLs by stabilizing newly formed three-way junctions by forming oligomers (Wang *et al*., 2016; Chen *et al.,* 2015), and by targeting ATL for degradation through ubiquitination in plants (Sun *et al*., 2020). A careful balance of each protein must be sustained in order for proper ER function.

*Atlastin's Orthologs*

*Sey1p*: Yeast have a single ATL functional and structural ortholog, Sey1p (synthetic enhancer of Yop1), which localizes to the reticular ER in *S. cerevisiae*, and interacts with Yop1 and yeast reticulons (Hu *et al.,* 2009). Sey1p works in conjunction with the ER SNARE Ufe1p to support ER morphology in yeast (Anwar *et al*., 2012), and catalyzes membrane fusion through a mechanism similar to that established for ATL (discussed below) (Yan *et al*., 2015). A new study suggests that Sey1p's major role is actually in membrane tethering with minimal, GTP hydrolysis-

independent fusion (Kim *et al.,* 2017). Sey1p requires Yop1p to synthesize an *in vitro* ER tubule network, unlike ATL which did not require additional factors (Powers *et al.*, 2017).

*RHD3*: Plants express three ATL analogs, called RHD3 (root hair defective 3), having been first identified in an *Arabidopsis thaliana* genetic screen looking for plants with defective root hair growth (Chen *et al*., 2011). It has since been shown to play a similar role in the ER as ATL with a similar catalytic mechanism (Sun and Zheng, 2018). A motivation for studying RHD3 has been the parallel drawn between the short, wavy root hair phenotype observed in RHD3-defective plants and the retrograde axonal degeneration seen in HSP patients with mutant forms of ATL1 (Zheng and Chen, 2011).

*dmATL*: Invertebrates have one ATL isoform, homologous to hATL1, which regulates ER morphology and is the minimal machinery required for ER fusion (Orso *et al.,* 2009; Powers *et al*., 2017). Since its discovery, this isoform has been studied extensively due to the fact that purified, FL dmATL has been shown to be fusion competent *in vitro*, while human ATL1 has not yet been shown to be so (Wu *et al*., 2015, Betancourt-Solis *et al*., 2018). Accordingly, it has been used as a model for characterization of FL ATL1, as it can functionally replace hATL1 in tissue culture, the soluble domain behaves in a similar pattern and there is high sequence similarity covering the protein's core domains (Wu *et al*., 2015; Liu *et al.,* 2015; Liu *et al*., 2012; Pendin *et al.*, 2011; Betancourt-Solis *et al*., 2018).

*ATL Structural domains*

In recent years, extensive investigation has been carried out to determine ATL's detailed mechanism. Much of this work began by identifying the functional and structural basis of ATL's domains, explored here.

*N-terminus:* The first 33 residues of ATL1 (59 in hATL2 and 25 in hATL3) were identified as being highly variable across isoforms but conserved across species' homologs early in the

study of ATLs (Zhu *et al.*, 2003), however it has never been functionally characterized. Until this time, none of the solved structures have been able to resolve this region. However, Chapter 2 will address novel regulatory functions attributed to the N-terminus.

*G domain:* ATL's GTPase domain (G domain) is highly conserved within the dynamin related protein family and is responsible for the binding and hydrolysis of GTP to GDP and $P_i$. The ATL G domains contain four canonical GTP-binding motifs: 1) G1/P-loop, which coordinates the inorganic phosphates, 2) G2/Switch 1/Walker A, which helps coordinate a $Mg^{2+}$ ion, 3) G3/Switch 2/WalkerB, which helps coordinate the γ phosphate and the $Mg^{2+}$ ion, and 4) G4 which coordinates the guanidine base (Praefcke and McMahon, 2004). ATLs and GBPs retain a characteristic "RD" motif", deviating from the conserved N/TK/RxD in the G4 sequence (Praefcke and McMahon, 2004).

*Linker region:* This is a short region (10 residues) between the G and middle domains that interconverts between two conformations to allow the rigid-body rotation of the G and middle domains from the engaged, pre-hydrolysis monomer to transition state and post-hydrolysis crossover dimer (Byrnes and Sondermann, 2011; Bian *et al*., 2011).

*Middle domain:* The middle domain is composed of a three-helix bundle proceeding the short linker region. In the pre-fusion state, the middle domain interacts with an adjacent area of the G domain in what is termed the "engaged state", making the GTP-binding site accessible. In the post-fusion state, the two middle domains take on a parallel conformation within the homodimer (Byrnes and Sondermann, 2011; Bian *et al.*, 2011; Byrnes *et al*., 2013). Although the middle domain does not interact directly with GTP, it is essential in supporting membrane fusion. The G domain alone is not capable of dimerization, and this is partially rescued with the *trans* addition of the middle domain (Moss *et al.*, 2011; Byrnes *et al.*, 2013). The middle domain's close proximity to the transmembrane domain is also crucial for ATL's fusion activity, with significantly reduced fusion when additional residues are added between these regions (Pendin *et al.*, 2011).

*Transmembrane domain:* The transmembrane domain is composed of two hydrophobic regions predicted to span the ER membrane, creating a “hairpin” structure (Hu *et al*., 2009). The main functions of this domain are to anchor ATL to the ER and facilitate nucleotide-independent oligomerization with other ATL molecules (Liu *et al.*, 2012; Rismanchi *et al*., 2008; Zhu *et al*., 2003), as well as other tubule-shaping proteins (discussed above). dmATL fusion activity is dependent on this domain, as when it is replaced in chimeric mutants with TM domains from other integral membrane proteins or shortened to contain only one hydrophobic region, fusion is ablated while GTPase activity is largely unaffected (Liu *et al*., 2012, Betancourt-Solis *et al*., 2018; Liu *et al.,* 2015). Despite this apparent specificity, it has been reported that no major conformational changes occur in this region during fusion, as is seen with other fusion proteins (Betancourt-Solis *et al*., 2018). Recently it has been proposed that, rather than creating a hairpin-like structure, each TM region forms a “V” in the outer lipid layer, resulting in a “W” shape (Betancourt-Solis *et al*., 2018). With this model, ATLs would have a greater role in inducing tubule curvature, in agreement with the fact that dmATL alone is capable of reconstituting an *in vitro* reticular tubule network (Betancourt-Solis *et al*., 2018; Powers *et al.*, 2017).

*C-terminal helix:* The last structural element is an amphipathic, C-terminal helix (CTH), which is required for fusion activity (Moss *et al.*, 2011; Faust *et al*., 2015; Liu *et al*., 2012). It is thought that this helix promotes fusion by introducing acyl chain disorder and membrane thinning, helping to lower the energy barrier for a fusion event (Faust *et al*., 2015). This is also supported by the evidence that the CTH can be added to a fusion reaction in trans to rescue activity of a ΔCTH mutant protein (Liu *et al*., 2012). The region of the CTH most proximal to the second TM region (~25 residues) is most conserved across species, and it has been shown that most of the fusion-supporting activity of the CTH is retained within this region (Faust *et al*., 2015).

*Catalytic mechanism*

The current model for ATL's catalytic mechanism is based on the conformations observed in catalytic core structures in various conformations when bound to different nucleotide and subsequent biochemical and biophysical experiments detailing the dynamics of each step (Figure 1.4) (Byrnes and Sondermann, 2011; Bian *et al.*, 2011; Byrnes *et al*., 2013; Liu *et al.,* 2015, O'Donnell *et al*., 2017). Generally, two ATL monomers, presumably on *trans* membranes, begin the cycle in the engaged state, leaving the nucleotide binding site accessible, allowing for GTP binding (~ 0.025sec) (Figure 1.4A). GTP binding is followed shortly by release of the middle domain (~ 0.1 sec) and initiation of GTP hydrolysis (~0.1 sec) (Figure 1.4B), proceeded first by dimerization of the G domains (~0.14 sec), and subsequently the middle domains (~0.17 sec). As shown in Figure 1.4C, the two ATL protomers form a tight crossover dimer in the intermediate stage (observed with the transition state analogue GDP•$AlF_4^-$), which promotes fusion through proximity of the membranes and bilayer disordering by the CTH. Inorganic phosphate is released after ~1.5 sec allowing the crossover dimer to relax. Release of GDP is an essential prerequisite for subsequent rounds of GTP hydrolysis, which is crucial as continuous hydrolysis is needed in effective membrane fusion (Liu *et al*., 2015). A recent ATL3 catalytic core structure revealed a critical residue (R109; R113 in ATL1) that facilitates GDP release by displacing the catalytic $Mg^{2+}$ and stabilizing a more open active-site conformation through post-hydrolysis hydrogen bonding. Corroborating evidence for this mechanism was presented for both ATL1 and ATL3 (O'Donnell *et al*., 2017).

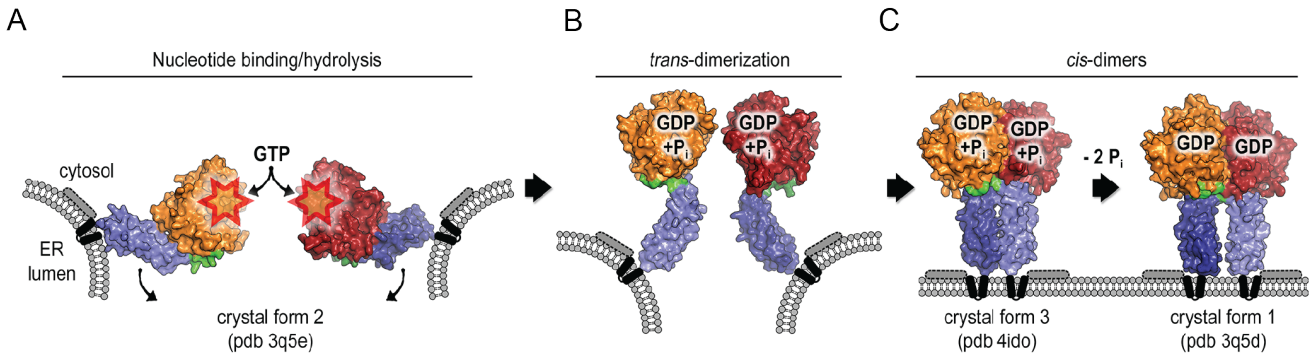


**Figure 1.4 Mechanism of ATL-mediated membrane fusion. (A)** ATL protomers on *trans* membranes are in the pre-hydrolysis, engaged conformation with contacts between the G (orange and red) and middle domains (purple), allowing GTP binding. Represented in crystal form 2, PDB 3Q5E, with the TM and CTH shown as cartoon representation on the membrane. **(B)** GTP hydrolysis is initiated by ATL monomers, releasing the engaged state. **(C)** Formation of a tight crossover dimer occurs with a transition state homolog (GDP•$AlF_4^-$; PDB 4IDO), which relaxes into a loose, parallel crossover dimer after hydrolysis (PDB 3Q5D). Protomers must reset before subsequent hydrolysis rounds.

Some studies have reported that GTP hydrolysis in ATL occurs after dimerization, as is observed with the oligomerization-dependent hydrolysis mechanism of dynamin (Bian *et al*., 2011; Morin-Leisk *et al*., 2011; Liu *et al*., 2015; Hu and Rapoport, 2016). However, there is substantial evidence demonstrating that ATL dimerization on a biologically relevant time scale requires at least the initiation of GTP hydrolysis. Although ATL does dimerize when bound to non-hydrolyzable or transition state nucleotide analogs (GppNHp and GDP•$AlF_4^-$, respectively), it occurs over the course of minutes rather than milliseconds. Similar time scales are observed with the ATL1 R77A point mutation that can bind nucleotides but is catalytically dead (Byrnes *et al*., 2013; O'Donnell *et al*., 2017). Importantly, rapid release of the pre-hydrolysis, engaged conformation (Figure 1.4A) only occurs in the presence of GTP, not its non-hydrolyzable analogs (O'Donnell *et al*., 2017). This release is a necessary pre-requisite for crossover dimer formation, supporting a model in which initiation of GTP hydrolysis is a requisite step for rapid dimerization.

Most members of the dynamin superfamily retain a conserved hydrolysis mechanism in which a monovalent cation directly coordinates the hydrolysis intermediate analog GDP•$AlF_4^-$ (Chappie *et al*., 2010). However, ATLs and the closely related GBPs instead utilize a conserved Arg residue (R77 in ATL1) in the P loop to carry out this same function, acting as an internal Arg finger (Byrnes and Sondermann, 2011; Bian *et al*., 2011; Ghosh *et al*., 2006). A similar mechanism has been described for Ras GTPases, although it is supplied *in trans* by a GTPase activating protein (Scheffzek *et al*., 1998).

## ATL in hereditary neuropathies

### *Hereditary Spastic Paraplegia*

Hereditary spastic paraplegias (HSPs) are a rare group of notably diverse neuropathies (both genetically and symptomatically) that result from axonal degeneration of motor neurons beginning at their distal ends (DeLuca *et al*., 2004; Fink, 2013; Fink, 2006; Blackstone, 2012). Causative mutations have been identified in up to 80 SPG (spastic gait) genes, with mutations in ATL1 accounting for approximately 10% of all cases, second only to *SPG4* (encoding spastin) (Zhao *et al*., 2001), and are the leading cause of early onset cases (Abel *et al*., 2004). Clinically, HSP presents as either “pure” or “complex”, with pure cases manifesting with progressive bilateral spasticity and weakness in the lower extremities, resulting in a characteristic spastic gait, with few additions such as urinary issues caused by bladder spasms. Complex cases present further neurological symptoms including visual impairment, intellectual disability, epileptic seizures, ataxia, and amyotrophy (Fink, 2013; Blackstone, 2018). The incidence rate of HSP is between 1.2 to 9.6 out of every 100,000 people (Fink, 2013; Willkom *et al*., 2016; Blackstone, 2018; Klebe *et al*., 2015; Blackstone, 2012), which are composed of cases of autosomal dominant, autosomal recessive, X-linked recessive, and mitochondrial modes of inheritance.

HSPs associated with mutations in ATL1 usually present as pure, autosomal dominant cases with slow disease progression (Battini *et al*., 2011; Depienne *et al*., 2007; Fink, 2006). A

majority of these cases are caused by missense mutations (Klebe *et al*., 2015; Zhu *et al.*, 2003; Zhao and Liu, 2017; Xiao *et al*., 2019) resulting in either truncated gene products, insoluble protein, or loss-of-function enzyme activity (O'Donnell *et al*., 2018; Byrnes and Sondermann, 2011; Meijer *et al*., 2007; Bian *et al*., 2011; Ulengin *et al*., 2015; Liu *et al*., 2019). Although these are primarily loss-of-function mutations, the most common mode of inheritance for ATL1 mutants is autosomal dominant presumably due to the formation of mixed dimers in the cell, trapping WT protein in non-productive complexes and reducing the effective concentration of functional ATL1. When expressed in mammalian tissue culture, ATL1 HSP mutant variants result in ER morphologies ranging from aggregated bundles and globules, puncta, unbranched tubules, and a shifted ratio of tubules to sheets (Botzolakis *et al*., 2011; Namekawa *et al*., 2007; Rismanchi et al., 2008; Ulengin et al., 2015; Liu et al., 2019; Montagna et al, 2020). The three most commonly mutated proteins in HSP, spastin (SPG4), ATL1, and REEP1 (SPG31), all localize to the tubules of the smooth ER and play crucial roles in maintaining its reticular, polygonal morphology; additional ER-shaping proteins known to cause HSP include reticulon-2 (SPG12), Arl6IP1 (SPG61), Rab3Gap2 (SPG69), protrudin (SPG33), and REEP2 (SPG72) (Blackstone, 2018).

While membrane tethering and fusion is ATL's most well-studied function, there is little evidence supporting that disruption of ER morphology alone would likely function as the only pathogenic mechanism in HSP. However, in an effort to uncover this mechanism, many studies have drawn links to less understood cellular functions of ATL1, the most prominent being a close functional link to the bone morphogenetic protein (BMP) signaling pathway. A number of neuronal and developmental processes have been linked to BMP signaling, including axonal transport and outgrowth guidance, formation and expansion of neuromuscular junctions, and regulation of the microtubule cytoskeleton, which is closely intertwined with the ER (Fassier *et al*., 2010; Wang *et al*., 2007). ATL1 along with several of its binding partners (NIPA1, spastin, and spartin) all appear to act as inhibitors to BMP signaling; when functional protein levels are altered, as they are in HSP, BMP signaling levels increase (Fassier *et al*., 2010; Summerville *et al*., 2016; Zhao and

Hedera, 2013; Zhao *et al*., 2016). It has been proposed that ATL1 aids in regulating accessible receptor levels on the cell surface through endocytic recycling (Summerville *et al*., 2016; Fassier *et al*., 2010).

ATL1 has also been implicated in other aspects of neuronal development and function, including enrichment at axonal growth cones (Zhu *et al*., 2006), regulation of dendritic spine formation (Shih and Hsueh, 2016), accumulation in areas of neuronal regeneration (Rao *et al*, 2016), formation of neuromuscular junction synapses, and organization of organelles in the post-synaptic muscle (Lee *et al*., 2009). When normal ATL1 function is disrupted in neurons through decreased expression or introduction of a HSP mutant, resulting effects range from abnormal axonal branching (Fassier *et al*., 2010) and inhibited elongation (Zhu *et al*., 2006) to impaired motor neuron synaptic function and axonal organelle organization (De Gregorio *et al*., 2017) and decreased neurotransmitter release (Summerville *et al*., 2017). ATL1 HSP mutants in animal models (*Drosophila melanogaster* and *Danio rerio*) closely parallel aspects of disease in humans including a number of mobility defects and disrupted axonal development (Fassier *et al*., 2010; De Gregorio *et al*., 2017; Summerville *et al*., 2016; Lee *et al*., 2008). Additional phenotypes include shortened life span, sterility, defects in microtubule dynamics, neurotransmitter release, synapse formation, and accumulation of aggregated membrane and protein in a length-dependent manner along motor neuron axons, which is a hallmark of neurodegenerative disease (Lee *et al*., 2008; De Gregorio *et al*., 2017; Lee *et al*., 2009; Summerville *et al*., 2016; Fassier *et al*., 2010). The study of ATL1 and other proteins mutated in this disease paradigm continues to yield insight to basic cellular functions.

*Hereditary Sensory Neuropathy*

Similar to HSPs, sensory neuropathies cause axonal degeneration of distal sensory neurons, causing a range of symptoms from local numbness to a complete lack of pain sensation. This often results in injury or abnormal weight-bearing patterns leading to bone injury (Kornak *et*

*al*., 2014). Familial mutations in both ATL1 and ATL3 have been implicated as causative in HSN (Guelly *et al*., 2011; Fischer *et al*., 2014; Kornak *et al*., 2014; Behrendt *et al*., 2019; Krols *et al*., 2018).

**Additional functional roles of ATL**

*Viral and bacterial proliferation:* Several classes of viral and bacterial pathogens have been found to coopt ATL's membrane-remodeling activity upon cellular infection to promote pathogen replication. Such a link has been reported in flaviviruses (Neufeldt *et al*., 2019; Monel *et al*., 2019), *Legionella pneumophila* (Steiner *et al*., 2017), and HIV-1 (Shen *et al*., 2017). In the cases of the first two pathogens, ER-derived membranes are sequestered to support formation of a replication vacuole. It is hypothesized that ATL isoforms function in the formation and maintenance of the vacuoles. In the case of HIV-1, a direct mechanism has not been identified.

*Lipid droplets:* Lipid droplets (LD) are the main storage mechanism for neutral lipids in eukaryotic cells and maintain a tight physical association with the ER, where many of the lipid synthesis enzymes reside. Several studies have identified a role for ATL1, in conjunction with REEP1, in regulating LD size (Klemm *et al.,* 2013; Falk *et al*., 2014). Direct interaction of ATL1 with the neuronal isoform of carnitine palmitoyl-transferase (*CPT1C*), which is both a regulator of LD biogenesis as well as a novel causative HSP mutant, have been observed (Rinaldi *et al*., 2015). More generally, mammalian cells lacking endogenous ATL displayed defects in adipocyte differentiation (Zhao *et al*., 2016).

*Cell cycle and the nuclear envelope*: During mitosis, the ER undergoes drastic morphological changes, with the complete breakdown of the nuclear envelope and changes in tubule to sheet ratios. While there is contradictory evidence as to whether there is a shift towards tubules (Puhka *et al*., 2007), cisternae (Lu *et al.*, 2009; McCullough and Lucocq, 2005), or small, interspersed sheets (Wang *et al.*, 2013), there is a unified theme of altered morphology. As one of the major ER morphological determinants, it follows that ATL plays a role in controlling these

dynamics, which was confirmed with *in vitro* experiments (Wang *et al*., 2013). The same study found that reformation of the nuclear envelope in post-mitotic cells relies on ER fusion catalyzed by ATL and an unidentified ER SNARE. Even during interphase, ATL sustains nuclear envelope homeostasis by promoting proper targeting of inner nuclear envelope membrane proteins (Pawar *et al*., 2017).

*Membrane contact site:* The reticular ER maintains membrane contact sites (MCS) with most organelles to specifically modulate membrane compositions through lipid transfer and to regulate cytosolic $Ca^{2+}$ concentrations in response to signaling events (Phillips and Voeltz, 2016). ATL has been implicated in a number of contact sites, including at ER-mitochondria (Lin and Liou, 2017) and ER-PM (Manfard *et al*., 2012) sites. There is also evidence that ATL and Rtn4 play a role in store-operated calcium entry (SOCE) at the PM to replenish ER lumenal $Ca^{2+}$, emphasizing the critical role ER morphology plays in proper MCS regulation (Li *et al*., 2017; Jozsef *et al*., 2014). This has been proposed as a mechanism of pathogenesis in HSP, as dysfunctional SOCE pathways have been shown to eliminate neurite outgrowth (Li *et al*., 2017).

*ER-phagy*: Selective autophagy of the ER (ER-phagy) can occur in response to starvation conditions or damage to the organelle. Several groups have identified that ATLs function in this pathway either through direct interactions with an Atg8 family member (Chen *et al*., 2019) or a more general link between ATL expression levels and extent of ER-phagy in a pathway downstream of the Fam134B receptor (Liang *et al*., 2018).

*Neurological health implications*: Beyond HSP and HSN, ATLs have been implicated in several other neurological disorders. Expression levels of ATL1 in patients with temporal lobe epilepsy was found to be significantly decreased, and a direct link was drawn between expression levels and seizure occurrence (Lu *et al*., 2020). A different study identified significantly increased expression levels of ATL3 in patients with schizophrenia (Piras *et al*., 2019). Mechanisms for these trends have not yet been described.

*Regulation of ATLs in cancer:* A report quantifying differential expression of membrane proteins in glioblastoma patients identified increased expression of ATL3 (Polisetty *et al*., 2012), which led us to some preliminary investigation of ATLs in cancer cells. We found that while ATL3 is upregulated in a number of tumor types, ATL1 is downregulated in several types. In collaboration with Dr. Ben Deneen at Baylor College of Medicine, we found that in oncogenic Ras-derived murine glioblastoma tumors had increased ATL3 expression and decreased ATL1 expression compared with control tumor tissues. While several proliferation and colony formation experiments corroborated this general trend between oncogenic behavior and ATL expression, the mechanism remains elusive.

**Regulation of G proteins**

*Stimulation and regulation of Dynamin's GTPase activity*

The regulation of dynamin's membrane fission activity has been well characterized, revealing multiple regulatory modes. Dynamin exists in the cytosol in a nucleotide-free and autoinhibited state as a tetramer, which is maintained by numerous low-affinity interactions, allowing for release of this state through various mechanisms (Reubold *et al*., 2015). Dynamin is recruited to sites of growing endocytic vesicles on the PM through interactions between its PRD and SH3 domain-containing proteins, such as endophilin, intersectin, syndapin, and amphiphysin (Jimah and Hinshaw, 2019). Dynamin interacts with the negatively charged phosphoinositide lipids through its positively charged PH domain, which undergoes a conformational switch from a closed state that inhibits oligomerization to an open state that promotes it (Srinivasan *et al*., 2016).

As dynamins are recruited to the PM, they form higher-order oligomers around the vesicular stalk in the form of helical rungs. Dynamins form dimers through their stalk domains, then tetramers through additional stalk domain contacts between dimer pairs (Faelber *et al*., 2011; Antonny *et al*., 2016; Jimah and Hinshaw, 2019). G domains from adjacent helical rungs dimerize, allowing stimulation of GTP hydrolysis rates about 100-fold, due to stabilization of a catalytic

cation by *trans* residues at the interface (Chappie *et al*., 2010). The bundle signaling element (BSE) is composed of helices from both the N- and C- termini of the G domain as well as one proceeding the stalk domain. Due to its composition, the BSE is particularly adept at its job of sensing the nucleotide-bound state of the GTPase domain and transmitting this signal through a significant conformational change, contributing to dynamin's power stroke (Chappie *et al*., 2009). It is noteworthy that ATL lacks a BSE-like regulatory domain, raising questions regarding GTPase regulation. These intrinsic mechanisms of dynamin provide spatiotemporal regulation to direct its activity and prevent futile hydrolysis cycles.

Dynamin activity is also regulated by post-translational modification, especially by phosphorylation. Depending on the residue modified, dynamin phosphorylation may either promote or inhibit endocytosis by affecting its propensity for oligomerization, membrane recruitment, or GTPase activity (Kar *et al*., 2017; Srinivasan *et al*., 2018). For example, in neurons, dynamin I is phosphorylated by cyclin-dependent kinase 5 (cdk5) within the PRD, then upon neuronal stimulation, it is rapidly dephosphorylated by calcineurin, resulting in recruitment to sites of synaptic vesicle endocytosis (Smillie and Cousin, 2005). Another well-studied phosphorylation event occurs in a c-Src-mediated manner upon epidermal growth factor receptor (EGFR) stimulation, causing internalization of the activated receptor upon promotion of dynamin self-assembly (Ahn *et al*., 2002; Cao *et al*., 2010).

*Small G protein regulation via a C-terminal hypervariable region*

Small G proteins, such as Ras, play critical roles in signal transduction pathways by acting as a molecular switch, toggling between an "on" GTP-bound state and an "off" GDP-bound state, regulating activation of downstream effectors. The four main human Ras isoforms: H-Ras, N-Ras, K-Ras4A, and K-Ras4B, exert distinct signaling outcomes despite having similar binding partners and their N-terminal G domains having 90-100% sequence identity (Hancock, 2003). Rather, these variations stem from a short, hypervariable region (HVR) at their C terminus. While the last

four residues retain a CAAX motif, which receives a farnesyl modification on the cysteine, each isoform differs in a second signal, with H-, N-, and K-Ras4A undergoing varying palmitoylation modifications and K-Ras4B having a poly-basic patch of eight Lys residues to promote interactions with acidic phospholipid head groups (Hancock, 2003). The HVR also promotes isoform-specific protein interactions provide, allowing specialization of cellular function (Paz *et al*, 2001; Nancy *et al*., 2002).

While all of these modifications aid in targeting Ras to its location of action at the PM, the inherent biophysical properties of the different prenylations on each isoform allows for their sorting to different microdomains (i.e., lipid rafts and smaller, dynamic nanoclusters). These small areas within the membrane allow enhanced spatiotemporal signal regulation through isoform clustering, which can be further regulated through post-translational modification (PTM) of the HVR. These modifications occur in an isoform-specific manner and include but are not limited to: *cis-trans* isomerization to regulate acylation state in H-Ras; phosphorylation of K-Ras4B within its polybasic path, reducing PM affinity resulting in endomembrane localization; and ubiquitylation (Ahearn *et al*., 2012).

Similar mechanisms are observed in the largest Ras subfamily, the Rabs, which play a variety of roles in vesicular trafficking pathways. Although the CAAX motif is not conserved in Rabs, they do undergo dual prenylation on cysteine residues at various locations at the end of a C-terminal HVR (Colicelli, 2004; Müller and Goody, 2018). Additionally, of the approximately 60 human Rabs, almost all are phosphorylated (Hornbeck *et al*., 2015). Although many of these modifications remain uncharacterized, the *Saccharomyces cerevisiae* Rab homolog Sec4p was found to be negatively regulated in a cell cycle-dependent manner via phosphorylation (Lepore *et al*., 2016).

While dynamins do not retain a HVR, a non-conserved hypervariable region at ATL's N-terminus may play a parallel role, providing isoform-specific, extrinsic regulation through post-

translational modifications, a novel mode of intrinsic membrane tethering regulation, and potential isoform identity, as outlined in the following chapter of this thesis.

*Coordinated function and regulation of ATL*

Determination of the mechanistic steps of GTP hydrolysis by the ATL catalytic core has provided foundational insight as to how ATL works to fuse membranes. However, by studying the soluble domain alone, we lack context in our understanding of how this mechanism translates to the dimensional confines of a membrane and the complex cellular environment of the ER membrane. For example, our current mechanistic model does not indicate how many ATL dimerization events are necessary for a successful fusion event, and evidence has shown that continuous rounds of GTP hydrolysis are required for fusion and that fusion efficiency increases cooperatively with increased surface density of ATL (Liu *et al*., 2015). Early work showed that nucleotide-independent ATL oligomerization occurs through the TM domain (Liu *et al*., 2012; Rismanchi *et al*., 2008; Zhu *et al*., 2003), and a cryo-ET experiment showed that dmATL forms a zipper-like ultra-structure at a proteoliposome membrane interface (Saini *et al*., 2014). Similarly, the closely related mitochondrial fusion protein, Mfn, was observed to form a docking ring structure, followed by tight tethering and membrane fusion (Brandt *et al*., 2016). These data would indicate that protein interactions on the *cis* membrane are crucial for efficient fusion, while our current model only addresses the contributions of *trans* protein interactions. Another critical consideration for ATL's cellular activity remains the prevalence of futile GTPase cycles between *cis* membrane protomers, which has been shown to occur and for which there is no known regulation (Liu *et al*., 2015). Chapter 2 will begin to address these unanswered questions by introducing several novel modes of regulation through ATL's N-terminal hypervariable region.

While there are a number of well-characterized extrinsic regulatory pathways controlling the activity of both large and small G proteins, very few have been described for ATL, and they remain ill-defined. The *A. thaliana* ATL homolog, RHD3, undergoes a number of PTMs known to

alter its cellular activity. Lunapark acts to counter ATL/RHD3 by stabilizing nascent 3-way junctions, and according to new evidence, by directing ubiquitination of RHD3 to target it for degradation (Sun *et al*., 2020). At the C-terminus of RHD3, multiple serine and threonine residues are phosphorylated, increasing fusion efficiency, putatively by promoting oligomerization (Ueda *et al*., 2016). In humans, the E3 ubiquitin ligase SYNV1 was found to ubiquitinate ATL1 on residues K285 and K287 resulting in decreased GTPase activity and decreased 3-way junction formation (Zhao *et al*., 2020).

Generally, we currently lack a comprehensive understanding of how ATLs are regulated in the cell, and continued efforts are required to identify and detail these mechanisms. While ATL does not retain a characteristic internal signaling element as the GED in other dynamins, we have identified novel intrinsic and extrinsic regulatory modes provided by ATL's short, hypervariable N-terminal region, which will be explored in Chapter 2.

## REFERENCES


Abel, A., Fonknechten, N., Hofer, A., Dürr, A., Cruaud, C., Voit, T., ... & Hazan, J. (2004). Early onset autosomal dominant spastic paraplegia caused by novel mutations in SPG3A. *Neurogenetics*, *5*(4), 239-243.

Ahearn, I. M., Haigis, K., Bar-Sagi, D., & Philips, M. R. (2012). Regulating the regulator: post-translational modification of RAS. *Nature reviews Molecular cell biology*, *13*(1), 39-51.

Ahn, S., Kim, J., Lucaveche, C. L., Reedy, M. C., Luttrell, L. M., Lefkowitz, R. J., & Daaka, Y. (2002). Src-dependent tyrosine phosphorylation regulates dynamin self-assembly and ligand-induced endocytosis of the epidermal growth factor receptor. *Journal of Biological Chemistry*, *277*(29), 26642-26651.

Antonny, B., Burd, C., De Camilli, P., Chen, E., Daumke, O., Faelber, K., ... & Kirchhausen, T. (2016). Membrane fission by dynamin: what we know and what we need to know. *The EMBO journal*, *35*(21), 2270-2284.

Anwar, K., Klemm, R. W., Condon, A., Severin, K. N., Zhang, M., Ghirlando, R., ... & Prinz, W. A. (2012). The dynamin-like GTPase Sey1p mediates homotypic ER fusion in S. cerevisiae. *Journal of Cell Biology*, *197*(2), 209-217.

Battini, R., Fogli, A., Borghetti, D., Michelucci, A., Perazza, S., Baldinotti, F., ... & Cioni, G. (2011). Clinical and genetic findings in a series of Italian children with pure hereditary spastic paraplegia. *European journal of neurology*, *18*(1), 150-157.

Behrendt, L., Kurth, I., & Kaether, C. (2019). A disease causing ATLASTIN 3 mutation affects multiple endoplasmic reticulum-related pathways. *Cellular and Molecular Life Sciences*, *76*(7), 1433-1445.

Betancourt-Solis, M. A., Desai, T., & McNew, J. A. (2018). The atlastin membrane anchor forms an intramembrane hairpin that does not span the phospholipid bilayer. *Journal of Biological Chemistry*, *293*(48), 18514-18524.

Bian, X., Klemm, R. W., Liu, T. Y., Zhang, M., Sun, S., Sui, X., ... & Hu, J. (2011). Structures of the atlastin GTPase provide insight into homotypic fusion of endoplasmic reticulum membranes. *Proceedings of the National Academy of Sciences*, *108*(10), 3976-3981.

Blackstone, C. (2012). Cellular pathways of hereditary spastic paraplegia. *Annual review of neuroscience*, *35*, 25-47.

Blackstone, C. (2018). Hereditary spastic paraplegia. In *Handbook of clinical neurology* (Vol. 148, pp. 633-652). Elsevier.

Blumenthal, R., Clague, M. J., Durell, S. R., & Epand, R. M. (2003). Membrane fusion. *Chemical Reviews*, *103*(1), 53-70.

Botzolakis, E. J., Zhao, J., Gurba, K. N., Macdonald, R. L., & Hedera, P. (2011). The effect of HSP-causing mutations in SPG3A and NIPA1 on the assembly, trafficking, and interaction between atlastin-1 and NIPA1. *Molecular and Cellular Neuroscience*, *46*(1), 122-135.

Brandt, T., Cavellini, L., Kühlbrandt, W., & Cohen, M. M. (2016). A mitofusin-dependent docking ring complex triggers mitochondrial fusion in vitro. *Elife*, *5*, e14618.

Bullough, P. A., Hughson, F. M., Skehel, J. J., & Wiley, D. C. (1994). Structure of influenza haemagglutinin at the pH of membrane fusion. *Nature*, *371*(6492), 37-43.

Byrnes, L. J., Singh, A., Szeto, K., Benvin, N. M., O'Donnell, J. P., Zipfel, W. R., & Sondermann, H. (2013). Structural basis for conformational switching and GTP loading of the large G protein atlastin. *The EMBO journal*, *32*(3), 369-384.

Byrnes, L. J., & Sondermann, H. (2011). Structural basis for the nucleotide-dependent dimerization of the large G protein atlastin-1/SPG3A. *Proceedings of the National Academy of Sciences*, *108*(6), 2216-2221.

Cao, H., Chen, J., Krueger, E. W., & McNiven, M. A. (2010). SRC-mediated phosphorylation of dynamin and cortactin regulates the “constitutive” endocytosis of transferrin. *Molecular and cellular biology*, *30*(3), 781-792.

Chang, J., Lee, S., & Blackstone, C. (2013). Protrudin binds atlastins and endoplasmic reticulum-shaping proteins and regulates network formation. *Proceedings of the National Academy of Sciences*, *110*(37), 14954-14959.

Chappie, J. S., Acharya, S., Leonard, M., Schmid, S. L., & Dyda, F. (2010). G domain dimerization controls dynamin's assembly-stimulated GTPase activity. *Nature*, *465*(7297), 435-440.

Chappie, J. S., Acharya, S., Liu, Y. W., Leonard, M., Pucadyil, T. J., & Schmid, S. L. (2009). An intramolecular signaling element that modulates dynamin function in vitro and in vivo. *Molecular biology of the cell*, *20*(15), 3561-3571.

Chappie, J. S., Mears, J. A., Fang, S., Leonard, M., Schmid, S. L., Milligan, R. A., ... & Dyda, F. (2011). A pseudoatomic model of the dynamin polymer identifies a hydrolysis-dependent powerstroke. *Cell*, *147*(1), 209-222.

Chen, S., Desai, T., McNew, J. A., Gerard, P., Novick, P. J., & Ferro-Novick, S. (2015). Lunapark stabilizes nascent three-way junctions in the endoplasmic reticulum. *Proceedings of the National Academy of Sciences*, *112*(2), 418-423.

Chen, J., Skehel, J. J., & Wiley, D. C. (1999). N-and C-terminal residues combine in the fusion-pH influenza hemagglutinin HA2 subunit to form an N cap that terminates the triple-stranded coiled coil. *Proceedings of the National Academy of Sciences*, *96*(16), 8967-8972.

Chen, J., Stefano, G., Brandizzi, F., & Zheng, H. (2011). Arabidopsis RHD3 mediates the generation of the tubular ER network and is required for Golgi distribution and motility in plant cells. *Journal of cell science*, *124*(13), 2241-2252.

Chen, Q., Xiao, Y., Chai, P., Zheng, P., Teng, J., & Chen, J. (2019). ATL3 is a tubular ER-phagy receptor for GABARAP-mediated selective autophagy. *Current Biology*, *29*(5), 846-855.

Colicelli, J. (2004). Human RAS superfamily proteins and related GTPases. *Sci. STKE*, *2004*(250), re13-re13.

Daumke, O., & Praefcke, G. J. (2016). Invited review: Mechanisms of GTP hydrolysis and conformational transitions in the dynamin superfamily. *Biopolymers*, *105*(8), 580-593.

DeLuca, G. C., Ebers, G. C., & Esiri, M. M. (2004). The extent of axonal loss in the long tracts in hereditary spastic paraplegia. *Neuropathology and applied neurobiology*, *30*(6), 576-584.

De Gregorio, C., Delgado, R., Ibacache, A., Sierralta, J., & Couve, A. (2017). Drosophila Atlastin in motor neurons is required for locomotion and presynaptic function. *Journal of Cell Science*, *130*(20), 3507-3516.

Depienne, C., Stevanin, G., Brice, A., & Durr, A. (2007). Hereditary spastic paraplegias: an update. Current opinion in neurology, 20(6), 674-680.

Dreier, L., & Rapoport, T. A. (2000). In vitro formation of the endoplasmic reticulum occurs independently of microtubules by a controlled fusion reaction. *The Journal of cell biology*, *148*(5), 883-898.

English, A. R., Zurek, N., & Voeltz, G. K. (2009). Peripheral ER structure and function. *Current opinion in cell biology*, *21*(4), 596-602.

Evans, K., Keller, C., Pavur, K., Glasgow, K., Conn, B., & Lauring, B. (2006). Interaction of two hereditary spastic paraplegia gene products, spastin and atlastin, suggests a common pathway for axonal maintenance. *Proceedings of the National Academy of Sciences*, *103*(28), 10666-10671.

Faelber, K., Posor, Y., Gao, S., Held, M., Roske, Y., Schulze, D., ... & Daumke, O. (2011). Crystal structure of nucleotide-free dynamin. *Nature*, *477*(7366), 556-560.

Falk, J., Rohde, M., Bekhite, M. M., Neugebauer, S., Hemmerich, P., Kiehntopf, M., ... & Beetz, C. (2014). Functional Mutation Analysis Provides Evidence for a Role of REEP 1 in Lipid Droplet Biology. *Human mutation*, *35*(4), 497-504.

Fassier, C., Hutt, J. A., Scholpp, S., Lumsden, A., Giros, B., Nothias, F., … & Hazan, J. (2010). Zebrafish atlastin controls motility and spinal motor axon architecture via inhibition of the BMP pathway. *Nature neuroscience*, *13*(11), 1380-1387.

Faust, J. E., Desai, T., Verma, A., Ulengin, I., Sun, T. L., Moss, T. J., ... & McNew, J. A. (2015). The Atlastin C-terminal tail is an amphipathic helix that perturbs the bilayer structure during endoplasmic reticulum homotypic fusion. *Journal of Biological Chemistry*, *290*(8), 4772-4783.

Fink, J. K. (2006). Hereditary spastic paraplegia. *Current neurology and neuroscience reports*, *6*(1), 65-76.

Fink, J. K. (2013). Hereditary spastic paraplegia: clinico-pathologic features and emerging molecular mechanisms. *Acta neuropathologica*, *126*(3), 307-328.

Fischer, D., Schabhüttl, M., Wieland, T., Windhager, R., Strom, T. M., & Auer-Grumbach, M. (2014). A novel missense mutation confirms ATL3 as a gene for hereditary sensory neuropathy type 1. *Brain*, *137*(7), e286-e286.

Ferguson, S. M., & De Camilli, P. (2012). Dynamin, a membrane-remodelling GTPase. *Nature reviews Molecular cell biology*, *13*(2), 75-88.

Gao, S., Von Der Malsburg, A., Dick, A., Faelber, K., Schröder, G. F., Haller, O., ... & Daumke, O. (2011). Structure of myxovirus resistance protein a reveals intra-and intermolecular domain interactions required for the antiviral function. *Immunity*, *35*(4), 514-525.

Gasper, R., Meyer, S., Gotthardt, K., Sirajuddin, M., & Wittinghofer, A. (2009). It takes two to tango: regulation of G proteins by dimerization. Nature reviews Molecular cell biology, 10(6), 423.

Ghosh, A., Praefcke, G. J., Renault, L., Wittinghofer, A., & Herrmann, C. (2006). How guanylate-binding proteins achieve assembly-stimulated processive cleavage of GTP to GMP. *Nature*, *440*(7080), 101-104.

González, C., & Couve, A. (2014). The axonal endoplasmic reticulum and protein trafficking: cellular bootlegging south of the soma. In *Seminars in cell & developmental biology* (Vol. 27, pp. 23-31). Academic Press.

Guelly, C., Zhu, P. P., Leonardis, L., Papić, L., Zidar, J., Schabhüttl, M., ... & Willems, J. (2011). Targeted high-throughput sequencing identifies mutations in atlastin-1 as a cause of hereditary sensory neuropathy type I. *The American Journal of Human Genetics*, *88*(1), 99-105.

Hancock, J. F. (2003). Ras proteins: different signals from different locations. *Nature reviews Molecular cell biology*, *4*(5), 373-385.

Harrison, S. C. (2015). Viral membrane fusion. *Virology*, *479*, 498-507.

Hornbeck, P.V., Zhang, B., Murray, B., Kornhauser, J.M., Latham, V., Skrzypek, E. (2015). PhosphoSitePlus, 2014: mutations, PTMs and recalibrations. *Nucleic Acids Res*. 43:D512-20.

Hu, J., & Rapoport, T. A. (2016, December). Fusion of the endoplasmic reticulum by membrane-bound GTPases. In *Seminars in cell & developmental biology* (Vol. 60, pp. 105-111). Academic Press.

Hu, J., Shibata, Y., Zhu, P. P., Voss, C., Rismanchi, N., Prinz, W. A., ... & Blackstone, C. (2009). A class of dynamin-like GTPases involved in the generation of the tubular ER network. *Cell*, *138*(3), 549-561.

Jahn, R., & Grubmüller, H. (2002). Membrane fusion. *Current opinion in cell biology*, *14*(4), 488-495.

Jimah, J. R., & Hinshaw, J. E. (2019). Structural insights into the mechanism of dynamin superfamily proteins. *Trends in Cell Biology*, *29*(3), 257-273.

Jozsef, L., Tashiro, K., Kuo, A., Park, E. J., Skoura, A., Albinsson, S., ... & Sessa, W. C. (2014). Reticulon 4 is necessary for endoplasmic reticulum tubulation, STIM1-Orai1 coupling, and store-operated calcium entry. *Journal of Biological Chemistry*, *289*(13), 9380-9395.

Kalia, R., Wang, R. Y. R., Yusuf, A., Thomas, P. V., Agard, D. A., Shaw, J. M., & Frost, A. (2018). Structural basis of mitochondrial receptor binding and constriction by DRP1. *Nature*, *558*(7710), 401-405.

Kar, U. P., Dey, H., & Rahaman, A. (2017). Regulation of dynamin family proteins by post-translational modifications. *Journal of Biosciences*, *42*(2), 333-344.

Khan, T. N., Klar, J., Tariq, M., Baig, S. A., Malik, N. A., Yousaf, R., ... & Dahl, N. (2014). Evidence for autosomal recessive inheritance in SPG3A caused by homozygosity for a novel ATL1 missense mutation. *European Journal of Human Genetics*, *22*(10), 1180-1184.

Kim, K. T., Moon, Y., Jang, Y., Lee, K. T., Lee, C., Jun, Y., & Lee, S. (2017). Molecular mechanisms of atlastin-mediated ER membrane fusion revealed by a FRET-based single-vesicle fusion assay. *Scientific reports*, *7*(1), 1-8.

Klebe, S., Stevanin, G., & Depienne, C. (2015). Clinical and genetic heterogeneity in hereditary spastic paraplegias: from SPG1 to SPG72 and still counting. *Revue neurologique*, *171*(6-7), 505-530.

Klemm, R. W., Norton, J. P., Cole, R. A., Li, C. S., Park, S. H., Crane, M. M., ... & Shibata, Y. (2013). A conserved role for atlastin GTPases in regulating lipid droplet size. *Cell reports*, *3*(5), 1465-1475.

Kornak, U., Mademan, I., Schinke, M., Voigt, M., Krawitz, P., Hecht, J., ... & Pou-Serradell, A. (2014). Sensory neuropathy with bone destruction due to a mutation in the membrane-shaping atlastin GTPase 3. *Brain*, *137*(3), 683-692.

Krols, M., Detry, S., Asselbergh, B., Almeida-Souza, L., Kremer, A., Lippens, S., ... & McMahon, H. T. (2018). Sensory-neuropathy-causing mutations in ATL3 cause aberrant ER membrane tethering. *Cell reports*, *23*(7), 2026-2038.

Kuzmin, P. I., Zimmerberg, J., Chizmadzhev, Y. A., & Cohen, F. S. (2001). A quantitative model for membrane fusion based on low-energy intermediates. *Proceedings of the National Academy of Sciences*, *98*(13), 7235-7240.

Jahn, R., Lang, T., & Südhof, T. C. (2003). Membrane fusion. *Cell*, *112*(4), 519-533.

Lee, Y., Paik, D., Bang, S., Kang, J., Chun, B., Lee, S., ... & Kim, J. (2008). Loss of spastic paraplegia gene atlastin induces age-dependent death of dopaminergic neurons in Drosophila. *Neurobiology of aging*, *29*(1), 84-94.

Lee, M., Paik, S. K., Lee, M. J., Kim, Y. J., Kim, S., Nahm, M., ... & Bae, Y. C. (2009). Drosophila Atlastin regulates the stability of muscle microtubules and is required for synapse development. *Developmental biology*, *330*(2), 250-262.

Lepore, D., Spassibojko, O., Pinto, G., & Collins, R. N. (2016). Cell cycle–dependent phosphorylation of Sec4p controls membrane deposition during cytokinesis. *Journal of Cell Biology*, *214*(6), 691-703.

Li, J., Yan, B., Si, H., Peng, X., Zhang, S. L., & Hu, J. (2017). Atlastin regulates store-operated calcium entry for nerve growth factor-induced neurite outgrowth. *Scientific reports*, *7*, 43490.

Liang, J. R., Lingeman, E., Ahmed, S., & Corn, J. E. (2018). Atlastins remodel the endoplasmic reticulum for selective autophagy. *Journal of Cell Biology*, *217*(10), 3354-3367.

Lin, Q., & Liou, Y. C. (2017). Fishing for key players in ER–mitochondrial contacts. *Journal of Biological Chemistry*, *292*(39), 16393-16394.

Liu, T. Y., Bian, X., Romano, F. B., Shemesh, T., Rapoport, T. A., & Hu, J. (2015). Cis and trans interactions between atlastin molecules during membrane fusion. *Proceedings of the National Academy of Sciences*, *112*(15), E1851-E1860.

Liu, T. Y., Bian, X., Sun, S., Hu, X., Klemm, R. W., Prinz, W. A., ... & Hu, J. (2012). Lipid interaction of the C terminus and association of the transmembrane segments facilitate atlastin-mediated homotypic endoplasmic reticulum fusion. *Proceedings of the National Academy of Sciences*, *109*(32), E2146-E2154.

Liu, X., Guo, X., Niu, L., Li, X., Sun, F., Hu, J., ... & Shen, K. (2019). Atlastin-1 regulates morphology and function of endoplasmic reticulum in dendrites. *Nature communications*, *10*(1), 1-15.

Lowe, M., & Barr, F. A. (2007). Inheritance and biogenesis of organelles in the secretory pathway. *Nature Reviews Molecular Cell Biology*, *8*(6), 429-439.

Lu, L., Ladinsky, M. S., & Kirchhausen, T. (2009). Cisternal organization of the endoplasmic reticulum during mitosis. *Molecular biology of the cell*, *20*(15), 3471-3480.

Lu, X., Yang, M., Yang, Y., & Wang, X. F. (2020). Atlastin-1 modulates seizure activity and neuronal excitability. *CNS Neuroscience & Therapeutics*, *26*(3), 385-393.

Lumb, J. H., Connell, J. W., Allison, R., & Reid, E. (2012). The AAA ATPase spastin links microtubule severing to membrane modelling. *Biochimica et Biophysica Acta (BBA)-Molecular Cell Research*, *1823*(1), 192-197.

Manford, A. G., Stefan, C. J., Yuan, H. L., MacGurn, J. A., & Emr, S. D. (2012). ER-to-plasma membrane tethering proteins regulate cell signaling and ER morphology. *Developmental cell*, *23*(6), 1129-1140.

McCullough, S., & Lucocq, J. (2005). Endoplasmic reticulum positioning and partitioning in mitotic HeLa cells. *Journal of Anatomy*, *206*(5), 415-425.

McNew, J. A. (2008). Regulation of SNARE-mediated membrane fusion during exocytosis. *Chemical reviews*, *108*(5), 1669-1686.

McNew, J. A., Sondermann, H., Lee, T., Stern, M., & Brandizzi, F. (2013). GTP-dependent membrane fusion. *Annual review of cell and developmental biology*, *29*, 529-550.

Meijer, I. A., Dion, P., Laurent, S., Dupré, N., Brais, B., Levert, A., ... & Soderblom, C. (2007). Characterization of a novel SPG3A deletion in a French-Canadian family. Annals of Neurology: Official Journal of the American Neurological Association and the Child Neurology Society, 61(6), 599-603.

Monel, B., Rajah, M. M., Hafirassou, M. L., Ahmed, S. S., Burlaud-Gaillard, J., Zhu, P. P., ... & Amraoui, S. (2019). Atlastin Endoplasmic Reticulum-Shaping Proteins Facilitate Zika Virus Replication. *Journal of virology*, *93*(23).

Montagna, A., Vajente, N., Pendin, D., & Daga, A. (2020). In vivo analysis of CRISPR/Cas9 induced atlastin pathological mutations in Drosophila. *Frontiers in Neuroscience*, *14*.

Morin-Leisk, J., Saini, S. G., Meng, X., Makhov, A. M., Zhang, P., & Lee, T. H. (2011). An intramolecular salt bridge drives the soluble domain of GTP-bound atlastin into the postfusion conformation. *Journal of Cell Biology*, *195*(4), 605-615.

Moss, T. J., Andreazza, C., Verma, A., Daga, A., & McNew, J. A. (2011). Membrane fusion by the GTPase atlastin requires a conserved C-terminal cytoplasmic tail and dimerization through the middle domain. *Proceedings of the National Academy of Sciences*, *108*(27), 11133-11138.

Müller, M. P., & Goody, R. S. (2018). Molecular control of Rab activity by GEFs, GAPs and GDI. *Small GTPases*, *9*(1-2), 5-21.

Namekawa, M., Muriel, M. P., Janer, A., Latouche, M., Dauphin, A., Debeir, T., ... & Sittler, A. (2007). Mutations in the SPG3A gene encoding the GTPase atlastin interfere with vesicle trafficking in the ER/Golgi interface and Golgi morphogenesis. *Molecular and Cellular Neuroscience*, *35*(1), 1-13.

Nancy, V., Callebaut, I., El Marjou, A., & de Gunzburg, J. (2002). The δ subunit of retinal rod cGMP phosphodiesterase regulates the membrane association of Ras and Rap GTPases. *Journal of Biological Chemistry*, *277*(17), 15076-15084.

Naslavsky, N., & Caplan, S. (2011). EHD proteins: key conductors of endocytic transport. *Trends in cell biology*, *21*(2), 122-131.

Neufeldt, C. J., Cortese, M., Scaturro, P., Cerikan, B., Wideman, J. G., Tabata, K., ... & Bartenschlager, R. (2019). ER-shaping atlastin proteins act as central hubs to promote flavivirus replication and virion assembly. *Nature microbiology*, *4*(12), 2416-2429.

O'Donnell, J. P., Byrnes, L. J., Cooley, R. B., & Sondermann, H. (2018). A hereditary spastic paraplegia–associated atlastin variant exhibits defective allosteric coupling in the catalytic core. *Journal of Biological Chemistry*, *293*(2), 687-700.

O'Donnell, J. P., Cooley, R. B., Kelly, C. M., Miller, K., Andersen, O. S., Rusinova, R., & Sondermann, H. (2017). Timing and reset mechanism of GTP hydrolysis-driven conformational changes of atlastin. *Structure*, *25*(7), 997-1010.

Orso, G., Pendin, D., Liu, S., Tosetto, J., Moss, T. J., Faust, J. E., ... & Daga, A. (2009). Homotypic fusion of ER membranes requires the dynamin-like GTPase atlastin. *Nature*, *460*(7258), 978-983.

Park, S. H., & Blackstone, C. (2010). Further assembly required: construction and dynamics of the endoplasmic reticulum network. *EMBO reports*, *11*(7), 515-521.

Park, S. H., Zhu, P. P., Parker, R. L., & Blackstone, C. (2010). Hereditary spastic paraplegia proteins REEP1, spastin, and atlastin-1 coordinate microtubule interactions with the tubular ER network. *The Journal of clinical investigation*, *120*(4), 1097-1110.

Pawar, S., Ungricht, R., Tiefenboeck, P., Leroux, J. C., & Kutay, U. (2017). Efficient protein targeting to the inner nuclear membrane requires Atlastin-dependent maintenance of ER topology. *Elife*, *6*, e28202.

Paz, A., Haklai, R., Elad-Sfadia, G., Ballan, E., & Kloog, Y. (2001). Galectin-1 binds oncogenic H-Ras to mediate Ras membrane anchorage and cell transformation. *Oncogene*, *20*(51), 7486-7493.

Pendin, D., Tosetto, J., Moss, T. J., Andreazza, C., Moro, S., McNew, J. A., & Daga, A. (2011). GTP-dependent packing of a three-helix bundle is required for atlastin-mediated fusion. *Proceedings of the National Academy of Sciences*, *108*(39), 16283-16288.

Phillips, M. J., & Voeltz, G. K. (2016). Structure and function of ER membrane contact sites with other organelles. *Nature reviews Molecular cell biology*, *17*(2), 69.

Piras, I. S., Manchia, M., Huentelman, M. J., Pinna, F., Zai, C. C., Kennedy, J. L., & Carpiniello, B. (2019). Peripheral biomarkers in schizophrenia: a meta-analysis of microarray gene expression datasets. *International Journal of Neuropsychopharmacology*, *22*(3), 186-193.

Poirier, M. A., Xiao, W., Macosko, J. C., Chan, C., Shin, Y. K., & Bennett, M. K. (1998). The synaptic SNARE complex is a parallel four-stranded helical bundle. *Nature structural biology*, *5*(9), 765-769.

Polisetty, R. V., Gautam, P., Sharma, R., Harsha, H. C., Nair, S. C., Gupta, M. K., ... & Sirdeshmukh, R. (2012). LC-MS/MS analysis of differentially expressed glioblastoma membrane proteome reveals altered calcium signaling and other protein groups of regulatory functions. *Molecular & Cellular Proteomics*, *11*(6).

Powers, R. E., Wang, S., Liu, T. Y., & Rapoport, T. A. (2017). Reconstitution of the tubular endoplasmic reticulum network with purified components. *Nature*, *543*(7644), 257-260.

Praefcke, G. J., & McMahon, H. T. (2004). The dynamin superfamily: universal membrane tubulation and fission molecules?. *Nature reviews Molecular cell biology*, *5*(2), 133-147.

Prakash, B., Praefcke, G. J., Renault, L., Wittinghofer, A., & Herrmann, C. (2000). Structure of human guanylate-binding protein 1 representing a unique class of GTP-binding proteins. *Nature*, *403*(6769), 567-571.

Puhka, M., Vihinen, H., Joensuu, M., & Jokitalo, E. (2007). Endoplasmic reticulum remains continuous and undergoes sheet-to-tubule transformation during cell division in mammalian cells. *The Journal of cell biology*, *179*(5), 895-909.

Rao, K., Stone, M. C., Weiner, A. T., Gheres, K. W., Zhou, C., Deitcher, D. L., ... & Rolls, M. M. (2016). Spastin, atlastin, and ER relocalization are involved in axon but not dendrite regeneration. *Molecular biology of the cell*, *27*(21), 3245-3256.

Renvoisé, B., & Blackstone, C. (2010). Emerging themes of ER organization in the development and maintenance of axons. *Current opinion in neurobiology*, *20*(5), 531-537.

Renvoisé, B., Malone, B., Falgairolle, M., Munasinghe, J., Stadler, J., Sibilla, C., ... & Blackstone, C. (2016). Reep1 null mice reveal a converging role for hereditary spastic paraplegia proteins in lipid droplet regulation. *Human molecular genetics*, *25*(23), 5111-5125.

Reubold, T. F., Faelber, K., Plattner, N., Posor, Y., Ketel, K., Curth, U., ... & Haucke, V. (2015). Crystal structure of the dynamin tetramer. *Nature*, *525*(7569), 404-408.

Rinaldi, C., Schmidt, T., Situ, A. J., Johnson, J. O., Lee, P. R., Chen, K. L., ... & Grunseich, C. (2015). Mutation in CPT1C associated with pure autosomal dominant spastic paraplegia. *JAMA neurology*, *72*(5), 561-570.

Rismanchi, N., Soderblom, C., Stadler, J., Zhu, P. P., & Blackstone, C. (2008). Atlastin GTPases are required for Golgi apparatus and ER morphogenesis. *Human molecular genetics*, *17*(11), 1591-1604.

Saini, S. G., Liu, C., Zhang, P., & Lee, T. H. (2014). Membrane tethering by the atlastin GTPase depends on GTP hydrolysis but not on forming the cross-over configuration. *Molecular biology of the cell*, *25*(24), 3942-3953.

Sanderson, C. M., Connell, J. W., Edwards, T. L., Bright, N. A., Duley, S., Thompson, A., ... & Reid, E. (2006). Spastin and atlastin, two proteins mutated in autosomal-dominant hereditary spastic paraplegia, are binding partners. *Human molecular genetics*, *15*(2), 307-318.

Scheffzek, K., Ahmadian, M. R., & Wittinghofer, A. (1998). GTPase-activating proteins: helping hands to complement an active site. *Trends in biochemical sciences*, *23*(7), 257-262.

Shen, W., Liu, B., Liu, Z., Feng, J., Liu, C., & Kong, X. (2017). Host protein atlastin-1 promotes human immunodeficiency virus (HIV-1) replication. *Virologica Sinica*, *32*(4), 338.

Shibata, Y., Shemesh, T., Prinz, W. A., Palazzo, A. F., Kozlov, M. M., & Rapoport, T. A. (2010). Mechanisms determining the morphology of the peripheral ER. *Cell*, *143*(5), 774-788.

Shibata, Y., Voss, C., Rist, J. M., Hu, J., Rapoport, T. A., Prinz, W. A., & Voeltz, G. K. (2008). The reticulon and DP1/Yop1p proteins form immobile oligomers in the tubular endoplasmic reticulum. *Journal of Biological Chemistry*, *283*(27), 18892-18904.

Shih, Y. T., & Hsueh, Y. P. (2016). VCP and ATL1 regulate endoplasmic reticulum and protein synthesis for dendritic spine formation. *Nature communications*, *7*(1), 1-16.

Smillie, K. J., & Cousin, M. A. (2005, January). Dynamin I phosphorylation and the control of synaptic vesicle endocytosis. In *Biochemical Society Symposia* (Vol. 72, pp. 87-97). Portland Press Limited.

Srinivasan, S., Burckhardt, C. J., Bhave, M., Chen, Z., Chen, P. H., Wang, X., ... & Schmid, S. L. (2018). A noncanonical role for dynamin-1 in regulating early stages of clathrin-mediated endocytosis in non-neuronal cells. *PLoS biology*, *16*(4), e2005377.

Srinivasan, S., Dharmarajan, V., Reed, D. K., Griffin, P. R., & Schmid, S. L. (2016). Identification and function of conformational dynamics in the multidomain GTP ase dynamin. *The EMBO journal*, *35*(4), 443-457.

Steiner, B., Swart, A. L., Welin, A., Weber, S., Personnic, N., Kaech, A., ... & Hilbi, H. (2017). ER remodeling by the large GTPase atlastin promotes vacuolar growth of Legionella pneumophila. *EMBO reports*, *18*(10), 1817-1836.

Sun, J., Movahed, N., & Zheng, H. (2020). LUNAPARK Is an E3 Ligase That Mediates Degradation of ROOT HAIR DEFECTIVE3 to Maintain a Tubular ER Network in Arabidopsis. *The Plant Cell*, *32*(9), 2964-2978.

Sun, J., & Zheng, H. (2018). Efficient ER fusion requires a dimerization and a C-terminal tail mediated membrane anchoring of RHD3. *Plant physiology*, *176*(1), 406-417.

Summerville, J. B., Faust, J. F., Fan, E., Pendin, D., Daga, A., Formella, J., ... & McNew, J. A. (2016). The effects of ER morphology on synaptic structure and function in Drosophila melanogaster. *Journal of cell science*, *129*(8), 1635-1648.

Sutton, R. B., Fasshauer, D., Jahn, R., & Brunger, A. T. (1998). Crystal structure of a SNARE complex involved in synaptic exocytosis at 2.4 Å resolution. *Nature*, *395*(6700), 347-353.

Terasaki, M., Chen, L. B., & Fujiwara, K. (1986). Microtubules and the endoplasmic reticulum are highly interdependent structures. *The Journal of cell biology*, *103*(4), 1557-1568.

Terasaki, M., Runft, L. L., & Hand, A. R. (2001). Changes in organization of the endoplasmic reticulum during Xenopus oocyte maturation and activation. *Molecular biology of the cell*, *12*(4), 1103-1116.

Ueda, H., Yokota, E., Kuwata, K., Kutsuna, N., Mano, S., Shimada, T., ... & Shimmen, T. (2016). Phosphorylation of the C terminus of RHD3 has a critical role in homotypic ER membrane fusion in Arabidopsis. *Plant physiology*, *170*(2), 867-880.

Ulengin, I., Park, J. J., & Lee, T. H. (2015). ER network formation and membrane fusion by atlastin1/SPG3A disease variants. *Molecular biology of the cell*, *26*(9), 1616-1628.

Voeltz, G. K., Prinz, W. A., Shibata, Y., Rist, J. M., & Rapoport, T. A. (2006). A class of membrane proteins shaping the tubular endoplasmic reticulum. *Cell*, *124*(3), 573-586.

Voeltz, G. K., Rolls, M. M., & Rapoport, T. A. (2002). Structural organization of the endoplasmic reticulum. *EMBO reports*, *3*(10), 944-950.

Wang, S., Romano, F. B., Field, C. M., Mitchison, T. J., & Rapoport, T. A. (2013). Multiple mechanisms determine ER network morphology during the cell cycle in Xenopus egg extracts. *Journal of Cell Biology*, *203*(5), 801-814.

Wang, S., Tukachinsky, H., Romano, F. B., & Rapoport, T. A. (2016). Cooperation of the ER-shaping proteins atlastin, lunapark, and reticulons to generate a tubular membrane network. *Elife*, *5*, e18605.

Willkomm, L., Heredia, R., Hoffmann, K., Wang, H., Voit, T., Hoffman, E. P., & Cirak, S. (2016). Homozygous mutation in Atlastin GTPase 1 causes recessive hereditary spastic paraplegia. *Journal of human genetics*, *61*(6), 571-573.

Wu, F., Hu, X., Bian, X., Liu, X., & Hu, J. (2015). Comparison of human and Drosophila atlastin GTPases. *Protein & cell*, *6*(2), 139-146.

Xiao, X. W., Du, J., Jiao, B., Liao, X. X., Zhou, L., Liu, X. X., ... & Lin, Z. Y. (2019). Novel ATL1 mutation in a Chinese family with hereditary spastic paraplegia: A case report and review of literature. *World Journal of Clinical Cases*, *7*(11), 1358.

Yan, L., Qi, Y., Huang, X., Yu, C., Lan, L., Guo, X., ... & Lou, Z. (2018). Structural basis for GTP hydrolysis and conformational change of MFN1 in mediating membrane fusion. *Nature structural & molecular biology*, *25*(3), 233-243.

Yan, L., Sun, S., Wang, W., Shi, J., Hu, X., Wang, S., ... & Lou, Z. (2015). Structures of the yeast dynamin-like GTPase Sey1p provide insight into homotypic ER fusion. *Journal of Cell Biology*, *210*(6), 961-972.

Zhao, G., Zhu, P. P., Renvoisé, B., Maldonado-Báez, L., Park, S. H., & Blackstone, C. (2016). Mammalian knock out cells reveal prominent roles for atlastin GTPases in ER network morphology. *Experimental cell research*, *349*(1), 32-44.

Zhao, G. H., & Liu, X. M. (2017). Clinical features and genotype-phenotype correlation analysis in patients with ATL1 mutations: A literature reanalysis. *Translational neurodegeneration*, *6*(1), 9.

Zhao, J., & Hedera, P. (2013). Hereditary spastic paraplegia-causing mutations in atlastin-1 interfere with BMPRII trafficking. *Molecular and Cellular Neuroscience*, *52*, 87-96.

Zhao, X., Alvarado, D., Rainier, S., Lemons, R., Hedera, P., Weber, C. H., ... & Bui, M. (2001). Mutations in a newly identified GTPase gene cause autosomal dominant hereditary spastic paraplegia. *Nature genetics*, *29*(3), 326-331.

Zhao, Y., Feng, Z., Zou, Y., & Liu, Y. (2020). The E3 Ubiquitin Ligase SYVN1 Ubiquitinates Atlastins to Remodel the Endoplasmic Reticulum Network. *Iscience*, *23*(9), 101494.

Zheng, H., & Chen, J. (2011). Emerging aspects of ER organization in root hair tip growth: lessons from RHD3 and Atlastin. *Plant Signaling & Behavior*, *6*(11), 1710-1713.

Zhong, J., & Zou, H. (2014). BMP signaling in axon regeneration. *Current opinion in neurobiology*, *27*, 127-134.

Zhu, P. P., Patterson, A., Lavoie, B., Stadler, J., Shoeb, M., Patel, R., & Blackstone, C. (2003). Cellular localization, oligomerization, and membrane association of the hereditary spastic paraplegia 3A (SPG3A) protein atlastin. *Journal of Biological Chemistry*, *278*(49), 49063-49071.

Zhu, P. P., Soderblom, C., Tao-Cheng, J. H., Stadler, J., & Blackstone, C. (2006). SPG3A protein atlastin-1 is enriched in growth cones and promotes axon elongation during neuronal development. *Human molecular genetics*, *15*(8), 1343-1353.

Zurek, N., Sparks, L., & Voeltz, G. (2011). Reticulon short hairpin transmembrane domains are used to shape ER tubules. *Traffic*, *12*(1), 28-41.

## CHAPTER TWO

## THE N-TERMINAL HYPERVARIABLE REGION OF ATLASTIN-1 IS A SITE FOR INTRINSIC AND EXTRINSIC REGULATION OF MEMBRANE TETHERING


### ABSTRACT

Atlastins (ATL) are members of the dynamin superfamily of large GTPases and function primarily in homotypic membrane fusion in the peripheral endoplasmic reticulum (ER) to generate and maintain its characteristic reticular structure. Previous studies established the molecular basis of GTP hydrolysis-dependent conformational changes in ATLs, which result in the tethering and subsequent fusion of membrane tubules. However, we currently lack a mechanistic understanding of how tethering events are biased towards opposing tubules and against futile events on the same tubule. We also lack insight into possible regulatory mechanisms that may enable the reorganization of the ER during cell division and other cellular processes that involve the responsive restructuring of this organelle. Here we present two modes of ATL1 regulation, intrinsic and extrinsic, that involve the poorly characterized, short, hypervariable region (HVR) at the N terminus of ATLs. Crystal structures of ATL1 and ATL3 presented here establish the HVR as distinct structural features of the ATL isoforms. Characterizing the functional role of ATL1's HVR reveals its positive effect on membrane tethering and ATL1's cellular function. We also establish the HVR as a site for phosphorylation-dependent regulation. Using a kinase screen, we identify candidates that modify the HVR of ATL1 at distinct sites *in vitro*, corresponding to the modifications on ATL1 detected in cells. The work presented here expands on the mechanisms that contribute to efficient and potentially regulated activity of ATLs, laying the foundation for the identification of cellular effectors of ATL-mediated membrane processes.

## INTRODUCTION

Atlastins (ATLs) are large GTPases in the dynamin superfamily that catalyze the fusion of tubules in the peripheral endoplasmic reticulum (ER) to generate and maintain its polygonal structure composed of 3-way junctions (Orso *et al*., 2009; Hu *et al*., 2009; Praefcke and McMahon, 2004). Dynamin-related proteins utilize the energy of GTP hydrolysis to carry out diverse cellular processes including fission of budding vesicles, fusion and fission of organelle membranes, and interferon-induced pathogen resistance (Praefcke and McMahon, 2004; Daumke and Praefcke, 2016). Dynamin superfamily members are comprised of several conserved structural domains including the canonical large GTPase (G) domain near the N terminus, followed by a stalk-like helical bundle domain. Towards the C terminus reside protein-specific features such as a pleckstrin homology (PH) domain, transmembrane domain, or lipid modification for cognate membrane association (Praefcke and McMahon, 2004). Another common feature is a GTPase effector domain (GED) that functions in intramolecular regulation of GTPase activity (Chappie *et al*., 2009), however this domain is absent in ATLs.

Three isoforms of ATL (ATL1-3) are found in invertebrates, while other eukaryotes express only one analogous protein, such as Sey1p (synthetic enhancer of enhancer of Yop1) in yeast (Hu *et al*., 2009) and dmATL in *D. melanogaster* (Orso *et al*., 2009). While all three mammalian isoforms retain high sequence identity and localize primarily to the reticular ER, they vary slightly in their sub-organellar localizations, with ATL1 and ATL2 distributing more evenly along tubules while ATL3 shows a stronger preference for puncta at 3-way junctions and dense tubular matrices (Rismanchi *et al*., 2008; Nixon-Abell *et al*., 2016). ATL isoforms also deviate in their tissue-specific expression patterns, with ATL1 predominantly present in the cerebral cortex and hippocampus (Zhu *et al*., 2003) and ATL2 and ATL3 more ubiquitous throughout the body (Rismanchi *et al*., 2008). However, co-occurrence of more than one ATL isoform in tissues and cell lines appears to be a common feature (Rismanchi *et al*, 2008).

ATL1 was first identified as a mutational hotspot in hereditary spastic paraplegia (HSP) (Zhao *et al*., 2001), and later ATL1 and ATL3 mutations were found associated with hereditary sensory neuropathy (HSN) (Guelly *et al*., 2011; Fischer *et al*., 2014; Kornak *et al*., 2014). Functional roles for ATLs continue to be identified and include: regulation of ER-phagy (Chen *et al*., 2019; Liang *et al*., 2018); formation and size regulation of lipid droplets (Klemm *et al.,* 2013; Falk *et al*., 2014); promoting pathogen propagation in infected cells (Neufeldt *et al*., 2019; Monel *et al*., 2019; Steiner *et al*., 2017; Shen *et al*., 2017); supporting store-operated calcium entry (SOCE) (Li *et al*., 2017); promoting cargo packaging into COPII-coated vesicles for proper exit of ER-processed proteins (Niu *et al*., 2019); regulation of the bone morphogenetic protein (BMP) signaling pathway (Fassier *et al*., 2010; Summerville *et al*., 2016; Zhao and Hedera, 2013; Zhao *et al*., 2016); aiding in cell cycle-dependent ER morphological changes including nuclear envelope reformation in daughter cells (Wang *et al*., 2013); and proper targeting of membranes proteins to the nuclear envelope inner membrane (Pawar *et al*., 2017).

Structurally, ATL's canonical, N-terminal G domain connects to the proceeding helical middle domain via a short, flexible linker that enables nucleotide-dependent conformational changes (Byrnes and Sondermann, 2011; Bian *et al*., 2011). The bulk of ATL faces the cytosol with the protein being anchored to the highly curved ER tubules by a wedge-like, membrane-associated domain (Hu *et al*., 2009; Betancourt-Solis *et al*., 2018). The C terminus contains an amphipathic helix that aids in membrane fusion through membrane thinning and acyl chain disorder (Faust *et al*., 2015; Liu *et al*., 2012). While the hydrolysis mechanism within dynamin-related protein G domains is largely conserved, using a monovalent cation to stabilize the transition state (Chappie *et al*., 2010), ATL and the closely related guanylate binding protein (GBP) deviate in their use of an arginine finger to serve this function (Byrnes and Sondermann, 2011; Bian *et al*., 2011; Ghosh *et al.,* 2006). Notably, the cytosolic G and middle domains of ATL function as its catalytic core with GTPase rates comparable to those reported for the full-length (FL) protein (Wu *et al*., 2015; Moss *et al*., 2011). The catalytic core is sufficient and required for

nucleotide-dependent dimerization of ATLs (Byrnes *et al*., 2013; O'Donnell *et al*., 2017) and acts as a concentration- and GTPase-dependent inhibitor of ATL-mediated membrane fusion *in vitro* and in cells (Bian *et al*., 2011; Moss *et al*., 2011, Wang *et al*., 2013). Together, these properties of the catalytic core established the C-terminally truncated, soluble protein as a proxy for the full-length protein in mechanistic and structural studies (Byrnes and Sondermann, 2011; Byrnes *et al*., 2013; Bian *et al*., 2011; Liu *et al*., 2015; O'Donnell *et al*., 2017; O'Donnell *et al*., 2018).

Based on structural and biochemical analyses of the catalytic core, a model has emerged detailing the catalytic mechanism for ATL's GTP hydrolysis-dependent dimerization cycle. Briefly, two ATL protomers, presumably on *trans* membranes, adopt an "engaged" state in which the middle domain docks at the G domain, allowing binding of GTP (Byrnes and Sondermann, 2011; Bian *et al*., 2011; Byrnes *et al*., 2013; O'Donnell *et al*., 2017). The engaged state is released upon GTP binding and initiation of hydrolysis through a rigid body rotation facilitated by the linker region between the two domains (O'Donnell *et al*., 2017). The conformational change allows for the dimerization of ATL involving an extensive dimerization interface that encompasses the G and middle domains, ultimately forming a tight membrane tether (O'Donnell *et al*., 2017; Byrnes and Sondermann, 2011; Bian *et al*., 2011; Liu *et al*., 2015). Upon completion of GTP hydrolysis, the dimer relaxes, and inorganic phosphate ($P_i$) is released (O'Donnell *et* al., 2017). The release of GDP from the active site is required for the cycle to reset (Liu *et al*., 2015; O'Donnell *et al*., 2017).

Despite our extensive understanding of the ATL catalytic cycle, a number of questions remain about how this mechanism translates to efficient membrane fusion in the cell. Firstly, how is efficient membrane fusion achieved by individual GTP hydrolysis-dependent dimerization events? Recent studies have shown that continuous GTP hydrolysis is required for efficient membrane tethering and fusion and that only a percentage of tethering events result in fusion (Liu *et al*., 2015; Saini *et al*., 2014). A similar requirement for continuous GTP hydrolysis was reported for fusion of outer mitochondrial membranes by the dynamin-related protein mitofusin (Mfn) (Brandt *et al*., 2016). Additionally, the efficiency of ATL-mediated membrane fusion increases

cooperatively with increasing surface density of ATL on the membrane, indicative of a mechanism beyond individual *trans* dimerization cycles (Liu *et al*., 2015). From these considerations, a second question arises: what role do protomer interactions on a *cis* membrane play in ATL's mechanism? Early works found that ATL likely forms dimers and/or tetramers in the cell in a nucleotide-independent manner, requiring the membrane-associated domain of ATL (Liu *et* al., 2012; Rismanchi *et al*., 2008; Zhu *et al*., 2003). More recently, a cryo-ET experiment indicated a zipper-like ultrastructure of ATL protomers at the interface of tethered proteoliposomes, suggesting a level of coordinated self-organization in the plane of a membrane (Saini *et al*., 2014). Such coordination mirrors events in Mfn-mediated membrane fusion, for which a "docking ring" ultra-structure was identified as a pre-requisite for mitochondrial membrane tethering and subsequent fusion pore formation (Brandt *et al*., 2016). Lastly, are there mechanisms to reduce GTP hydrolysis and dimerization cycles between protomers on a *cis* membrane that would be futile in the context of membrane tethering and fusion? Such *cis* cycles have been found to occur between ATLs *in vitro*, in competition with *trans* interactions, raising the question as to whether this also occurs in the cell (Liu *et al*., 2015).

This last question is of particular interest given that there are a number of mechanisms in place to prevent futile GTP hydrolysis in dynamin: dynamin exists in the cytosol as an autoinhibited tetramer, maintained by a number of low-affinity interactions (Reubold *et al*., 2015). Dynamin is recruited to its site of action on the plasma membrane at the stalks of budding vesicles in part through interactions between its proline-rich domain (PRD) and Src-homology 3 (SH3) domain containing proteins (Jimah and Hinshaw, 2019). Dynamin also interacts with phosphoinositide lipids through its pleckstrin homology (PH) domain and polymerizes into helical rungs, stabilized through intermolecular interactions between adjacent stalk domains (Antonny *et al*., 2016; Jimah and Hinshaw, 2019). Additionally, nucleotide- and lipid-dependent events trigger coordinated, large-scale conformational changes, communicated through the bundle signaling element (BSE or GED in other dynamins), a structural motif composed of helices from the N- and

C- terminal ends of the G domain and a helix proceeding the PH and stalk domains (Chappie *et al*., 2009; Kong *et al*., 2018; Chappie *et al*., 2011). Finally, dynamin's GTPase rate is stimulated over 100-fold as its G domain dimerizes with a G domain from an adjacent helical rung, which stabilizes the catalytic machinery (Tuma and Collins, 1994; Warnock *et al*., 1996; Chappie *et al*., 2010; Kong *et al*., 2018; Chappie *et al*., 2009; Ford and Chappie, 2019). Posttranslational modifications of dynamin yield another level of control for this process (Srinivasan *et al*., 2108; Kar *et al*., 2017; Smillie and Cousin, 2005; Ahn *et al*., 2002; Cao *et al*., 2010).

ATLs lack a BSE, or GED, and coordinated conformational changes within higher-order assemblies have not been reported to date, correlating with a lack of cooperative GTPase activity to the level observed with dynamin (Winsor *et al*., 2017). There is however emerging evidence of post-translational regulation of ATL and ATL-related proteins. The E3 ubiquitin ligase SYNV1 modifies G domain residues K285 and K287 of ATL1, resulting in decreased GTPase activity and formation of 3-way junctions in the mammalian ER (Zhao *et al*., 2020). In the *A. thaliana* homolog RHD3 (root hair defective 3), ubiquitination targets RHD3 for degradation upon stabilization of 3-way ER tubule junctions (Sun *et al*., 2020), and phosphorylation within its C-terminal helix increases fusion efficiency (Ueda *et al*., 2016). ATLs have been reported as hits in a number of unbiased phosphoproteomics screens (Hornbeck *et al*., 2015), including one that identified the targets of aurora kinase, an enzyme important for cell proliferation (Kettenbach *et al*., 2011), but individual confirmation of these post-translational modifications of ATLs remains elusive. Their functional relevance has also not been established so far.

Here we present novel regulatory mechanisms that involve the short, understudied N-terminal motifs of vertebrate ATLs and that contribute to the efficiency and function of ATLs. Early studies identified these short motifs preceding the G domain, pointing out their conservation in sequence across homologs but divergence across isoforms (Zhu *et al*., 2003). Based on novel structures, we demonstrate that these hypervariable regions or "HVRs" can adopt isoform-specific conformations, and in the case of ATL1 contribute to tethering efficiency. These motifs also

contain some of the most reproducible phosphorylation sites found in unbiased screens for post-translational modifications in cellular proteomes (Hornbeck *et al*., 2015). We verify phosphorylation of ATL1's HVR on conserved serine residues, identify candidate kinases that are capable of introducing these modifications site-specifically, and demonstrate a requirement of HVR phosphorylation for wild-type ATL1 function. Together, these studies indicate intrinsic and extrinsic modes of ATL regulation in vertebrates that rely on sequences outside the catalytic core and may contribute to the dynamic remodeling of ER membranes.

## RESULTS

*ATL1 and ATL3 contain structured amino-terminal, hypervariable regions.*

Previous crystal structures of human atlastin isoforms (referred to here as ATL1-3) reported the enzyme adopts multiple, nucleotide-dependent conformations. These structures of ATL1 and ATL3 in combination with biochemical investigations revealed the basis for how GTP-hydrolysis orchestrates key events that results in membrane tethering and fusion (Byrnes and Sondermann, 2011; Bian *et al*., 2011; Byrnes *et al*., 2013; O'Donnell *et al*., 2017). In all preceding structures, the amino-terminal residues leading from the initiator methionine to the G domain were largely disordered. Two structures presented here of ATL1 and ATL3 reveal an ordered segment of secondary structure in this previously unresolved region. The conservation across different species is strong within distinct isoforms, but highly divergent when isoforms within a particular species are compared to each other (Figure 2.1A). Considering these characteristics, we refer to the N-terminal motif of ATLs as the hypervariable region (HVR), in analogy to the C-terminal segments in small G proteins.

Datasets for native and selenomethionine-derived protein crystals grown from GDP-bound catalytic core of ATL1 were collected at a resolution of 2.2 Å and 3.5 Å, respectively. Phases were experimentally calculated using the selenomethionine dataset and combined with the high-resolution reflections of the native dataset (Table 2.1). Similar to other GDP-bound structures, the G and middle domains are engaged in the pre-hydrolysis state, with an RMSD of 0.49Å for ATL1 $R^{77}A$ and 0.56Å for ATL1 WT (PDBs 6B9D and 3Q5E) (Figure 2.1B) (Byrnes and Sondermann, 2011; O'Donnell *et al.*, 2018). At the N terminus, the HVR was partially resolved and consists of a short β-hairpin with strong electron density in an $F_o$-$F_c$ omit map (residues 18-31, Figure 2.1B and D). The structure of the isolated ATL3 G domain was determined in the presence of GDP•$Mg^{2+}$ at a resolution of 2.1 Å and solved by molecular replacement using the corresponding fragment of the ATL3 catalytic core (PDB 5VGR; O'Donnell *et al*., 2017) as the search model. In

contrast to ATL1, the HVR of ATL3 forms a single α-helix protruding from the G domain in one of the two ATL3 protomers in the asymmetric unit (residues 1-23 in Figures 2.1C and D).

**Table 2.1: X-ray data collection and refinement statistics**

| | ATL1 1-439 SeMet SAD | ATL1 1-439 Native refinement | ATL3 1-334 Mol Rep (PDB: 5VGR) |
|---|---|---|---|
| **Data collection** | | | |
| X-ray source | CHESS A1 | CHESS A1 | CHESS F1 |
| X-ray wavelength (Å) | 0.9767 | 0.9767 | 0. 9770 |
| Space group | *I222* | *I222* | $P2_12_12_1$ |
| Unit cell parameters | | | |
| a, b, c (Å) | 54.0 139.4 200.6 | 54.2 138.9 202.2 | 44.5 88.0 168.8 |
| α, β, γ (º) | 90.0 90.0 90.0 | 90.0 90.0 90.0 | 90.0 90.0 90.0 |
| Resolution range (Å) | 50.00–3.50 (3.59–3.50) | 45.16-2.20 (2.32–2.20) | 50.00-2.10 (2.15-2.10) |
| No. of reflections | | | |
| Total | 165958 (12547) | 350545 (51572) | 317439 (23823) |
| Unique | 18450 (1375) | 39278 (5640) | 39632 (2864) |
| Completeness (%) | 99.9 (100.0) | 100.0 (100.0) | 99.9 (100.0) |
| Multiplicity | 9.0 (9.1) | 8.9 (9.1) | 8.0 (8.3) |
| I/σ(I) | 12.6 (11.8) | 16.2 (3.2) | 14.7 (1.5) |
| $R_{meas}$ (%) | 34.8 (36.1) | 7.8 (73.5) | 10.5 (151.7) |
| $CC_{1/2}$ (%) | 97.2 (96.9) | 99.8 (90.2) | 99.9 (66.5) |
| Anomalous Corr. (%) | 43 (18) | - | - |
| **Refinement** | | | |
| $R_{work}$ / $R_{free}$ (%) | - | 20.1 / 23.7 | 17.9 / 23.1 |
| RMS deviations | | | |
| Bond length (Å) | - | 0.007 | 0.008 |
| Bond angle (º) | - | 0.905 | 0.913 |
| No. of atoms | | | |
| Protein | - | 3283 | 4785 |
| Ligands | - | 29 | 58 |
| Water | - | 85 | 240 |
| Average B-factors (Å$^2$) | | | |
| Total | - | 67.2 | 53.0 |
| Protein | - | 67.4 | 53.4 |
| Ligands | - | 65.5 | 34.8 |
| Waters | | 60.3 | 49.6 |
| Ramachandran (%) | | | |
| Favored | - | 95.6 | 97.5 |
| Outliers | - | 0.0 | 0.0 |
| PDB Code: | - | 6XJN | 6XJO |

(*) Values in brackets are for the highest resolution bin

Most strikingly, we determined that the HVR of ATL1 made direct contacts with the G domain of the adjacent protomer within the crystal lattice in a manner that, if extrapolated to predicted membrane orientations, would yield an array of HVR-dependent oligomers on a single membrane (Figure 2.1E). Such an oriented oligomer could work to both coordinate the catalytic cycles of many ATLs and prime them for *trans* interactions by presenting the G domain dimerization interface outwards towards the cytosol. The interface surface area between HVR and G domain of ATL1 is 312 $Å^2$ and provides a favorable solvation free energy gain ($\Delta^iG$) of -6.2 kcal/mol (Krissinel and Henrick, 2007). The $\alpha$-helical HVR of ATL3 also makes a crystal contact with neighboring unit cell G domain, though exhibits a different mode of interaction when compared to ATL1. As the ATL3 structure is comprised of the isolated G domain, the mechanistic implication of this interaction remains to be investigated.

**Figure 2.1. Novel ATL1 (catalytic core fragment) and ATL3 (G domain) structures. (A)** Sequence logos of the HVR in ATl1 (1-33), ATL2 (1-59), and ATL3 (1-25) created using WebLogo (Crooks *et al*., 2004) from ATL sequences in human, dog, horse, rat, mouse, chicken, frog, zebrafish, and cow. **(B)** Structure of human ATL1 soluble domain (1-446) displayed in blue and the HVR (residues 18-31) in magenta. Substrate (GDP and $Mg^{2+}$) shown with ball and stick representation. **(C)** Cartoon representation of human ATL3 G domain structure (1-334). Protomer 1 shown as orange and its HVR (1-25) represented in teal and GDP•$Mg^{2+}$ substrates in ball and stick representation. Protomer 2 shown in grey. **(D)** $F_O$-$F_C$ maps show electron density of ATL1 (left) and ATL3 (right) hypervariable regions from structures in (B) and (C). Stick models for each structure shown in grey and colored by element. Electron density maps are contoured at 3σ. **(E)** Organization of ATL1 structure with the HVR within the crystal lattice and extrapolated orientation relative to membranes (grey bars on top and bottom). Each protomer is represented in cartoon and surface view to display contacts. G, M, and HVR domains are labeled in either row of protomers.

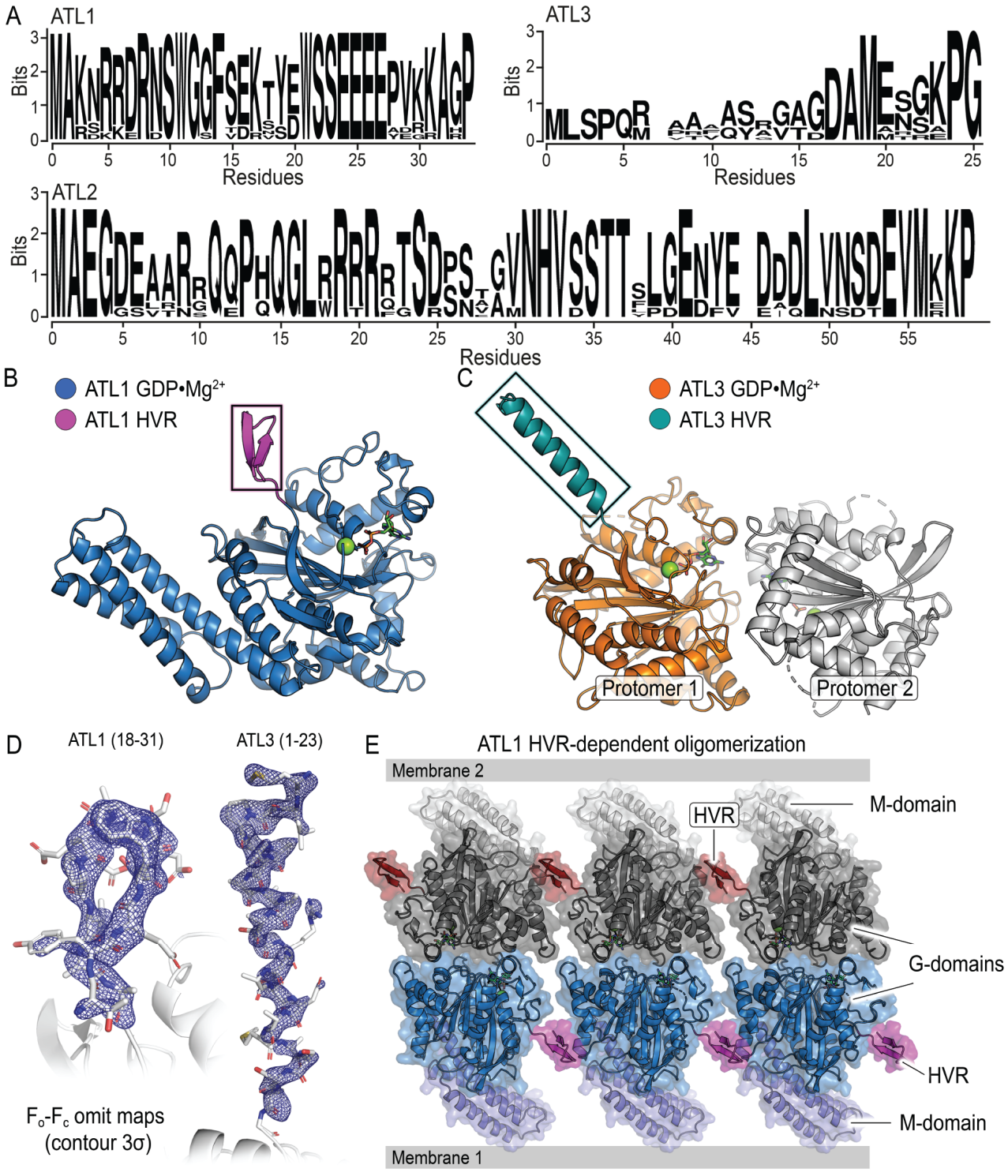
A
ATL1
ATL3
ATL2
Bits
Residues
B
ATL1 GDP•Mg2+
ATL1 HVR
C
ATL3 GDP•Mg2+
ATL3 HVR
Protomer 1
Protomer 2
D
ATL1 (18-31)
ATL3 (1-23)
Fo-Fc omit maps
(contour 3σ)
E
ATL1 HVR-dependent oligomerization
Membrane 2
HVR
M-domain
G-domains
HVR
M-domain
Membrane 1

*HVR deletion does not affect GTPase activity or nucleotide-dependent dimerization.*

The HVR is not expected to contribute to catalytic rate or oligomerization of soluble ATL protein fragments, considering the lack of evidence for higher-order interaction in solution and as based on the structural analysis suggesting a rather weak interaction. To formally assess the effect of the HVR on ATL's GTPase activity in solution, we determined phosphate release kinetics using ATL catalytic cores (*i.e.*, constructs with G and middle domains) with or without deletion of the HVR. Phosphate release rates were determined at various protein concentrations, and the turnover numbers ($k_{cat}$) for wild-type and ΔHVR proteins were found to be nearly identical for corresponding isoforms (Figure 2.4A). Since deletion of the HVR does not affect catalytic activity of ATL1 or ATL3, we would similarly assume that nucleotide-dependent dimerization would not be disrupted. This was experimentally verified through size-exclusion chromatography coupled to multi-angle light scattering (SEC-MALS) in several nucleotide-bound conditions for ATL1 and ATL3 with and without HVRs (Figure 2.2). Calculated molecular weights confirmed that the oligomerization states were not affected by deletion of the HVR and agree with dimerization trends previously reported (Byrnes and Sondermann, 2011; O'Donnell *et al.*, 2017). Additionally, small-angle X-ray scattering (SAXS) experiments were conducted with the same wild-type and ΔHVR proteins in the presence of GDP and $Mg^{2+}$. Both the pair-wise distance distributions (Figure 2.3A) and the Kratky plots (Figure 2.3B) show negligible deviations for either ATL1 or ATL3 with the deletion of the HVR, which indicates that the conformation and folded state of the proteins are equivalent. Together and as predicted, the data confirm that the HVR deletion in ATLs does not influence the solution characteristics of the protein's catalytic core.

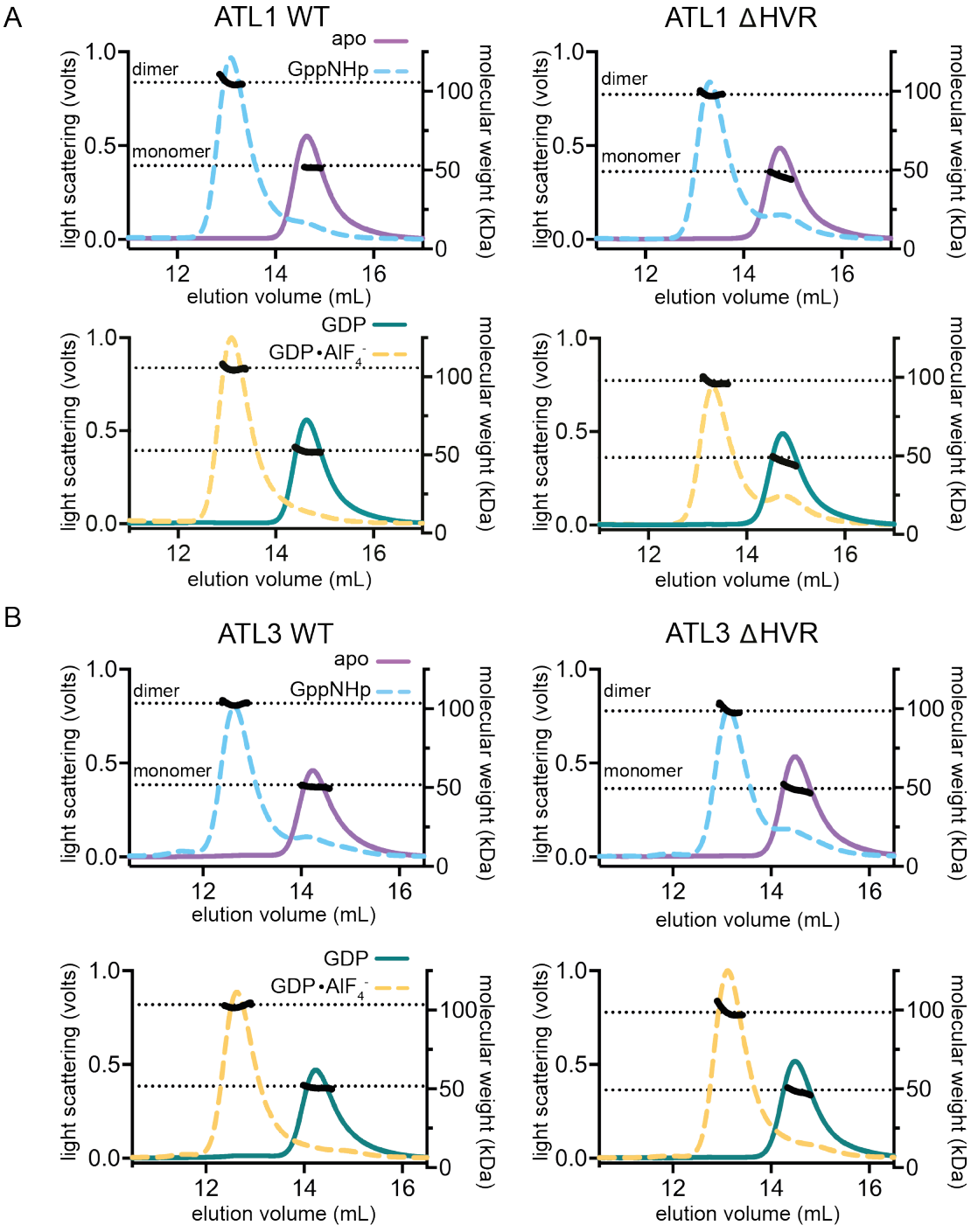
A
ATL1 WT
apo
GppNHp
dimer
monomer
light scattering (volts)
molecular weight (kDa)
elution volume (mL)
GDP
GDP•AlF4-
ATL1 ΔHVR
B
ATL3 WT
ATL3 ΔHVR

**Figure 2.2. Nucleotide-dependent oligomerization of ATL1 and ATL3 +/- the HVR. (A)** Molecular weight determination with size exclusion chromatography in tandem with multi-angle light scattering (SEC-MALS) was used to monitor oligomerization of catalytic core of WT (left) and ΔHVR (right) $ATL1^{10xHIS}$ in several nucleotide-bound conditions: apo (purple), GppNHp (blue), GDP (teal), or GDP•$AlF_4^-$ (yellow). The left Y-axis shows light scattering signal in volts as colored lines, the right Y-axis shows calculated molecular weights in kDa as black lines across elution peaks (with dashed lines at theoretical dimer/monomer weights), and the X-axis is the elution volume in mL. **(B)** ATL3 WT and ΔHVR was used in the same experimental set-up as in (A).

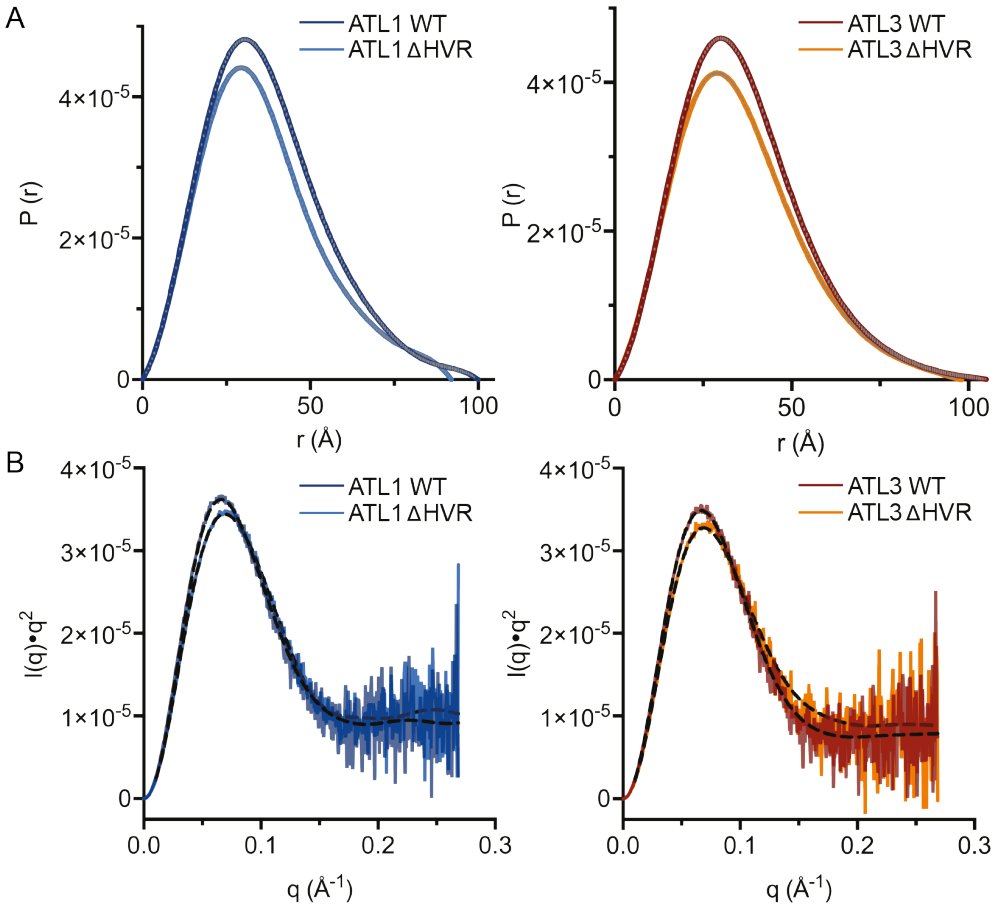


C

| | Guinier | | GNOM P(r) | | |
|---|---|---|---|---|---|
| | qRg | Rg | Quality estimate | Rg (Å) | Dmax (Å) |
| ATL1 WT | 0.32 - 1.29 | 28.55 +/- 0.065 | 82.49 | 28.92 +/- 0.074 | 100 |
| ATL1 ΔHVR | 0.28 - 1.18 | 27.75 +/- 0.071 | 80.41 | 28.13 +/- 0.053 | 92 |
| ATL3 WT | 0.28 - 1.30 | 27.68 +/- 0.071 | 85.62 | 28.32 +/- 0.11 | 106 |
| ATL3 ΔHVR | 0.28 - 1.29 | 27.20 +/- 0.090 | 85.77 | 27.75 +/- 0.077 | 94 |

**Figure 2.3. Small-angle X-ray scattering of ATL1 and ATL3 +/- the HVR. (A)** Small-angle X-ray scattering was carried out on the catalytic core of ATL1 and ATL3 with and without their respective HVR in the presence of 2 mM GDP. Plotted here is the pair-wise distance distribution, with the relative P(r) scale on the Y-axis and real-space distances (Å) on the X-axis. **(B)** Kratky plots for each condition above with experimental data represented in the corresponding colors and theoretical data shown by the dotted black lines. **(C)** Additional characteristic values determined by SAXS for each protein construct.

*Deletion of the HVR compromises membrane tethering kinetics in ATL1 but not ATL3*.

Based on the structural model, we posit that the HVR may be involved in higher-order oligomerization of ATLs but exudes functionality only when ATLs are restricted to a two-dimensional membrane where weak interactions can become more robust due to increased protein concentrations (Kuriyan & Eisenberg, 2007). To test whether the HVR plays a functional role in membrane fusion efficiency, which we would predict based on our model, we assessed the ability of ATLs to tether membranes, a crucial step in fusion. The catalytic core proteins were encoded with a C-terminal decahistidine tag that enables association with the surface of membrane vesicles containing NTA-($Ni^{2+}$)-modified lipids (at a 1% molar ratio). The protein's orientation on the vesicle surface is conducive for trans dimerization akin to the full-length transmembrane protein on the surface of the ER (Liu *et al*., 2015). Upon the addition of GTP, ATL catalyzes the tethering of vesicles, resulting in formation of vesicle clusters that increase the solution's turbidity, which can be measured by light scattering at 360 nm. We carried out this experiment across increasing protein concentrations while keeping lipid concentrations constant.

For ATL1 wild-type, the rate of tethering exhibited a strong dependency on protein concentration, and this dependency was abolished with the deletion of the HVR (Figure 2.4B and C). Tethering rates were substantially slower in wild-type ATL3, and neither wild-type nor ΔHVR displayed concentration dependent tethering kinetics (Figure 2.4B and D). Due to ATL3's lower GTPase activity, we wanted to rule out the possibility that concentrations used were insufficient to detect an effect of the HVR. Reactions with ATL3 at 10 μM, which more than compensates for differences in GTPase rates between ATL1 and ATL3, showed no difference (Figure 2.5A).

To rule out the possibility that differences in apparent tethering rates were caused by reduced lipid loading efficiency of the ΔHVR construct, we subjected both wild-type ATL1 and ΔHVR to a density gradient centrifugation in the presence and absence of lipids (Liu *et al*., 2015) and analyzed fractions from each gradient on an SDS-PAGE gel (Figure 2.5B). The protein gel confirmed that deletion of ATL1's HVR did not impact lipid binding of the proteins used in these

assays. Additional controls for tethering reactions were carried out (Figure 2.5C), including addition of 100 mM EDTA or 500 mM imidazole after 45 minutes resulting in elution of protein from lipid vesicles and subsequent drop in $OD_{360}$ signal. Reactions were also carried out in the absence of $MgCl_2$ or with GDP instead of GTP. These controls confirmed that tethering required ATL proteins on the surface of liposomes as well as GTP hydrolysis.

Observed tethering rate constants as a function of protein concentration indicate a robust tethering enhancement of wild-type ATL1 and a strong dependence on the HVR (Figure 2.4B). At later time-points, wild-type ATL1 samples produced macroscopic tethering clusters that were visually discernable and occurred when tether formation began to plateau causing high signal variation (Figure 2.4C and E). Tethered clusters cleared from solution upon elution of ATL from vesicles as shown in Figure 2.5C. Macroscopic tethering and signal variation did not occur at later time-points in ATL3 (Figure 2.4D).

**Figure 2.4. Effect of ATL1 and ATL3 HVR on enzyme kinetics. (A)** Phosphate release kinetics (left) across increasing protein concentrations and $k_{cat}$ values (right) for the catalytic core fragments of ATL1 and ATL3, WT and ΔHVR. All kinetic experiments were carried out with two biological and three technical replicates, with error bars showing standard deviation (SD; where not visible, errors were smaller than symbols representing means). ATL1 WT and ΔHVR are 6.05 ± 0.039 $min^{-1}$ and 5.94 ± 0.028 $min^{-1}$, respectively, with P=0.049; ATL3 WT and ΔHVR are 1.81 ± 0.062 $min^{-1}$ and 1.51 ± 0.084 $min^{-1}$, respectively, with P=0.015. **(B)** Left - tethering rates ($min^{-1}$) were plotted for each construct at increasing concentrations with linear regressions shown for each, and error bars showing SD. Right – specific tethering ($min^{-1}$•$\mu M^{-1}$) was calculated for each protein construct on the left and statistical significance was determined with an unpaired t-test (ATL1 WT and ΔHVR P=0.0055; ATL3 WT and ΔHVR P=0.5642). **(C)** Tethering reactions of $ATL1^{10xHIS}$ WT (dark blue) and ΔHVR (light blue) at increasing protein concentrations and fixed lipid concentration (1 mM). All tethering reactions were carried out with two biological and three technical replicates. The mean signal at $OD_{360}$ is shown with the SD in grey across the 45 minute reaction. **(D)** As in (C) but with $ATL3^{10xHIS}$ WT (maroon) and ΔHVR (orange). **(E)** Images of $ATL1^{10xHIS}$ +/- HVR tethering reactions after 45 minutes with and without GTP.

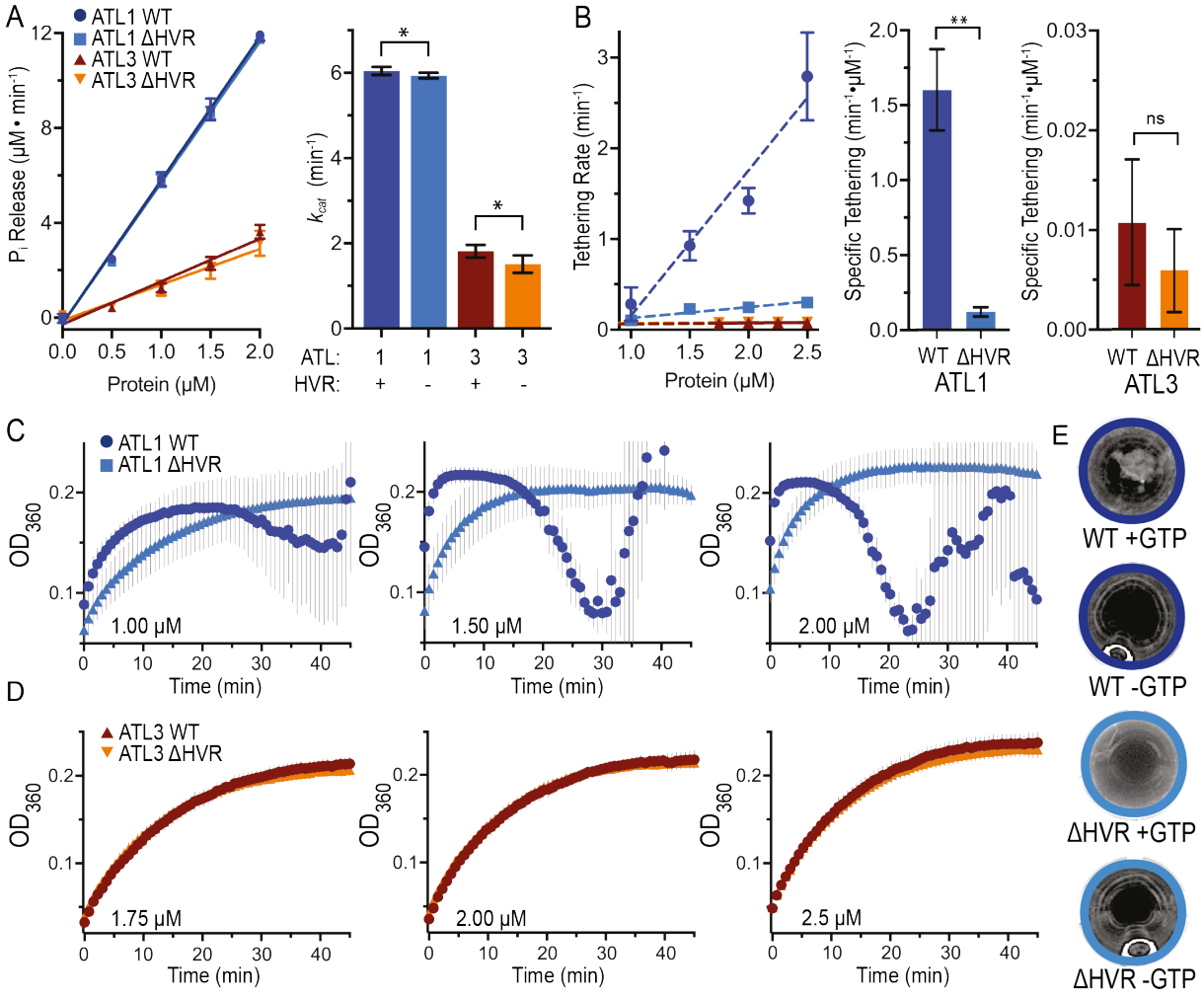
A
ATL1 WT
ATL1 ΔHVR
ATL3 WT
ATL3 ΔHVR
Pi Release (μM • min-1)
Protein (μM)
kcat (min-1)
ATL: 1 1 3 3
HVR: + - + -
B
Tethering Rate (min-1)
Protein (μM)
Specific Tethering (min-1•μM-1)
WT ΔHVR
ATL1
ATL3
ns
C
OD360
Time (min)
1.00 μM
1.50 μM
2.00 μM
D
1.75 μM
2.00 μM
2.5 μM
E
WT +GTP
WT -GTP
ΔHVR +GTP
ΔHVR -GTP

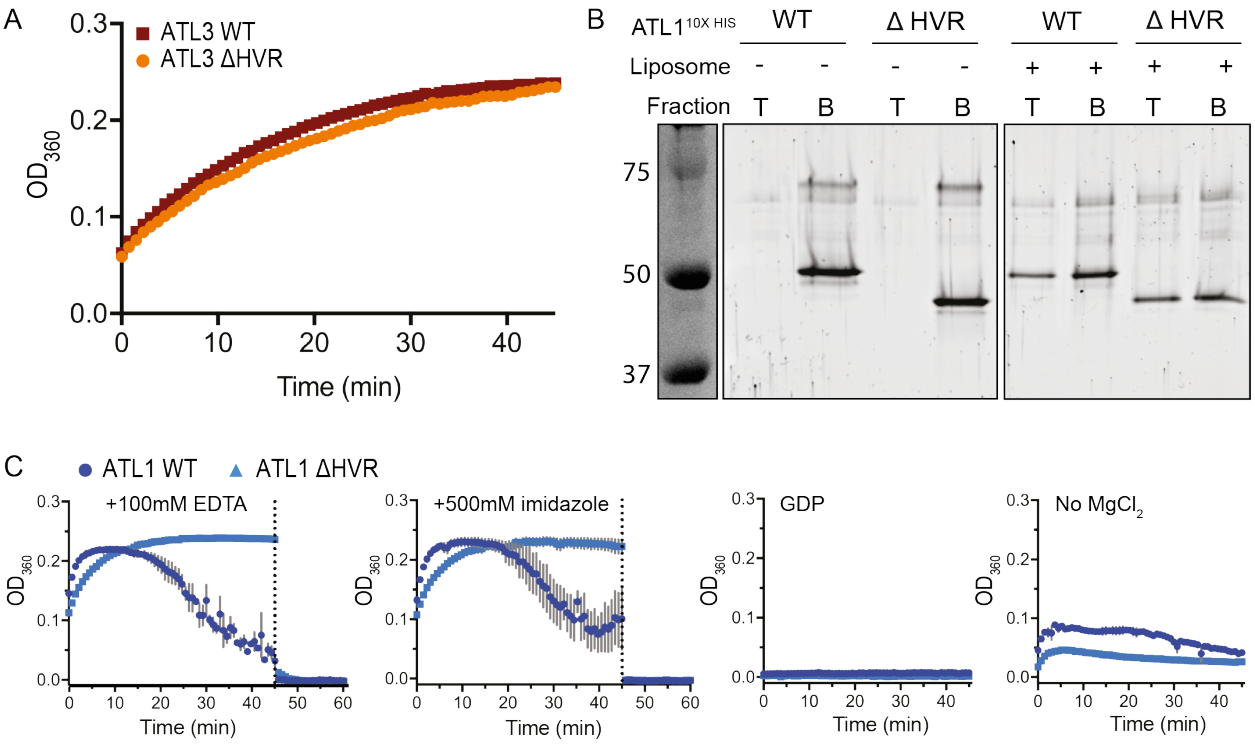


**Figure 2.5. Vesicle tethering controls. (A)** Tethering reaction of ATL3 WT (maroon) and ΔHVR (orange) as in Figure 2.4D but at 10 μM protein. **(B)** Flotation assay using Nycodenz with 1 μM ATL1$^{10xHIS}$ WT or ΔHVR catalytic-core fragment in the presence (right) or absence (left) or lipids containing 1% molar ratio of Ni-NTA-modified lipids. Top ("T") and bottom ("B") fractions were analyzed by SDS-PAGE and stained with SYPRO Ruby gel stain. The protein ladder on the left is labeled with molecular weights in kDa and was stained with Coomassie stain. **(C)** Controls for tethering reactions in Figure 2.4 carried out with 1 μM ATL1$^{10xHIS}$ and either addition of 100 mM EDTA or 500 mM imidazole at 45 minutes, or in the absence of $MgCl_2$ or presence of 2 mM GDP.

*ATL1's HVR is phosphorylated on three conserved serine residues.*

During sequence analysis, it was noted that the HVR of ATL1 was predicted to be post-translationally modified. Given the strong HVR-dependent phenotype in membrane tethering, we speculated that HVR modification in ATL1 may provide a mode of regulation *in vivo*. Unbiased proteomic screens report modifications at 11 locations, with the most reproducible modifications being phosphorylation within the HVR at S10, S22, and S23 (PhosphoSitePlus v.6.5.9.3) (Figure 2.6A).

To confirm the validity of the proteomic predictions and screens, we first probed the phosphorylation status of exogenously expressed ATL1 in U2OS cells. Cell lysates were analyzed by immunoblotting both denaturing SDS-PAGE and Phos-tag gels against a C-terminal c-myc epitope on the recombinant proteins (Figure 2.6B) (Kinoshita *et al.*, 2009). The Phos-tag reagent interacts specifically with phosphorylated species, affecting their electrophoretic mobility. The wild-type sample exhibited two distinct populations in the Phos-tag immunoblot (indicated in Figure 2.6B as "1" and "2"), which collapsed to a single species in the SDS-PAGE immunoblot without Phos-Tag reagent. Upon deletion of the ATL1 HVR, both Phos-tag and standard denaturing SDS-PAGE immunoblots depicted single populations (Figure 2.6B). These data suggest that wild-type ATL1 is phosphorylated at one or more locations in the HVR.

To gain residue-specific resolution of the phosphorylation events on ATL1, we used liquid chromatography with tandem mass spectrometry (LC-MS/MS). Exogenously expressed, wild-type ATL1 was immunoprecipitated from U2OS cell lysate, trypsin digested, and subjected to LC-MS/MS. We observed phosphorylation on the three highest confidence residues listed in the PhosphoSitePlus database: S10, S22, and S23 (Figure 2.6C). Shown are the two phosphorylated peptides identified by mass spectroscopy: peptide 1 (green) included S10, which was only observed in its phosphorylated state; and peptide 2 (maroon) included S22 and S23, which were found to be present in one of two states, both phosphorylated or neither phosphorylated. The fraction of total peptides with the phosphorylated residues is shown in Figure 2.6D, with pS10

observed on 100% of S10 and pS22/pS23 occurring on 24% of observed S22/S23-containing peptides. As shown in Figure 2.6E, these three serine residues are strictly conserved within ATL1's HVR.

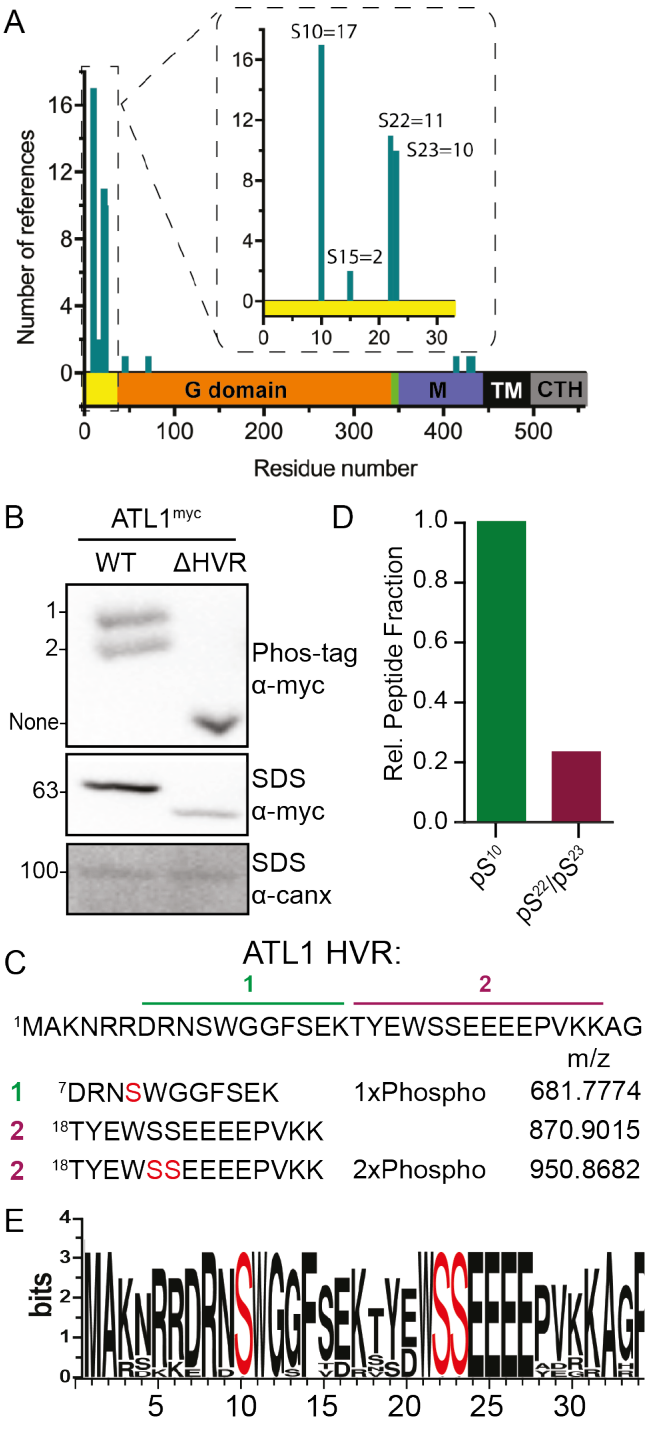

**Figure 2.6. Phosphorylation of S10, S22, S23 within ATL1's HVR. (A)** Reported phosphorylation of individual residues within human ATL1, compiled by PhosphoSitePlus v.6.5.9.3 (Hornbeck et al, 2015) with teal bars showing number of reports from unbiased proteomics screens citing a phosphorylation. The X-axis color codes residue number by structural domain. The inset of the graph magnifies the HVR and labels total reference numbers for each Ser in database. **(B)** Western blots of U2OS lysates transfected with $ATL1^{myc}$ +/- its HVR. Blots of a Phos-tag gel (top) and SDS-PAGE (middle) are shown, both probed with α-c-myc. The bottom blot (SDS-PAGE) was probed with α-calnexin as a loading control. Total protein in lysate was quantified and normalized before gel loading. Molecular weights indicated as kDa on the left (SDS-PAGE only). **(C)** LC-MS/MS of WT $ATL1^{myc}$ identified two peptides within the HVR with variably phosphorylated serine residues (peptide 1, green, S10-containing; peptide 2, maroon, S22/S23-containing). Number of modifications is indicated as well as m/z for each peptide. **(D)** Graph indicating the relative peptide fraction containing the phosphorylated species for peptide 1 and 2, respectively. **(E)** WebLogo of ATL1 HVR with its three phosphorylated serine residues identified in mass spec shown in red.

*The S10E phosphomimetic mutant decreases ATL1 tethering rates but not catalytic activity.*

Having verified that ATL1 was phosphorylated *in vivo*, we were interested if these modifications would impact catalytic activity. This was achieved by comparing wild-type protein to proteins with serine-to-glutamate mutations at sites of phosphorylation, which mimic the charge density of phosphorylated serine residues. The $k_{cat}$ values for each protein were similar between wild-type and those of proteins with phosphomimic mutations at sites that we confirmed to be modified in cells (S10E and S22E/S23E) (WT: 6.05 ± 0.04 $min^{-1}$, S10E: 5.97 ± 0.40 $min^{-1}$, and S22E/S23E: 6.31 ± 0.55 $min^{-1}$; Figure 2.7A). Since we observed that S10 was entirely phosphorylated in cells, this modification must coexist with phosphorylation of S22/S23. Therefore, the S10E/S22E/S23E triple mutant was tested and showed a minor decrease in $P_i$ release to 5.41 ± 0.15 $min^{-1}$.

Similar to experiments described for the HVR deletion mutants, we used a vesicle tethering assay to elucidate how ATL1 phosphorylation may regulate function at the membrane.

Protein concentration-dependent tethering assays were conducted with wild-type and phosphomimetic mutations that correspond to *in vivo* phosphorylation states. Figure 2.7B-C shows that the variant with a glutamate substitution at the most prevalent phosphorylation site, S10E, displayed a strong reduction in the rates of tethering. A corresponding mutant mimicking the less abundant pS22/pS23 modifications was not statistically different from wild-type. Combination of all phosphomimetic positions resulted in in a tethering phenotype comparable to that of S10E alone, indicating that modification of S10 is the major contributor to decreased tethering kinetics. The effect of the S10E/S22E/S23E mutant was noticeable also upon inspections of the reaction wells, with the mutant not showing the macroscopic vesicle aggregates that were observed with the wild-type protein.

Catalytic activity and vesicle tethering experiments were conducted with serine-to-alanine mutations in the same combinations used to mimic phosphorylation to ensure mutations were specific to the characteristics of the sidechain rather than general effects of altering the sequence. In all cases, ATL1 proteins with alanine substitutions in S10, S22 and S23 reflected the catalytic and tethering rates of wild-type ATL1 (Figure 2.8A-C).

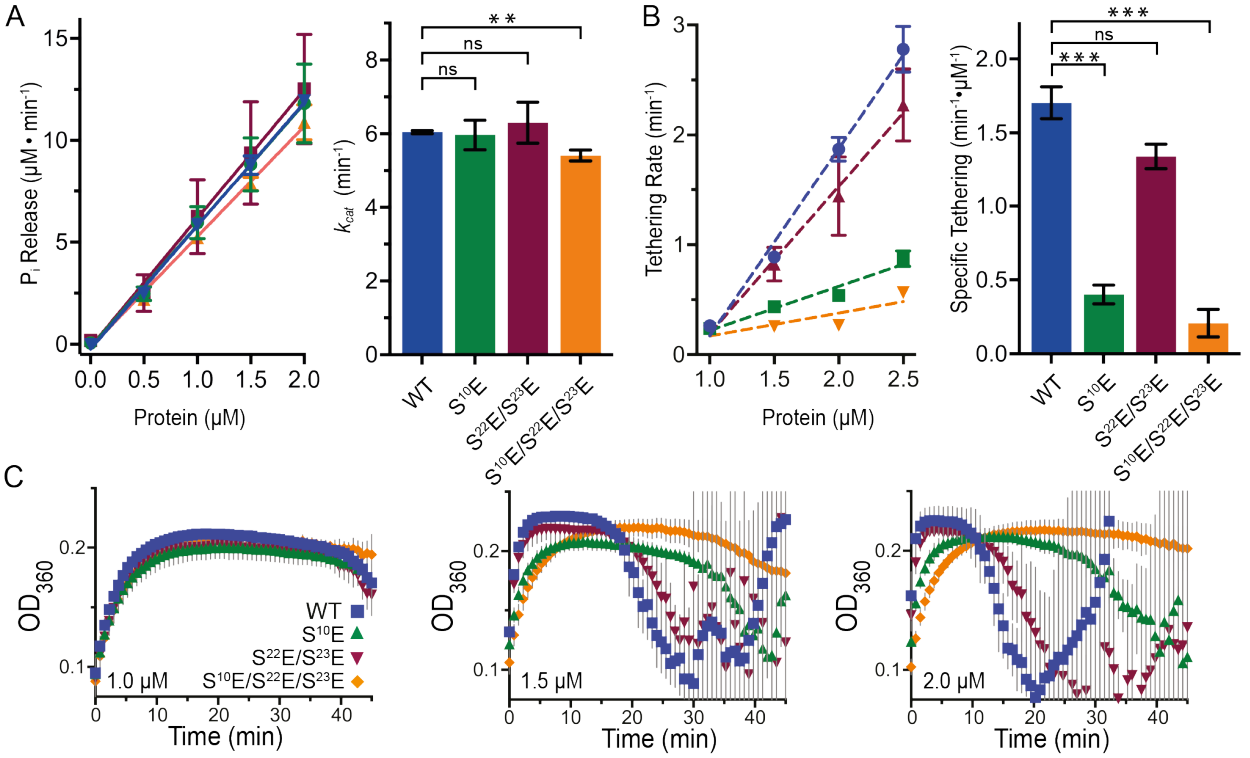


**Figure 2.7. Phosphomimetic ATL1 variants show altered vesicle tethering kinetics without affecting GTPase rates. (A)** Left - phosphate release kinetics of ATL1 WT (blue), S10E (green), S22E/S23E (maroon), and S10E/S22E/S23E (orange) across protein concentrations of 0 to 2 μM. Each data point is the average μM Pi/min released across 3 technical and 2 biological replicates with error bars showing SD. Right – $k_{cat}$ for each mutant. Statistical significance was calculated using unpaired t-test against ATL1 WT (ATL1 S10E P=0.8567; S22E/S23E P=0.6498; and S10E/S22E/S23E P=0.0019). **(B)** Left – initial tethering rate ($min^{-1}$) for each mutant at each protein concentration. The slope for each mutant construct was calculated and values plotted in graph on the right with statistical significance compared to WT protein (P=0.0005 for ATL1 S10E; P=0.0557 for ATL1 S22E/S23E; P=0.005 for ATL1 S10E/S22E/S23E). **(C)** Vesicle tethering reactions of ATL1 WT and phosphomimetic mutants at increasing protein concentrations (indicated) and constant lipid concentration (1 mM). Replicate type and number as described in Figure 2.4C and 2D.

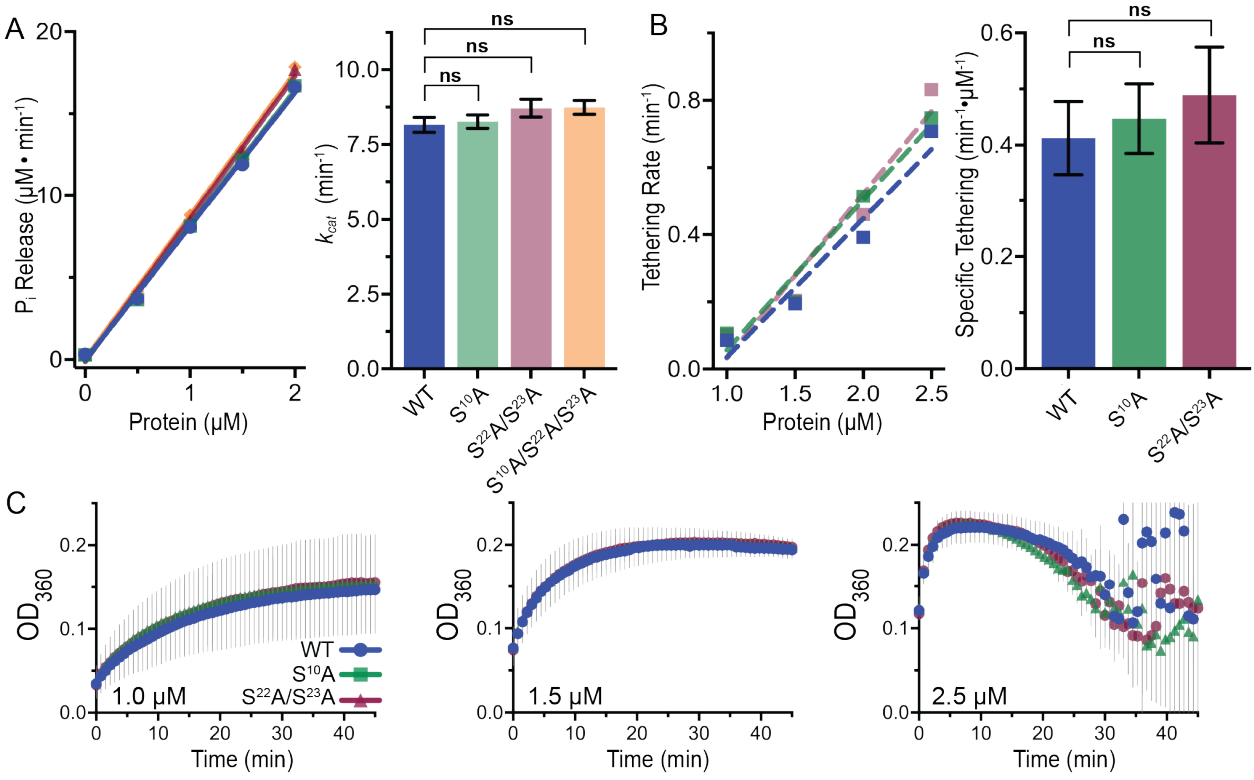


**Figure 2.8. Phosphate release and tethering kinetics for ATL1 S-to-A mutants. (A)** Left – phosphate release kinetics of the catalytic core of ATL1 WT (blue), S10A (light green), S22A/S23A (pink), and S10A/S22A/S23A (light orange) in units of μM $P_i$ released per min at increasing protein concentration (0 to 2 μM). Right – apparent turnover rates for each mutant. Experimental set-up and analysis as in Figure 2.7A. **(B)** Tethering rate analysis as described in Figure 2.7B. **(C)** Tethering reactions for ATL1$^{10xHIS}$ WT (blue), S10A (light green), and S22A/S23A (pink) measured at $OD_{360}$ across 45 minute reactions.

*ATL1 HVR phosphomimetic mutants alter protein localization and ER morphology.*

We established that incorporating phosphomimetic mutations at sites of endogenous phosphorylation modulates ATL function *in vitro*. This effect was exclusive to measurements made while ATLs were associated with membranes. To investigate how phosphorylation may regulate ATL function at the ER, we conducted immunofluorescence imaging of cells expressing either serine-to-glutamate or serine-to-alanine mutations that mimic the phosphorylated and dephosphorylated states respectively.

To exclusively measure the effects of phosphomimetic mutations, we utilized a NIH-3T3 cell line, in which all three ATL isoforms were deleted using CRISPR/Cas9-mediated gene editing (Zhao *et al*., 2016). Upon addback of wild-type ATL1 to the triple knockout (TKO) cell line, ER morphology reverted to the same as in the parent NIH-3T3 cell line (Figure 2.9A), showing a branched ER network in lieu of long, unbranched ER tubules reported for the TKO cell line. The S10, S22/S23, S10/S22/S23 phosphorylation site iterations were tested with both glutamate and alanine mutations. All ATL1 phosphomimetic mutants were shown to express by immunoblotting (Figure 2.10A) and correctly localize to the ER by imaging co-transfected cells with an mCherry tagged ER resident membrane protein, SEC61β (Figure 2.10B-H) (Zurek *et al.*, 2011).

Addback experiments resulted in changes to ATL localization and, by extension, ER morphology. ATLs were found at two major ER locations, ER tubes (wild-type phenotype) and ER puncta. Based on the ATL1 staining, two ER morphologies are also reported, the reticular structure (wild-type phenotype) and a largely diffuse structure, which adopted a 'fuzzy' appearance. The aforementioned localizations and morphologies were found across all exogenously expressed ATL constructs and were subsequently quantified (Figure 2.9B-F)**.** All mutation iterations of the phosphorylation sites resulted in a subtle reduction in the number of cells having discernable ER tubules, except for the protein with glutamate mutations at S22/S23 (Figure 2.9C and E). The phosphorylation mimetic at S22/S23 resulted in a more substantial reduction in cells with discernable ER tubules (~40%) while the corresponding alanine mutation

had no such effect. It is noteworthy that combining glutamate mutation at S22/S23 with S10E results in a rescue of tubules, indicating that normal phosphorylation and/or turnover at site S10 exhibits dominance over the phenotype (Figure 2.9D-E). In contrast, all mutants expressed result in their accumulation of puncta at the ER with position S10 contributing the most to this phenotype as seen in the variants with S10 modified alone and in combination with S22/S23 (Figure 2.9E). Additionally, the alanine mutation of S10 caused more cells with puncta than the corresponding glutamate mutation (Figure 2.9B and E). The prevalence of cells with discernable ER tubules and puncta were observed to varying degrees for both S10E and S10A variants, which indicates that regulation may require cycling between phosphorylated and dephosphorylated states. At least, it suggests that for wild-type function the unphosphorylated ATL1 is required as well as the phosphorylated species.

We also observed variable shifts in ATL's reticular localization pattern to a diffuse, fuzzy appearance depending on the phosphomimetic combination expressed. While the S10 glutamate and alanine mutants did not display this shift, expression of the S22/S23 glutamate mutant resulted in nearly all cells containing a fuzzy ATL localization (Figure 2.9B-C and F). Strikingly, expression of the S22/S23 alanine mutant remained reticular comparable to wild-type ATL1. The physiological relevance of this result is unclear since phosphorylation of S22/S23 appears unlikely to exist in the absence of S10 phosphorylation, which when combined lessens the morphology's prevalence (Figure 2.9D and F).

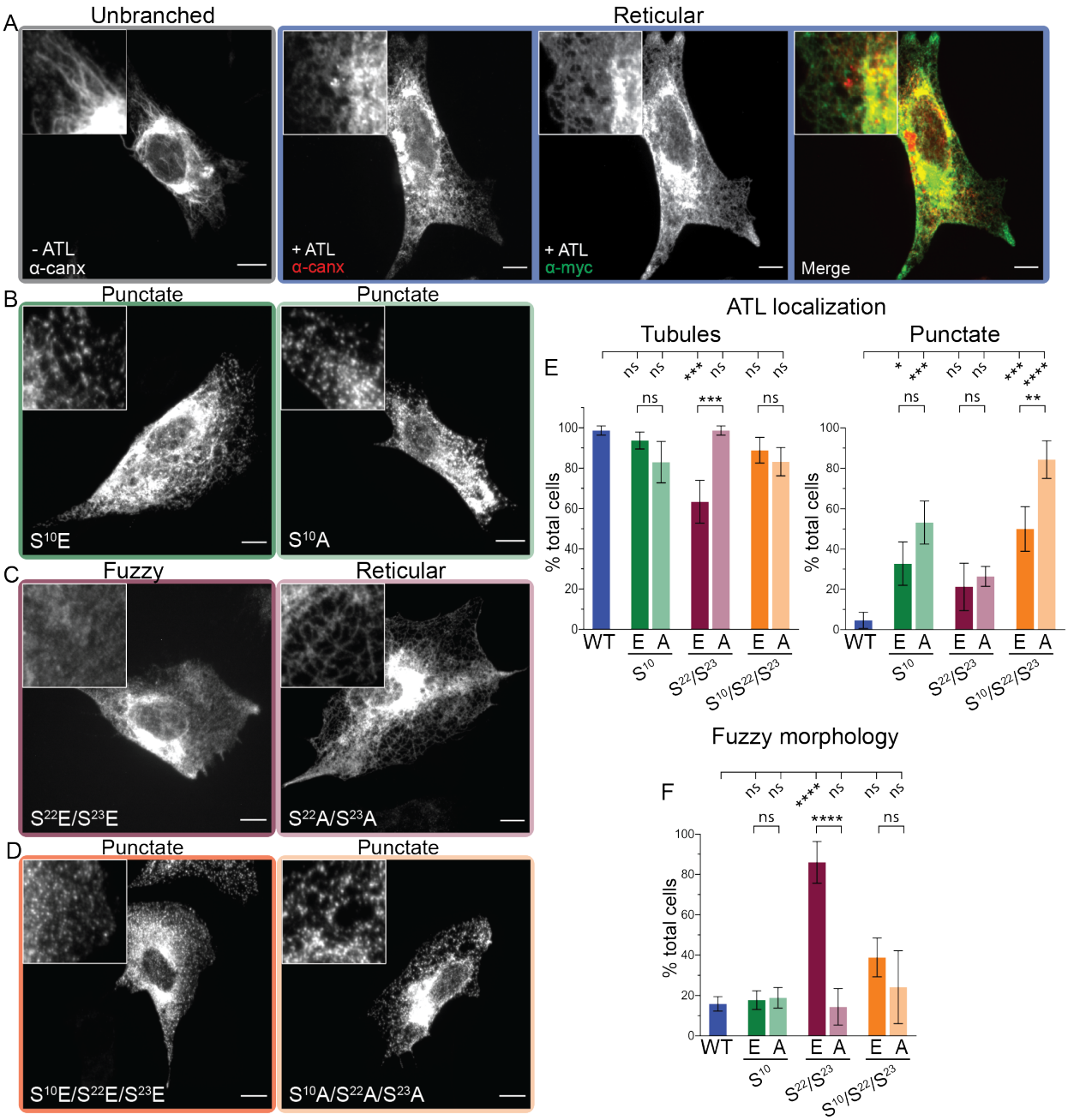
A
Unbranched
Reticular
- ATL
α-canx
+ ATL
α-canx
+ ATL
α-myc
Merge
B
Punctate
Punctate
S10E
S10A
C
Fuzzy
Reticular
S22E/S23E
S22A/S23A
D
Punctate
Punctate
S10E/S22E/S23E
S10A/S22A/S23A
ATL localization
E
Tubules
Punctate
% total cells
WT
E A
S10
S22/S23
S10/S22/S23
Fuzzy morphology
F

**Figure 2.9. HVR phosphomimetic mutations alter ATL1 ER distribution in mammalian cells.** **(A)** NIH-3T3 WT ALT1/2/3 TKO cell imaged by immunofluorescence against endogenous ER-resident protein calnexin (grey box). Same cell type exogenously expressing c-myc-tagged wild-type ATL1 and imaged by immunofluorescence against endogenous calnexin (left) and c-myc (middle). Merged signals on the right (blue box). Scale bar = 10 μm. **(B-D)** Representative images of NIH 3T3 ATL1/2/3 TKO cells transiently transfected with c-myc-tagged, phosphomimetic mutant ATL1 constructs, probed against c-myc: (B) S10E (green) or S10A (light green); (C) S22E/S23E (maroon) or S22A/S23A (pink); and (D) S10E/S22E/S23E (orange) or S10A/S22A/S23A (light orange). Each image is labeled with the most prominent phenotype observed for that condition. **(E)** Percentage of cells in (A-D) with tubule (left) and punctate (right) ATL localization. For each sample, a minimum of 70 cells were imaged (or 44 for ATL1 WT). The mean of three experiments is represented with SD represented by error bars. Statistical significance was determined by one-way ANOVA. **(F)** Quantification of cells in each condition with a fuzzy morphology of ATL signal. Represented as in (E).

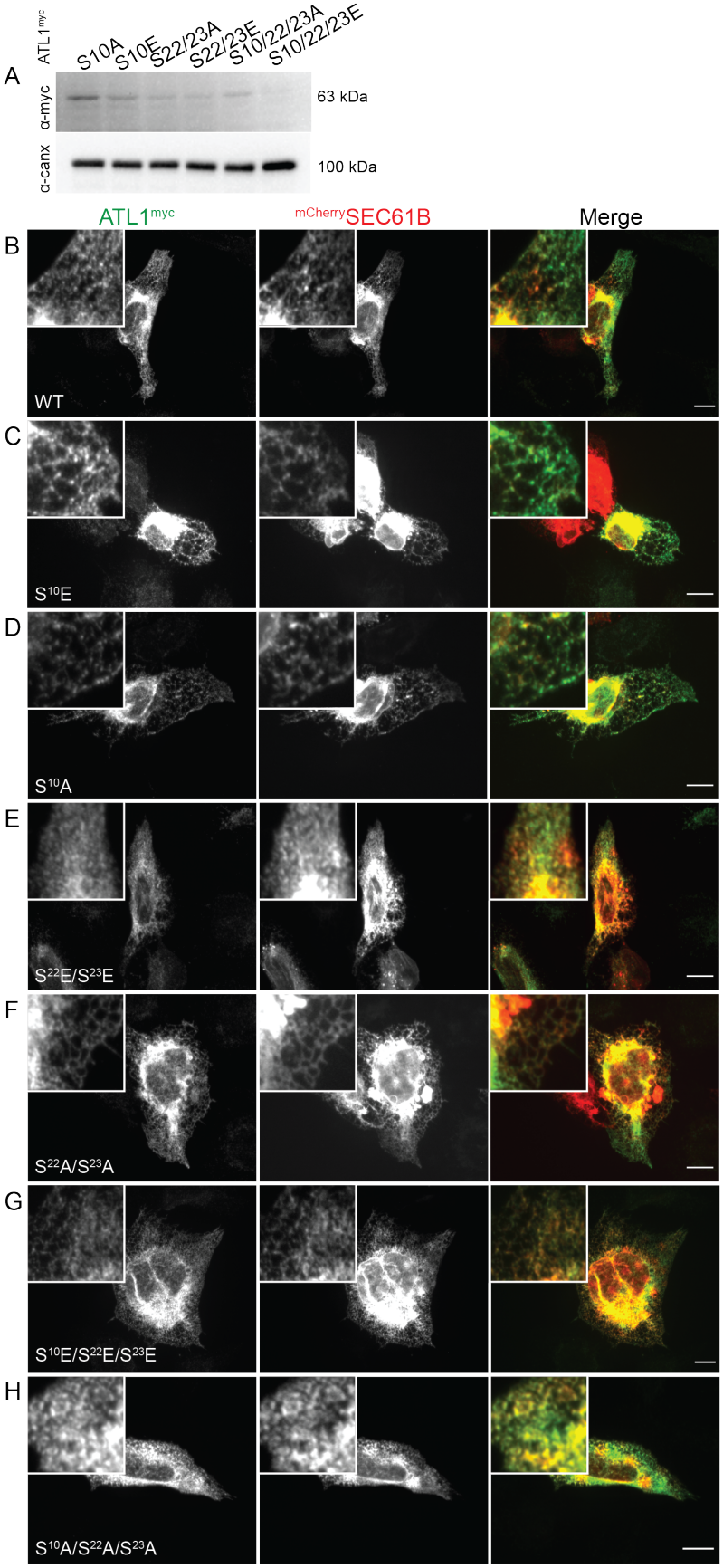
A
ATL1myc
S10A
S10E
S22/23A
S22/23E
S10/22/23A
S10/22/23E
α-myc
63 kDa
α-canx
100 kDa
ATL1myc
mCherrySEC61B
Merge
B
WT
C
S10E
D
S10A
E
S22E/S23E
F
S22A/S23A
G
S10E/S22E/S23E
H
S10A/S22A/S23A

**Figure 2.10. Expression and ER localization of ATL1 mutants: ATL1 WT, S10E, S10A, S22E/S23E, S22A/S23A, S10E/S22E/S23E, and S10A/S22A/S23A. (A)** Western blots of NIH-3T3 ATL1/2/3 TKO cells transiently transfected with S-to-A and S-to-E mutants in biologically relevant combinations as identified in WT ATL1 mass spec. Total lysate protein for each condition was quantified and normalized before loading. Both blots were transferred from SDS-PAGE gels and blotted with α-c-myc (top) and α-calnexin (bottom). **(B-H)** $ATL1^{myc}$ constructs used in Figure 2.9 transiently co-transfected with mCherry-SEC61β in U2OS cells. Cells were processed for immunofluorescence using α-c-myc antibodies, with $ATL1^{myc}$ mutants shown in green and SEC61β in red. Scale bars = 10 μM.

*Hierarchical order of ATL1 HVR phosphorylation*.

Biochemical and cellular experiments resulted in varying phenotypes depending on which phosphorylation site was investigated. In addition, the abundance of phosphorylation at a given site varies as determined by mass spectroscopy. These observations lead us to posit that phosphorylation of S10, S22, and S23 may be dependent on each other and occur hierarchically. To test this, we investigated the phosphorylation state of the aforementioned serine-to-alanine point mutants. Lysates from U2OS cells expressing each mutant were investigated using LC-MS/MS, and the peptides of interest and their corresponding mass to charge ratios are reported (Figure 2.11). We first evaluated the S22A/S23A mutant to determine if S10 could be phosphorylated. Similar to the mass spectrometry experiment with wild-type ATL1 (Figure 2.6), all identified peptides containing S10 in the ATL1 S22A/S23A sample were found to be phosphorylated (Figure 2.11A-B). This indicates phosphorylation at position S10 occurs independently of S22 or S23 modification. In contrast, the ATL1 S10A sample displays a variety of phosphorylation states on residues S22 and S23 which were not represented in the wild-type sample (Figure 2.11A and C). In the wild-type ATL1 sample, S22 and S23 were always modified together; pS22 or pS23 did not exist independently. In the ATL1 S10A sample, 17.2% of the relative peptide fraction was fully un-modified, 18.8% was phosphorylated at both S22 and S23, 43.8% was singly phosphorylated on residue S22, and 20.3% was singly phosphorylated on S23.

The differences in phosphorylation patterns observed on residues S22 and S23 in the absence of pS10 imply a coordination of these modifications relying on an intact S10 site for phosphorylation. It remains unclear what the impact of such a regulatory mechanism may be, as S10 appears to be phosphorylated nearly, if not entirely constitutively. However, as previously noted, the fact that we see significant ER morphological disruptions in both glutamate and alanine mutants at position 10 would indicate that there should be a transition from unphosphorylated to phosphorylated or turnover of this modification, the extent and kinetics of which are not yet understood.

A

| Mutant | Peptide | Phospho-Ser | m/z |
|---|---|---|---|
| $S^{22}A/S^{23}A$ | 1-$^{7}$DRNSWGGFSEK | 1 | 681.777 |
| $S^{10}A$ | 2-$^{18}$TYEWSSEEEEPVKK | None | 870.901 |
| | 2-$^{18}$TYEWSSEEEEPVKK | 1 | 910.885 |
| | 2-$^{18}$TYEWSSEEEEPVKK | 1 | 910.885 |
| | 2-$^{18}$TYEWSSEEEEPVKK | 2 | 950.868 |
| $S^{10}A/S^{22}A/S^{23}A$ | 1-$^{7}$DRNAWGGFSEK | None | 633.797 |
| | 2-$^{18}$TYEWAAEEEEPVKK | None | 854.909 |

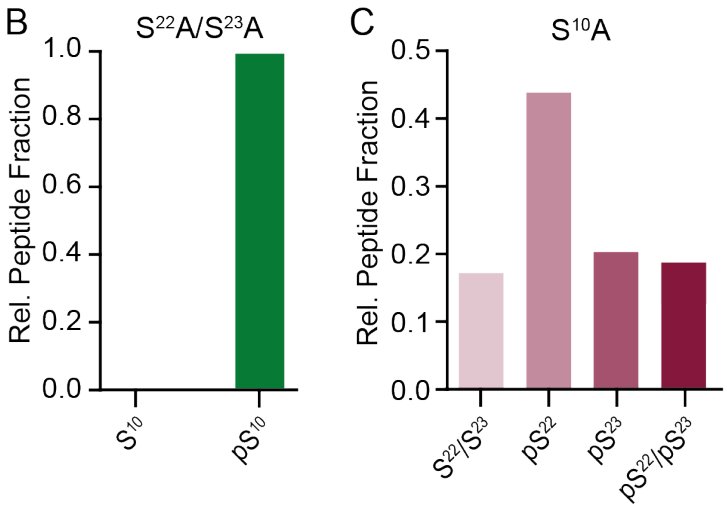


**Figure 2.11. Hierarchical order of ATL1 HVR phosphorylation. (A)** Peptides identified in LC-MS/MS analysis of ATL1 mutant proteins indicated. Phosphorylated Ser residues shown in red, and the number of phosphorylated residues specified for each peptide. **(B)** Relative peptide fraction identified in LC-MS/MS analysis of ATL1 S22A/S23A for the phosphorylated peptide 1 (from A). **(C)** As in (B), but for the variably phosphorylated peptide 2 from LC-MS/MS analysis of ATL1 S10A.

*Identification of putative kinases modifying conserved Ser residues in ATL1's HVR.*

Due to hierarchical (or coordinated) phosphorylation of the HVR, we hypothesized that one or more specific kinase(s) may recognize ATL1. Determining the kinase candidates would be a first step in uncovering ATL regulation and the cellular pathways involved. To identify kinases that specifically phosphorylate ATL1, we screened a library containing 58 Ser/Thr kinase domains (Albanese *et al*., 2018). Small-scale reactions were conducted for each kinase, with and without ATP and recombinant ATL1 catalytic core. Reactions were analyzed by denaturing SDS-PAGE and the acrylamide gels were stained with ProQ Diamond phosphoprotein stain, which selectively stains phosphoproteins; the fluorescent signal was quantified using ImageJ (Schneider *et al*., 2012). The ratio of ProQ stain signal between reactions with and without ATP represents the fold-increase of phosphorylation over background (Figure 2.12A). To exclude the possibility of signal attributed to auto-phosphorylation of the kinase, reactions without ATP and/or ATL1 were conducted for each kinase (Figure 2.13A). The screen identified several kinase families to be strong modifiers of ATL1 *in vitro*, including casein kinase II (CK2 α and α' catalytic subunits), p21-activated kinases (PAK7/5, PAK 6, and PAK4), $Ca^{2+}$/calmodulin-dependent kinase II (CaMKII α, δ, and γ isoforms), cAMP-dependent protein kinase (PKA catalytic α subunit), phosphorylase b (γ subunit), Aurora kinase A, and casein kinase I (CK1 δ, ϵ, and γ-2 subunits).

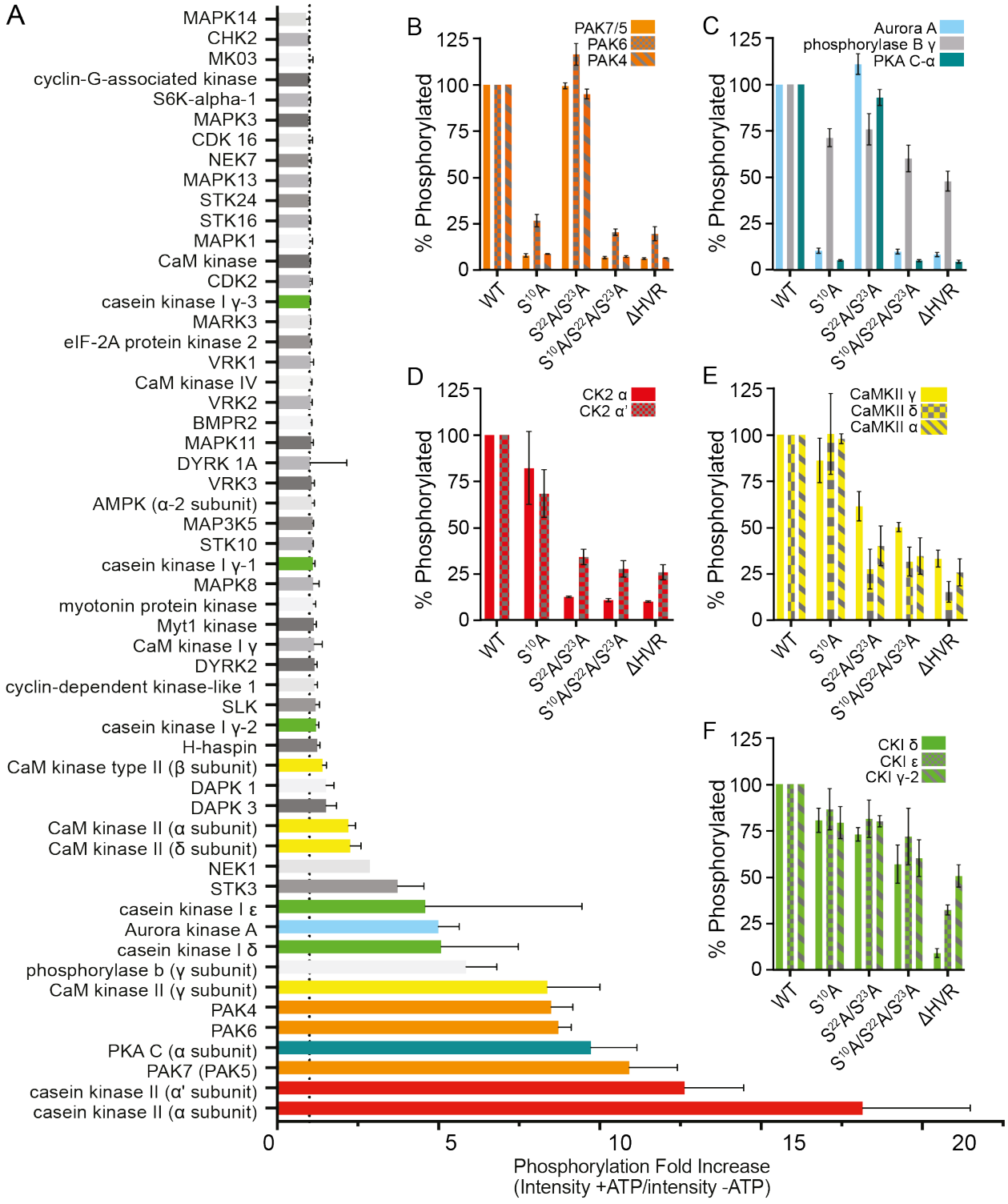
A
MAPK14
CHK2
MK03
cyclin-G-associated kinase
S6K-alpha-1
MAPK3
CDK 16
NEK7
MAPK13
STK24
STK16
MAPK1
CaM kinase
CDK2
casein kinase I γ-3
MARK3
eIF-2A protein kinase 2
VRK1
CaM kinase IV
VRK2
BMPR2
MAPK11
DYRK 1A
VRK3
AMPK (α-2 subunit)
MAP3K5
STK10
casein kinase I γ-1
MAPK8
myotonin protein kinase
Myt1 kinase
CaM kinase I γ
DYRK2
cyclin-dependent kinase-like 1
SLK
casein kinase I γ-2
H-haspin
CaM kinase type II (β subunit)
DAPK 1
DAPK 3
CaM kinase II (α subunit)
CaM kinase II (δ subunit)
NEK1
STK3
casein kinase I ε
Aurora kinase A
casein kinase I δ
phosphorylase b (γ subunit)
CaM kinase II (γ subunit)
PAK4
PAK6
PKA C (α subunit)
PAK7 (PAK5)
casein kinase II (α' subunit)
casein kinase II (α subunit)
0
5
10
15
20
Phosphorylation Fold Increase
(Intensity +ATP/intensity -ATP)
B
PAK7/5
PAK6
PAK4
% Phosphorylated
0
25
50
75
100
125
WT
S10A
S22A/S23A
S10A/S22A/S23A
ΔHVR
C
Aurora A
phosphorylase B γ
PKA C-α
D
CK2 α
CK2 α'
E
CaMKII γ
CaMKII δ
CaMKII α
F
CKI δ
CKI ε
CKI γ-2

**Figure 2.12. Kinase screen identifies enzymes that phosphorylate ATL1's HVR site-specifically *in vitro*. (A)** Kinase reactions were carried out using a screen of S/T kinase domains with the ATL1$^{6xHIS}$ catalytic core as the substrate. All reactions were carried out in triplicate, run on SDS-PAGE gels, stained with ProQ Diamond phosphoprotein stain, and band intensity quantified using ImageJ (Schneider *et al*., 2012). The phosphorylation fold-increase (plotted on the X-axis) was determined by the ratio of band intensity for the +ATP condition over the -ATP condition. Bars colored by kinase family where relevant. **(B-F)** In vitro phosphorylation reactions as in (A) but with mutant ATL1 constructs (biologically relevant S-to-A combinations and ΔHVR) using a subset of kinase candidates identified in (A): (B) PAK7/5, PAK6, and PAK4 (C) miscellaneous kinases (Aurora kinase A, phosphorylase B gamma, and PKA P-α) (D) CK2 α and CK2 α' (E) CaMKII γ, CaMKII δ, and CaMKII α (F) CKI δ, CKI ϵ, and CKI γ-2. All quantifications are displayed as percent of wild-type ATL1 phosphorylation.

Having identified candidate kinases, we next tested if their activity is specific to the conserved residues in the HVR by analyzing various mutant ATL1 proteins. Kinase reactions as described above were conducted with the following ATL1 proteins: wild-type, S10A, S22A/S23A, S10A/S22A/S23A, and ΔHVR. Results are presented as the phosphorylation percentage when compared to wild-type ATL1. Phosphorylation of S10 was specifically catalyzed by p21-activated kinases (PAK7/5, PAK6, and PAK4) (Figure 2.12B), Aurora A, and PKA C- α (Figure 2.12C). Phosphorylation of S22/S23 was specific to casein kinase II (both α and α') (Figure 2.12D) and $Ca^{2+}$/calmodulin-dependent kinase II (γ, δ, and α) (Figure 2.12E). Other kinases appeared less specific with CK I δ uniquely phosphorylating the HVR but devoid of apparent residue specificity (Figure 2.12F). CK I ϵ, CK I γ-2, and phosphorylase B γ largely phosphorylated regions of the protein within the HVR but also outside of the HVR without any obvious residue specificity (Figure 2.12C and F).

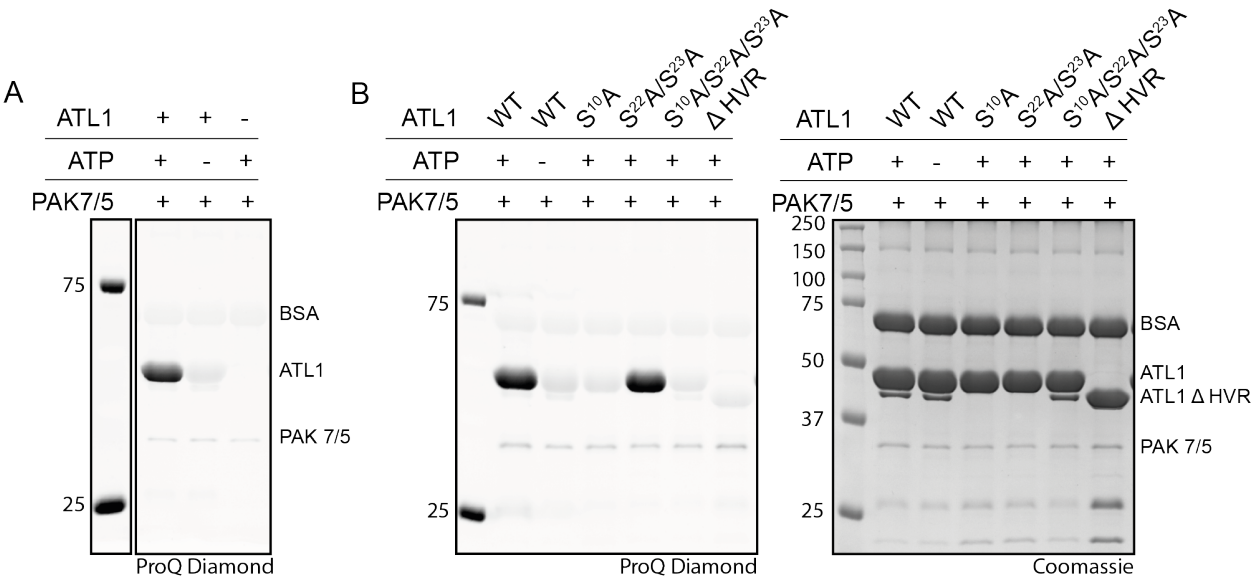


**Figure 2.13. *In vitro* phosphorylation controls and gel staining. (A)** ProQ Diamond phosphoprotein stained-SDS-PAGE analysis of kinase reaction with PAK7/5 +\- recombinant ATL1 substrate and +\- ATP. BSA was included in the reaction buffer. Bands of interest labeled on right of the gel: BSA (69.3 kDa), the catalytic core of ATL1 (52.8 kDa), and PAK7/5 (36.7 kDa). Molecular weights labeled on the left in kDa. **(B)** Follow-up kinase reactions from (A) corresponding to Figure 2.12B-F. Experimental set-up as in (A) except point mutants and HVR deletion mutant of ATL1 were used as the substrates. Reactions analyzed by SDS-PAGE stained with phosphoprotein-specific ProQ Diamond (left) and Coomassie (right). Bands of interest labeled on the right as in (A), with the addition of ΔHVR ATL1 (48.9 kDa). Molecular weights as indicated on the left in kDa.

## DISCUSSION

Here we have presented two novel ATL structures that provide the first structural insights to the short, hypervariable N-terminal region, with ATL1's HVR forming a short, B-hairpin, and ATL3's HVR forming an α-helix (Figure 2.1). The structure of ATL1's soluble, catalytic core fragment has previously been solved in three conformational forms, corresponding to steps in its catalytic cycle (Byrnes and Sondermann, 2011; Bian *et al*., 2011; Byrnes *et al*., 2013), and a similar structure for ATL3's catalytic core was solved in one of these state (O'Donnell *et al*., 2017). In all of these structures, the first ~30 or 25 residues (in ATL1 and ATL3, respectively) were not resolved. While short, these motifs are well-conserved across homologs for each ATL isoform but are highly variable across isoforms (Figure 2.1A).

The ATL1 HVR was found not only to have secondary structure, but to participate in a novel intermolecular protein interface with a small groove on the side of an adjacent G domain. In the crystal lattice, this manifests as long rows of protomers, that if extrapolated to a set of *trans* membranes, would support a model in which the HVR works to coordinate aligned ATL1 protomers on the *cis* membrane in an optimal orientation to dimerize with aligned protomers on the *trans* membrane. The benefit for orchestrated membrane fusion would be two-fold: 1) increased membrane fusion efficiency through a potential avidity effect, with hydrolysis and subsequent dimerization cycles likely to occur in a primed and coordinated manner and interactions potentially spanning longer length scales; and 2) reduction of futile *cis* hydrolysis cycles, as the orientation of the coordinated polymer would not allow it. The ATL3 HVR structure did not demonstrate any such intermolecular interactions that could support a similar mechanism.

We tested the HVR's functional relevance by studying the kinetics of the catalytic core of ATL1 and ATL3 *in vitro* in the presence or absence of the corresponding HVR motifs. We did not see changes in GTPase kinetics for the mutant proteins (Figure 2.4A), but when we compared the membrane tethering activity for each, a significant, concentration-dependent decrease in tethering rates was observed upon deletion of ATL1's HVR, while ATL3 tethering rates remained

unaffected (Figure 2.4B-D). These results support the hypothesis that ATL1's HVR provides a cooperative benefit in tethering when the protein is confined to the two-dimensional space of a membrane, while ATL3's HVR may not function in the same manner.

The canonical mechanism of action for dynamin-catalyzed membrane fission involves stimulation of GTP hydrolysis upon membrane recruitment and higher-order oligomerization (Tuma and Collins, 1996; Warnock *et al*., 1996; Chappie *et al*., 2009; Chappie *et al*., 2010). Many studies have also identified higher-order oligomerization, specifically helical ring structures, in other dynamin related proteins (Ford and Chappie, 2019), but no evidence of such behavior has been reported for ATLs. Since ATL participates in membrane fusion rather than fission, we may expect oligomerization patterns to deviate from these other examples, especially considering that homotypic fusion inherently necessitates interactions of two protein populations: those on *cis* versus *trans* membranes. While much of the research on ATL's catalytic mechanism has focused on how *trans* interactions contribute to membrane fusion, much remains unknown regarding *cis* interactions (Liu *et al*., 2015). Accumulating evidence supports the crucial role such interactions play. Mitofusins (Mfn), which are responsible for homotypic fusion of outer mitochondrial membranes, undergo *cis* oligomerization in a redox- and GTP-dependent manner, which increases mitochondrial fusion efficiency (Shutt *et al*., 2012; Mattie *et al*., 2018). More strikingly, cryo-electron tomography experiments have shown that Mfns form a more clustered array at the docking site of opposing membranes, which, with multiple rounds of GTP hydrolysis, is proceeded by formation of fusion pores (Brandt *et al*., 2016).

Initial characterizations of ATL indicated that it may exist in the cell as functional dimers or tetramers dependent on the transmembrane (TM) domain (Rismanchi *et al*., 2008; Zhu *et al*., 2003), but this has not been worked into the functional model in detail. However, visualization of ATL-containing, docked proteoliposomes by electron microscopy has revealed that an ATL tether-trapping (non-fusogenic) mutation exhibited a zipper-like ultra-structure at the vesicle interface (Saini *et al*., 2014), strongly suggesting pre-fusion coordination of ATLs. This is also supported

by the fact that fusion efficiency increases cooperatively with increased membrane surface density of ATLs (Liu *et al*., 2015). The HVR-dependent *cis* oligomer model proposed here for human ATL1 suggests one structural solution, by which formation of ATL oligomeric arrays could provide cooperative improvements to membrane fusion efficiency.

Dynamins prevent futile GTPase cycles using mechanisms to adjust hydrolysis rates depending on their environment (e.g. stimulation of activity at the membrane upon which they act while remaining in an auto-inhibited tetrameric state in the cytosol (Reubold *et al*, 2015)). However, the question of how other dynamin related proteins mitigate unproductive hydrolysis cycles remains unanswered. The model for ATL1 suggests a mechanism that may rely on a reduced likelihood of *cis* protomers undergoing futile hydrolysis-dependent dimerization, with *trans* dimerization being more favorable due to the orientation of ATL1s within the HVR-dependent array.

Based on minimal intermolecular crystal packing interactions of ATL3's HVR in the structure presented here, we propose the ATL3 HVR conformation does not represent a physiologically relevant state, but rather allows us to hypothesize that the HVR may have divergent functions in different isoforms. This notion is supported for ATL3's HVR by *in vitro* GTPase and tethering kinetics, both showing no effect with deletion of the corresponding HVR (Figure 2.4B and D). With ATL isoforms retaining such a high overall sequence identity, study of each HVR could shed light on observed discrepancies amongst the isoforms including innate kinetic and cellular fusion efficiencies (Wu *et al*., 2015; O'Donnell *et al*., 2017) as well as roles in other cellular pathways such as ER-phagy (Liang *et al*., 2018; Chen *et al*., 2019), lipid droplet formation (Klemm *et al*., 2013; Falk *et al*., 2014), and viral and bacterial proliferation (Steiner *et al*., 2017; Neufeldt *et al*., 2019; Monel *et al*., 2019). Future studies may also look at whether the HVR functions in isoform segregation, as most cell types express multiple ATL isoforms (Rismanchi *et al*., 2008) and it is not known whether mixed-isoform dimers or oligomers are functional. A recent study demonstrated isoform-specific roles of ATLs in supporting replication

of dengue and Zika virus in infected cells, implicating the HVR in this process (Neufeldt *et al*., 2019). In this context, it also was posited that the HVR may confer isoform specificity in regard to functional homodimerization in the cell, a model our present study may support.

While characterizing the ATL HVR, we found reports identifying phosphorylation of a number of conserved serine residues in ATL1, specifically in the HVR, from large, unbiased mass spectrometry-based screens (Hornbeck *et al*., 2015). Conversely, the ATL3 HVR had very few reports of phosphorylation. We were first able to confirm that phosphorylation was occurring in mammalian cells on residues S10, S22, and S23 (Figure 2.6C-D), with S10 modified in 100% of identified peptides, and S22 and S23 existing only in the same phosphorylation state. Mass spectroscopy experiments carried out on ATL1 serine-to-alanine mutant proteins established that while S10 remains completely phosphorylated in the absence of S22/S23 phosphorylation, S22 and S23-containing peptides are variably phosphorylated within a S10A mutant protein (Figure 2.11). This could result from alteration of kinase binding or recognition site(s) or downstream signaling events due to the absence of S10 phosphorylation.

Upon investigation of the effects of the biologically relevant phosphorylation states using phosphomimetic point mutations (S10E, S22E/S23E, and S10E/S22E/S23E), we discovered that, like the ATL1 ΔHVR mutant, GTPase rates were unaffected (Figure 2.7A). However, there was a significant decrease in tethering rates for both of the ATL1 constructs containing an S10E mutation (Figure 2.7B-C), with the effect being specific to the phosphomimetic mutation, as the corresponding serine-to-alanine mutant proteins were unaffected (Figure 2.8). Although our mass spectrometry results indicated that S10 was completely phosphorylated in our mammalian cell-derived sample, immunofluorescence experiments revealed that expression of either the ATL1 phosphomimetic S10E or the S10A control mutant resulted in redistribution from ER tubules to puncta (Figure 2.9B and E). This is suggestive of a crucial turnover of this modification, even if transient or within small subpopulations. Together with the delayed tethering kinetics, one functional mode for the phosphorylation could be in regulating turnover of ATLs by priming for

subsequent hydrolysis through regulation of HVR structure and/or interactions, explaining why similar kinetic trends were observed with the phosphorylation-mimetic mutants as with the ATL1 ΔHVR protein (Figure 2.4 and 2.7). A similar mechanism was identified for the regulation of mitochondrial fusion by ubiquitination state of Mfns, found to alter its oligomerization state (Anton et al., 2013). However, as our ATL1 HVR structure begins at residue 18, any model remains speculative at this point.

Unlike with the ATL1 S10 mutants, expression of ATL1 S22E/S23E and S22A/S23A mutant proteins in mammalian cells yielded different phenotypes, with expression of the S22E/S23E mutant causing a decrease in percentage of cells with discernible ATL1-positive tubules and an increase of cells lacking distinct boundaries of ATL1 signal localization (“fuzzy” signal), while expression of the S22A/S23A mutant protein presented as ATL1 WT (Figure 2.9C, E, and F). As the effects were specific to the mimicked phosphorylation state, modification of S22 and/or S23 appears to result in a more binary regulatory mode, with little impact on tethering kinetics (Figure 2.7). As S22 and S23 are located within the first β-sheet of the HVR and near the turn of the hairpin, phosphorylation of these residues may influence its secondary structure and/or electrostatic potential (figure 2.14A). While the mechanism of how this translates to cellular activity and ER sub-localization is not yet clear, the regulatory mode appears to deviate from that of S10 phosphorylation.

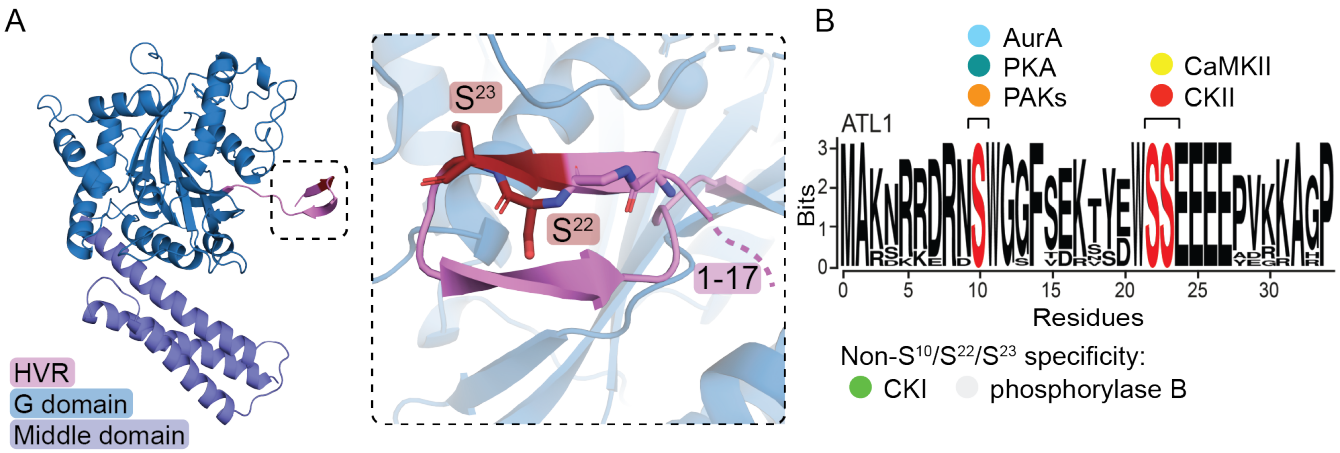


**Figure 2.14. Phosphorylation of conserved serine residues in the ATL1 HVR. (A)** Cartoon representation of the ATL1 catalytic core structure presented in Figure 2.1 (G domain, blue; middle domain, purple; structured portion of the HVR spanning residues 18-31, pink; S22 and S23, red; residues 1-17, disordered). The inset shows a close-up view of the HVR with S22 and S23 side chains and main chain represented as sticks and colored in red and according to atom type. **(B)** WebLogo of the ATL1 HVR with the conserved serine residues found to be phosphorylated shown in red. Above the phosphorylated residues are listed their cognate kinase candidates. Less specific kinase candidates are listed below.

When the ATL1 triple phosphomimetic mutant and corresponding alanine control (S10E/S22E/S23E or S10A/S22A/S23A) were expressed in cells, phenotypes appeared to more strongly match those seen with S10 mutants (Figure 2.9B-F). Along with our mass spectroscopy and kinetic data, this indicates that S10 phosphorylation retains a dominant effect over S22 and/or S23 modification.

In order to uncover the biological implications of ATL1 regulation through phosphorylation, the kinases and phosphatases carrying out these modifications must be identified. We initiated this effort by employing a kinase screen consisting of the catalytic domains of 58 Ser/Thr kinases (Albanese *et al*., 2018). One caveat of this screen remains the potential for false positives of promiscuous or non-biological modifications as only the active kinase domains were used. Nevertheless, our studies revealed several candidate families that showed site-specific effects.

Casein kinase II (CK2) α and α' catalytic subunits were the two top hits, modifying ATL1 primarily on residues S22 and/or S23 (Figure 2.12D and Figure 2.14B), which each lie within CK2's consensus sequence: S/T-X-X-E/D/pS/pY (Venerando *et al*., 2014). CK2 has chiefly been reported as playing a role in cell survival and progression, but links have also been drawn to ER stress levels (Venerando *et al*., 2014) and neuronal development (Blanquet, 2000). Both ATL1 and CK2 are primarily expressed in the brain, and while much of the time CK2 is present in the nucleus (Blanquet, 2000), the α, α', and β subunits have been located at the smooth ER (Faust *et al*., 2001).

Kinases with apparent specificity for residue S10 include the group II p21-activited kinases (PAK7/5, PAK6, and PAK4), Aurora kinase A (AurA), and cAMP-dependent protein kinase (PKA). Group II PAKs act as intermediary regulators in a wide range of cellular signaling pathways, including cytoskeletal dynamics, cell survival, and proliferation (Kumar *et al*., 2017; Eswaran *et al*., 2008). They recognize substrates with arginine residues at positions -1 to -5 and small, aliphatic residues at +2 and +3 (Rennefahrt *et al*., 2007), which deviates only slightly from the sequence surrounding S10. They have also been implicated in multiple facets of neuronal development and health, with mutations contributing to neurodegenerative disease (Eswaran *et al*., 2008). These associations render them intriguing candidates, as ATL1 is primarily expressed in the brain and mutations are causative in hereditary spastic paraplegia (Zhao *et al*., 2001) and hereditary sensory neuropathy (Guelly *et al*., 2011).

AurA also remains a top candidate for phosphorylation of S10 as it was the subject of one of the large, unbiased screens initially reporting phosphorylation on this residue (Kettenbach *et al*., 2011). AurA plays a critical role in mitotic progression through centrosome maturation, formation of bipolar microtubules spindles, and coordination of cytokinesis (Nikonova *et al*., 2013). It modifies substrates with the consensus sequence R/K/N-R-X-S/T-Φ (Ferrari *et al*., 2005), where Φ is a hydrophobic residue. While ATL is not known to function directly in these processes, it is well established that the distribution of ER throughout the cell periphery is closely linked to

microtubule cytoskeletal dynamics (Terasaki *et al*., 1986; Park *et al*., 2010) and that during mitosis, the ER undergoes drastic morphological changes (Puhka *et al.,* 2007; Wang *et al*., 2013; McCullough and Lucocq, 2005) which ATL helps regulate (Wang *et al*., 2013). Phosphorylation of ATL1 by AurA would be a novel mechanism through which ER morphology is controlled through the cell cycle. This could mirror conceptually a mechanism identified for controlling mitochondrial dynamics during G2/M phase via the phosphorylation of the dynamin-related Drp1 homolog, important for fission, through an AurA homolog (Kato *et al.,* 2019).

The catalytic subunit of PKA also modifies ATL1 on S10 *in vitro*. This kinase is activated upon increases in cellular concentration of cyclic AMP in response to diverse signaling events, including activation of G protein coupled receptors (GPCRs) (Turnham and Scott, 2016), and phosphorylates substrates with a di-arginine motif preferentially at the -2 and -3 positions and a hydrophobic residue at +1 (Walsh and Van Patten, 1994). Several studies have also reported regulation of mitochondrial dynamics by PKA by phosphorylation of Drp1 (Chang and Blackstone, 2007; Cribbs and Strack, 2007) and Mfn2 (Zhou *et al*., 2010), suggesting a common theme in regulating organelle dynamics.

Several CaMKII isoforms (α, δ, and γ) phosphorylate ATL1, primarily on S22 and/or S23, although there is also apparent modification outside of the HVR. CaMKII plays a crucial role in learning and memory formation putatively by promoting long-term potentiation in dendritic spines (Lisman *et al*., 2002). Substrates usually display an R-X-X-S/T motif (Kennelly and Krebs, 1991). A number of reports have identified functional phosphorylation of Drp1 by CaMKII resulting in altered mitochondrial morphology (Xu *et al*., 2016; Hu *et al*., 2019; Bo *et al*., 2018; Jiang *et al*., 2015). Of particular interest was a study that drew a direct connection between the action of CaMKII in murine neurons with a somatosensory-activated disruption of ER structure and the function of a dynamin-related protein in restoring a continuous structure (Kucharz and Lauritzen, 2018). Although speculation at this point, the observed events of ER collapse and recovery through a reversible, CaMKII-mediated phosphorylation of ATL1 could provide a plausible model.

While ATL1 regulation by phosphorylation has not yet been reported in humans, it has been described for its *A. thaliana* homolog root hair defective 3 (RHD3), in which C-terminal phosphorylation events increased membrane fusion activity by promoting oligomerization (Ueda *et al*., 2016). Additionally, both RHD3 and human ATL1 are regulated by ubiquitylation modifications altering protein levels through targeted protein degradation (Sun *et al*., 2020) or decreased GTPase activity (Zhao *et al*., 2020), respectively.

Based on evidence we have shown here, it appears that the ATL1's HVR encodes innate aspects of the enzyme's tethering efficiency and potentially membrane fusion. We have laid the groundwork for better understanding of how this ill-defined motif contributes to regulation of ATL1 intrinsically through putative inter-molecular interactions and extrinsically through phosphorylation of conserved serine residues by candidate kinases identified here. Future work may expand upon these models and continue to define how ATL function is regulated, especially in the context of the majority of cells that express more than one isoform with distinct HVRs, allowing for distinct control. It will also be interesting to explore how the features described here may play into the dynamic remodeling of the ER during cell division and in other pathways in which ATLs have been implicated.

## MATERIALS AND METHODS

*Protein expression and purification.*

The catalytic core with or without the N terminal hypervariable motif of hATL1 (1-449 and 33-449) and hATL3 (1-445 and 25-445) were cloned into a pET21 vector with a C terminal decahistidine tag using standard molecular cloning methods. Overexpression of each construct was carried out using BL21(DE3) *E. coli*, having induced with 0.5 mM IPTG at 18°C for 16 hours. Cells were harvested by spinning at 4500 x *g* and resuspended in $Ni^{2+}$-NTA Buffer A (25 mM tris pH 8.5, 500 mM NaCl, 20 mM imidazole), snap frozen in liquid nitrogen, and stored at -80°C. To purify, cells were thawed at room temperature, sonicated, and spun at 39,000 *x g* to remove membrane aggregates. Supernatant was loaded onto $Ni^{2+}$-NTA Superflow resin (Qiagen) at 1 mL resin: 1 L culture. Flow through was discarded and resin was washed with 15 column volumes (CV) buffer A followed by elution with $Ni^{2+}$-NTA buffer B (25 mM tris pH 7.5, 500 mM NaCl, 500 mM imidazole) in 3 CV. Protein was then desalted using a HiPrep 26/10 Desalting column (GE Life Sciences) into buffer containing 25 mM tris pH7.5, 400 mM NaCl, 5 mM EDTA. Desalted protein was concentrated with a 30,000 MWCO filter protein concentrator (Millipore) then gel filtered on a GE S200 16/60 column equilibrated in 25 mM tris pH7.5, 100 mM NaCl. Peak fractions were concentrated and snap frozen in liquid nitrogen and stored at -80°C.

*Crystallization of atlastins.*

All atlastin crystals were attained by initial sitting drop vapor diffusion screening and optimized via hanging drop vapor diffusion by mixing 1 µL of protein and 1 µL of reservoir solution followed by incubation at 20ºC. For ATL1 residues 1-439, crystals grown from either native or selenomethionine-derivatized protein were attained from a 30 mg/mL protein solution containing 2 mM Guanosine-5'-[(β,γ)-methyleno]triphosphate (Jena Biosciences) and 4 mM $MgCl_2$, and a reservoir solution containing 3.5 M sodium formate at pH 7. For ATL3 residues 1-334, crystals were attained from a 20 mg/mL protein solution containing 2mM Guanosine 5′-diphosphate

(Sigma) and 4 mM $MgCl_2$, and a reservoir solution containing 187.5 mM ammonium acetate, 21.5% PEG3350, and 100 mM Bis-Tris at pH 6.5. Crystals were transferred to reservoir solution supplemented with 25% glycerol for cryoprotection and flash frozen in liquid nitrogen.

*Crystallographic data collection and analysis.*

Data were collected on ATL1 and ATL3 using Cornell High Energy Synchrotron Source (CHESS) beamlines A1 and F1 respectively. For ATL1, single anomalous diffraction (SAD) experiments were conducted on both native and selenomethionine containing proteins for experimental phases. ATL1 data sets were collected at a lambda = 0.9767 Å with 1.0º oscillations on an ADSC Q210 CCD area detector. For ATL3, data were collected at a lambda = 0.9770 Å with 1.0º oscillations on a Pilatus 6M detector. Images were integrated and scaled using XDS and XSCALE for all data sets (Kabsch, 2010). The ATL1 selenomethionine data were truncated at 3.5 Å where the anomalous correlation was calculated to be 18% in the high resolution bin. Substructure and phases were attained though Autosol (Terwilliger *et al*., 2009) using the selenomethionine data for phase information and native data for high resolution reflections. Phases for ATL3 were attained through Molecular Replacement (MR) methods using PHENIX (Liebschner *et al*., 2019) and the coordinates of ATL3 (PDB 5VGR) as the search model. All structures were subsequently built and refined against the native datasets using PHENIX (Liebschner *et al*., 2019) and *Coot* (Emsley *et al*., 2010). The aforementioned software packages were accessed through SBGrid (www.sbgrid. org; (Morin *et al*., 2013)).

*Phosphate release kinetics.*

GTP hydrolysis activity for all ATL catalytic core constructs was determined using Enzchek phosphate assay kit from Thermo Fisher Scientific. Reactions were scaled to a final volume of 200 µL with a total concentration of 0.5 µM GTP (Thermo Fisher Scientific). Reactions contained a range of ATL concentrations, from 0 µM to 2 µM, run in the presence of reaction buffer (25 mM

tris pH 7.5, 100 mM NaCl, and 2 mM $MgCl_2$). Starting at the time of GTP addition, release of $P_i$ was measured as a spectrophotometric shift from 330 to 360 nm with the conversion of 2-amino-6-mercapto-7-methylpurine riboside (MESG) to ribose 1-phosphate and 2-amino-6-mercapto-7-methylpurine by purine nucleoside phosphorylase. $k_{cat}$ values were calculated using 3 technical replicates and 2 biological replicates for each protein construct.

*Size-exclusion chromatography tandem multi-angle light scattering (SEC-MALS).*

The catalytic core constructs of ATL1 and ATL3 with and without their HVR used for kinetic experiments were loaded onto a Superdex Increase 200 10/300 GL column (GE) at 50 μM after column equilibration with MALS buffer (25 mM tris pH 7.5, 100 mM NaCl, 2 mM EGTA, 4 mM $MgCl_2$), run at approximately 0.7 mL/min. ATL WT and mutant protein constructs were first incubated with indicated nucleotides (2 mM GDP, 2 mM GppNHp, 2 mM GDP in the presence of 2 mM $AlCl_2$, 20 mM NaF, and 4 mM EGTA, or without nucleotide). After column separation, protein was run through a static 18-angle light scattering detection unit (DAWN HELEOS-II) and a refractive index detector (Optilab T-rEX). Determination of molecular mass was calculated using Wyatt's Astra VI software. Monomeric bovine serum albumin (BSA; Sigma) was used to normalize signal intensity across light scattering detectors.

*Size exclusion chromatography coupled to small angle X-ray scattering (SEC-SAXS).*

Experimental set-up was exactly as described in SEC-MALS section. Data was collected at Cornell High Energy Synchrotron Source (CHESS) at the BioSAXS beamline (Beamline ID7A1). Background signal was established as baselined scattering signal at the beginning of each SEC run, within the void volume of the column (after buffer equilibration). All data were processed using the ATSAS suite (Manalastas-Cantos *et al*., 2021) and BioXTAS RAW (Nielsen *et al*., 2009). Frames from monodisperse peak maxima (determined by X-ray scattering intensity and absorbance intensity at 280nm) were averaged for analysis. Guinier analysis was carried out

to assess quality of the experimental data, with a maximum $qR_g$<1.3. Indirect Fourier transform of experimental data yielded the distance distribution plot, or P(r). Kratky plots were derived from P(r) functions and report protein foldedness.

*Liposome preparation.*

Lipids were purchased from Avanti Polar Lipids either reconstituted in chloroform or as desiccate and subsequently reconstituted after purchase. For liposome tethering and flotation assays, lipids were prepared at 10 mM at a molar ratio of 1% 18:1 DGS-NTA(Ni) to 99% 18:1 (Δ9-cis) PC by transferring indicated molar amounts of each lipid to glass vials and evaporating chloroform under a $N_2$ air stream for 15-20 minutes then desiccating for 1.5 hours. Multilamellar vesicles (MLV) were produced by reconstituting lipids in reaction buffer (25 mM tris pH7.5, 100 mM NaCl) with intermittent vortexing for 30 minutes. MLVs were subjected to 10 freeze-thaw cycles between liquid $N_2$ and a 25°C water bath to reduce multilamellar structures in favor of unilamellar vesicles. Liposomes were stored at -80°C until needed. Liposomes were thawed at room temperature then extruded to establish a homogenous population size of unilamellar vesicles by extruding samples through a 100nm filter 21 times and used immediately.

*Liposome tethering assay.*

Catalytic core ATL protein was loaded onto extruded vesicles as a 2X reaction stock with 2 mM lipids (1 mM final) and 2 to 5 μM protein (1 to 2.5 μM final) by incubating at room temperature for 30 minutes. Reaction was initiated by dilution of 2X reaction stock with reaction buffer (25 mM tris pH 7.5, 100 mM NaCl, 4 mM $MgCl_2$) either in the presence or absence of 500 μM GTP. Reaction was measured spectrophotometrically at $OD_{360}$ for 45 minutes. Reactions were imaged at the end of 45 minutes using a BioRad Chemidoc imaging system. Each reaction condition was carried out in triplicate with two biological replicates, and all data analysis was done in GraphPad Prism. For each triplicate condition, the signal from the reactions lacking GTP was averaged and

subtracted from the reactions containing GTP. For calculating apparent tethering rates, data were truncated after signal plateaued at the maximum and before the signal dropped off (only in conditions where a drop-off in signal was observed). A single-phase association rate was fitted to each replicate then averaged and plotted against protein concentration. The rate constant for each protein construct was determined by calculating the linear regression of rates versus protein concentration. An unpaired t-test was carried out to determine statistical significance.

*Liposome flotation assay.*

Flotation assays were conducted using a Nycodenz concentration gradient as described by Liu *et al*., 2015. Nycodenz stock solutions were prepared at 25% and 70% in tethering reaction buffer. 2X liposomes stocks were prepared and loaded with ATL as described above at 2 μM protein and 2 mM lipids. The 2X loaded vesicle stock was combined at a 1:1 ratio with the 70% Nycodenz solution, for a final mixture composed of 35% Nycodenz, 1 μM protein, and 1 mM lipids. This solution comprised the bottom 20% of the total volume of concentration gradient. The middle 70% of the gradient consisted of the 25% Nycodenz solution and the top 10% of the volume was composed of vesicle tethering reaction buffer. The gradients were spun for 2 hours at 200,310 *x g* at 4°C. Fractions were taken from the top, middle, and bottom for analysis on SDS-PAGE by SYPRO Ruby staining (Thermo Fisher Scientific).

*Mass spectroscopy.*

ATL1 (1-558) WT, S10A, S22A/S23A, and S10A/S22A/S23A were cloned into a pcDNA4 mammalian expression vector containing a C-terminal c-myc tag using standard molecular cloning techniques. U2OS cells were transiently transfected using polyethylenimine (PEI) and harvested after 24 hours by washing three times in cold PBS. Cells were lysed in 25mM tris pH7.5, 100mM NaCl, 1% Triton X-100. Cleared lysates were loaded onto EZview Red α-c-myc affinity resin pre-equilibrated in wash buffer (same as lysis buffer but with 0.1% Triton X-100) and

incubated, rotating at 4°C for 2 hours. Supernatant was removed and resin was washed three times with wash buffer for 15 minutes each. Protein was eluted in 0.1M glycine pH 2.5 by incubating for 10 minutes, followed by pH adjustment to pH 7.5 with tris-HCl. All buffers used in sample processing contained Halt protease and phosphatase inhibitor cocktail (Thermo Scientific), except for the last resin wash step and elution buffer. Samples were cleaved with trypsin following elution, then applied to LC-MS/MS for analysis.

*Western blot analysis.*

As described above, all mammalian expression vectors contained a C-terminal c-myc tag. Transfections in U2OS cells were carried out with PEI and transfections in NIH-3T3 ATL1/2/3 TKO cells were carried out using Avalanche-Omni (EZ Biosystems) according to the manufacturer's instructions. Cells were washed three times in cold PBS then harvested by scraping and lysed in cold lysis buffer containing either Halt protease and phosphatase inhibitors or cOmplete protease inhibitors (Millipore Sigma) depending on the experiment. After clearing aggregates by centrifugation, total lysate protein concentration was determined by Bradford reagent (Bio-Rad) and samples were normalized before loading on either SDS-PAGE or Phos-tag gels (FujiFilm WAKO) and run according to manufacturer's instruction, followed by transfer to polyvinylidene difluoride (PVDF) membranes. Before transfer, Phos-tag gels were washed in transfer buffer containing 10 mM EDTA a total of 3 times for more efficient protein transfer. PVDF blots were blocked either overnight at 4°C or at room temperature for 2 hours using SuperBlock T20 (TBS) Blocking Buffer (Thermo Fisher Scientific). Blots were incubated either with 1:1000 mouse α-c-myc monoclonal 9E10 antibody (Abcam) or 1:60,000 rabbit α-calnexin (Abcam) in tris-buffered saline with 0.1% Tween-20 (TBST) for 1 hour at room temperature, followed by a 30-minute incubation period with either 1:5000 goat α-mouse- HRP polyclonal antibody or 1:5000 goat α-rabbit-HRP polyclonal antibody (ThermoFisher Scientific) diluted in TBST. Blots were washed three times PBS between antibody incubation steps. Blots were developed with

enhanced chemiluminescent HRP substrate (Thermo Fisher Scientific) and imaged with a ChemiDoc XRS+ System (BioRad).

*Mammalian cell immunofluorescence and imaging.*

NIH-3T3 ATL1/2/3 TKO and U2OS cells were seeded in Nunc Lab-Tek chamber slides and transfected as described above and processed 24 hours after transfection. Cells were washed three times with cold PBS then fixed with 4% formaldehyde for 20 minutes followed by permeabilization with 0.1% Triton X-100 in PBS for 10 minutes then blocked in 10% BSA in PBS for 2 hours. Cells were incubated with primary antibody for 1.5 hours in a 5% BSA PBS solution containing 1:400 mouse α-c-myc monoclonal antibody, then washed and incubated with a 1:400 dilution of secondary antibody of α-mouse AlexaFluor 488 (Invitrogen) for an hour. Cells were washed a final set of times and treated with ProLong Gold Antifade mountant (ThermoFisher Sientific) then sealed with a cover slip. Imaging was carried out on a Perkins-Elmer UltraView spinning disc confocal microscope with a Nikon Plan Apo 60xA/1.4 oil objective.

Image brightness and contrast were adjusted using ImageJ (Schneider *et al*, 2015). Each image was scored on the presence or absence of apparent tubule and/or puncta localization of ATL as well as whether the ATL signal was diffuse (“fuzzy”) throughout the cell. These phenotypes were not mutually exclusive. For each condition, a minimum of 70 cells were imaged across three experiments and categorized (with the exception of ATL1 WT with 44 cells). Statistical comparisons determined using one-way ANOVA, with significance defined as $P<0.05$.

*Kinase screen expression and purification.*

Kinase screen (Addgene kit #1000000094) was received as bacterial glycerol stocks. Expression and purification protocols were adapted from the published protocol in Albanese *et al*., 2018. Plasmids containing all the Ser/Thr kinases were isolated by miniprep of overnight cultures inoculated from glycerol stocks. Plasmids containing kinases conferred carbenicillin

resistance and were co-transformed into Rosetta2 DE3 cells (Novagen) with a lambda phosphatase-encoding plasmid conferring resistance for spectinomycin (provided in Addgene kit). 60 mL cultures containing MagicMedia (Invitrogen), 100 µg/mL carbenicillin, and 100 µg/mL spectinomycin were inoculated with Rosetta2 DE3 co-transformations and grown at 37°C for 4 hours then 16°C for 40 hours. Cells were harvested by centrifugation at 3,000 *x g* and resuspension in buffer A and frozen in liquid $N_2$. Frozen cells pellets were thawed to room temperature followed by sonication on ice until lysates were homogenous. Lysates were cleared by centrifugation at 3,000 *x g* at 4°C then loaded onto 100 µL NiNTA resin (Qiagen) pre-equilibrated with buffer A. Resin was washed with 100CV buffer A then eluted into 250 µL buffer B. Protein concentration was measured by Bradford reagent (BioRad) then aliquoted and frozen in liquid $N_2$ and stored at -80°C until needed.

*In vitro phosphorylation experiments.*

All kinase reactions were carried out in triplicate with a final concentration of 0.5 µM kinase, 20 µM catalytic core ATL substrate, 5 µM ATP, and 1X Halt protease and phosphatase inhibitor (Thermo Fisher Scientific) in a volume of 50 µL in kinase reaction buffer (30 mM tris pH 7.5, 100 mM NaCl, 20 mM $MgCl_2$, 1 mg/mL BSA). Control reactions were run in the absence of either ATP or ATL substrate. Reactions were run for 1.5 hours at room temperature then 10% total reaction volume was analyzed by separation by SDS-PAGE followed by staining with ProQ Diamond phosphoprotein stain (Thermo Fisher Scientific) and imaging with a ChemiDoc XRS+ System (BioRad). Quantification of phosphorylation levels were determined by band intensity quantification in ImageJ (Schneider *et al*., 2012). In Figure 2.12A, the ratio of ATL1 band intensity in the presence and absence of ATP was reported as an average across triplicate experiments. In Figure 2.12B-F, phosphorylation levels of ATL1 mutant proteins were reported as a percentage of the ATL1 WT band intensity in the presence of ATP. Values here were also reported as an average across three replicates.

## REFERENCES


Ahn, S., Kim, J., Lucaveche, C. L., Reedy, M. C., Luttrell, L. M., Lefkowitz, R. J., & Daaka, Y. (2002). Src-dependent tyrosine phosphorylation regulates dynamin self-assembly and ligand-induced endocytosis of the epidermal growth factor receptor. *Journal of Biological Chemistry*, *277*(29), 26642-26651.

Albanese, S. K., Parton, D. L., Işık, M., Rodríguez-Laureano, L., Hanson, S. M., Behr, J. M., ... & Chodera, J. D. (2018). An open library of human kinase domain constructs for automated bacterial expression. *Biochemistry*, *57*(31), 4675-4689.

Anton, F., Dittmar, G., Langer, T., & Escobar-Henriques, M. (2013). Two deubiquitylases act on mitofusin and regulate mitochondrial fusion along independent pathways. *Molecular cell*, *49*(3), 487-498.

Antonny, B., Burd, C., De Camilli, P., Chen, E., Daumke, O., Faelber, K., ... & Kirchhausen, T. (2016). Membrane fission by dynamin: what we know and what we need to know. *The EMBO journal*, *35*(21), 2270-2284.

Betancourt-Solis, M. A., Desai, T., & McNew, J. A. (2018). The atlastin membrane anchor forms an intramembrane hairpin that does not span the phospholipid bilayer. *Journal of Biological Chemistry*, *293*(48), 18514-18524.

Bian, X., Klemm, R. W., Liu, T. Y., Zhang, M., Sun, S., Sui, X., ... & Hu, J. (2011). Structures of the atlastin GTPase provide insight into homotypic fusion of endoplasmic reticulum membranes. *Proceedings of the National Academy of Sciences*, *108*(10), 3976-3981.

Blanquet, P. R. (2000). Casein kinase 2 as a potentially important enzyme in the nervous system. *Progress in neurobiology*, *60*(3), 211-246.

Bo, T., Yamamori, T., Suzuki, M., Sakai, Y., Yamamoto, K., & Inanami, O. (2018). Calmodulin-dependent protein kinase II (CaMKII) mediates radiation-induced mitochondrial fission by regulating the phosphorylation of dynamin-related protein 1 (Drp1) at serine 616. *Biochemical and biophysical research communications*, *495*(2), 1601-1607.

Brandt, T., Cavellini, L., Kühlbrandt, W., & Cohen, M. M. (2016). A mitofusin-dependent docking ring complex triggers mitochondrial fusion in vitro. *Elife*, *5*, e14618.

Byrnes, L. J., Singh, A., Szeto, K., Benvin, N. M., O'donnell, J. P., Zipfel, W. R., & Sondermann, H. (2013). Structural basis for conformational switching and GTP loading of the large G protein atlastin. *The EMBO journal*, *32*(3), 369-384.

Byrnes, L. J., & Sondermann, H. (2011). Structural basis for the nucleotide-dependent dimerization of the large G protein atlastin-1/SPG3A. *Proceedings of the National Academy of Sciences*, *108*(6), 2216-2221.

Cao, H., Chen, J., Krueger, E. W., & McNiven, M. A. (2010). SRC-mediated phosphorylation of dynamin and cortactin regulates the “constitutive” endocytosis of transferrin. *Molecular and cellular biology*, *30*(3), 781-792.

Chang, C. R., & Blackstone, C. (2007). Cyclic AMP-dependent protein kinase phosphorylation of Drp1 regulates its GTPase activity and mitochondrial morphology. *Journal of Biological Chemistry*, *282*(30), 21583-21587.

Chappie, J. S., Acharya, S., Leonard, M., Schmid, S. L., & Dyda, F. (2010). G domain dimerization controls dynamin's assembly-stimulated GTPase activity. *Nature*, *465*(7297), 435-440.

Chappie, J. S., Acharya, S., Liu, Y. W., Leonard, M., Pucadyil, T. J., & Schmid, S. L. (2009). An intramolecular signaling element that modulates dynamin function in vitro and in vivo. *Molecular biology of the cell*, *20*(15), 3561-3571.

Chappie, J. S., Mears, J. A., Fang, S., Leonard, M., Schmid, S. L., Milligan, R. A., ... & Dyda, F. (2011). A pseudoatomic model of the dynamin polymer identifies a hydrolysis-dependent powerstroke. *Cell*, *147*(1), 209-222.

Chen, Q., Xiao, Y., Chai, P., Zheng, P., Teng, J., & Chen, J. (2019). ATL3 is a tubular ER-phagy receptor for GABARAP-mediated selective autophagy. *Current Biology*, *29*(5), 846-855.

Cribbs, J. T., & Strack, S. (2007). Reversible phosphorylation of Drp1 by cyclic AMP-dependent protein kinase and calcineurin regulates mitochondrial fission and cell death. *EMBO reports*, *8*(10), 939-944.

Crooks, G. E., Hon, G., Chandonia, J. M., & Brenner, S. E. (2004). WebLogo: a sequence logo generator. *Genome research*, *14*(6), 1188-1190.

Daumke, O., & Praefcke, G. J. (2016). Invited review: Mechanisms of GTP hydrolysis and conformational transitions in the dynamin superfamily. *Biopolymers*, *105*(8), 580-593.

Emsley, P., Lohkamp, B., Scott, W. G., & Cowtan, K. (2010). Features and development of Coot. *Acta Crystallographica Section D: Biological Crystallography*, *66*(4), 486-501.

Eswaran, J., Soundararajan, M., Kumar, R., & Knapp, S. (2008). UnPAKing the class differences among p21-activated kinases. *Trends in biochemical sciences*, *33*(8), 394-403.

Falk, J., Rohde, M., Bekhite, M. M., Neugebauer, S., Hemmerich, P., Kiehntopf, M., ... & Beetz, C. (2014). Functional Mutation Analysis Provides Evidence for a Role of REEP 1 in Lipid Droplet Biology. *Human mutation*, *35*(4), 497-504.

Fassier, C., Hutt, J. A., Scholpp, S., Lumsden, A., Giros, B., Nothias, F., … & Hazan, J. (2010). Zebrafish atlastin controls motility and spinal motor axon architecture via inhibition of the BMP pathway. *Nature neuroscience*, *13*(11), 1380-1387.

Faust, J. E., Desai, T., Verma, A., Ulengin, I., Sun, T. L., Moss, T. J., ... & McNew, J. A. (2015). The Atlastin C-terminal tail is an amphipathic helix that perturbs the bilayer structure during endoplasmic reticulum homotypic fusion. *Journal of Biological Chemistry*, *290*(8), 4772-4783.

Faust, M., Jung, M., Günther, J., Zimmermann, R., & Montenarh, M. (2001). Localization of individual subunits of protein kinase CK2 to the endoplasmic reticulum and to the Golgi apparatus. *Molecular and cellular biochemistry*, *227*(1-2), 73-80.

Ferrari, S., Marin, O., Pagano, M. A., Meggio, F., Hess, D., El-Shemerly, M., ... & Pinna, L. A. (2005). Aurora-A site specificity: a study with synthetic peptide substrates. *Biochemical Journal*, *390*(1), 293-302.

Fischer, D., Schabhüttl, M., Wieland, T., Windhager, R., Strom, T. M., & Auer-Grumbach, M. (2014). A novel missense mutation confirms ATL3 as a gene for hereditary sensory neuropathy type 1. *Brain*, *137*(7), e286-e286.

Ford, M. G., & Chappie, J. S. (2019). The structural biology of the dynamin-related proteins: New insights into a diverse, multitalented family. *Traffic*, *20*(10), 717-740.

Ghosh, A., Praefcke, G. J., Renault, L., Wittinghofer, A., & Herrmann, C. (2006). How guanylate-binding proteins achieve assembly-stimulated processive cleavage of GTP to GMP. *Nature*, *440*(7080), 101-104.

Guelly, C., Zhu, P. P., Leonardis, L., Papić, L., Zidar, J., Schabhüttl, M., ... & Willems, J. (2011). Targeted high-throughput sequencing identifies mutations in atlastin-1 as a cause of hereditary sensory neuropathy type I. *The American Journal of Human Genetics*, *88*(1), 99-105.

Hornbeck, P.V., Zhang, B., Murray, B., Kornhauser, J.M., Latham, V., Skrzypek, E. (2015). PhosphoSitePlus, 2014: mutations, PTMs and recalibrations. *Nucleic Acids Res*. 43:D512-20.

Hu, J., Shibata, Y., Zhu, P. P., Voss, C., Rismanchi, N., Prinz, W. A., ... & Blackstone, C. (2009). A class of dynamin-like GTPases involved in the generation of the tubular ER network. *Cell*, *138*(3), 549-561.

Hu, J., Zhang, Y., Jiang, X., Zhang, H., Gao, Z., Li, Y., ... & Gao, N. (2019). ROS-mediated activation and mitochondrial translocation of CaMKII contributes to Drp1-dependent

mitochondrial fission and apoptosis in triple-negative breast cancer cells by isorhamnetin and chloroquine. *Journal of Experimental & Clinical Cancer Research*, *38*(1), 225.

Hu, X., Wu, F., Sun, S., Yu, W., & Hu, J. (2015). Human atlastin GTPases mediate differentiated fusion of endoplasmic reticulum membranes. *Protein & cell*, *6*(4), 307-311.

Jiang, H. C., Hsu, J. M., Yen, C. P., Chao, C. C., Chen, R. H., & Pan, C. L. (2015). Neural activity and CaMKII protect mitochondria from fragmentation in aging Caenorhabditis elegans neurons. *Proceedings of the National Academy of Sciences*, *112*(28), 8768-8773.

Jimah, J. R., & Hinshaw, J. E. (2019). Structural insights into the mechanism of dynamin superfamily proteins. *Trends in Cell Biology*, *29*(3), 257-273.

Kabsch, W. (2010). XDS. *Acta Crystallogr. D*, *66*, 125-132.

Kar, U. P., Dey, H., & Rahaman, A. (2017). Regulation of dynamin family proteins by post-translational modifications. *Journal of Biosciences*, *42*(2), 333-344.

Kato, S., Okamura, E., Matsunaga, T. M., Nakayama, M., Kawanishi, Y., Ichinose, T., ... & Nomura, Y. (2019). Cyanidioschyzon merolae aurora kinase phosphorylates evolutionarily conserved sites on its target to regulate mitochondrial division. *Communications biology*, *2*(1), 1-9.

Kennelly, P. J., & Krebs, E. G. (1991). Consensus sequences as substrate specificity determinants for protein kinases and protein phosphatases. *Journal of biological chemistry*, *266*(24), 15555-15558.

Kettenbach, A. N., Schweppe, D. K., Faherty, B. K., Pechenick, D., Pletnev, A. A., & Gerber, S. A. (2011). Quantitative phosphoproteomics identifies substrates and functional modules of Aurora and Polo-like kinase activities in mitotic cells. *Science signaling*, *4*(179), rs5-rs5.

Kinoshita, E., Kinoshita-Kikuta, E., & Koike, T. (2009). Separation and detection of large phosphoproteins using Phos-tag SDS-PAGE. *Nature protocols*, *4*(10), 1513-1521.

Klemm, R. W., Norton, J. P., Cole, R. A., Li, C. S., Park, S. H., Crane, M. M., ... & Shibata, Y. (2013). A conserved role for atlastin GTPases in regulating lipid droplet size. *Cell reports*, *3*(5), 1465-1475.

Kong, L., Sochacki, K. A., Wang, H., Fang, S., Canagarajah, B., Kehr, A. D., ... & Hinshaw, J. E. (2018). Cryo-EM of the dynamin polymer assembled on lipid membrane. *Nature*, *560*(7717), 258-262.

Kornak, U., Mademan, I., Schinke, M., Voigt, M., Krawitz, P., Hecht, J., ... & Pou-Serradell, A. (2014). Sensory neuropathy with bone destruction due to a mutation in the membrane-shaping atlastin GTPase 3. *Brain*, *137*(3), 683-692.

Krissinel, E., & Henrick, K. (2007). Protein interfaces, surfaces and assemblies service PISA at European Bioinformatics Institute. *J Mol Biol*, *372*, 774-797.

Kucharz, K., & Lauritzen, M. (2018). CaMKII-dependent endoplasmic reticulum fission by whisker stimulation and during cortical spreading depolarization. *Brain*, *141*(4), 1049-1062.

Kumar, R., Sanawar, R., Li, X., & Li, F. (2017). Structure, biochemistry, and biology of PAK kinases. *Gene*, *605*, 20-31.

Kuriyan, J., & Eisenberg, D. (2007). The origin of protein interactions and allostery in colocalization. *Nature*, *450*(7172), 983-990.

Li, J., Yan, B., Si, H., Peng, X., Zhang, S. L., & Hu, J. (2017). Atlastin regulates store-operated calcium entry for nerve growth factor-induced neurite outgrowth. *Scientific reports*, *7*, 43490.

Liang, J. R., Lingeman, E., Ahmed, S., & Corn, J. E. (2018). Atlastins remodel the endoplasmic reticulum for selective autophagy. *Journal of Cell Biology*, *217*(10), 3354-3367.

Liebschner, D., Afonine, P. V., Baker, M. L., Bunkóczi, G., Chen, V. B., Croll, T. I., ... & Moriarty, N. W. (2019). Macromolecular structure determination using X-rays, neutrons and electrons: recent developments in Phenix. *Acta Crystallographica Section D: Structural Biology*, *75*(10), 861-877.

Lisman, J., Schulman, H., & Cline, H. (2002). The molecular basis of CaMKII function in synaptic and behavioural memory. *Nature Reviews Neuroscience*, *3*(3), 175-190.

Liu, T. Y., Bian, X., Romano, F. B., Shemesh, T., Rapoport, T. A., & Hu, J. (2015). Cis and trans interactions between atlastin molecules during membrane fusion. *Proceedings of the National Academy of Sciences*, *112*(15), E1851-E1860.

Liu, T. Y., Bian, X., Sun, S., Hu, X., Klemm, R. W., Prinz, W. A., ... & Hu, J. (2012). Lipid interaction of the C terminus and association of the transmembrane segments facilitate atlastin-mediated homotypic endoplasmic reticulum fusion. *Proceedings of the National Academy of Sciences*, *109*(32), E2146-E2154.

Manalastas-Cantos, K., Konarev, P. V., Hajizadeh, N. R., Kikhney, A. G., Petoukhov, M. V., Molodenskiy, D. S., ... & Franke, D. (2021). ATSAS 3.0: expanded functionality and new tools for small-angle scattering data analysis. *Journal of Applied Crystallography*, *54*(1).

Mattie, S., Riemer, J., Wideman, J. G., & McBride, H. M. (2018). A new mitofusin topology places the redox-regulated C terminus in the mitochondrial intermembrane space. *Journal of Cell Biology*, *217*(2), 507-515.

McCullough, S., & Lucocq, J. (2005). Endoplasmic reticulum positioning and partitioning in mitotic HeLa cells. *Journal of Anatomy*, *206*(5), 415-425.

Monel, B., Rajah, M. M., Hafirassou, M. L., Ahmed, S. S., Burlaud-Gaillard, J., Zhu, P. P., ... & Amraoui, S. (2019). Atlastin Endoplasmic Reticulum-Shaping Proteins Facilitate Zika Virus Replication. *Journal of virology*, *93*(23).

Morin, A., Eisenbraun, B., Key, J., Sanschagrin, P. C., Timony, M. A., Ottaviano, M., & Sliz, P. (2013). Cutting edge: Collaboration gets the most out of software. *elife*, *2*, e01456.

Moss, T. J., Andreazza, C., Verma, A., Daga, A., & McNew, J. A. (2011). Membrane fusion by the GTPase atlastin requires a conserved C-terminal cytoplasmic tail and dimerization through the middle domain. *Proceedings of the National Academy of Sciences*, *108*(27), 11133-11138.

Neufeldt, C. J., Cortese, M., Scaturro, P., Cerikan, B., Wideman, J. G., Tabata, K., ... & Bartenschlager, R. (2019). ER-shaping atlastin proteins act as central hubs to promote flavivirus replication and virion assembly. *Nature microbiology*, *4*(12), 2416-2429.

Nielsen, S. S., Toft, K. N., Snakenborg, D., Jeppesen, M. G., Jacobsen, J. K., Vestergaard, B., ... & Arleth, L. (2009). BioXTAS RAW, a software program for high-throughput automated small-angle X-ray scattering data reduction and preliminary analysis. *Journal of applied crystallography*, *42*(5), 959-964.

Nikonova, A. S., Astsaturov, I., Serebriiskii, I. G., Dunbrack, R. L., & Golemis, E. A. (2013). Aurora A kinase (AURKA) in normal and pathological cell division. *Cellular and Molecular Life Sciences*, *70*(4), 661-687.

Niu, L., Ma, T., Yang, F., Yan, B., Tang, X., Yin, H., ... & Hu, J. (2019). Atlastin-mediated membrane tethering is critical for cargo mobility and exit from the endoplasmic reticulum. *Proceedings of the National Academy of Sciences*, *116*(28), 14029-14038.

Nixon-Abell, J., Obara, C. J., Weigel, A. V., Li, D., Legant, W. R., Xu, C. S., ... & Blackstone, C. (2016). Increased spatiotemporal resolution reveals highly dynamic dense tubular matrices in the peripheral ER. *Science*, *354*(6311).

O'Donnell, J. P., Byrnes, L. J., Cooley, R. B., & Sondermann, H. (2018). A hereditary spastic paraplegia–associated atlastin variant exhibits defective allosteric coupling in the catalytic core. *Journal of Biological Chemistry*, *293*(2), 687-700.

O'Donnell, J. P., Cooley, R. B., Kelly, C. M., Miller, K., Andersen, O. S., Rusinova, R., & Sondermann, H. (2017). Timing and reset mechanism of GTP hydrolysis-driven conformational changes of atlastin. *Structure*, *25*(7), 997-1010.

Orso, G., Pendin, D., Liu, S., Tosetto, J., Moss, T. J., Faust, J. E., ... & Daga, A. (2009). Homotypic fusion of ER membranes requires the dynamin-like GTPase atlastin. *Nature*, *460*(7258), 978-983.

Park, S. H., Zhu, P. P., Parker, R. L., & Blackstone, C. (2010). Hereditary spastic paraplegia proteins REEP1, spastin, and atlastin-1 coordinate microtubule interactions with the tubular ER network. *The Journal of clinical investigation*, *120*(4), 1097-1110.

Pawar, S., Ungricht, R., Tiefenboeck, P., Leroux, J. C., & Kutay, U. (2017). Efficient protein targeting to the inner nuclear membrane requires Atlastin-dependent maintenance of ER topology. *Elife*, *6*, e28202.

Praefcke, G. J., & McMahon, H. T. (2004). The dynamin superfamily: universal membrane tubulation and fission molecules?. *Nature reviews Molecular cell biology*, *5*(2), 133-147.

Puhka, M., Vihinen, H., Joensuu, M., & Jokitalo, E. (2007). Endoplasmic reticulum remains continuous and undergoes sheet-to-tubule transformation during cell division in mammalian cells. *The Journal of cell biology*, *179*(5), 895-909.

Rennefahrt, U. E., Deacon, S. W., Parker, S. A., Devarajan, K., Beeser, A., Chernoff, J., ... & Peterson, J. R. (2007). Specificity profiling of Pak kinases allows identification of novel phosphorylation sites. *Journal of Biological Chemistry*, *282*(21), 15667-15678.

Reubold, T. F., Faelber, K., Plattner, N., Posor, Y., Ketel, K., Curth, U., ... & Haucke, V. (2015). Crystal structure of the dynamin tetramer. *Nature*, *525*(7569), 404-408.

Rismanchi, N., Soderblom, C., Stadler, J., Zhu, P. P., & Blackstone, C. (2008). Atlastin GTPases are required for Golgi apparatus and ER morphogenesis. *Human molecular genetics*, *17*(11), 1591-1604.

Saini, S. G., Liu, C., Zhang, P., & Lee, T. H. (2014). Membrane tethering by the atlastin GTPase depends on GTP hydrolysis but not on forming the cross-over configuration. *Molecular biology of the cell*, *25*(24), 3942-3953.

Schneider, C. A., Rasband, W. S., & Eliceiri, K. W. (2012). NIH Image to ImageJ: 25 years of image analysis. *Nature methods*, *9*(7), 671-675.

Shen, W., Liu, B., Liu, Z., Feng, J., Liu, C., & Kong, X. (2017). Host protein atlastin-1 promotes human immunodeficiency virus (HIV-1) replication. *Virologica Sinica*, *32*(4), 338.

Shutt, T., Geoffrion, M., Milne, R., & McBride, H. M. (2012). The intracellular redox state is a core determinant of mitochondrial fusion. *EMBO reports*, *13*(10), 909-915.

Smillie, K. J., & Cousin, M. A. (2005, January). Dynamin I phosphorylation and the control of synaptic vesicle endocytosis. In *Biochemical Society Symposia* (Vol. 72, pp. 87-97). Portland Press Limited.

Srinivasan, S., Burckhardt, C. J., Bhave, M., Chen, Z., Chen, P. H., Wang, X., ... & Schmid, S. L. (2018). A noncanonical role for dynamin-1 in regulating early stages of clathrin-mediated endocytosis in non-neuronal cells. *PLoS biology*, *16*(4), e2005377.

Steiner, B., Swart, A. L., Welin, A., Weber, S., Personnic, N., Kaech, A., ... & Hilbi, H. (2017). ER remodeling by the large GTPase atlastin promotes vacuolar growth of Legionella pneumophila. *EMBO reports*, *18*(10), 1817-1836.

Summerville, J. B., Faust, J. F., Fan, E., Pendin, D., Daga, A., Formella, J., ... & McNew, J. A. (2016). The effects of ER morphology on synaptic structure and function in Drosophila melanogaster. *Journal of cell science*, *129*(8), 1635-1648.

Sun, J., Movahed, N., & Zheng, H. (2020). LUNAPARK Is an E3 Ligase That Mediates Degradation of ROOT HAIR DEFECTIVE3 to Maintain a Tubular ER Network in Arabidopsis. *The Plant Cell*, *32*(9), 2964-2978.

Terasaki, M., Chen, L. B., & Fujiwara, K. (1986). Microtubules and the endoplasmic reticulum are highly interdependent structures. *The Journal of cell biology*, *103*(4), 1557-1568.

Terwilliger, T. C., Adams, P. D., Read, R. J., McCoy, A. J., Moriarty, N. W., Grosse-Kunstleve, R. W., ... & Hung, L. W. (2009). Decision-making in structure solution using Bayesian estimates of map quality: the PHENIX AutoSol wizard. *Acta Crystallographica Section D: Biological Crystallography*, *65*(6), 582-601.

Tuma, P. L., & Collins, C. A. (1994). Activation of dynamin GTPase is a result of positive cooperativity. *Journal of Biological Chemistry*, *269*(49), 30842-30847.

Turnham, R. E., & Scott, J. D. (2016). Protein kinase A catalytic subunit isoform PRKACA; History, function and physiology. *Gene*, *577*(2), 101-108.

Ueda, H., Yokota, E., Kuwata, K., Kutsuna, N., Mano, S., Shimada, T., ... & Shimmen, T. (2016). Phosphorylation of the C terminus of RHD3 has a critical role in homotypic ER membrane fusion in Arabidopsis. *Plant physiology*, *170*(2), 867-880.

Venerando, A., Ruzzene, M., & Pinna, L. A. (2014). Casein kinase: the triple meaning of a misnomer. *Biochemical Journal*, *460*(2), 141-156.

Walsh, D. A., & Van Patten, S. M. (1994). Multiple pathway signal transduction by the cAMP-dependent protein kinase. *The FASEB Journal*, *8*(15), 1227-1236.

Wang, S., Romano, F. B., Field, C. M., Mitchison, T. J., & Rapoport, T. A. (2013). Multiple mechanisms determine ER network morphology during the cell cycle in Xenopus egg extracts. *Journal of Cell Biology*, *203*(5), 801-814.

Warnock, D. E., Hinshaw, J. E., & Schmid, S. L. (1996). Dynamin self-assembly stimulates its GTPase activity. *Journal of Biological Chemistry*, *271*(37), 22310-22314.

Winsor, J., Hackney, D. D., & Lee, T. H. (2017). The crossover conformational shift of the GTPase atlastin provides the energy driving ER fusion. *Journal of Cell Biology*, *216*(5), 1321-1335.

Wu, F., Hu, X., Bian, X., Liu, X., & Hu, J. (2015). Comparison of human and Drosophila atlastin GTPases. *Protein & cell*, *6*(2), 139-146.

Xu, S., Wang, P., Zhang, H., Gong, G., Cortes, N. G., Zhu, W., ... & Wang, W. (2016). CaMKII induces permeability transition through Drp1 phosphorylation during chronic β-AR stimulation. *Nature communications*, *7*(1), 1-13.

Zhao, G., Zhu, P. P., Renvoisé, B., Maldonado-Báez, L., Park, S. H., & Blackstone, C. (2016). Mammalian knock out cells reveal prominent roles for atlastin GTPases in ER network morphology. *Experimental cell research*, *349*(1), 32-44.

Zhao, J., & Hedera, P. (2013). Hereditary spastic paraplegia-causing mutations in atlastin-1 interfere with BMPRII trafficking. *Molecular and Cellular Neuroscience*, *52*, 87-96.

Zhao, X., Alvarado, D., Rainier, S., Lemons, R., Hedera, P., Weber, C. H., ... & Bui, M. (2001). Mutations in a newly identified GTPase gene cause autosomal dominant hereditary spastic paraplegia. *Nature genetics*, *29*(3), 326-331.

Zhao, Y., Feng, Z., Zou, Y., & Liu, Y. (2020). The E3 Ubiquitin Ligase SYVN1 Ubiquitinates Atlastins to Remodel the Endoplasmic Reticulum Network. *iScience*, 101494.

Zhou, W., Chen, K. H., Cao, W., Zeng, J., Liao, H., Zhao, L., & Guo, X. (2010). Mutation of the protein kinase A phosphorylation site influences the anti-proliferative activity of mitofusin 2. *Atherosclerosis*, *211*(1), 216-223.

Zhu, P. P., Patterson, A., Lavoie, B., Stadler, J., Shoeb, M., Patel, R., & Blackstone, C. (2003). Cellular localization, oligomerization, and membrane association of the hereditary spastic paraplegia 3A (SPG3A) protein atlastin. *Journal of Biological Chemistry*, *278*(49), 49063-49071.

Zurek, N., Sparks, L., & Voeltz, G. (2011). Reticulon short hairpin transmembrane domains are used to shape ER tubules. *Traffic*, *12*(1), 28-41.

**CHAPTER THREE**

# CLINICAL AND MOLECULAR CHARACTERIZATION OF A NOVEL ATL1 MUTATION ASSOCIATED WITH SPASTIC QUADRIPLEGIA

## ABSTRACT

Hereditary spastic paraplegia (HSP) comprises a heterogenous group of neurodegenerative disorders affecting the long axons of motor neurons and causing progressive weakness and spasticity in the lower extremities. Here, we report a novel disease-causing codon insertion mutation in the *SPG3A/atlastin-1 (ATL1)* gene, leading to an additional asparagine residue at position 417 (N417ins). The mutation correlates with complex, early-onset HSP manifesting with spastic quadriplegia, generalized dystonia, and a thinning corpus callosum. ATL proteins belong to the dynamin superfamily and utilize the energy from GTP hydrolysis for membrane tethering and fusion for the formation of a highly branched smooth endoplasmic reticulum (ER). The novel insertion mutation locates within the stalk-like middle domain of the protein, adjacent to its N-terminal GTPase domain near a crucial site for intramolecular interactions. While innate nucleotide binding and GTP hydrolysis remain unaffected by the insertion mutation, membrane tethering rates are increased, indicative of a gain-of-function disease mechanism uncommon for ATL-associated pathologies. Limited proteolysis and FRET-based studies suggest an aberrant pre-hydrolysis conformational change leads to excessive membrane tethering. Continued efforts in elucidating HSP disease mutations and their underlying mechanisms are crucial not only for furthering our understanding of pathogenesis and potential treatments, but also in advancing our knowledge of ATL's basic cellular and molecular functions.

## INTRODUCTION

Hereditary spastic paraplegias (HSP) are a heterogenous group of neuropathies. They share disease presentation characterized by progressive spasticity and weakness of the legs caused by axonal degeneration of motor neuron, which begins at their distal ends (DeLuca *et al*., 2004; Fink *et al*., 2013; Fink, 2006; Blackstone, 2012). Causative mutations have been identified in at least 80 genes, denoted *SPG1-80*, due to the characteristic spastic gait and named in order of their identification (Blackstone, 2020; Fink, 2020). The clinical manifestations of this disorder also vary significantly and are defined as either “pure” or “complex”, with pure cases primarily causing lower leg spasticity and complex cases involving additional neurological symptoms such as visual impairment, intellectual disability, epileptic seizures, and amyotrophy (Blackstone, 2018; Fink, 2013). Incidence rates of HSPs are reported between 1.2 to 9.6 out of every 100,000 people (Fink, 2013; Willkom, 2016; Blackstone, 2018; Klebe *et al*., 2015; Blackstone, 2012), with inheritance modes ranging from autosomal dominant, autosomal recessive, X-linked recessive, and mitochondrial. Mutations in *SPG3A* (encoding human atlastin-1/ATL1) account for approximately 10% of all HSP cases, second only to *SPG4*, encoding spastin (Zhao *et al*., 2001), and are the leading cause of early onset cases (Abel *et al*, 2004). There have been 68 HSP-causing mutations identified in ATL1, with a majority being autosomal dominant and resulting in early onset and/or pure cases in patients (Blackstone, 2020; Depienne *et al*., 2007; Fink, 2006; Blackstone, 2012).

ATL1 is a member of the dynamin superfamily, which comprise a canonical large GTPase (G) domain and function in a variety of cellular pathways including vesicle fission, remodeling of organelle membranes, and immunity through antiviral activity (Praefcke and McMahon, 2004). Other, structurally or functionally conserved domains within the dynamin superfamily include a stalk-like middle domain, a membrane-localization feature (e.g. transmembrane domain, PH domain, lipid modification), and, in many cases, a GTPase effector domain (GED) for regulation of GTP hydrolysis. Canonically, coordinated GTPase activity in dynamin-related proteins (DRPs)

is stimulated upon higher order oligomerization including intra- and intermolecular interactions, orchestrated in part through the GED (Tuma and Collins, 1994; Warnock *et al*., 1996; Gasper *et al*., 2009; Ford and Chappie, 2019).

ATL1 is a resident ER enzyme, residing in the high-curvature tubules of the smooth ER, where it tethers and fuses tubules following GTPase-driven reaction cycles to generate and maintain the ER's polygonal morphology (Orso *et al*., 2009; Hu *et al*., 2009). The N-terminus of ATL1 is composed of the canonical large G domain followed by a flexible linker region and middle domain, facing the cytoplasm, followed by a short, membrane-associated wedge motif with preference for high-curvature ER tubules (Betancourt-Solis *et al*., 2018). At its C terminus, it contains a cytosolic, short, amphipathic helix that induces membrane disorder and is required for efficient fusion (Liu *et al*., 2012; Faust *et al*., 2015). Unlike most DRPs, ATL1 lacks a GED and catalyzes membrane fusion through hydrolysis-dependent homodimerization across *trans* membranes (Liu *et al*., 2015; Byrnes and Sondermann, 2011; Bian *et al*., 2011; Byrnes *et al*., 2013). ATL is the minimal machinery necessary for membrane fusion (Orso *et al*., 2009) and formation of a reticular ER network *in vitro* (Powers *et al*., 2017). The N-terminal, cytoplasmic fragment comprising the G and middle domain acts as the catalytic core as it confers comparable GTPase activity as full-length ATL (Wu *et al*., 2015; Moss *et al*., 2011) and functionally dimerizes with native ATL, evidenced by its action as a concentration-dependent inhibitor of membrane fusion *in vitro* (Bian *et al*., 2011; Moss *et al*., 2011) and its dominant negative effect on ER morphology when expressed in mammalian cells (Moss *et al*., 2011).

All invertebrates encode three isoforms of ATL (ATL1-3), which retain high sequence homology (61-64%) and localize to the ER where they all catalyze membrane fusion (Wu *et al*., 2015). Despite these similarities, they vary in catalytic efficiency, ER spatial distribution, cellular fusion efficiency, and expression levels in tissues throughout the body, with ATL1 primarily present in the brain (Rismanchi *et al*., 2008; Wu *et al*., 2015; Morin-Leisk *et al*., 2011). In addition to their role in HSP, familial mutations in ATL1 and ATL3 have been found to cause hereditary

sensory neuropathy (HSN), another neurodegenerative disorder affecting sensory neurons (Guelly *et al*., 2011; Fischer *et al*., 2014; Krols *et al*., 2018).

Here we present a case of an early onset, complex HSP caused by a novel ATL1 mutation, where an asparagine residue is inserted into the middle domain between Arg 416 and Tyr 417 (N417ins). The proband presented with spastic quadriplegia and complex symptoms including generalized dystonia and thinning of the corpus callosum. Investigations into the structure and function of this novel ATL1 variant illustrate that while mutant ATL1 preserves many core functions, changes to sub-cellular localization and an uncommon gain-of-function phenotype underlie HSP pathologies.

## RESULTS

*Patient case study.*

The proband is the first male child of a Hispanic and Caucasian/Asian couple born at term after an emergency caesarian section due to fetal heart rate decelerations. Birth weight was around 3600 gm at 53 cm of height. Apgar scores were normal, and neither resuscitation nor intensive care support was required. Hospital discharge occurred at 3 days of age and proband was specified normal as a neonate. Normal health ensued until 3 months, when adrenocorticotropic hormone (ACTH)-responsive infantile spasms developed. Magnetic resonance imaging (MRI) at the time was normal and an electroencephalogram (EEG) showed features of epilepsy. Cognitive function remained near normal, but in contrast, motor development was slow. Developmental hallmarks such as rolling and crawling were reached at 6 and 14 months, respectively. At this point, motor development ceased, which resulted in the inability to walk. The patient was diagnosed with spastic quadriplegic cerebral palsy at 1.5-2 years. Cognitive development was near normal. He has been treated with intermittent injections of botulinum toxin, physical and occupational therapy, and has braces and splints.

At age 7, the proband had a feeding tube inserted and at age 15 was able to eat smaller pieces of food and drink through a straw. Speech was slow but fairly clear. Limited movement existed in the arms and hands. Straightening of the arms at the elbows proved difficult, stiffness was present in the flexor group of the arm muscles, and a weak grip with contractures were present in both hands. Difficulties with movements and stiffness occurred in the extensor muscles of the legs. There was equinovarus posture of the feet and no movement. There was extensor tonus at the quadriceps, and mobility was enabled with the use of a motorized wheelchair. Cognitive development continued as exhibited through school attendance and normal intelligence. A follow-up brain MRI was reported as normal but showed thinning and down-sloping of the posterior body of the corpus callosum (Figure 3.1A). This was unchanged in comparison to a prior imaging study done at age 3 years.

Using whole exome sequencing, a heterozygous *de novo* variant c.1248_1249insAAT:p.Arg416_Tyr417insAsn (referred to here as N417ins) was identified in exon 12 of the *ATL1* gene (NM_015915.4). This caused an in-frame insertion of a single asparagine residue in a non-repeat region. In silico analysis supported a deleterious effect. The CADD score was 21.3. The variant was not found in gnomAD or Clinvar databases that catalog genomic variations, and in the latter case, link those to their relationship to human health (Karczewski *et al*, 2020; Landrum *et al*, 2014). Sanger sequencing of the variant was confirmed in the proband in a Clinical Laboratory Improvement Amendments (CLIA) laboratory (Figure 3.1B).

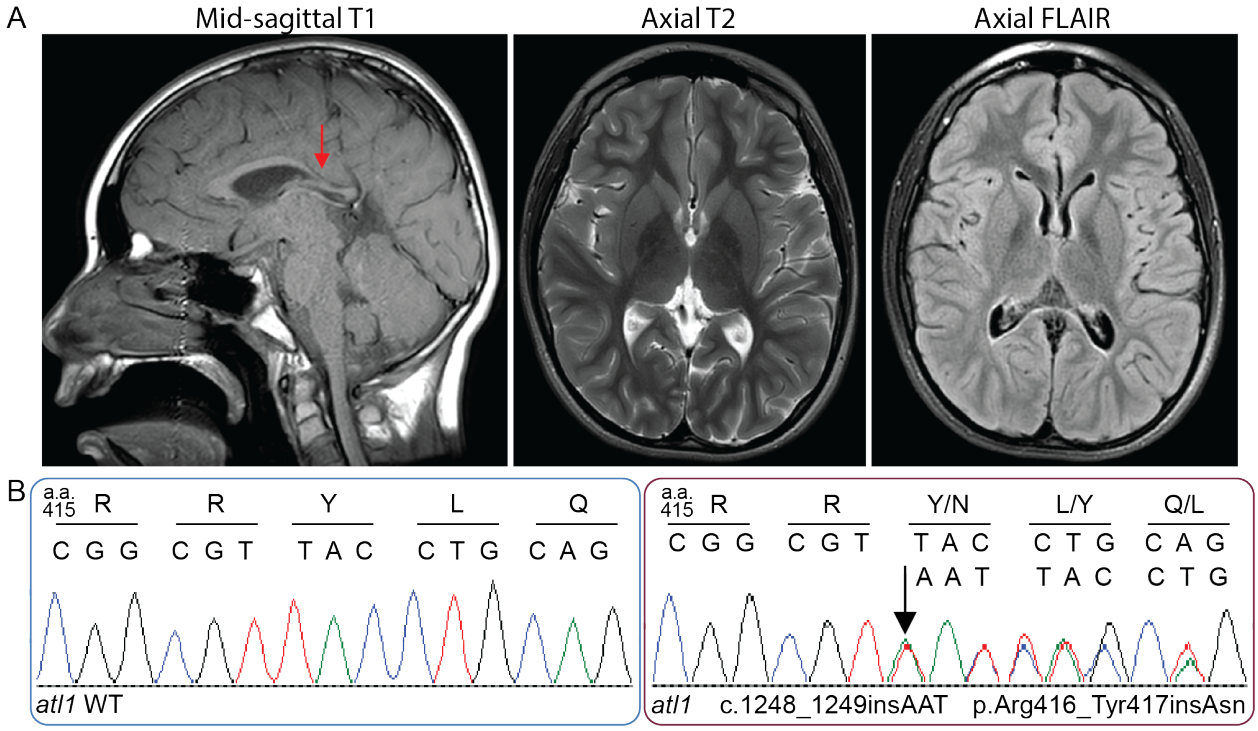


**Figure 3.1. MRI and Sanger sequencing of proband. (A)** MRI at 15 years showing thinning and down-sloping of the posterior body of the corpus callosum. Arrow (left) indicates the thinning and down-sloping corpus callosum. **(B)** Sanger sequencing chromatograms of atl1 WT (left) and mutant (right) from the proband, starting at position 415 (amino acid), 1243 (nucleotide). Arrow indicates location of the inserted codon (AAT) between position 1248 and 1249. Single letter amino acid and nucleotide codes indicated above.

*Mutation N417ins alters ATL1's ER distribution in cells.*

Previous studies have found that disease-causing mutations in ATLs can lead to ER morphologies ranging from large-scale aggregation to long, unbranched tubules or a relatively normal reticular structure depending on the mutation (Namekawa *et al*., 2007; Rismanchi *et al*., 2008; Krols *et al*., 2018). Often, these mutations act in a dominant-negative fashion. Here we probed the impact of expressing the novel ATL1 N417ins mutation on ER structure in both wild-type (WT) NIH-3T3 and NIH-3T3 ATL1/2/3 triple-knockout (TKO) mammalian cell lines (Zhao *et al*., 2016). Usage of WT and TKO cells allowed us to investigate whether the mutation exerts a dominant effect over endogenous ATL isoforms, and whether the mutant variant of ATL1 can stand in for wild-type alleles, respectively.

We first compared protein abundance of exogenously expressed ATL1 WT and N417ins mutant variant with a C-terminal myc-tag. Immunoblotting verifies that both constructs express in WT and TKO cells (Figure 3.2A). To assess impact of the mutant on ER morphology, we carried out immunofluorescence staining in NIH-3T3 WT and TKO cells exogenously expressing ATL1 WT and N417ins and imaged the cells with confocal microscopy. Wild-type protein localization and ER morphology matches published results, with ATL1 evenly decorating the highly reticular ER tubules (Figure 3.2C; Rismanchi *et al*., 2008). Strikingly, the N417ins variant appears to be largely excluded from the ER tubules and primarily localizes to many puncta and small globules throughout the smooth ER (Figure 3.2B). This feature is observed both in WT and TKO cell lines, indicating it is an effect independent of endogenous ATL expression. Although the N417ins-containing protein has fractured ER localization, the ER remains largely intact and colocalizes with the N417ins mutant as determined by co-transfection of U2OS cells with $^{mCherry}$SEC61β (Figure 3.3).

Of the NIH-3T3 cells quantified, 100% and 98.6% of N417ins transfected cells had puncta while only 10.7% and 2.2% of WT-transfected showed this feature, in WT and TKO cells, respectively (Figure 3.2B). The primary variation amongst N417ins transfected cells was the

extent of discernable tubule signal, which ranged from 1) no tubules (individual puncta that don't appear to trace to a reticular pattern), 2) puncta that clearly trace along tubule patterns, 3) puncta with faint homogenous tubule signal, to 4) strong tubule signal (with or without puncta) (Figure 3.2C). We determined the percentage of observed cells with any discernable tubule signal (categories 2 to 4) and found that 100% of exogenous ATL1 WT generated a tubular signal to only 36.9% and 62.7% of N417ins-transfected cells, in WT and TKO cells respectively. It is noteworthy that while the percentage of cells with punctate N417ins variant signal in WT and TKO cells was not significantly different, the difference of cells with tubular localization of the exogenous. protein was statistically significant. Lastly, of the cells with any level of tubule signal, 18.4% and 15.6% of N417ins transfections had visibly reduced 3-way junctions, in WT and TKO cells, respectively (Figure 3.2B). This phenotype has been observed with expression of some HSP variants and catalytically inactive ATL1 mutants (Namekawa *et al*., 2007; Rismanchi *et al*., 2008; Zhao *et al*., 2016; Montagna *et al*, 2020; Ulengin *et al*., 2015; Liu *et al*., 2019). Overall, the apparent dominant effect of the ATL1 N417ins mutant in WT cells correlates with the heterozygosity of the mutation in the proband.

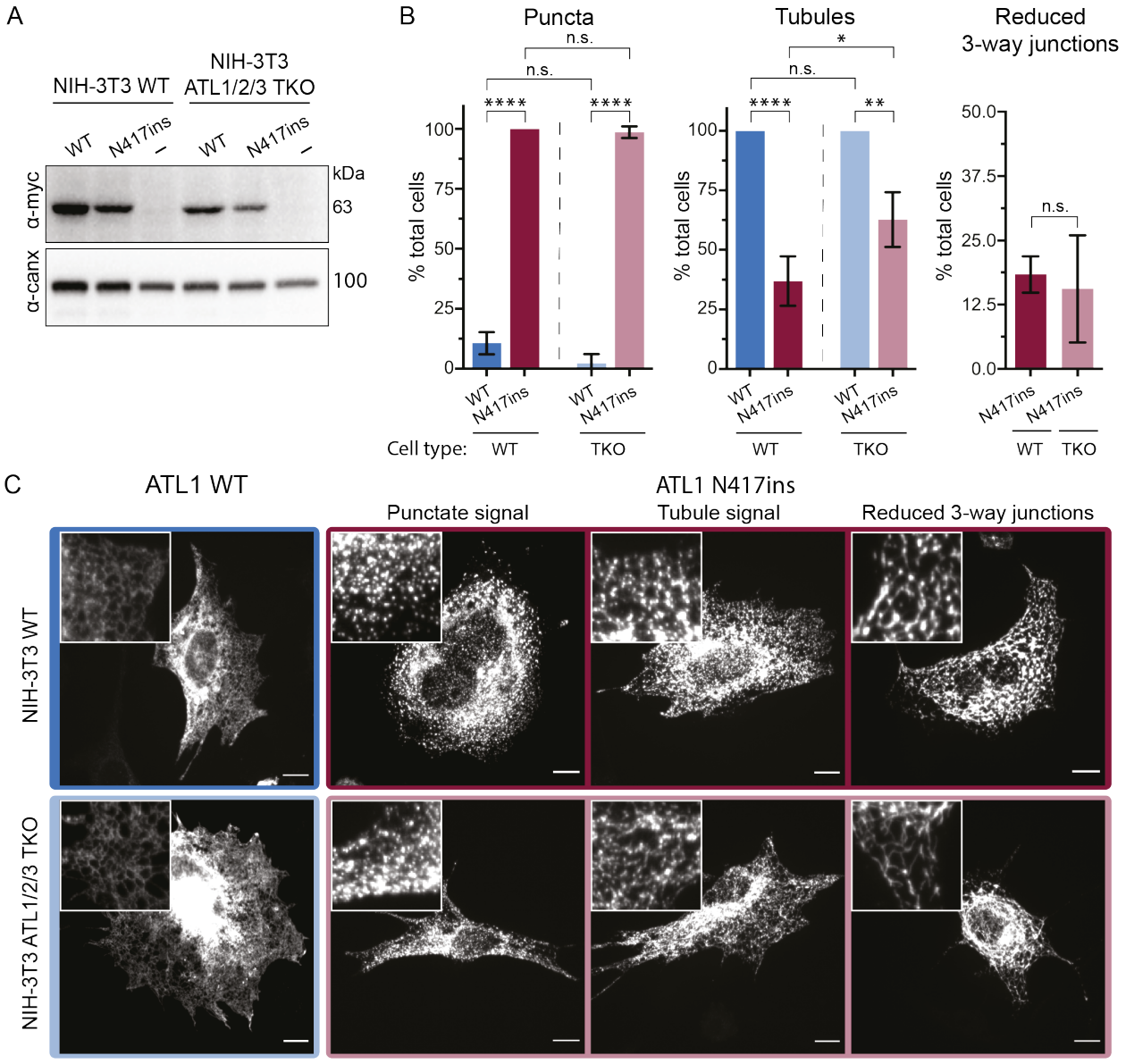
A
NIH-3T3 WT
NIH-3T3 ATL1/2/3 TKO
WT
N417ins
–
WT
N417ins
–
kDa
α-myc
63
α-canx
100
B
Puncta
Tubules
Reduced 3-way junctions
% total cells
n.s.
****
**
*
Cell type:
WT
TKO
N417ins
C
ATL1 WT
ATL1 N417ins
Punctate signal
Tubule signal
Reduced 3-way junctions
NIH-3T3 WT
NIH-3T3 ATL1/2/3 TKO

**Figure 3.2. Effect of ATL1 N417ins expression on ER morphology. (A)** ATL1 expression levels in transiently transfected NIH-3T3 (WT) and NIH 3T3 ATL1/2/3 triple knockout (TKO) cells (Zhao et al, 2016). Recombinantly expressed, myc-tagged ATL1 WT and N417ins was detected by Western blotting with a c-myc-specific primary antibody; empty pcDNA vector was included as a control. Total protein concentration from lysates was normalized before loading, and the signal from an anti-calnexin Western blot was used as a loading control. **(B)** Quantification of observed ER phenotypes including punctate (left), tubular (middle), and reduced visible 3-way junctions (right); categories are not mutually exclusive. A minimum of 70 cells were imaged and quantified from three individual experiments (except NIH-3T3 ATL1/2/3 TKO expressing ATL1 wild-type, which had 46 cells). Bars represent mean percentages with error bars showing SD. One-way ANOVA tests established statistical significance. **(C)** Immunofluorescence of NIH-3T3 WT (top) and NIH-3T3 ATL1/2/3 TKO (bottom) transiently transfected with either ATL1 $WT^{myc}$ (blue/light blue box) or $N417ins^{myc}$ (maroon/pink box) and probed with α-c-myc antibodies for imaging with confocal microscopy. Representative images of reported phenotypes in cells expressing ATL1 N417ins are labeled along the top (punctate, tubule, or reduced 3-way junctions). Scale bar = 10 μm.

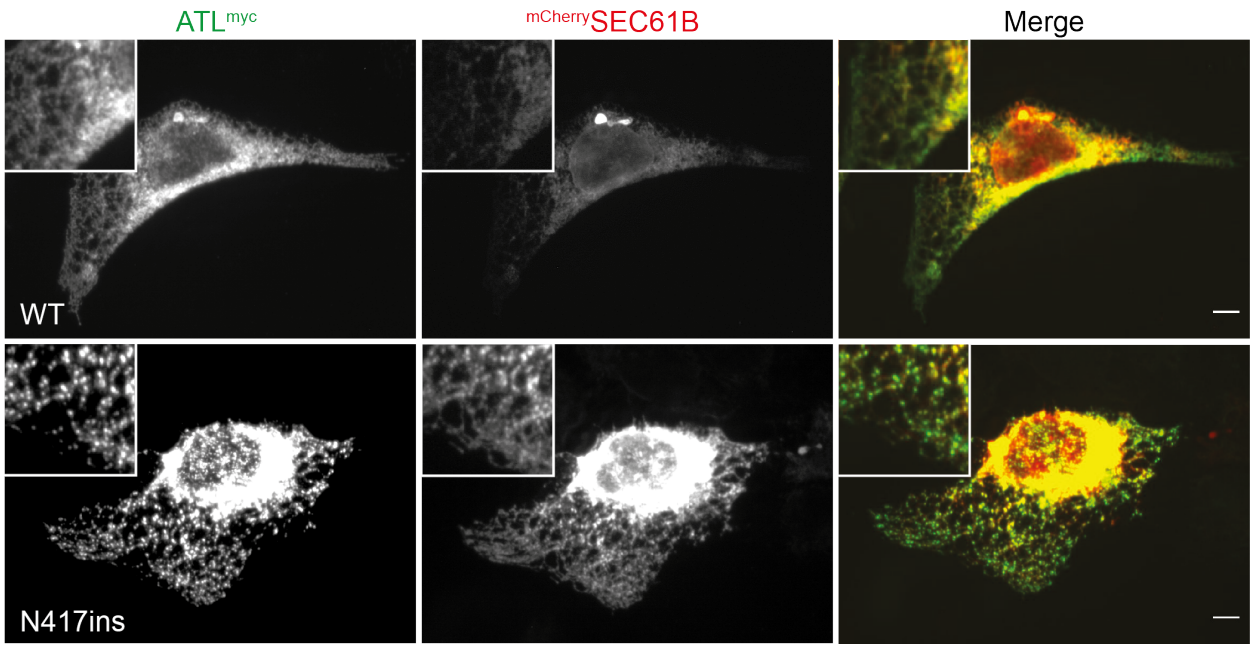


**Figure 3.3. Colocalization of ATL1 with ER marker in U2OS cells.** Immunofluorescence was carried out on U2OS cells transiently co-transfected with mCherry-SEC61β and either ATL1 WT$^{myc}$ (top) or ATL1 N417ins$^{myc}$ (bottom). The first column shows ATL1 signal (green), the second column shows SEC61β (red), and the third column overlays the signals. Scale bars = 10 μm.

*GTP hydrolysis and oligomerization by ATL1 are not affected by the N417ins mutation.*

Having established a pronounced cellular phenotype, we set out to characterize the effect of the ATL1 N417ins mutation on the protein's molecular mechanism. It has been established that the N-terminal soluble module of ATL1 consisting of the conserved G and middle domains, which we refer to as the catalytic core, is sufficient to carry out GTP hydrolysis and nucleotide-dependent oligomerization (Wu *et al*., 2015; Moss *et al*., 2011; Byrnes and Sondermann, 2011). The fragment also interacts with the full-length protein in a GTPase-dependent manner, suggesting that its functional cycle tracks that of the native protein (Bian *et al*., 2011; Moss *et al*., 2011; Wang *et al*., 2013). For those reasons, we can employ the soluble, near-full-length catalytic core as a proxy for the native protein in biochemical studies reporting on intrinsic properties of ATL. Both WT and mutant proteins expressed to comparable levels in *E. coli*, and purifications produced similar

overall protein yields, suggesting no major impact of the sequence alteration on protein stability. As a first test, we used an established spectrophotometric assay to measure the release of inorganic phosphate ($P_i$) over time for both WT and mutant protein. The catalytic activity was the same for both proteins with no statistically significant difference in $k_{cat}$ values of ATL1 WT and ATL1 N417ins (apparent rates of 5.6 +/- 0.18 $min^{-1}$ for WT and 6.0 +/- 0.13 $min^{-1}$ for the N417ins mutant protein) (Figure 3.4A).

A key characteristic of ATLs is their ability to form dimers upon GTP hydrolysis, a state that can be trapped by incubating the proteins with non-hydrolyzable GTP analogs (GppNHp or GTPγS) or a transition state analog (GDP•$AlF_4^-$) (Byrnes and Sondermann, 2011; Bian *et al.*, 2011; O'Donnell *et al*., 2017). In contrast, the ATL catalytic core remains monomeric in the absence of nucleotides and GDP (Byrnes and Sondermann, 2011; O'Donnell *et al*, 2017). This pattern of dimerization is crucial in conferring ATL's ability to tether and fuse membranes and is retained across all isoforms and orthologs, even extending to yeast Sey1p and mitofusins (O'Donnell *et al*., 2017; Wu *et al*., 2015; Moss *et al*., 2011; Pendin *et al*., 2011; Yan *et al*., 2015; Cao *et al*., 2017; Qi *et al*., 2016). We tested whether the novel disease mutation affects this conserved pattern by using size exclusion chromatography in tandem with multi-angle light scattering (SEC-MALS) (O'Donnell *et al*., 2020). As established previously, this assay reports on the molecular weight and conformation of proteins in solution. We found that, like ATL1 WT, the N417ins mutant protein remained a monomer in apo and GDP conditions and dimerized in the presence of GppNHp and GDP•$AlF_4^-$ (Figure 3.4B). Only a minor fraction of the mutant protein eluted as a monomer upon incubation with GppNHp, and less so with GDP•$AlF_4^-$, suggesting that dimer stability could be affected by the mutation. Another notable deviation from WT was the retention time on the column, with N417ins eluting 0.32 mL earlier as a monomer and 0.37 to 0.38 mL earlier as a dimer (Figure 3.4B). Since we saw no change in calculated molecular weight accompanying these shifts in retention time, they may indicate deviations in the hydrodynamic radius of the proteins and their oligomers, likely due to conformational differences.

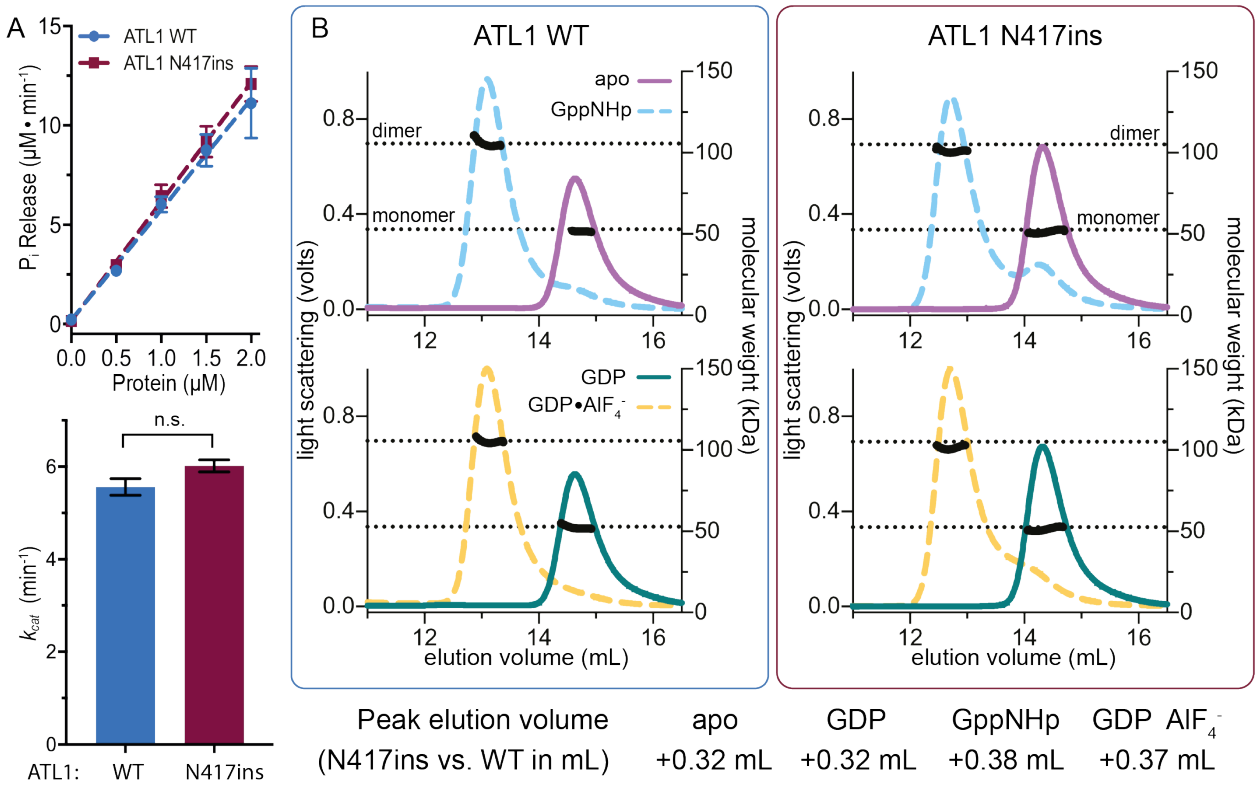


**Figure 3.4. GTP hydrolysis and nucleotide-dependent dimerization of ATL1 N417ins. (A)** GTP hydrolysis release kinetics of $P_i$ for ATL1 WT and ATL1417ins across protein concentrations (0 to 2 μM) are shown (top panel). Symbols represent the mean of two biological and three technical replicates with error bars showing standard deviations (SD). Apparent turnover rates ($k_{cat}$) were calculated from the $P_i$-release kinetics with SD shown by error bars. An unpaired t-test evaluated significance (P=0.0858). **(B)** Nucleotide-dependent oligomerization. Chromatograms from SEC-MALS experiments with either ATL1 WT (left) or N417ins (right), with all colored lines representing light scattering signal in volts denoted on the left axis (GppNHp, apo, GDP•$AlF_4^-$, and GDP) and black lines indicating calculated molecular weight in kDa (right axis). Dotted lines represent the theoretical molecular weights of the monomer and dimer (52.9 kDa and 105.8 kDa for N417ins; 52.8 kDa and 105.6 kDa for WT). For each nucleotide condition, the volume at the maximum light scattering signal for WT was subtracted from that of N417ins and the shift is indicated in mL (bottom text).

*Structure of ATL1 with the N417ins mutation bound to GDP•$AlF_4^-$.*

Having not seen a significant difference in the intrinsic activity of ATL1 with the N417ins mutation, we set out to solve the crystal structure to determine the extent of conformational disruptions in the protein by the mutation. The protein with the insertion mutation crystallized in the presence of the transition state analog GDP•$AlF_4^-$ and $Mg^{2+}$, diffracting to a resolution of 1.9 Å. The structure was solved by molecular replacement in space group $P2_12_12_1$ with two molecules in the asymmetric unit using isolated G and middle domain fragments as the search models (Table 3.1). The novel structure aligns with the ATL1 WT structure bound to GDP•$AlF_4^-$ (Byrnes *et al.*, 2013) with a rmsd value of 0.386 Å with both structures depicting a tight crossover dimer of ATL1's catalytic core (Figure 3.5A). The individual protomers superimpose nearly exactly with the corresponding chains in the WT structure (rmsd chain A=0.294 Å; rmsd chain B=0.514 Å).

| Table 3.1. Data collection and refinement statistics. | ATL1 N417ins |
|---|---|
| **Wavelength** | |
| **Resolution range** | 45.15 - 1.9 (1.968 - 1.9) |
| **Space group** | P 21 21 21 |
| **Unit cell** | 49.09 115.003 184.008 90 90 90 |
| **Total reflections** | 165391 (15828) |
| **Unique reflections** | 82940 (8042) |
| **Multiplicity** | 2.0 (2.0) |
| **Completeness (%)** | 99.75 (97.83) |
| **Mean I/sigma(I)** | 8.61 (1.03) |
| **Wilson B-factor** | 21.59 |
| **R-merge** | 0.09203 (0.8204) |
| **R-meas** | 0.1301 (1.16) |
| **R-pim** | 0.09203 (0.8204) |
| **CC1/2** | 0.992 (0.326) |
| **CC*** | 0.998 (0.701) |
| **Reflections used in refinement** | 82908 (8019) |
| **Reflections used for R-free** | 2000 (194) |
| **R-work** | 0.1791 (0.2935) |
| **R-free** | 0.2217 (0.2977) |
| **CC(work)** | 0.963 (0.680) |
| **CC(free)** | 0.950 (0.758) |
| **Number of non-hydrogen atoms** | 7838 |
| **macromolecules** | 6827 |
| **ligands** | 68 |
| **solvent** | 943 |
| **Protein residues** | 852 |
| **RMS(bonds)** | 0.011 |
| **RMS(angles)** | 1.65 |
| **Ramachandran favored (%)** | 98.34 |
| **Ramachandran allowed (%)** | 1.31 |
| **Ramachandran outliers (%)** | 0.36 |
| **Rotamer outliers (%)** | 0 |
| **Clashscore** | 6.35 |
| **Average B-factor** | 25.34 |
| **macromolecules** | 24.36 |
| **ligands** | 14.52 |
| **solvent** | 33.23 |

Statistics for the highest-resolution shell are shown in parentheses.

The inserted N417 residue is surface exposed within the middle domain's third helix. In this state, the α-helix rung containing the insertion accommodates the additional residue by bulging out slightly, resulting in minimal long-range structural changes. According to the DSSP secondary structure assignment, the inserted residue results in formation of π-helix from residues 415 to 419 (Touw *et al.*, 2015; Kabsch and Sander, 1983). The primary variation between WT and insertion-mutant structures lies within the middle domain dimer, where we observe a slight translation toward the second protomer's middle domain within the dimeric assembly of the mutant, with the middle domain interface tightening by ~0.7–1.2Å (interface-proximal) to 1.0–1.6 Å (solvent-proximal). The only exception to this observed domain translation is residue R416, directly preceding the insertion mutation, which shifts 3.6 Å in Cα position and rotates outward (Figure 3.5B).

The only other notable structural change occurs at the interface of the G domain and linker region of chain B at residues E339 and E340. Here we observe a 180° flip of the E339 side chain and a 4 Å shift of the corresponding Cα's and ~60° side chain rotation and 1.8 Å shift in the E340 Cα. This disturbance remains localized to these two residues (and specific to chain B) but appears to have a subtle effect on where the last helix of the G domain terminates (Figure 3.5C).

Although we only obtained the structure of ATL1 N417ins in a crossover dimer state so far, the GDP-bound, wild-type monomer structure we determined previously for ATL1 places the insertion region adjacent to the first helix of middle domain (Figure 3.5D-E). This region is of functional importance since it is proximal to the G-middle domain interface in this engaged state, characteristic for the GDP-bound conformation and likely involved in the allosteric coupling between the two domains (Byrnes *et al*., 2013; O'Donnell *et al*., 2017).

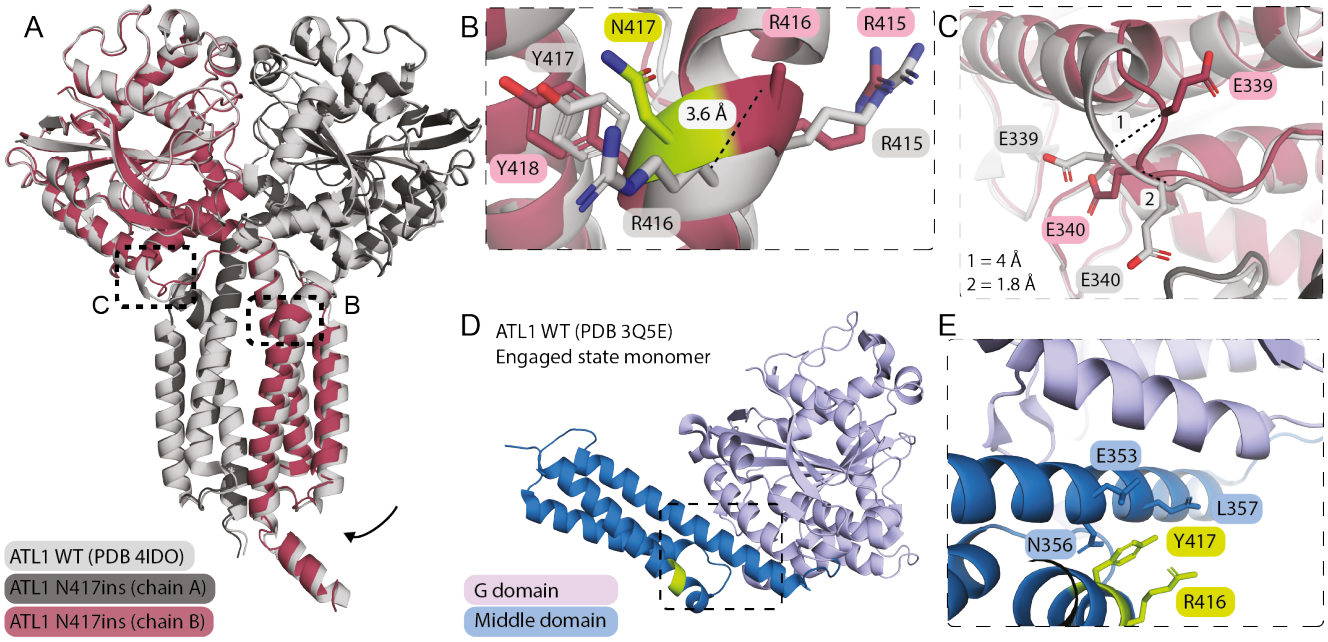


**Figure 3.5. Structure of the ATL1 N417ins crossover dimer bound to GDP•$AlF_4^-$. (A)** Structural overview. ATL1 N417ins (dark grey and maroon) superimposed with ATL1 WT (light grey; PDB 4IDO) each bound to GDP•$AlF_4^-$ and $Mg^{2+}$. Black boxes indicate boundaries of zoom-in views in B and C. Arrow indicates slight rotation of mutant middle domain. **(B)** Zoom-in view of the insertion mutation in chain B. Each residue is labeled (number of N417ins residues were adjusted after residue N417 to accommodate the extra residue). The distance between the R416 Cα positions in each structure is indicated (3.6 Å). N417 is colored in green while other residues were colored as in A. **(C)** Magnified view of the transition between the G domain and linker region of chain B, with both E339 and E340 of each structure labeled. Distances between the same residue in both structures is indicated in the lower left corner. **(D)** Structure of the monomeric, engaged ATL1 WT state (PDB 3Q5E) bound to GDP and $Mg^{2+}$. The residues directly pre- and proceeding the N417ins mutation (R416 and Y417) are indicated in green. The black box indicates the region shown in E. **(E)** Position of the insertion mutation. R416 and Y417 lie directly adjacent to middle and G domain helices integral in engaged state formation.

*ATL1 N417ins has significantly increased membrane tethering rates in vitro.*

Since we saw no effect of the mutation on GTP hydrolysis or nucleotide-dependent dimerization and the crossover state structure is largely unaffected, we next investigated what effect the mutant had on membrane-related functions of ATL1. Since full-length, human ATL1 has not been reconstituted in a membrane fusion-competent form, we tested for this function using an accepted vesicle-tethering assay using the soluble catalytic core of ATL1 (Liu *et al*., 2015). Tethering events are en route to fusion and may signify a native ATL function (Liu *et al.*, 2015; Wang and Rapoport, 2019). To assay for GTPase-dependent membrane tethering, purified WT or mutant ATL1 catalytic cores with a decahistidine tag at their C-termini was loaded onto vesicles containing 1% (molar ratio) Ni(NTA)-modified lipids. The resulting presentation of the soluble ATL1 domains mimics the topology of the full-length, transmembrane protein. Flotation assays confirmed that both WT and mutant protein partitioned to the vesicles fraction (Figure 3.7A). Upon the addition of GTP, continual vesicle tethering caused an increase in solution turbidity, which was measured spectrophotometrically (at $OD_{360}$). Figure 3.6A shows representative tethering reactions of ATL1 WT and N417ins at increasing concentrations from 0.25 to 1.5 μM. At all concentrations, the signal increases over time as expected. At higher concentrations (1 μM and above), the signal drops after reaching a plateau at the maximum ($OD_{360}$ ~0.2) followed by erratic fluctuations. This pattern is the product of large, macroscopically visible vesicle clumps (Figure 3.6D). The effect was reversed upon addition of EDTA or imidazole (Figure 3.7B). Additional control reactions were carried out with GDP or without $MgCl_2$, which did not support vesicle tethering (Figure 3.7B).

To compare tethering of WT and mutant protein, the initial tethering rates of each reaction (Figure 3.6C) were calculated across protein concentration. From this, it is apparent that there are two linear regions of increasing tethering rates (0.25 μM to 0.75 μM and 0.75 μM to 1.5 μM), with ATL1 N417ins demonstrating both higher initial tethering rates as well as a faster rate of

increase per protein concentration compared to WT protein (ATL1 at 0.959 +/- 0.28 and N417ins at 3.46 +/- 0.65 $min^{-1}$ $\mu M^{-1}$).

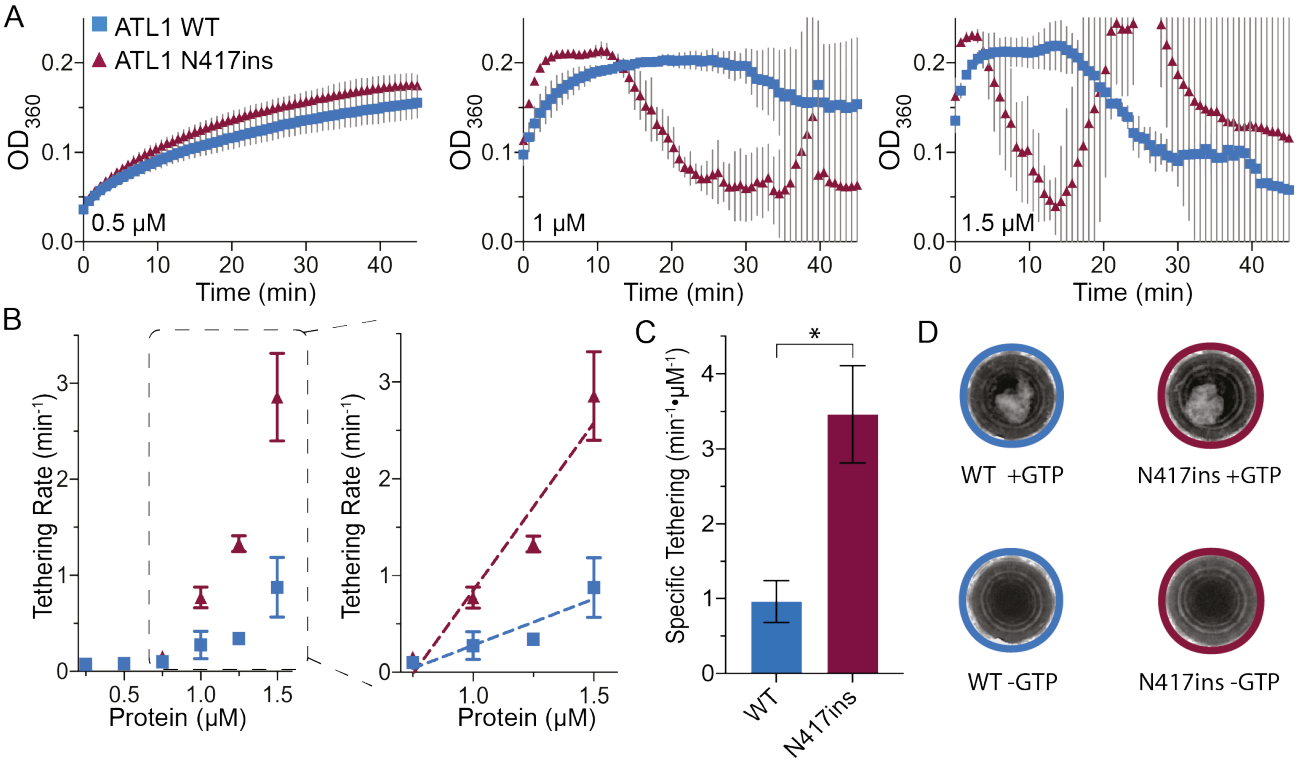


**Figure 3.6. The N417ins mutation increases membrane tethering efficiency of the ATL1 catalytic-core fragment. (A)** Select tethering reactions at increasing protein concentrations (between 0.5 and 1.5 μM protein) for ATL1 WT (blue) and N417ins (maroon). Each point is the average of two biological and three technical replicates, with grey error bars for the SD. **(B)** Initial tethering rates ($min^{-1}$) were calculated for each ATL1 concentration, displayed as the mean and SD across replicates. The inset (right panel) shows concentrations used to calculate values plotted in C (reactions with 0.75 μM to 1.5 μM protein). **(C)** Specific tethering rates ($min^{-1}$•$\mu M^{-1}$) for each construct. An unpaired t-test was used to determine the significance between the WT and mutant rates (P = 0.0237). **(D)** Images of tethering reactions after 45 minutes +/- GTP at 1.5 μM.

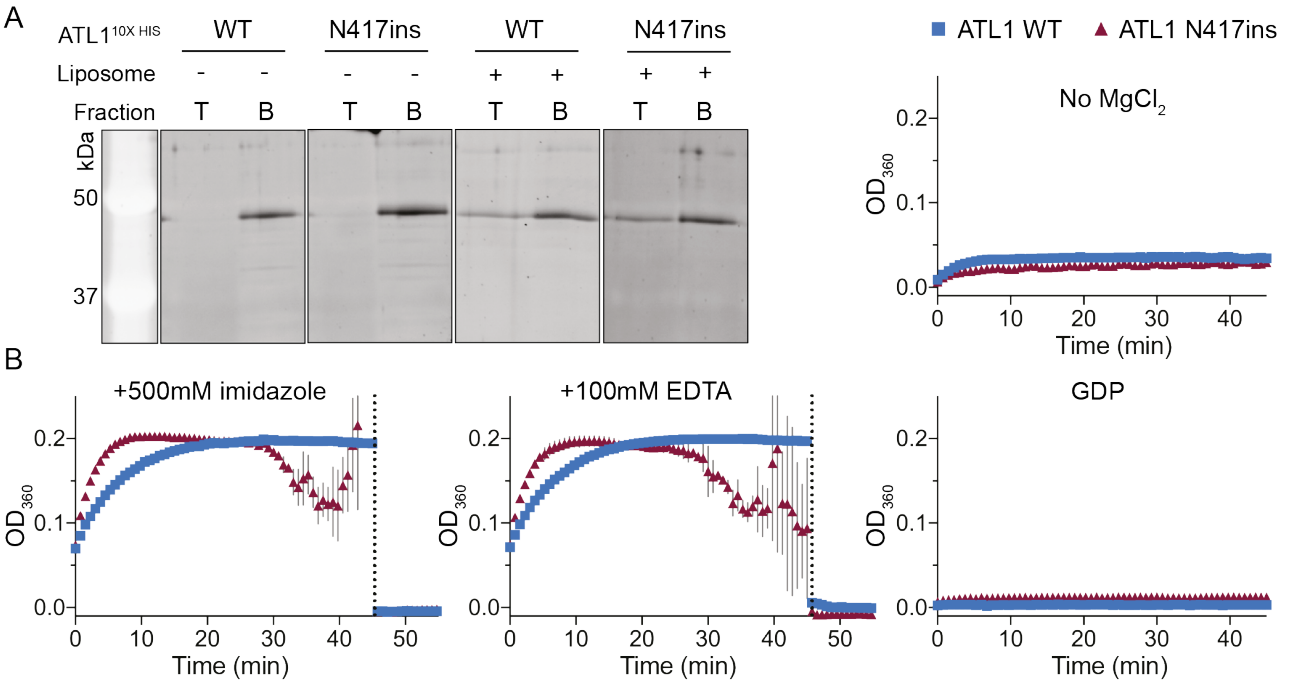


**Figure 3.7. Vesicle tethering controls. (A)** Flotation assay with 1 μM ATL1 WT or N417ins catalytic-core fragment with a C-terminal $His_{10}$-tag in the presence (right two panes) or absence (left two panes) or lipids containing 1% molar ratio of Ni-NTA-modified lipids. Top fraction (indicated by "T") contains vesicles and bottom fraction ("B") contains unbound protein. **(B)** Tethering reactions with 1 μM protein including addition of 100 mM EDTA or 500 mM imidazole at 45 minutes, or in the absence of $MgCl_2$ or presence of 2 mM GDP.

*The GDP-bound catalytic core of ATL1 N417ins is more susceptible to limited proteolysis than WT.*

With the unusual pattern of *in vitro* activity observed for the N417ins variant with only subtle deviations in the crossover dimer structure, we sought to determine if conformational changes in the pre-dimer could account for increased tethering rates and observed cellular phenotypes. To test this, we used proteinase K at low concentrations (0, 1, and 10 μg/mL) in a limited proteolysis experiment. We expected that if variations in conformation exist, it could result in different banding patterns on a SDS-PAGE gel based on accessibility of cleavage sites. For

each reaction, the catalytic core of ATL1 WT and ATL1 N417ins, as well as the ATL1 G domain (residues 1-339) were pre-incubated with the indicated nucleotide prior to addition of PK. In the apo state (Figure 3.8A), both WT and mutant protein have a single primary band in the absence of PK and at 10 μg/mL have a series of bands clustered near 30 kDa and a number of bands under ~20 kDa, which corresponds with size and relative amounts of bands seen in the G domain control.

However, when bound to GDP, the WT protein is largely protected from degradation, with the most prominent band only a few kDa below the intact protein (Figure 3.8B). While the N417ins mutant does contain a band of the same size at the highest PK concentration, the most pronounced band appears as a diffuse band at ~35 kDa (Figure 3.8B, red box). This band corresponds very closely to the size of the G domain alone (residues 1-339 assemble to a protein of 39 kDa). Since we know ATL1 undergoes substantial conformational changes pertaining to the relative positions between the G and middle domains (Byrnes and Sondermann, 2011), the G domain is a rational candidate for this band. When samples are pre-incubated with the transition state analog GDP•$AlF_4^-$, both WT and N417ins are largely protected from degradation (Figure 3.8C), indicating that the relevant cleavage sites for the given protease concentrations are protected in the tight crossover-dimer state of both proteins (Figure 3.5; Byrnes *et al*., 2013). These reactions were also carried out with the protein loaded on vesicles to determine if these cleavage patterns would be altered in the presence of a membrane, but we found banding patterns nearly identical to the reactions lacking liposomes (Figure 3.9).

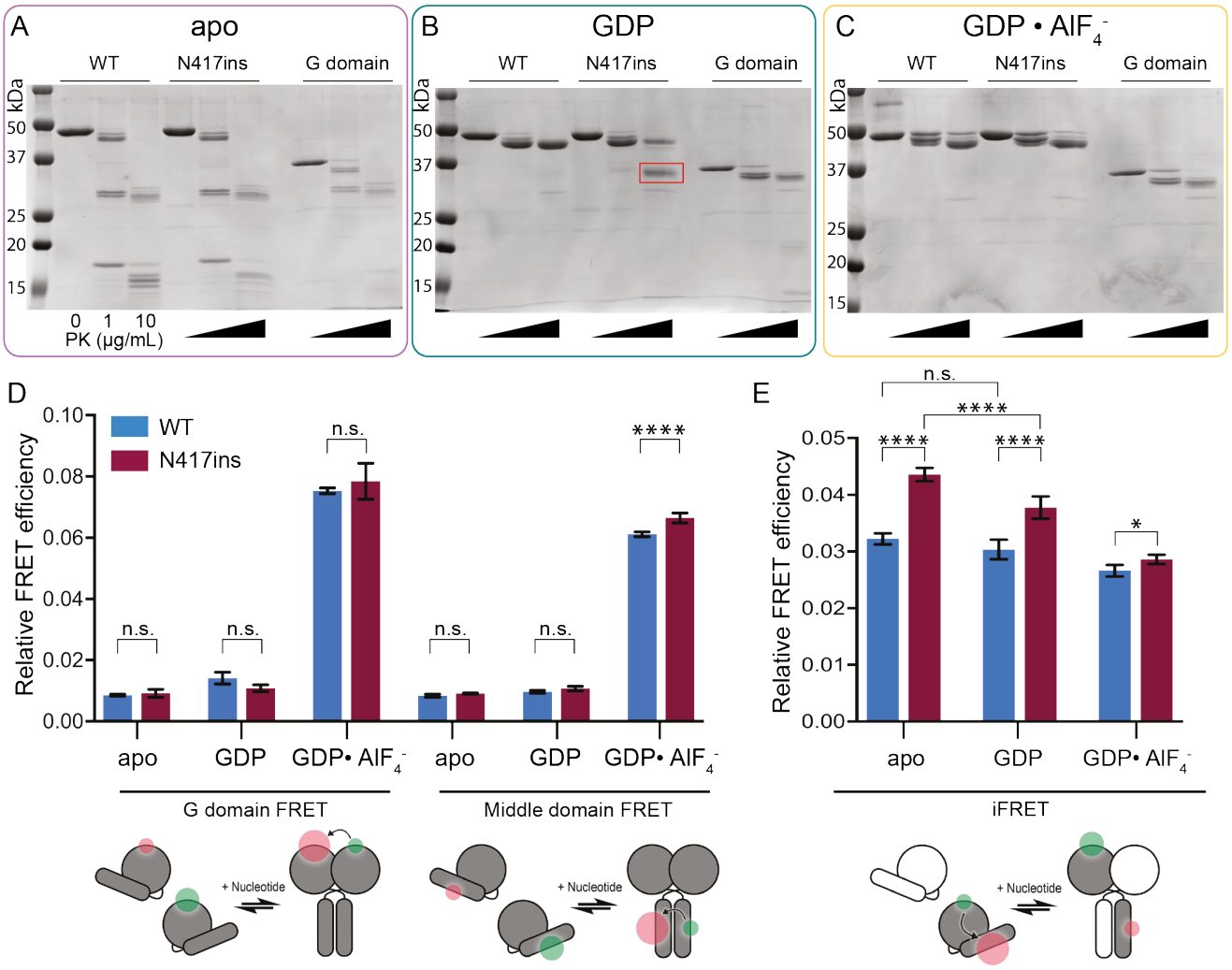


**Figure 3.8. Altered conformation of the monomeric ATL1 N417ins. (A-C)** SDS-PAGE gels show limited proteolysis reactions with increasing concentrations of proteinase K (PK) from 0 to 10 µg/mL and 2 µM ATL1 (catalytic core of WT and N417ins ATL1; purified G domain) for 15 minutes on ice. Reactions were incubated either in the absence of nucleotide (A), with 2 mM GDP (B), or with GDP•$AlF_4^-$ (C). The red box in (B) indicates a band of interest for the mutant and molecular weight markers are indicated on the left of each gel. **(D)** Intermolecular FRET between G domains (left) and middle domains (right) for ATL1 WT (blue) and ATL1 N417ins (maroon) in the presence of indicated nucleotides (X-axis). Relative FRET efficiencies calculated for each condition and error bars representative of SD for three technical and two biological replicates were plotted. **(E)** iFRET within ATL1 WT (blue) or N417ins (maroon) carried out with a 1:10 excess of unlabeled protein. Conditions and statistics are the same as in (D). Cartoons at the bottom of (D) and (E) represent experimental setups.

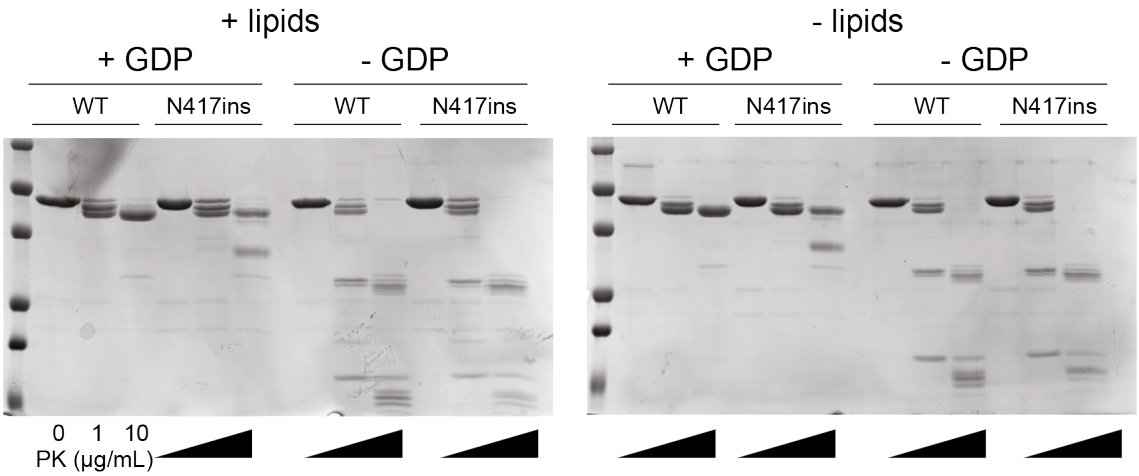


**Figure 3.9. Limited proteolysis controls.** SDS-PAGE gels show limited proteolysis reactions as described in Figure 3.8, but in the presence and absence of liposomes as prepared for vesicle tethering assays (Figure 3.6). Reactions were carried out with increasing concentrations of PK (0 to 10 µg/mL) as indicated at the bottom of the gel and by the black triangles.

*Inter- and intramolecular FRET indicate conformational variations of the monomeric ATL1 N417ins.*

The results of the structural analysis and limited proteolysis suggested changes in conformation between ATL1 WT and the N417ins variant, which could give insight to the disease mechanism. To further describe these, we used a Förster resonance energy transfer (FRET) assay to assess relative distances within the homodimer and the relative intramolecular distance between the G and middle domain within a single protomer, an approach we established previously for ATLs (Byrnes *et al*., 2013; O'Donnell *et al*., 2017). Briefly, intermolecular FRET was carried out with either the WT or mutant catalytic core with all surface-exposed cysteine residues mutated to alanine and a cysteine introduced either on the surface of the G or middle domain. For intramolecular FRET, two cysteine residues were introduced strategically in the middle and G domain of a single protein. These cysteine residues were labeled with a maleimide-conjugated AlexaFluor dye with peak excitation at either 488 nm (donor) or 647 nm (acceptor). For intermolecular G or middle domain FRET, protein was labeled with either donor or acceptor

AlexaFluor dye in separate reactions; for intramolecular FRET experiments, both cysteine residues were labeled stochastically in one reaction with both dyes present.

Relative FRET efficiencies were measured for steady-state intermolecular interactions between the G domains or the middle domains after pre-incubation with various nucleotides (Figure 3.8D). All reactions were equilibrated for 1 hour before measurement based on previously established nucleotide equilibration times (Byrnes *et al*., 2013; O'Donnell *et al*., 2017). Based on intermolecular FRET signals (Figure 3.8D), there was no significant difference between ATL1 WT and N417ins with the exception of the middle domain of the N417ins mutant bound to GDP•$AlF_4^-$, which had a small, but significant increase for the mutant indicating a shorter average Förster distance. This is in agreement with the middle domain translation observed in our structure (Figure 3.5A).

A previously described intramolecular FRET (iFRET) sensor was used next to measure changes in distances between the G and middle domains within a monomer in the same nucleotide-bound states (O'Donnell *et al*., 2017). In this system, we expect the engaged monomer to have a higher relative signal, which would decrease as the G domain is released and a crossover dimer is formed. A 1:10 ratio of unlabeled to labeled protein was used to minimize contribution of intermolecular signal across a homodimer. As predicted, we see that for ATL1 WT the apo state has the highest iFRET with a slight decrease upon GDP binding and a larger decrease upon GDP•$AlF_4^-$ binding (Figure 3.8E). However, we see several notable differences for the protein with the N417ins mutation. In both the apo and GDP-bound states, there was a significant increase in signal compared to that observed with the WT protein under identical conditions ($P < 0.0001$ for each). In addition, we see lower relative iFRET signals for GDP•$AlF_4^-$ as is seen with the WT. While the decrease in FRET signal between apo and GDP for WT was not significant (loss of 0.002 in relative FRET efficiency, $P = 0.056$), there was a much greater

loss for the N417ins mutant (loss of 0.006, $P < 0.0001$), indicating a notable conformational change upon nucleotide binding that was not observed with ATL1 WT.

## DISCUSSION

Here we have identified a novel mutation in ATL1 that causes a complex form of spastic paraplegia that involves all four extremities of the proband. We demonstrate that the mutant protein has an increased membrane tethering potential *in vitro* despite unaltered GTPase activity, correlating with cellular defects in the subcellular distribution of the full-length protein. To date, there have been at least 68 HSP disease-causing mutations identified in the *ATL1/SPG3A* gene, with a majority being missense mutations, a small number caused by single nucleotide insertions or deletions, and only one di-nucleotide insertion (Zhao ant Liu, 2017; Xiao *et al*., 2019). The disease-causing mutation described in this study is the first report of a whole codon insertion.

The proband in this study has generalized weakness and bilateral spasticity of his legs, the symptoms appear to be more severe with generalized dystonia and difficulty moving both the arms and legs. The involvement of arm and grip weakness, difficulty straightening out at his elbows, and limited hand movements indicate that the pathology is more than spastic paraplegia. Tendon reflexes were brisk at the biceps and present at the knees, which suggested that the patient does not have a generalized motor or sensory neuropathy. We propose that the N417ins variant contributes to the child's symptoms and describes a new phenotype that could be a part of a spectrum of disorders resulting from mutations in the *ATL1* gene.

When ATL1 HSP mutants are expressed in mammalian cells, a variety of morphological aberrations affecting the ER have been observed, including aggregated bundles and globules, pervasive puncta, long, unbranched tubules, and a shift in sheet to tubule ratios (Botzolakis *et al*., 2011; Namekawa *et al*., 2007; Rismanchi *et al*., 2008; Ulengin *et al*., 2015; Liu *et al*., 2019; Montagna *et al*, 2020). Expression of the novel ATL1 N417ins variant in NIH-3T3 cells both with and without endogenous ATL present resulted most prominently in the localization of the protein to puncta and small globules along ER tubules and at tubule junctions. Of the observed phenotypes, the only notable difference between the WT and TKO cells was the increased percentage of cells with visible tubules in the cells lacking all endogenous ATL isoforms (Figure

3.2B-C). This observation suggests that the ATL1 protein with the insertion mutation retains basal membrane tethering and/or fusion activity but the effect of the mutation on the spatial distribution of the protein and ER structure is dominant.

In order to probe what may cause these cellular disruptions and disease pathogenesis, we assessed the effect of the N417ins mutation on the activity and structure of the ATL1 protein. Previous reports that took a similar approach in characterizing HSP mutations have found varying levels of deviations in GTP hydrolysis rates, extent of nucleotide-dependent dimerization, and structural conformations as assessed by X-ray crystallography (O'Donnell *et al*., 2018; Byrnes and Sondermann, 2011; Meijer *et al*., 2007; Bian *et al*., 2011; Ulengin *et al*., 2015; Liu *et al*., 2019). We found that the innate GTP hydrolysis rate of the ATL1 N417ins mutant variant does not differ significantly from its native (WT) counterpart (Figure 3.4A). Similarly, nucleotide-dependent oligomerization of the protein appeared unaffected by the mutation (Figure 3.4B). However, differences in hydrodynamic radius as read out by the peak elution volume in size-exclusion chromatography of the mutant protein compared to WT suggests an impact of the mutation on the global conformation of the protein. This result mirrored altered inter- and intramolecular distances observed in the ATL1 protein carrying the mutation by equilibrium FRET measurements (Figures 3.8D and 3.8E). While the crystal structure of a soluble transition-state dimer of ATL1 only showed subtle deviations compared to a corresponding WT structure (Byrnes *et al*., 2013), a protein stability assay revealed a particular protease sensitivity of the mutant protein in its GDP-bound state (Figures 3.8B). One feature of interest in the novel insertion mutation structure is the α- to π- helix transition observed from residues 415 to 419. A previous link has been drawn between evolutionary α- to π- helix transitions caused by a single residue insertions and gain of protein function (Cooley *et al*, 2010), however our study may be the first report of such a mechanism resulting in human pathogenesis.

The structural alterations correlate with an impact of the mutation on ATL1's function. Specifically, *in vitro* vesicle tethering using the catalytic core as a proxy for the full-length protein's

function on the ER membrane showed a significantly increased vesicle tethering rate of the mutant protein compared to the corresponding WT (Figure 3.6). This apparent gain-of-function effect of the mutation is in contrast to reports on other HSP-associated ATL1 variants that usually act as loss-of-function alleles, where a deviation from WT activity was detected (Byrnes and Sondermann, 2011; Ulengin *et al*., 2015; Bian *et al*., 2011; O'Donnell *et al*., 2018; Meijer *et al*., 2007; Liu *et al*., 2019). The higher tethering rate *in vitro* is in line with the corresponding full-length protein supporting basal membrane fusion function in cells while also showing a more concentrated localization to puncta that may present sites of hyper-tethering/fusion (Nixon-Abell *et al*., 2016). Microscopic investigations at higher spatial and temporal resolution will be required to corroborate the potential link between tethering rates supported by the soluble core fragment and the function of the full-length proteins in cells. Nevertheless, our observations raise subsequent questions about the mechanism leading to altered ER structure and potentially dynamics while the innate GTPase activity in the N417 insertion mutant is unaltered.

Although the proteolytic sensitivity of the mutant protein in the GDP-bound state implicates the pre-fusion state of ATL1 in the pathogenic mechanism, the crystal structure of the transition state also shows subtle conformational changes that were corroborated by FRET-based experiments. The residues directly pre- and proceeding the insertion lie adjacent to the region of the middle domain α-helix 1 that interacts with the G domain. It has been previously established that the G domain of the pre-hydrolysis monomer interacts with α-helix 1 of the middle domain (Byrnes and Sondermann, 2011; Bian *et al*., 2011) and its release on a biologically relevant time scale is dependent upon GTP binding and hydrolysis (O'Donnell *et al*., 2017). The undocking of the middle domain from the G domain is a prerequisite for protein dimerization, membrane tethering and fusion (Moss *et al*., 2011; Byrnes *et al*., 2013; O'Donnell *et al*., 2017). In this context, we hypothesize that the N417ins mutation may alter the pre-hydrolysis state in such a way that the propensity of the middle domain being released from the G domain increases, which could lead to faster membrane tethering without altering the innate activity of the enzyme. Such a model

is consistent with our observation that the insertion mutation leads to increased cleavage between G and middle domains in the catalytic-core fragment upon limited proteinase K treatment. Whether the middle domain is destabilized by the mutation and more prone to further degradation compared the WT middle domain is currently an open question. In summary, the limited proteolysis and FRET studies indicate a conformational disruption of the apo and GDP-bound monomer and potential destabilization of the engaged state with the middle domain docked at the G domain. Membrane tethering rates are increased likely due to this dysregulation of release of the G and middle domains upon GTP hydrolysis and initiation of *trans* dimer formation.

Interestingly, there is a cluster of HSP-associated mutations surrounding the N417ins mutation studied here, ranging from residues Lys 407 to Arg 416 (Table 3.2). Figure 3.10 illustrates the localization of this cluster in both the pre-hydrolysis (form 2) and the tight crossover dimer (form 3) between α-helix 2 and 3 of the middle domain, and adjacent to the linker region between the G and middle domains. While the molecular mechanisms of these mutations have not been characterized, there is a general clinical trend of early onset of symptoms and autosomal dominant inheritance. The only report of recombinant expression for any of these mutations (F413L and R415W) found them to be insoluble, likely explaining their pathogenesis (Byrnes and Sondermann, 2011). Additionally, while a majority of *SPG3A* HSP-causing mutations result in pure cases (especially with autosomal dominant cases) (Battini *et al*., 2011; Depienne *et al*., 2007; Fink, 2006), many of the mutations in this cluster are found in complex cases including the case we present here. While we do not anticipate the pathogenic mechanism of every mutation within this cluster to be the same or similar, it is evident that this region of the middle domain is crucial in maintaining proper ATL1 function. The variability observed across the cases within this cluster points towards a more complex physiological mechanism beyond what enzyme kinetics alone would likely explain, for example, involving a potential gain-of-function mechanism on the level of the protein's cellular role, in this case membrane tethering and fusion.

| Mutation | Pure or complex case(s) | Inheritance | Early vs. late onset | Refs |
|---|---|---|---|---|
| K407R | Pure | AD | Early | Svenstrup *et al*., 2009 |
| M408V | Complex and pure | AD | Early | Dalpozzo *et al*., 2003 |
| M408T | Complex | AD | Early | Haberlová *et al*., 2008 |
| G409D | Complex | S | Early | Zhao and Liu, 2017; Yonekawa *et al*., 2014 |
| G410R | Complex | AD | (Mostly) early | Chen *et al*., 2005 |
| F413V | Complex | AD | Early | Álvarez *et al*., 2010 |
| F413L* | Pure | AD | Early | Dürr *et al*., 2004 |
| S414R | Not described | AD | Early | Lu *et al*., 2014 |
| R415W* | Pure (one complex) | AD | (Mostly) early | D'amico *et al*., 2004; Elert-Dobkowska *et al*., 2015; Ishiura *et al*., 2014; Varga *et al*., 2013 |
| R415Q | Pure | AD | Early | Varga *et al*., 2013 |
| R416C | Complex and pure | AD | (Mostly) late | Magariello *et al*., 2012; Orlacchio *et al*., 2011 |
| R416H | Complex | AD | Early and late | De Leva *et al*., 2010 |
| N417ins | Complex | | Early | |

**Table 3.2. HSP-causative *SPG3A* mutations clustered in the middle domain near the N417ins mutation.** All mutations within this cluster are caused by missense mutations and result in single amino acid replacements, indicated in the first column. Subsequent columns detail whether the reported case(s) are pure or complex, the mode of inheritance (autosomal dominant = AD, sporadic = S), early vs. late symptom onset (early is defined as <10 years old), and references. Mutants with an asterisk (*) are insoluble when expressed recombinantly as the catalytic core (Byrnes and Sondermann, 2011).

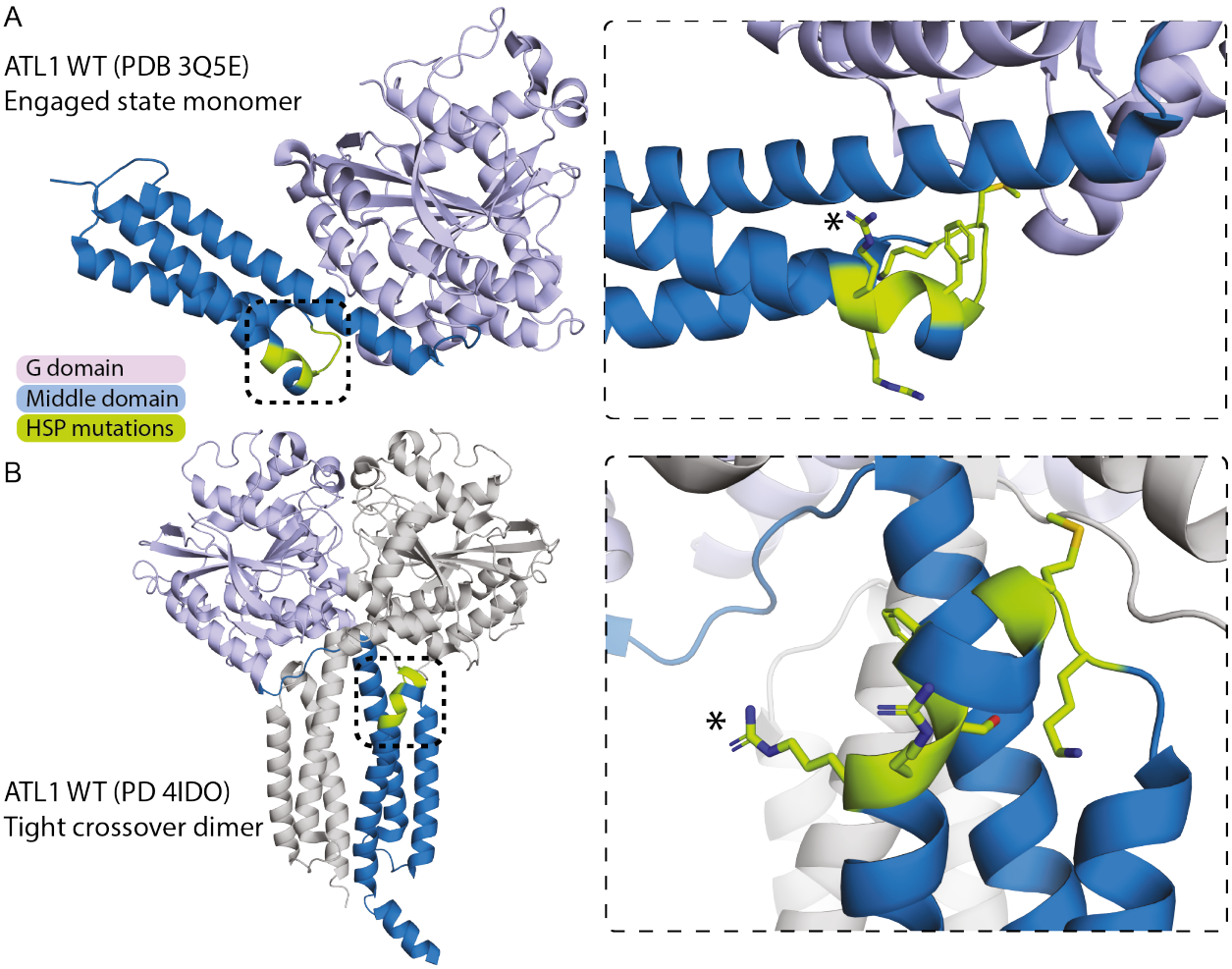


**Figure 3.10. Cluster of SPG3A HSP-causative mutations proximal to the N416 insertion. (A)** Localization of the cluster demarcated on the structure of ATL1 WT in the pre-hydrolysis, engaged state (PDB 3Q5E; Byrnes and Sondermann, 2011). HSP-associated mutated residues shown in green and colored by atom on the right. Asterisk (*) indicates R416, which directly precedes the insertion mutation described here. Black boxes indicate boundaries of zoom-in view on the right in (A) and (B). **(B)** Localization of the cluster in the structure of the tight crossover dimer bound to GDP•$AlF_4^-$ (PDB 4IDO; Byrnes et al., 2013). Coloring as in (A) for chain B and chain A is shown in grey.

While the HSP-associated mutation presented here demonstrates a novel gain-of-function disease mechanism in ATL1, a recent study characterized two gain-of-function mutations in ATL3 (Y192C and P338R) that have been identified in hereditary sensory neuropathy patients (Fischer *et al*., 2014; Kornak *et al*., 2014; Krols *et al*., 2018). Like the novel ATL1 insertion mutation reported here, both ATL3 disease-associated variants show unaltered GTPase activity and increased membrane tethering rates; however, in contrast to ATL1 N417ins, the propensity for nucleotide-dependent dimerization of the ATL3 mutants appears more severely reduced (Krols *et al*., 2018). In several mammalian cells models, including HSN patient fibroblasts and murine cortical neurons, expression of the ATL3 Y192C and P338R variants caused a striking phenotype characterized by lateral bundling of ER tubules caused by excessive tethering, with a partial collapse of the reticular ER caused by significant membrane fusion defects. Unlike the model proposed for the ATL3 HSN-associated mutants, which suggests a failure in establishing nucleotide-dependent ATL crossover dimers required for fusion, ATL1 N417ins proteins is able to adopt this conformation similar to the wild-type protein, with the mutation likely affecting a pre-GTP hydrolysis step. Notably, both Y192 and P338 in ATL3 are proximal to the intramolecular G-middle domain interface of the engaged state that we hypothesize is disrupted in the ATL1 N417ins mutation, potentially suggesting a common pathogenic mechanism. Mutations at residues corresponding to Y192 and P338 of ATL3 in ATL1 (Y196 and P342, respectively) have been identified in HSP patients (McCorquodale *et al.*, 2011; de Bot *et al*., 2013). In addition, the conserved P342 along with P344 have been shown to play a pivotal role in rigid body rotation between the G and middle domain in ATL (Byrnes and Sondermann, 2011) and the bundle signaling element in dynamin (Chappie *et al*., 2010). The parallels between the behavior of ATL1 N417ins and ATL3 Y192C and P338R mutations support our proposed mechanism and highlights the critical role of the G-middle domain interface plays in ATL fusion regulation.

Another notable feature of the case described in this study is the presence of a thinning corpus callosum (TCC; Figure 3.1A), which has been described as a sub-category of complex

HSP, most commonly attributed to autosomal recessive mutations in *SPG11* (spatacsin), with fewer cases caused by *SPG21* (maspardin), *SPG32*, *SPG15*, and *TUBB4A* (Depienne *et al*., 2007; Lamartine *et al*., 2020). A more recent study identified a family in South Africa with three generations of late-onset AD-HSP with a pattern of TCC stemming from the *SPG3A* R416C mutation (Orlacchio *et al*., 2011; Table 3.2/Figure 3.10). Although the cases in the study by Orlacchio *et al.* and a majority of HSP-TCC cases display some level of cognitive impairment, the proband in the present study has normal cognitive functioning.

As is the case in some complex HSP cases, the proband here has shown features of epilepsy as established by an EEG. Recently, significantly decreased ATL1 expression levels have been identified in the temporal lobe neocortex of patients with temporal lobe epilepsy (TLE) (Lu *et al.*, 2020). Upon overexpression of ATL1 in an epileptic mouse model, seizure occurrence decreased resulting from inhibition of spontaneous action potential. While the exact mechanism remains elusive, a link may be drawn in *SPG3A* HSP patients who experience epileptic symptoms.

A frequent theme with HSP patients is an early diagnosis of cerebral palsy (CP), as seen in the case reported here. Because HSPs are very rare and genetically heterogeneous disorders, they can be difficult to clinically identify and diagnose, especially if there is no family history. Since CP usually manifests at the beginning of life, it is not uncommon for patients with early onset HSP and spastic di- or quadriplegia to first be diagnosed with CP (Salinas *et al*., 2008). Since ATL1 is the most frequently mutated in early onset cases, it is not surprising that many of these patients first receive a CP diagnosis, especially if disease progression is slow, since CP is considered a static condition (Andersen *et al*., 2016; Rainier *et al*., 2006; Yonekawa *et al*., 2014; Dalpozzo *et al*., 2003; Kwon *et al*., 2010; Leonardi *et al*., 2015). Differentiating between the two conditions based on gait patterns is one potential diagnostic tool (Wolf *et al*., 2011). A definitive diagnosis relies on genetic testing, and even then, pathogenic mechanisms can vary drastically requiring a detailed analysis of the underlying molecular mechanisms, as exemplified here.

## MATERIALS AND METHODS

*Whole exome sequencing.*

The proband and both parents were consented and enrolled into the research study WIRB Protocol #20120789. The patient was fourteen years of age at the time of enrollment and verbal assent was obtained. Whole exome sequencing was performed on all three, and an annotated file containing variants in the family members was filtered to include novel, private, or rare variants according to the Genome Aggregation Database (gnomAD, https://gnomad.broadinstitute.org/). Mode of inheritance and disease association, followed by detailed analyst assessment for genotype-phenotype correlation, disease mechanism, and literature review were performed. Variants predicted to be damaging by multiple tools (the Combined Annotation Dependent Depletion (CADD, https://cadd.gs.washington.edu/), ExAC's probability of loss-of-function intolerance score and missense z-score (pLi, z-score), and Genomic Evolutionary Rate Profiling (GERP, http://mendel.stanford.edu/SidowLab/downloads/gerp/) algorithms) were considered as candidate genes responsible for the proband's phenotype.

*Protein expression and purification.*

The catalytic core of hATL1 WT (1-449) and N417ins (1-447 for X-ray crystallography; 1-450 for kinetics) were each cloned into a pET21 vector using standard molecular cloning methods. Each construct had a C terminal 10X-HIS tag, expect the crystallography construct that had a 6x-HIS tag. Protein was overexpressed in BL21(DE3) *E. coli* grown in Terrific Broth to an OD ~0.8, followed by induction for 16 hours at 18°C with 0.5 mM IPTG. Cells were harvested at 4500 x *g* and resuspended in $Ni^{2+}$-NTA Buffer A (25 mM tris pH 8.5, 500 mM NaCl, 20 mM imidazole), flash frozen in liquid nitrogen, and stored at -80°C. For purification, cell pellets were thawed at RT, sonicated, and spun at 39,000 *x g* to clear insoluble material. Supernatant was loaded onto $Ni^{2+}$-NTA resin (Qiagen) equilibrated in buffer A at a ratio of 1 mL resin: 1 L culture. Loaded resin was washed with 15 column volumes (CV) of Buffer A, then eluted with 3 CV $Ni^{2+}$-NTA buffer B (25

mM tris pH8.5, 500 mM NaCl, 500 mM imidazole). Elution was buffer exchanged into desalt buffer (25 mM tris pH 7.5, 400 mM NaCl, 5 mM EDTA) using a HiPrep 26/10 desalting column (GE Life Sciences). Concentrated elution was run on a GE S200 16/60 equilibrated with gel filtration buffer (25 mM tris pH 7.5, 100 mM NaCl). Peak fractions were run on a gel, concentrated, frozen in liquid nitrogen and stored at -80°C. The G domain (1-339) and middle domain (340-446) of hATL1 WT were purified as above with the following exceptions. Both constructs were cloned into a pET28-based vector with an N-terminal 6x-HIS tag followed by a SUMO tag and a Ulp1 cleavage site. After buffer exchange into desalt buffer, removal of the 6x-HIS-SUMO tag was carried out on ice overnight with Ulp1 protease. The protease and affinity tag were removed with a 5 mL HisTrap HP column (GE), and flowthrough was collected, concentrated, and loaded onto a GE S200 16/60 as above.

*X-ray crystallography data collection and structure determination.*

hATL1 N417ins$^{6xHIS}$ (1-447) was crystallized using the hanging drop vapor diffusion method. Protein at 20 and 30 mg/mL was first incubated with 4 mM $MgCl_2$, 2 mM GDP, 2 mM $AlCl_2$, and 20 mM NaF on ice for 1 hour. Reservoir buffer containing 0.1 M tris pH 8.1, 2% tacsimate pH 8, 18% PEG 3350 was combined with protein mixture at 1:1 ratio on a glass cover slip before sealing and incubating at 20°C. Prior to freezing, crystals were soaked in a cryoprotectant solution containing crystallization buffer with 25% glycerol for ~5 minutes. X-ray diffraction data were collected at Cornell High Energy Synchrotron Source (CHESS). Phase determination was carried out with molecular replacement using PHENIX (Liebschner *et al*., 2019) and coordinates of the WT ATL1 catalytic core (1-446) bound to GDP•$AlF_4^-$ (PDB 4IDO; Byrnes *et al*., 2013). The N417ins mutant structure was built and refined in PHENIX (Liebschner *et al*., 2019) and *Coot* (Emsley *et al*., 2010). Statistics for data collection and refinement are summarized in Table 3.1.

*Phosphate release kinetics.*

An Enzchek phosphate kit (ThermoFisher Scientific) was used to measure apparent catalytic efficiencies for the catalytic-core ATL1 WT and N417ins mutant proteins. Reactions were set up according to the manufacturer's instructions but were scaled to 200 µL and run in the presence of reaction buffer (25 mM tris pH 7.5, 100 mM NaCl, and 2 mM $MgCl_2$ with protein concentrations ranging from 0 to 2 µM and GTP concentration constant at 500 µM. Over a 45-minute reaction period, accumulation of $P_i$ was measured as a spectrophotometric shift from 330 nm to 360 nm as 2-amino-6-mercapto-7-methylpurine riboside (MESG) was converted to ribose 1-phosphate and 2-amino-6-mercapto-7-methylpurine by purine nucleoside phosphorylase. Absorbance values were converted to $P_i$ concentrations based on a standard curve. Turnover efficiencies ($k_{cat}$) were calculated using 3 technical replicates and 2 biological replicates for each construct.

*Size-exclusion chromatography coupled to multi-angle light scattering.*

ATL1 WT and N417ins catalytic-core constructs used for kinetic experiments were loaded at 50 µM onto a Superdex Increase 200 10/300 GL column (GE) equilibrated in 25 mM tris pH 7.5, 100 mM NaCl, 2 mM EGTA, 4 mM $MgCl_2$. All samples were pre-incubated with 2 mM GDP, 2 mM GppNHp, 2 mM GDP in the presence of 2 mM $AlCl_2$, 20 mM NaF, and 4 mM EGTA, or without nucleotide. As protein eluted from the column, it was passed through a static 18-angle light scattering detection unit (DAWN HELEOS-II) and a refractive index detector (Optilab T-rEX), both of which record signal intensity in volts. Wyatt's Astra VI software was used to determine both molecular weight and mass distribution through each sample experiment. Monomeric BSA (Sigma) was used to normalize signal measured by light scattering detectors.

*Liposome preparation.*

All lipids were purchased from Avanti Polar Lipids either reconstituted in chloroform or as desiccate, which were reconstituted after purchase. For all experiments, lipids were prepared as 10 mM stocks at a molar ratio of 1% 18:1 DGS-NTA(Ni) to 99% 18:1 (Δ9-cis) PC. Appropriate volumes of chloroform stocks were transferred to glass tubes and chloroform was evaporated under a $N_2$ air stream for 15 - 20 minutes followed by desiccation for at least 1.5 hours to remove remaining solvent. Lipids were reconstituted in 25 mM tris pH7.5, 100 mM NaCl and vortexed intermittently for 30 minutes to create multilamellar vesicles (MLV). MLVs were then subjected to 10 freeze-thaw cycles between liquid $N_2$ and a room temperature water bath to reduce the multilamellar structures in favor of unilamellar vesicles. Lipids were stored at -80°C until needed. Upon thawing, lipids were extruded 21 times through a filter with 100 nm pore size to achieve a relatively homogenous size solution of unilamellar vesicles. Vesicles were used immediately.

*Liposome tethering assay.*

Decahistidine-tagged ATL1 WT or N417ins protein was loaded onto $Ni^{2+}$-modified vesicles as a 2X reaction stock with 2 mM lipid vesicles (1 mM final) and 0.5 μM to 3 μM protein (0.25 μM to 1.5 μM final) by incubating at room temperature for 30 minutes in the presence of reaction buffer (25 mM tris pH 7.5, 100 mM NaCl, 4 mM $MgCl_2$). Vesicle tethering was measured spectrophotometrically at $OD_{360}$ for 45 minutes upon dilution of reaction stock with reaction buffer +/- 500 μM GTP. Images of aggregate vesicles were taken on a BioRad Chemidoc imaging system. All reactions were carried out in triplicate with two biological replicates and data processing was done in GraphPad Prism. Signal for the three minus GTP reactions per condition were averaged and subtracted from each plus GTP reaction. To determine apparent tethering rates, data were excluded after signal plateau was reached and before signal drop-off (if there was no terminal signal drop, data was not excluded), and the single-phase association rate was calculated and averaged across replicates. The rates were plotted, and the regression for the

second linear region was calculated to determine the rate constant for each protein. Statistical significance was determined using an unpaired t-test.

*Liposome flotation assay.*

Liposome flotation assays were conducted using a Nycodenz concentration gradient, as detailed in Liu *et al*., 2015. Nycodenz powder was dissolved in vesicle tethering reaction buffer at 25% and 70% stock concentrations. Protein-loaded vesicles, prepared as described above, with 2 μM protein and 2 mM lipids, were combined at a 1:1 ratio with the 70% Nycodenz stock, for a final 35% Nycodenz solution (final concentrations of 1 μM protein and 1 mM lipids). The concentration gradient was set up with the bottom 20% of the total volume consisting of the 35% Nycodenz and loaded vesicle solution, the middle 70% consisting of the 25% Nycodenz solution, and the top 10% of the volume being vesicle tethering reaction buffer. These gradients were subjected to ultracentrifugation at 200,310 *x g* for 2 hours at 4°C, then fractions were taken from the top, middle, and bottom of each gradient and analyzed via SDS-PAGE and stained with SYPRO Ruby according to manufacturer's instructions.

*Western blot analysis.*

ATL1 WT (1-558) or ATL1 N417ins (1-559) were cloned into a pcDNA4 vector containing a C terminal c-myc affinity tag using standard molecular cloning methods. These were used to transiently transfect NIH 3T3 WT and NIH 3T3 ATL1/2/3 TKO cells using Avalanche-Omni (EZ Biosystems) according to manufacturer's recommendations. Cells were washed in cold PBS three times then harvested by scraping and lysed in 25 mM tris pH 7.5, 100 mM NaCl, 1% Triton X-100. Total protein in lysates were determined by Bradford reagent (Bio-Rad) and normalized before loading. Gels were run for 1 hour at 210 V, then transferred to a PVDF membrane. Blots were blocked either 1.5 hours at room temperature or overnight at 4°C, followed by incubation with 1:1000 mouse α-c-myc monoclonal 9E10 antibody (Abcam) or 1:60,000 rabbit α-calnexin

(Abcam) in tris-buffered saline with 0.1% Tween-20 (TBST) for 1 hour at room temperature, followed by a 30-minute incubation with 1:5000 goat α-mouse- HRP polyclonal antibody or 1:5000 goat α-rabbit-HRP polyclonal antibody (ThermoFisher Scientific) diluted in TBST. Each incubation period was proceeded by 3 x 5-minute washes with TBST. Blots were developed using an enhanced chemiluminescent HRP substrate and imaged with a BioRad Chemidoc imaging system.

*Mammalian cell immunofluorescence and imaging.*

Mammalian expression vectors containing ATL1 WT or N417ins mutant protein were transfected into NIH 3T3 WT and NIH 3T3 ATL1/2/3 TKO cells using Avalanche-Omni (EZ Biosystems) as described above, or co-transfected with $^{mCherry}$SEC61β into U2OS cells using polyethylenimine (PEI). 24 hours after transfections, cells were processed. Cells were washed three times with PBS between each step. They were first fixed for 20 minutes with 4% formaldehyde followed by permeabilization with 0.1% Triton X-100 for 10 minutes then blocked in 10% BSA for 1.5 hours. Cells were then incubated for 1.5 hours with a 1:400 dilution of mouse α-c-myc monoclonal 9E10 antibody (Abcam) in 5% BSA, then finally in 1:400 α-mouse AlexaFluor-488 in 5% BSA for 1 hour. Cells were washed a final time then treated with ProLong Gold Antifade mountant (ThermoFisher Sientific) before sealing with a coverslip. Images were taken on a Perkins-Elmer UltraView spinning disc confocal microscope with a Nikon Plan Apo 60xA/1.4 oil objective. For each condition, a minimum of 70 cells were imaged for quantification across three experimental replicates (except for ATL1 WT in NIH 3T3 ATL1/2/3 TKO cells, for which 46 cells were imaged). Image brightness and contrast were adjusted using ImageJ (Schneider *et al.*, 2015) then visually assessed for the presence of puncta and tubules. For each category, the percent of total cells was averaged across replicates, then statistical significance was determined by one-way ANOVA.

*Limited proteolysis assay.*

A 2X stock of each the ATL1 WT and N417ins catalytic cores and the WT G domain were prepared in Gel Filtration buffer (with 4 mM $MgCl_2$ added) at 4 μM. Each was incubated with corresponding nucleotides (2 mM GDP or 2 mM GDP, 2 mM $AlCl_2$, 20 mM NaF, and 4 mM EGTA) for 30 minutes at RT then placed on ice. Proteinase K (New England Biolabs) was also prepared as 2X stocks at 2 μg/mL and 20 μg/mL in Gel Filtration buffer and kept on ice. ATL1 samples were combined with PK stocks at 1:1 ratio and reactions were carried out on ice for 15 minutes, then quenched with 2 mM PMSF in DMSO and 5X SDS loading buffer. Samples were boiled immediately and analyzed with SDS-PAGE gels. Gels were stained with Coomassie Brilliant Blue.

*Fluorescent dye labeling.*

To achieve site specificity of protein labeling with maleimide conjugated dyes, a surface-exposed cysteine was mutated to alanine (C375C) and a single cysteine was introduced either on the G domain (K296C) or middle domain (K400C). When labeled, these combinations of mutations were shown to singly and efficiently modify ATL1 (Byrnes *et al*., 2013; O'Donnell *et al*., 2017). For all FRET labeling reactions, catalytic-core fragments of $ATL1^{6xHIS}$ WT or N417ins mutant protein were used with the mutations indicated above. Each reaction contained 100 μM protein and 150 μM maleimide-conjugated AlexaFluor-488, AlexaFluor-647, or both (ThermoFisher Scientific) in FRET labeling buffer (25 mM HEPES pH7, 100 mM NaCl). Reactions were incubated on ice for 30 minutes then excess dye was removed with a NAP-5 column (GE) equilibrated with FRET reaction buffer (25 mM HEPES pH 7.5, 100 mM NaCl, 2 mM $MgCl_2$). Final protein and dye concentrations were determined spectrophotometrically using a nanodrop.

*Equilibrium inter- and intramolecular FRET measurements.*

All steady-state intermolecular FRET experiments were carried out at a concentration of 5 μM total protein with a 1:1 molar ratio of donor to acceptor-labeled protein (2.5 μM donor: 2.5

μM acceptor) in FRET reaction buffer, pre-incubated with 2 mM GDP, 2 mM GDP in the presence of 2 mM $AlCl_2$, 20 mM NaF, and 4 mM EGTA, or without nucleotide at room temperature for 30 minutes. Reactions were measured using a Gemini EM microplate reader (Molecular Devices) at an excitation wavelength of 473 nm and emission spectra between 495 and 745 nm in 10 nm steps. iFRET equilibrium measurements were carried out with the same parameters, except that reactions contained a total of 5 μM protein with a 1:10 ratio of labeled to unlabeled protein (0.5 μM dually labeled and 4.5 μM unlabeled protein).

GraphPad Prism was used for all data analysis, with FRET efficiencies calculated with the ratio $I_{acceptor}/(I_{donor} + I_{acceptor})$ where I was the signal intensity at peak emission wavelengths (515 nm and 655 nm for the donor and acceptor, respectively). All reactions were carried out in triplicate with two biological replicates. One-way ANOVA tests were carried out to determine statistically significant changes in FRET efficiencies.

## REFERENCES


Álvarez, V., Sánchez-Ferrero, E., Beetz, C., Díaz, M., Alonso, B., Corao, A. I., ... & de Munain, A. L. (2010). Mutational spectrum of the SPG4 (SPAST) and SPG3A (ATL1) genes in Spanish patients with hereditary spastic paraplegia. BMC neurology, 10(1), 89.

Andersen, E. W., Leventer, R. J., Reddihough, D. S., Davis, M. R., & Ryan, M. M. (2016). Cerebral palsy is not a diagnosis: A case report of a novel atlastin-1 mutation. Journal of paediatrics and child health, 52(6), 669-671.

Battini, R., Fogli, A., Borghetti, D., Michelucci, A., Perazza, S., Baldinotti, F., ... & Cioni, G. (2011). Clinical and genetic findings in a series of Italian children with pure hereditary spastic paraplegia. *European journal of neurology*, *18*(1), 150-157.

Betancourt-Solis, M. A., Desai, T., & McNew, J. A. (2018). The atlastin membrane anchor forms an intramembrane hairpin that does not span the phospholipid bilayer. *Journal of Biological Chemistry*, *293*(48), 18514-18524.

Bian, X., Klemm, R. W., Liu, T. Y., Zhang, M., Sun, S., Sui, X., ... & Hu, J. (2011). Structures of the atlastin GTPase provide insight into homotypic fusion of endoplasmic reticulum membranes. *Proceedings of the National Academy of Sciences*, *108*(10), 3976-3981.

Blackstone, C. (2012). Cellular pathways of hereditary spastic paraplegia. *Annual review of neuroscience*, *35*, 25-47.

Blackstone, C. (2020). Early-onset hereditary spastic paraplegia: the possibility of a genetic diagnosis. Developmental Medicine & Child Neurology.

Blackstone, C. (2018). Hereditary spastic paraplegia. In Handbook of clinical neurology (Vol. 148, pp. 633-652). Elsevier.

Botzolakis, E. J., Zhao, J., Gurba, K. N., Macdonald, R. L., & Hedera, P. (2011). The effect of HSP-causing mutations in SPG3A and NIPA1 on the assembly, trafficking, and interaction between atlastin-1 and NIPA1. *Molecular and Cellular Neuroscience*, *46*(1), 122-135.

Byrnes, L. J., Singh, A., Szeto, K., Benvin, N. M., O'donnell, J. P., Zipfel, W. R., & Sondermann, H. (2013). Structural basis for conformational switching and GTP loading of the large G protein atlastin. *The EMBO journal*, *32*(3), 369-384.

Byrnes, L. J., & Sondermann, H. (2011). Structural basis for the nucleotide-dependent dimerization of the large G protein atlastin-1/SPG3A. *Proceedings of the National Academy of Sciences*, *108*(6), 2216-2221.

Cao, Y. L., Meng, S., Chen, Y., Feng, J. X., Gu, D. D., Yu, B., ... & Gao, S. (2017). MFN1 structures reveal nucleotide-triggered dimerization critical for mitochondrial fusion. *Nature*, *542*(7641), 372-376.

Chappie, J. S., Acharya, S., Leonard, M., Schmid, S. L., & Dyda, F. (2010). G domain dimerization controls dynamin's assembly-stimulated GTPase activity. *Nature*, *465*(7297), 435-440.

Chen, S. Q., Zhou, Y., Li, X. Y., La, B., Huang, S., Huang, W. J., ... & Wang, Y. M. (2005). Severe hereditary spastic paraplegia caused by a de novo SPG3A mutation. Sci China, 51(15), 1854-6.

Cooley, R. B., Arp, D. J., & Karplus, P. A. (2010). Evolutionary origin of a secondary structure: π-helices as cryptic but widespread insertional variations of α-helices that enhance protein functionality. *Journal of molecular biology*, *404*(2), 232-246.

Dalpozzo, F., Rossetto, M. G., Boaretto, F., Sartori, E., Mostacciuolo, M. L., Daga, A., ... & Martinuzzi, A. (2003). Infancy onset hereditary spastic paraplegia associated with a novel atlastin mutation. Neurology, 61(4), 580-581.

D'Amico, A., Tessa, A., Sabino, A., Bertini, E., Santorelli, F. M., & Servidei, S. (2004). Incomplete penetrance in an SPG3A-linked family with a new mutation in the atlastin gene. Neurology, 62(11), 2138-2139.

de Bot, S. T., Veldink, J. H., Vermeer, S., Mensenkamp, A. R., Brugman, F., Scheffer, H., ... & van de Warrenburg, B. P. (2013). ATL1 and REEP1 mutations in hereditary and sporadic upper motor neuron syndromes. *Journal of neurology*, *260*(3), 869-875.

De Leva, M. F., Filla, A., Criscuolo, C., Tessa, A., Pappatà, S., Quarantelli, M., ... & Santorelli, F. M. (2010). Complex phenotype in an Italian family with a novel mutation in SPG3A. Journal of neurology, 257(3), 328-331.

DeLuca, G. C., Ebers, G. C., & Esiri, M. M. (2004). The extent of axonal loss in the long tracts in hereditary spastic paraplegia. *Neuropathology and applied neurobiology*, *30*(6), 576-584.

Depienne, C., Stevanin, G., Brice, A., & Durr, A. (2007). Hereditary spastic paraplegias: an update. Current opinion in neurology, 20(6), 674-680.

Dürr, A., Camuzat, A., Colin, E., Tallaksen, C., Hannequin, D., Coutinho, P., ... & Ruberg, M. (2004). Atlastin1 mutations are frequent in young-onset autosomal dominant spastic paraplegia. Archives of neurology, 61(12), 1867-1872.

Elert-Dobkowska, E., Stepniak, I., Krysa, W., Rajkiewicz, M., Rakowicz, M., Sobanska, A., ... & Lipczynska-Lojkowska, W. (2015). Molecular spectrum of the SPAST, ATL1 and REEP1 gene

mutations associated with the most common hereditary spastic paraplegias in a group of Polish patients. Journal of the neurological sciences, 359(1-2), 35-39.

Fassier, C., Hutt, J. A., Scholpp, S., Lumsden, A., Giros, B., Nothias, F., … & Hazan, J. (2010). Zebrafish atlastin controls motility and spinal motor axon architecture via inhibition of the BMP pathway. *Nature neuroscience*, *13*(11), 1380-1387.

Fink, J. K. (2006). Hereditary spastic paraplegia. *Current neurology and neuroscience reports*, *6*(1), 65-76.

Fink, J. K. (2013). Hereditary spastic paraplegia: clinico-pathologic features and emerging molecular mechanisms. Acta neuropathologica, 126(3), 307-328.

Fink, J. K. (2020). The hereditary spastic paraplegias. *Rosenberg's Molecular and Genetic Basis of Neurological and Psychiatric Disease*, 147-170.

Fischer, D., Schabhüttl, M., Wieland, T., Windhager, R., Strom, T. M., & Auer-Grumbach, M. (2014). A novel missense mutation confirms ATL3 as a gene for hereditary sensory neuropathy type 1. *Brain*, *137*(7), e286-e286.

Ford, M. G., & Chappie, J. S. (2019). The structural biology of the dynamin-related proteins: New insights into a diverse, multitalented family. *Traffic*, *20*(10), 717-740.

Fusco, C., Frattini, D., Farnetti, E., Nicoli, D., Casali, B., Fiorentino, F., ... & Della Giustina, E. (2010). Hereditary spastic paraplegia and axonal motor neuropathy caused by a novel SPG3A de novo mutation. Brain and Development, 32(7), 592-594.

Gasper, R., Meyer, S., Gotthardt, K., Sirajuddin, M., & Wittinghofer, A. (2009). It takes two to tango: regulation of G proteins by dimerization. *Nature reviews Molecular cell biology*, *10*(6), 423-429.

Guelly, C., Zhu, P. P., Leonardis, L., Papić, L., Zidar, J., Schabhüttl, M., ... & Willems, J. (2011). Targeted high-throughput sequencing identifies mutations in atlastin-1 as a cause of hereditary sensory neuropathy type I. *The American Journal of Human Genetics*, *88*(1), 99-105.

Haberlová, J., Claeys, K. G., Zamecnik, J., De Jonghe, P., & Seeman, P. (2008). Extending the clinical spectrum of SPG3A mutations to a very severe and very early complicated phenotype. Journal of neurology, 255(6), 927.

Hu, X., Wu, F., Sun, S., Yu, W., & Hu, J. (2015). Human atlastin GTPases mediate differentiated fusion of endoplasmic reticulum membranes. Protein & cell, 6(4), 307-311.

Ishiura, H., Takahashi, Y., Hayashi, T., Saito, K., Furuya, H., Watanabe, M., ... & Shibuya, K. (2014). Molecular epidemiology and clinical spectrum of hereditary spastic paraplegia in the

Japanese population based on comprehensive mutational analyses. Journal of human genetics, 59(3), 163-172.

Kabsch, W., & Sander, C. (1983). Dictionary of protein secondary structure: pattern recognition of hydrogen-bonded and geometrical features. *Biopolymers: Original Research on Biomolecules*, *22*(12), 2577-2637.

Karczewski, K. J., Francioli, L. C., Tiao, G., Cummings, B. B., Alföldi, J., Wang, Q., ... & Gauthier, L. D. (2020). The mutational constraint spectrum quantified from variation in 141,456 humans. *Nature*, *581*(7809), 434-443.

Kornak, U., Mademan, I., Schinke, M., Voigt, M., Krawitz, P., Hecht, J., ... & Kurth, I. (2014). Sensory neuropathy with bone destruction due to a mutation in the membrane-shaping atlastin GTPase 3. *Brain*, *137*(3), 683-692.

Krols, M., Detry, S., Asselbergh, B., Almeida-Souza, L., Kremer, A., Lippens, S., ... & McMahon, H. T. (2018). Sensory-neuropathy-causing mutations in ATL3 cause aberrant ER membrane tethering. *Cell reports*, *23*(7), 2026-2038.

Kwon, M. J., Lee, S. T., Kim, J. W., Sung, D. H., & Ki, C. S. (2010). Clinical and genetic analysis of a Korean family with hereditary spastic paraplegia type 3. Annals of Clinical & Laboratory Science, 40(4), 375-379.

Lamartine S. Monteiro, M., Vandernoot, I., Desmyter, L., Wermenbol, V., Naeije, G., & Remiche, G. (2020). Corpus callosum thinning in autosomal dominant hereditary spastic paraplegia associated with a novel TUBβ4A mutation. Clinical Genetics.

Landrum, M. J., Lee, J. M., Riley, G. R., Jang, W., Rubinstein, W. S., Church, D. M., & Maglott, D. R. (2014). ClinVar: public archive of relationships among sequence variation and human phenotype. *Nucleic acids research*, *42*(D1), D980-D985.

Leonardi, L., Marcotulli, C., Santorelli, F. M., Tessa, A., & Casali, C. (2015). De novo mutations in SPG3A: a challenge in differential diagnosis and genetic counselling. Neurological Sciences, 36(6), 1063-1064.

Liebschner, D., Afonine, P. V., Baker, M. L., Bunkóczi, G., Chen, V. B., Croll, T. I., ... & Moriarty, N. W. (2019). Macromolecular structure determination using X-rays, neutrons and electrons: recent developments in Phenix. *Acta Crystallographica Section D: Structural Biology*, *75*(10), 861-877.

Liu, T. Y., Bian, X., Romano, F. B., Shemesh, T., Rapoport, T. A., & Hu, J. (2015). Cis and trans interactions between atlastin molecules during membrane fusion. Proceedings of the National Academy of Sciences, 112(15), E1851-E1860.

Liu, T. Y., Bian, X., Sun, S., Hu, X., Klemm, R. W., Prinz, W. A., ... & Hu, J. (2012). Lipid interaction of the C terminus and association of the transmembrane segments facilitate atlastin-mediated homotypic endoplasmic reticulum fusion. *Proceedings of the National Academy of Sciences*, *109*(32), E2146-E2154.

Liu, X., Guo, X., Niu, L., Li, X., Sun, F., Hu, J., ... & Shen, K. (2019). Atlastin-1 regulates morphology and function of endoplasmic reticulum in dendrites. *Nature communications*, *10*(1), 1-15.

Lu, X., Cen, Z., Xie, F., Ouyang, Z., Zhang, B., Zhao, G., & Luo, W. (2014). Genetic analysis of SPG4 and SPG3A genes in a cohort of Chinese patients with hereditary spastic paraplegia. Journal of the neurological sciences, 347(1-2), 368-371.

Lu, X., Yang, M., Yang, Y., & Wang, X. F. (2020). Atlastin-1 modulates seizure activity and neuronal excitability. CNS Neuroscience & Therapeutics, 26(3), 385-393.

Magariello, A., Tortorella, C., Citrigno, L., Patitucci, A., Tortelli, R., Mazzei, R., ... & Muglia, M. (2012). The p. Arg416Cys mutation in SPG3a gene associated with a pure form of spastic paraplegia. Muscle & nerve, 45(6), 919-920.

McCorquodale III, D. S., Ozomaro, U., Huang, J., Montenegro, G., Kushman, A., Citrigno, L., ... & Züchner, S. (2011). Mutation screening of spastin, atlastin, and REEP1 in hereditary spastic paraplegia. *Clinical genetics*, *79*(6), 523-530.

Meijer, I. A., Dion, P., Laurent, S., Dupré, N., Brais, B., Levert, A., ... & Soderblom, C. (2007). Characterization of a novel SPG3A deletion in a French-Canadian family. Annals of Neurology: Official Journal of the American Neurological Association and the Child Neurology Society, 61(6), 599-603.

Montagna, A., Vajente, N., Pendin, D., & Daga, A. (2020). In vivo analysis of CRISPR/Cas9 induced atlastin pathological mutations in Drosophila. *Frontiers in Neuroscience*, *14*.

Morin-Leisk, J., Saini, S. G., Meng, X., Makhov, A. M., Zhang, P., & Lee, T. H. (2011). An intramolecular salt bridge drives the soluble domain of GTP-bound atlastin into the postfusion conformation. *Journal of Cell Biology*, *195*(4), 605-615.

Moss, T. J., Andreazza, C., Verma, A., Daga, A., & McNew, J. A. (2011). Membrane fusion by the GTPase atlastin requires a conserved C-terminal cytoplasmic tail and dimerization through the middle domain. *Proceedings of the National Academy of Sciences*, *108*(27), 11133-11138.

Namekawa, M., Muriel, M. P., Janer, A., Latouche, M., Dauphin, A., Debeir, T., ... & Sittler, A. (2007). Mutations in the SPG3A gene encoding the GTPase atlastin interfere with vesicle trafficking in the ER/Golgi interface and Golgi morphogenesis. *Molecular and Cellular Neuroscience*, *35*(1), 1-13.

Namekawa, M., Ribai, P., Nelson, I., Forlani, S., Fellmann, F., Goizet, C., ... & Brice, A. (2006). SPG3A is the most frequent cause of hereditary spastic paraplegia with onset before age 10 years. Neurology, 66(1), 112-114.

Nixon-Abell, J., Obara, C. J., Weigel, A. V., Li, D., Legant, W. R., Xu, C. S., ... & Blackstone, C. (2016). Increased spatiotemporal resolution reveals highly dynamic dense tubular matrices in the peripheral ER. *Science*, *354*(6311).

O'Donnell, J. P., Byrnes, L. J., Cooley, R. B., & Sondermann, H. (2018). A hereditary spastic paraplegia–associated atlastin variant exhibits defective allosteric coupling in the catalytic core. *Journal of Biological Chemistry*, *293*(2), 687-700.

O'Donnell, J. P., Cooley, R. B., Kelly, C. M., Miller, K., Andersen, O. S., Rusinova, R., & Sondermann, H. (2017). Timing and reset mechanism of GTP hydrolysis-driven conformational changes of atlastin. *Structure*, *25*(7), 997-1010.

O'Donnell, J. P., Kelly, C. M., & Sondermann, H. (2020). Nucleotide-Dependent Dimerization and Conformational Switching of Atlastin. In *Dynamin Superfamily GTPases* (pp. 93-113). Humana, New York, NY.

Orlacchio, A., Montieri, P., Babalini, C., Gaudiello, F., Bernardi, G., & Kawarai, T. (2011). Late-onset hereditary spastic paraplegia with thin corpus callosum caused by a new SPG3A mutation. Journal of neurology, 258(7), 1361-1363.

Orso, G., Pendin, D., Liu, S., Tosetto, J., Moss, T. J., Faust, J. E., ... & Daga, A. (2009). Homotypic fusion of ER membranes requires the dynamin-like GTPase atlastin. *Nature*, *460*(7258), 978-983.

Pendin, D., Tosetto, J., Moss, T. J., Andreazza, C., Moro, S., McNew, J. A., & Daga, A. (2011). GTP-dependent packing of a three-helix bundle is required for atlastin-mediated fusion. *Proceedings of the National Academy of Sciences*, *108*(39), 16283-16288.

Powers, R. E., Wang, S., Liu, T. Y., & Rapoport, T. A. (2017). Reconstitution of the tubular endoplasmic reticulum network with purified components. *Nature*, *543*(7644), 257-260.

Praefcke, G. J., & McMahon, H. T. (2004). The dynamin superfamily: universal membrane tubulation and fission molecules?. *Nature reviews Molecular cell biology*, *5*(2), 133-147.

Qi, Y., Yan, L., Yu, C., Guo, X., Zhou, X., Hu, X., ... & Hu, J. (2016). Structures of human mitofusin 1 provide insight into mitochondrial tethering. *Journal of Cell Biology*, *215*(5), 621-629.

Rainier, S., Sher, C., Reish, O., Thomas, D., & Fink, J. K. (2006). De novo occurrence of novel SPG3A/atlastin mutation presenting as cerebral palsy. Archives of neurology, 63(3), 445-447.

Rismanchi, N., Soderblom, C., Stadler, J., Zhu, P. P., & Blackstone, C. (2008). Atlastin GTPases are required for Golgi apparatus and ER morphogenesis. *Human molecular genetics*, *17*(11), 1591-1604.

Salinas, S., Proukakis, C., Crosby, A., & Warner, T. T. (2008). Hereditary spastic paraplegia: clinical features and pathogenetic mechanisms. The Lancet Neurology, 7(12), 1127-1138.

Shih, Y. T., & Hsueh, Y. P. (2016). VCP and ATL1 regulate endoplasmic reticulum and protein synthesis for dendritic spine formation. *Nature communications*, *7*(1), 1-16.

Svenstrup, K., Bross, P., Koefoed, P., Hjermind, L. E., Eiberg, H., Born, A. P., ... & Nielsen, J. E. (2009). Sequence variants in SPAST, SPG3A and HSPD1 in hereditary spastic paraplegia. Journal of the neurological sciences, 284(1-2), 90-95.

Touw, W. G., Baakman, C., Black, J., Te Beek, T. A., Krieger, E., Joosten, R. P., & Vriend, G. (2015). A series of PDB-related databanks for everyday needs. *Nucleic acids research*, *43*(D1), D364-D368.

Tuma, P. L., & Collins, C. A. (1994). Activation of dynamin GTPase is a result of positive cooperativity. *Journal of Biological Chemistry*, *269*(49), 30842-30847.

Ulengin, I., Park, J. J., & Lee, T. H. (2015). ER network formation and membrane fusion by atlastin1/SPG3A disease variants. *Molecular biology of the cell*, *26*(9), 1616-1628.

Varga, R. E., Schüle, R., Fadel, H., Valenzuela, I., Speziani, F., Gonzalez, M., ... & Alvarez, V. (2013). Do not trust the pedigree: reduced and sex-dependent penetrance at a novel mutation hotspot in ATL1 blurs autosomal dominant inheritance of spastic paraplegia. Human Mutation, 34(6), 860-863.

Wang, N., & Rapoport, T. A. (2019). Reconstituting the reticular ER network–mechanistic implications and open questions. *Journal of Cell Science*, *132*(4).

Wang, S., Romano, F. B., Field, C. M., Mitchison, T. J., & Rapoport, T. A. (2013). Multiple mechanisms determine ER network morphology during the cell cycle in Xenopus egg extracts. *Journal of Cell Biology*, *203*(5), 801-814.

Wang, X., Shaw, W. R., Tsang, H. T., Reid, E., & O'Kane, C. J. (2007). Drosophila spichthyin inhibits BMP signaling and regulates synaptic growth and axonal microtubules. *Nature neuroscience*, *10*(2), 177-185.

Warnock, D. E., Hinshaw, J. E., & Schmid, S. L. (1996). Dynamin self-assembly stimulates its GTPase activity. *Journal of Biological Chemistry*, *271*(37), 22310-22314.

Wolf, S. I., Braatz, F., Metaxiotis, D., Armbrust, P., Dreher, T., Döderlein, L., & Mikut, R. (2011). Gait analysis may help to distinguish hereditary spastic paraplegia from cerebral palsy. Gait & posture, 33(4), 556-561.

Wu, F., Hu, X., Bian, X., Liu, X., & Hu, J. (2015). Comparison of human and Drosophila atlastin GTPases. *Protein & cell*, *6*(2), 139-146.

Xiao, X. W., Du, J., Jiao, B., Liao, X. X., Zhou, L., Liu, X. X., ... & Lin, Z. Y. (2019). Novel ATL1 mutation in a Chinese family with hereditary spastic paraplegia: A case report and review of literature. *World Journal of Clinical Cases*, *7*(11), 1358.

Yan, L., Sun, S., Wang, W., Shi, J., Hu, X., Wang, S., ... & Lou, Z. (2015). Structures of the yeast dynamin-like GTPase Sey1p provide insight into homotypic ER fusion. *Journal of Cell Biology*, *210*(6), 961-972.

Yonekawa, T., Oya, Y., Higuchi, Y., Hashiguchi, A., Takashima, H., Sugai, K., & Sasaki, M. (2014). Extremely severe complicated spastic paraplegia 3A with neonatal onset. Pediatric neurology, 51(5), 726-729.

Zhao, G. H., & Liu, X. M. (2017). Clinical features and genotype-phenotype correlation analysis in patients with ATL1 mutations: A literature reanalysis. *Translational neurodegeneration*, *6*(1), 9.

Zhao, G., Zhu, P. P., Renvoisé, B., Maldonado-Báez, L., Park, S. H., & Blackstone, C. (2016). Mammalian knock out cells reveal prominent roles for atlastin GTPases in ER network morphology. *Experimental cell research*, *349*(1), 32-44.

Zhao, X., Alvarado, D., Rainier, S., Lemons, R., Hedera, P., Weber, C. H., ... & Bui, M. (2001). Mutations in a newly identified GTPase gene cause autosomal dominant hereditary spastic paraplegia. *Nature genetics*, *29*(3), 326-331.

# CHAPTER FOUR

# CONCLUSIONS AND FUTURE DIRECTIONS

## SUMMARY OF FINDINGS

*Intrinsic and extrinsic regulation of atlastin-1 by a short, N-terminal hypervariable region*

Membrane fusion in the context of the eukaryotic cell is a crucial process that allows communication between organelles and transport of proteins and biomolecules within and outside of the cell. The extensive study of SNAREs and viral fusion proteins has established the basis of our understanding of how proteins can harness energy to overcome the energy barrier of fusing membranes (Harrison, 2015; McNew, 2008 Jahn *et al*., 2003). Unlike these classic examples that rely on favorable protein folding energy to manipulate membranes, the dynamin superfamily of large G proteins utilizes energy from GTP hydrolysis to remodel eukaryotic membranes through fission and fusion (Praefcke and McMahon, 2004). Our lab is interested in examining a newer member, atlastin (ATL), as it appears to functionally deviate from other canonical dynamins (Praefcke and McMahon, 2004; McNew *et al*., 2013), and mutation of two isoforms is associated with rare, neurodegenerative disease (Guelly *et al*., 2011; Fischer *et al*., 2014; Zhao *et al*, 2001; Krols *et al*., 2018).

The works presented in the previous chapters detail our continued efforts to understand the mechanisms controlling the activity of ATL. Previous work studying the structures and kinetic behaviors of the soluble, catalytic core of ATL has yielded a fairly comprehensive picture of the order and timing of events within the catalytic cycle and the accompanying conformational changes (Byrnes and Sondermann, 2011; Bian *et al*., 2011; Byrnes *et al*., 2013; O'Donnell *et al*., 2017). However, a number of questions remain regarding how this mechanism translates to a complex cellular environment in which many ATLs must work together to successfully stimulate membrane fusion, especially considering our current lack of knowledge surrounding regulation of ATL activity.

We have proposed a model in which an N-terminal hypervariable region (HVR) of ATL1 interacts with the G domain of an adjacent protomer on a *cis* membrane, forming arrays to coordinate larger-scale *trans* ATL interactions for more efficient fusion and reduction of futile, *cis*-acting events. This model was based on a novel structure of the catalytic core of ATL1 that revealed these HVR intermolecular contacts and was supported by trends in its membrane tethering behavior in which HVR deletion caused significant defects in tethering rates, while having no effect on innate nucleotide binding and GTP hydrolysis of the protein in solution. This indicates that the HVR plays a crucial role in membrane-specific control of ATL1-dependent tethering.

As we began inspecting this short motif, we found numerous reports of phosphorylation of three conserved serine residues: S10, S22, and S23 from large, unbiased proteomics-based studies (Hornbeck *et al*., 2015). Since little is known about cellular regulation of ATL, this was a noteworthy finding and we set out to confirm the presence and determine the relevance of these modifications. We found that all three of these residues are phosphorylated in mammalian cells, with S10 being present primarily in its phosphorylated state. Use of phosphomimetic ATL1 mutant variations revealed a vesicle tethering defect and an altered sub-cellular localization from ER tubules to puncta with a modified S10 residue. However, the phosphomimetic S22/S23 variants had WT-level *in vitro* kinetic behavior but caused the appearance of a “fuzzy” ER. Interestingly, we saw that the S10 residue requires an apparent phosphorylation turnover for native function, while modification of the S22/S23 residues act more as a binary switch. Based on our evidence, we hypothesize that two separate mechanisms control these phosphorylation events.

Lastly, we employed a curated kinase screen to identify putative cellular ATL1 modifiers. A number of top candidates emerged, including casein kinase II (CK2 α and α’ catalytic subunits), p21-activated kinases (PAK7/5, PAK 6, and PAK4), Ca2+/calmodulin-dependent kinase II (CaMKII α, δ, and γ isoforms), cAMP-dependent protein kinase (PKA catalytic α subunit), phosphorylase b (γ subunit), Aurora kinase A, and casein kinase I (CK1 δ, ϵ, and γ-2 subunits).

We also established the preferential phosphorylation sites for each of these kinases within the three conserved serine residues studied here. Future work will reveal which of these kinases modifies ATL1 in a biological setting and continue defining the effects on ER morphology and less understood cellular roles of ATL1.

Moreover, uncovering structural, functional, and regulatory mechanisms of the HVR has been a crucial step in the next phase of understanding ATL's cellular mechanism. We have provided additional evidence supporting an emerging model for ATL-mediated ER fusion through coordination of *cis* membrane protomer interactions for orchestrated fusion events (Liu *et al*., 2015; Saini *et al*., 2014; Rismanchi *et al*., 2008; Zhu *et al*., 2003) and a similar observed trend with the mitochondrial fusion protein mitofusin (MFN) (Shutt *et al*., 2012; Mattie *et al*., 2018; Brandt *et al*., 2016). Further investigation of the structural and functional consequences of ATL phosphorylation will provide novel insight toward its cellular regulation.

*Clinical and molecular characterization of a novel ATL1 mutation associated with spastic quadriplegia*

The earliest reports containing descriptions of ATL1 described its causative role in the rare neuronopathy Hereditary Spastic Paraplegia (Zhao *et al*., 2001). Since this time, the field has continued to study disease-associated mutations as a means of unraveling the intricate details of ATL's catalytic and cellular mechanisms. In Chapter 3, we presented a case of complex HSP caused by a *de novo* mutation in ATL1, resulting in the whole codon insertion of an asparagine proceeding R416 (N417ins) at the top of the third α-helix of the middle domain. Expression of the ATL1 N417ins mutation in mammalian cells resulted in redistribution of ATL1 localization from tubules to puncta and small globules throughout the reticular ER. However, the ATL1 catalytic core with the insertion mutation retained innate nucleotide binding and GTP hydrolysis rates. The structure of the ATL1 N417ins catalytic core bound to the transition state analog GDP•$AlF_4^-$

revealed surprisingly few deviations from the comparable ATL1 WT structure (PDB 4IDO; Byrnes *et al*., 2013), both in a tight cross-over dimer conformation.

Based on this, we were surprised to see a rare gain-of-function mechanism in vesicle tethering activity. Since we had shown that nucleotide binding and hydrolysis were not altered and the transition state structure only showed subtle deviations, we set out to probe conformational states at various points in the catalytic cycle using limited proteolysis and FRET-based experiments. We were able to detect variations between the WT and N417ins proteins in the apo and GDP-bound states, both representing the pre-hydrolysis state which exists in an engaged conformation, mediated by a crucial intramolecular interaction between the G and middle domain (Byrnes *et al*., 2013; O'Donnell *et al*., 2017). The residues participating in this interface lie adjacent to the N417 insertion residue. We have proposed a model for the pathogenic mechanism of this disease-associated mutation in which the allosteric coupling of the G and middle domains has been disrupted, allowing for increased tethering rates while leaving innate GTP activity unaffected.

## FUTURE DIRECTIONS

*Structural determination of the ATL1 N417ins pre-fusion conformation.*

In Chapter 3 we presented a case of complex HSP associated with a novel ATL1 insertion mutation of an Asp residue at position 417. Based on structural data and kinetic and conformational behaviors of this novel mutant, we proposed a model in which the inserted residue prevents a critical intramolecular interface between the G and middle domains that dictate the formation of an engaged, pre-hydrolysis state. Without this contact, the insertion mutation variant allows for excessive membrane tethering. However, we currently lack the structural data to corroborate this model. We plan to crystallize the ATL1 N417ins mutant protein in the presence of GDP to determine the pre-fusion, engaged state, assuming such a conformation is compatible with crystal growth. We have already screened several ATL1 N417ins protein constructs and have several crystallization-condition hits, but none that diffracted at a resolution needed for structural analysis. Recently, we have cloned the insertion mutation into the same protein construct used to solve the GDP-bound ATL1 WT structure (Byrnes and Sondermann, 2011), and will continue screening crystallization conditions. We anticipate that the structure of this HSP-associated ATL1 mutation in the pre-hydrolysis state will extend our understanding of the pathogenic mechanism, as hypothesized in Chapter 3.

As has been demonstrated previously (O'Donnell *et al*., 2018; Byrnes and Sondermann, 2011; Meijer *et al*., 2007; Bian *et al*., 2011; Ulengin *et al*., 2015; Liu *et al*., 2019), by studying the molecular basis of pathogenic mechanisms of HSP-associated mutations in ATL1, we can continue to learn more about its native function and nuances of its regulation.

*Single molecule tracking for quantitative analysis of HVR-dependent oligomerization.*

In Chapter 2, we proposed our model for HVR-dependent *cis* oligomerization and its contribution to coordinated and efficient membrane tethering and fusion. Our vesicle tethering assay strongly supported this mechanism, showing that without the HVR, ATL1 tethering is

significantly reduced. However, a more quantitative approach would further bolster our model and further elucidate the mechanism by which the HVR contributes to *cis* protein interactions. To do this, we plan to use single molecule tracking techniques as previously described (Rozovsky *et* al., Axmann *et al*., 2015; Deatherage *et al*., 2020; Groves *et al*., 2008; Nye and Groves, 2008). Similar to the vesicle tethering experiments, C-terminally decahistidine-tagged catalytic-core ATL will be loaded onto supported lipid bilayers (SLB) containing NiNTA-modified lipids, so their orientation mimics that observed on biological membranes. Proteins will be fluorescently labeled in a site-specific manner on the G domain, as described in Chapter 3, allowing detection of lipid-bound protein using total internal reflection fluorescence (TIRF) microscopy (Figure 4.1A). With this experimental setup, we can use single molecule tracking to determine the oligomerization state by measuring stochastic photobleaching steps, changes in diffusivity coefficients, or colocalization with multiple fluorescent markers. With the first method, we can count the number of spontaneous photobleaching steps that occur within a single particle before the signal disappears, which will be indicative of the number of ATL protomers that were in the particle. When we do this with ΔHVR mutant protein, we would anticipate a reduction or ablation of oligomerization. With the second method, we would calculate diffusion coefficients (in units of $\mu m^2$/sec) of individual particles, with a reduction in oligomerization state correlating with a higher diffusion rate. Lastly, if we label the protein with fluorescent dyes that have different excitation and emission wavelengths, we can track colocalization by tracking particles at both wavelengths.

Preliminary work has been done in the lab to establish and optimize conditions for these experiments. We have generated fluid SLBs with diffusion coefficient of about 1 $\mu m^2$/sec, demonstrated by a fluorescence recovery after photobleaching (FRAP) experiment using rhodamine-labeled lipids (Figure 4.1B). We also determined that ATL particles were mobile when loaded onto the SLB, with ATL3 particles at a calculated a diffusion rate of 0.28 ± 0.17 $\mu m^2$/sec (Figure 4.1C), which was slower than the reported value for the comparable *D. melanogaster* protein construct (Liu *et al*., 2015).

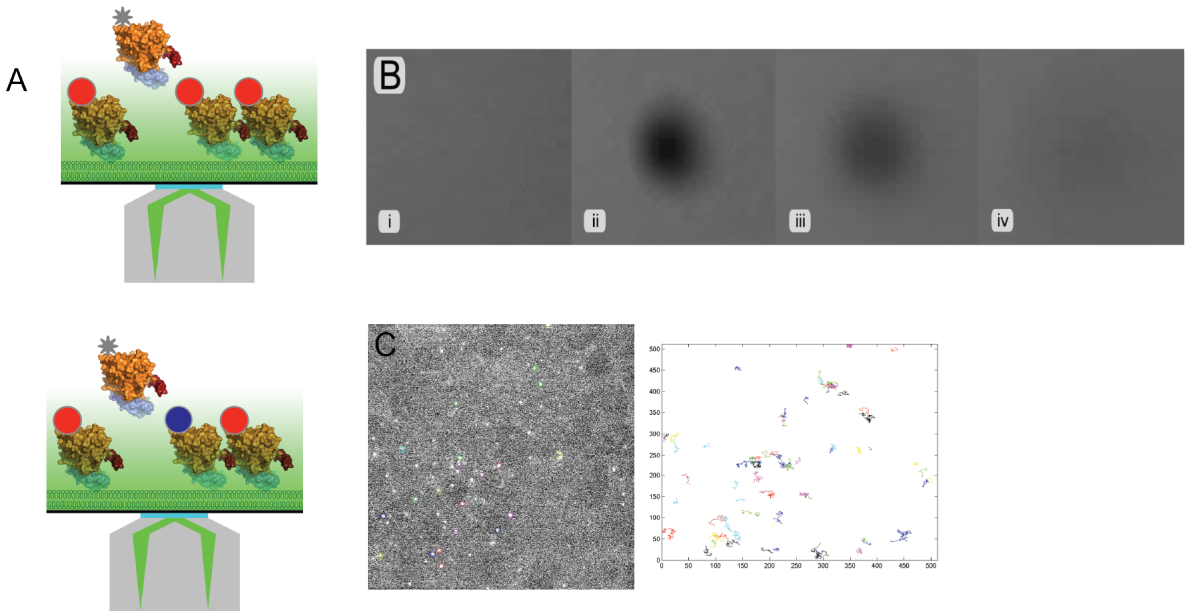


**Figure 4.1 Single molecule tracking-based studies for HVR-dependent oligomerization. (A)** Illustration demonstrating experimental setup for single particle tracking using TIRF microscopy detection of fluid SLBs loaded with the catalytic core ATL. Proteins will be labeled with either one or two different fluorophores (shown as red or blue here) and detection only occurs within ~100 nm of the bilayer. **(B)** Individual frames (i-iv) from a FRAP experiment of rhodamine-labeled lipids in a SLB demonstrating a fluid and homogenous bilayer. **(C)** Image from a particle tracking experiment with the ATL3 catalytic core (left) and path of each particle tracked (right; individual particles in both images shown outlined in different colors). These tracking experiments yielded a diffusion coefficient of 0.28 ± 0.17 $\mu m^2$/sec.

*Characterization of the isoform-specific nature of the ATL HVR.*

As presented in Chapter 2, each ATL isoform consists of a divergent hypervariable N-terminal region (Figure 4.2A). Although we have solved a structure of the ATL3 HVR, it was solved in the context of the G domain alone, lacking the rest of the catalytic core, yet it did not create any inter-molecular crystal contacts, and no link could be drawn to the identified function of the ATL1 HVR. However, preliminary *in vitro* experiments with the ATL2 HVR indicated a similar function to the ATL1 HVR in promoting vesicle tethering efficiency, while not impacting innate GTP hydrolysis rates (Figure 4.2B and C). These initial results motivate further investigation. Since the

ATL3 HVR seemingly has a divergent function from ATL1, it remains possible that ATL2's HVR also has additional or variable function.

We also hypothesize that the HVR of each ATL isoform could function in segregating isoforms in the cell or otherwise aid in self/other identification of ATL isoforms. This would be particularly intriguing if we can determine if and how the different ATL HVRs functionally deviate. To address these questions, we plan on using single particle tracking as described above with isoforms labeled with different fluorophores. We can determine if isoforms form heterooligomers or remain separated by tracking colocalization patterns with WT protein, ΔHVR mutant protein, or chimeric protein constructs with swapped HVRs.

Expression of swapped-HVR chimeric ATL protein constructs in mammalian cells may also yield further perspective on cellular functions of this motif. Previous studies have reported the effects of swapped-HVR chimeras in Ras proteins in mammalian cells (Walsh and Bar-Sagi, 2001; Roy *et al*., 2002).

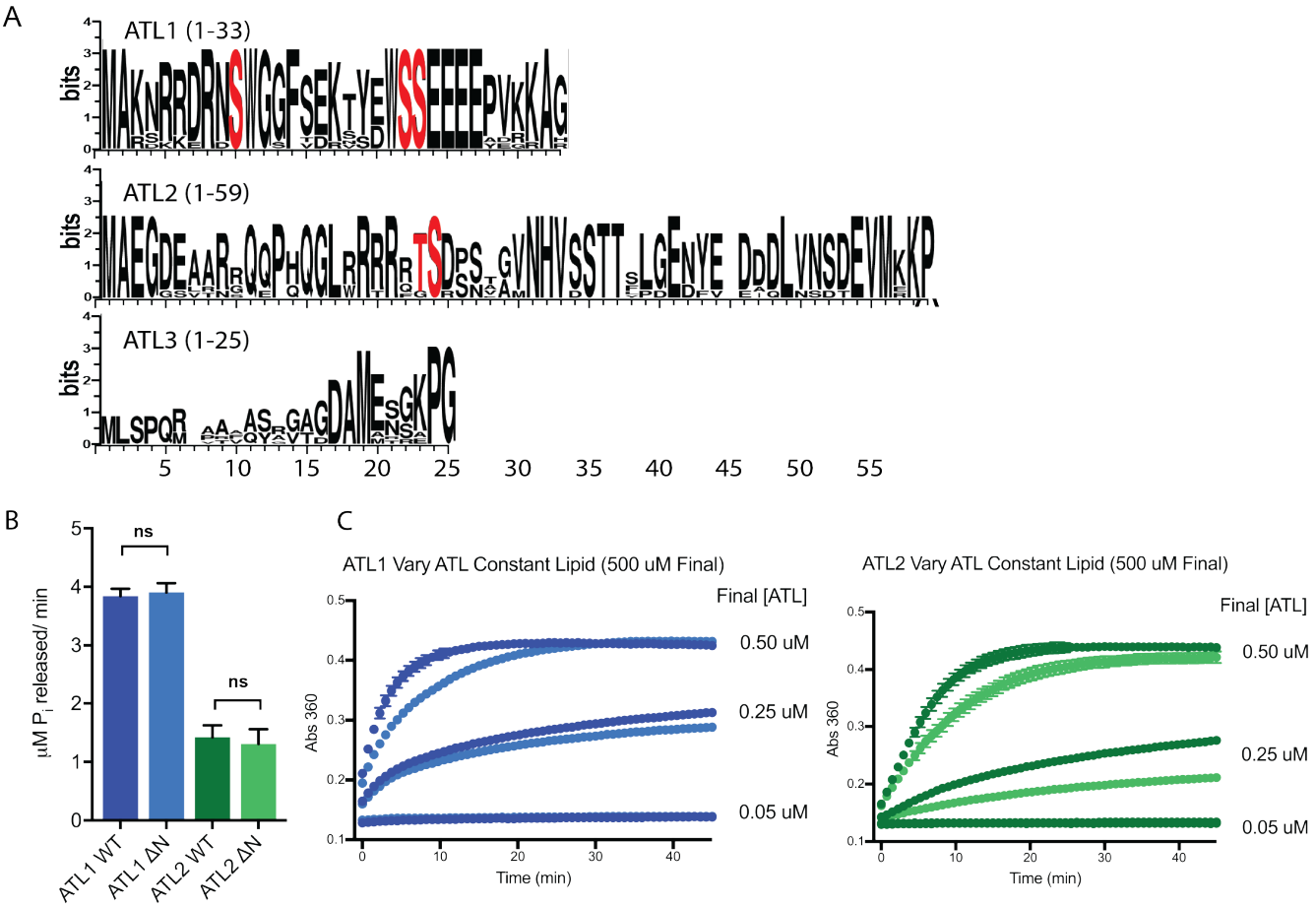


**Figure 4.2 Kinetic behavior of ATL2 ΔHVR mirrors that of ATL1 ΔHVR. (A)** WebLogo representation of ATL1-3 HVRs. Conserved residues reported to be phosphorylated shown in red. **(B)** Catalytic efficiencies of GTP hydrolysis determined for the catalytic core fragments of ATL1 and ATL2 with and without their respective HVRs. **(C)** Vesicle tethering reactions of protein constructs used in (A), at increasing protein concentrations (0.05 to 0.5 µM) with lipid concentration held constant at 0.5 mM. ATL1 WT shown in blue; ATL1 ΔHVR in light blue; ATL2 WT in green; and ATL2 ΔHVR in light green.

Towards the goal of characterizing the ATL2 HVR, we have begun efforts to solve the X-ray structure of the ATL2 catalytic core with the HVR. Until this point, we have not tried to solve the ATL2 structure due to the high sequence identity with the other two isoforms and its *in vitro* kinetic efficiencies and apparent cellular membrane fusion efficiencies matching closely with those of ATL1 (Morin-Leisk *et al*., 2011; Wu *et al*., 2015). However, with this motif lending putative

isoform identity, we became interested in its structural basis for each isoform. After optimizing crystallization protein construct design, we found several conditions that supported crystal growth (Figure 4.3). We have not yet improved the diffraction resolution of these crystals past ~ 6 Å (Figure 4.3B), but continued optimization may yield improvement required for structural determination.

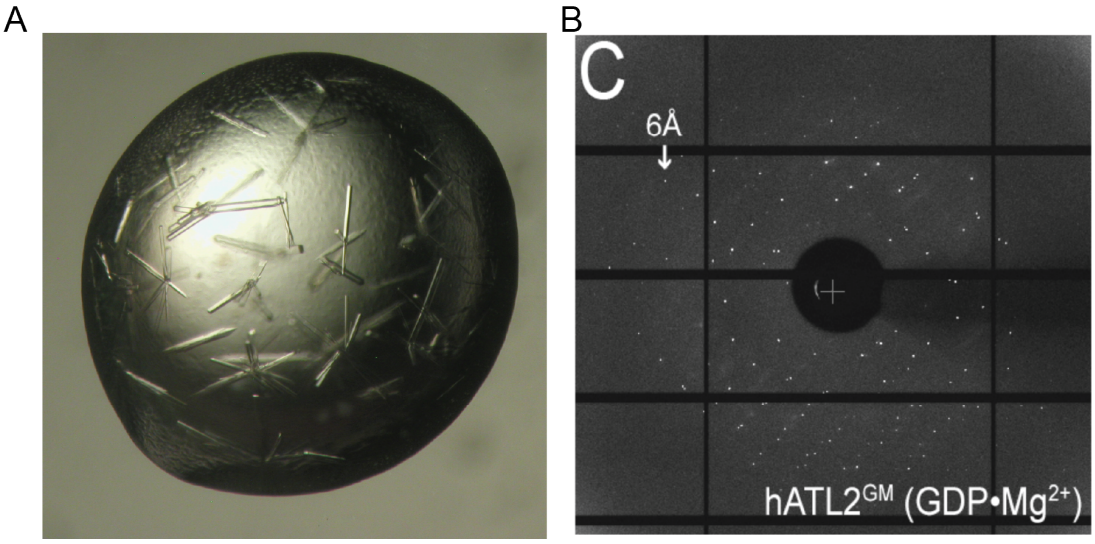


**Figure 4.3 Structural studies of ATL2 to elucidate structure of HVR. (A)** Crystals of the catalytic core fragment of ATL2 (including its HVR) in the presence of GDP•$Mg^{2+}$. **(B)** Example of X-ray diffraction of ATL2 crystals, with diffraction spots to approximately 6 Å resolution.

*Characterization of isoform-specific post-translational modifications.*

In Chapter 2, we established both that ATL1 is post-translationally modified in its HVR and that there are kinetic and cellular consequences of these modifications. We initially identified reports of phosphorylation of S10, S22, and S23 from the PhosphoSitePlus database (Hornbeck *et al*., 2015), with these three residues having the largest number of references by far above other

reported modifications (Table 4.1). Strikingly, we found that ATL2 also has several conserved HVR residues (T23 and S24) that are reported to be phosphorylated. This strong preference for extrinsic regulation of either isoform through modification of the HVR strengthens the case that it is a crucial regulatory motif and warrants further investigation.

Not only does ATL3 show dissimilar kinetic trends with deletion of its HVR as ATL1 and ATL2, but it also has only one identified HVR phosphorylation site (S3), with only five references. However, there is a highly identified phosphorylation site at the end of ATL3's C-terminal amphipathic helix on residue S535. While this may support the hypothesis that ATL3's N-terminal HVR is not the main mode of regulation, regulation through the C-terminal phosphorylation site has been reported within the *A. thaliana* homolog of ATL, RHD3 (Ueda *et al*., 2016). Here, the modified state was reported to increase membrane fusion by promoting oligomerization. This could be an intriguing parallel if this C-terminal regulation is found to affect oligomerization for ATL3, as the HVR may do for ATL1.

| | Phosphorylated residue | Number of references |
|---|---|---|
| ATL1 | S10 | 17 |
| | S22 | 11 |
| | S23 | 10 |
| ATL2 | T23 | 40 |
| | S24 | 71 |

**Table 4.1. Reported phosphorylation sites within ATL HVRs.** For each isoform, both the residue and the number of large, unbiased screens identifying phosphorylation for that residue are listed (Hornbeck *et al*., 2015). Only residues with at least 10 reports were included here.

*Confirmation of specific kinase modifications of ATL.*

We have carried out a screen of kinase reactions with 58 characterized Ser/Thr kinase domains (Albanese *et al*., 2018) with the catalytic core fragment of ATL1 as substrate. We identified a subset of kinases that phosphorylate ATL1 *in vitro*, with variable levels of specificity for conserved HVR serine resides. Based on investigation of the literature, we gave context for

both kinase substrate recognition and either cellular pathways or sub-cellular localizations that could implicate novel regulatory modes for ATL1. However, to improve confidence of positive hits and begin understanding ATL1's roles in these novel pathways, more direct experiments must follow-up our efforts.

One of the kinase hits of particular interest was Aurora kinase A (AurA), as it was found to phosphorylate ATL1 S10 in an unbiased proteomic screen (Kettenbach *et al*., 2011), which was corroborated by our kinase screen. AurA plays a critical role in cell cycle progression through mitosis through centrosome maturation, formation of bipolar spindles, and coordination of cytokinesis (Nikonova *et al*., 2013). The microtubule cytoskeletal structure maintains an intricate relationship with the reticular ER, especially during the highly dynamic process of mitosis (Puhka *et al.,* 2007; Wang *et al*., 2013; McCullough and Lucocq, 2005). Specifically, ATL1 remains a critical actor in these mitotic ER dynamics, with the absence of functional ATL causing fragmentation in the ER and blocking of nuclear envelope reformation (Wang *et al*., 2013; Wang *et al*., 2016).

In order to establish with more confidence that ATL1 is phosphorylated by AurA in a biological setting, we would like to study ATL1's phosphorylation pattern, cellular localization, and apparent ER fusion activity in the presence of AurA-specific kinase inhibitors. There are a number of characterized inhibitors known to act against Aurora kinases, including CCT137690 (Faisal *et al*., 2011) and SNS-314 (Oslob *et al*., 2008), both of which are selective, pan-Aurora inhibitors, which are readily available (Millipore Sigma). ATL1 phosphorylation by AurA can be confirmed by treating ATL1-expressing cells with an AurA-specific inhibitor, followed by ATL1 immunoprecipitation (IP) and analysis with a gel-based phosphate-detection method such as ProQ Diamond phosphoprotein stain or Phos-tag BTL-104 (a chemiluminescent method using a biotinylated Phos-Tag moiety). Similar experimental designs using kinase inhibitors of other positive hits from our kinase screen in Chapter 2 would be equally informative.

*Site-specific phosphoserine incorporation into ATL.*

Our current understanding of the effects of ATL1 phosphorylation rely on the use of site-specific phosphomimetic mutant proteins, in which a known or putative phosphorylated serine residue is substituted with glutamate to mimic the charge density of a phosphoserine (Figure 4.4A). While this remains a widely accepted tool for studying effects of site-specific phosphorylation, these mutants do not exactly mimic the actual charge and shape of phosphoserine, which may result in loss of nuance or specificity. One example of this was demonstrated with a PKA-catalyzed phosphorylation of Drp1 on S637, resulting in reduced *in vitro* GTPase activity while the corresponding phosphomimetic mutation only slightly affected the activity (Chang and Blackstone, 2007). In recent years, however, a technique has been developed to address this issue by introducing site-specific phosphoserine residues into recombinant protein for bacterial (Zhu *et al*., 2019; Rogerson *et al*., 2015) or mammalian tissue culture (Beránek *et al*., 2018). This system employs the use of genetic code expansion with the amber stop codon (UAG) coding instead for incorporation of a phosphoserine residue, coopting a naturally occurring metabolic precursor of serine incorporation (Rogerson *et al*., 2015). Alternatively, a nonhydrolyzable phosphoserine analog can be used for incorporation to ensure the phosphoryl moiety will be retained (Figure 4.4B). This system has also been optimized for efficient expression of multi-phosphorylated constructs (Rogerson *et al*., 2015), allowing for study of ATL1's multiple phosphorylation state combinations as described in Chapter 2. We have already carried out proof-of-concept experiments to show that we can express and purify site-directed phosphoserine ATL1 pS10 catalytic core protein (Figure 4.4C) with similar purity as recombinant ATL1 WT.

This technology expands our ability to characterize the functional impact of phosphorylation on ATL activity. Initial experiments would focus on recapitulating experiments carried out with the corresponding phosphomimetic mutant proteins, including *in vitro* GTPase and vesicle tethering experiments, and mammalian cell experiments assessing impact on ER

morphology, assuming the mammalian phosphoserine incorporation system is compatible with our model.

Alternatively, if challenges arise in the bacterial expression of specific ATL phosphoserine combinations, recombinant ATL protein could be phosphorylated *in vitro*, with desired phosphoserine combination achieved either by using kinases specific to the desired residue or using ATL1 S-to-A mutations.

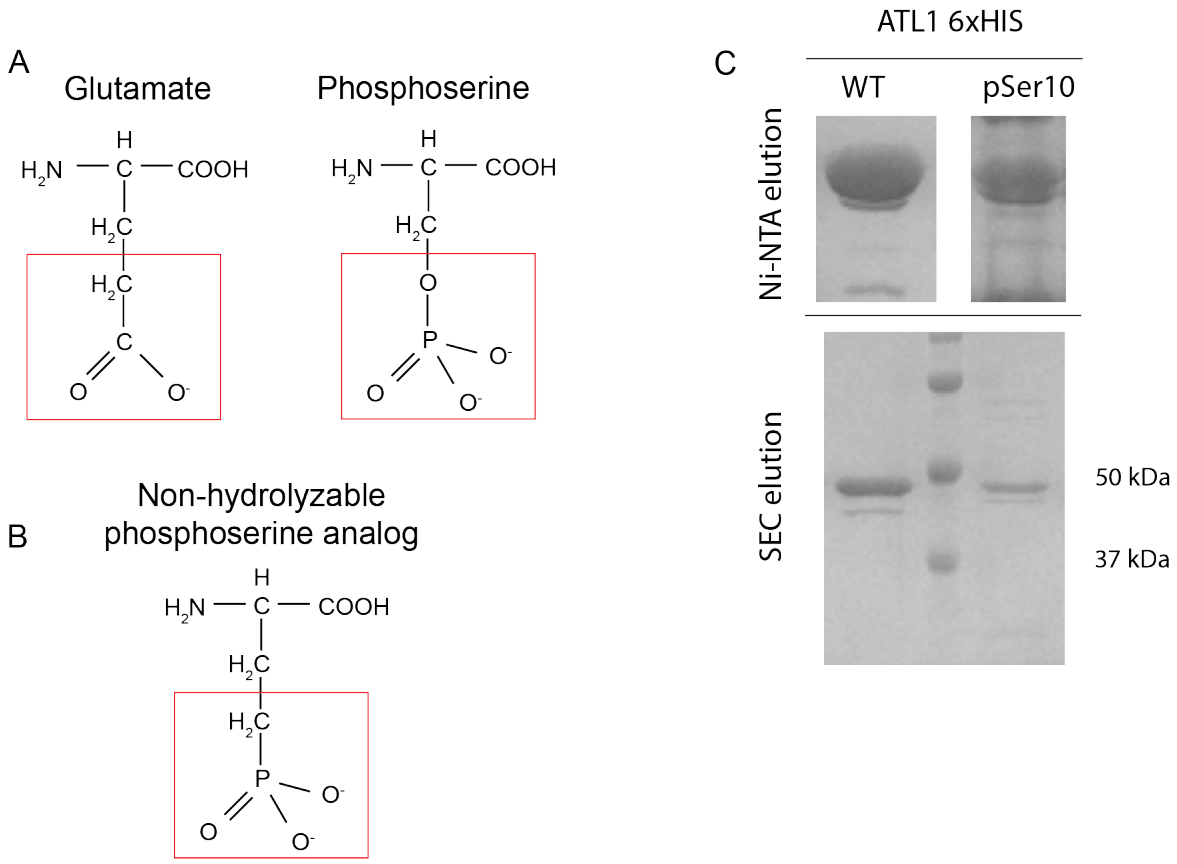


**Figure 4.4. Recombinant site-specific phosphoserine incorporation. (A)** Chemical structure of a glutamate residue and a phosphoserine residue, with the red boxes indicating the size and charge distribution similarities as the basis for a phosphomimetic mutation. **(B)** Structure of a non-hydrolyzable phosphoserine residue that can be used in genetic code expansion systems allowing for site-specific phosphoserine incorporation. **(C)** Test expression of the catalytic core of ATL1 with a C-terminal hexa-histidine tag as a WT protein construct (left) or with the incorporation of a phosphoserine at position S10. The top two gels contain elution samples from a Ni-NTA purification, and the bottom gel has the same samples after size exclusion chromatography.

*Structural analysis and single particle behaviors of phosphorylated ATLs.*

One of the questions posed in Chapter 2 that remains unanswered is in regard to the structural consequences of HVR phosphorylation. The S10 residue sits within the first half of the ATL1 HVR, for which no structural information was determined, and the S22 and S23 sit adjacent to the β-hairpin turn, pointing toward a putative conformational change upon phosphorylation or a charge-based attraction/repulsion mechanism. However, solving the structure of either the phosphomimetic mutant proteins or site-specific phosphoserine incorporated protein could shed light on the mechanisms at play. This would not only expand our understanding of these modifications, but the more general function of the HVR. Similar experiments for ATL2 could also yield mechanistic insights.

Quantitative assessment of oligomerization patterns for each phosphorylation state observed will also help shed light on the mechanistic basis of altered tethering efficiency and cellular distribution. As described above for studying the functional role of the HVR, introducing phosphomimetic mutations or site-specific phosphoserine incorporation into protein constructs for single particle tracking analysis will address how *cis* membrane protein-protein interactions are affected by these post-translational modifications.

*Identifying cellular binding partners of ATL.*

One result of post-translational modifications is alteration of protein-protein interactions in the cell. Identification of ATL's binding partners in the presence and absence of the HVR and of the phosphorylated residues we've characterized in the HVR will inform of the cellular pathways in which ATLs participate and which may regulate ATL's activity. One of several approaches may be taken to address these questions, including pull-downs either *in vitro* with recombinant ATL as the bait or cell-based IP experiments with the mammalian-expressed ATL as the bait. The first of these two approaches has the benefit of controlling the ATL input. We know we can easily express and purify ATL with or without its HVR, with singly, doubly, or triply mutated S-to-E

phosphomimetic or S-to-A control, and we have proof-of-concept expression for single site-specific phosphoserine incorporation. Additionally, we have cloned the HVR peptide alone in a construct compatible with site-specific phosphoserine incorporation, allowing a second means of studying HVR- or phosphorylation-dependent interactions. We can also use isoform swapped-HVR chimeric protein constructs for further investigation of HVR-specific nature of protein interactions. After incubation with mammalian cell lysates and subsequent α-ATL (or epitope tag) pulldown, mass spectrometry will identify binding partners, and comparisons across different ATL protein constructs or mutations as the input will reveal which of these novel partners are dependent on the HVR or phosphorylation state.

Conversely, cell-based experiments have the advantage of observing ATL's binding partners in a biologically relevant environment, which may be necessary to detect certain interactions. Similar to the *in vitro* pulldowns, we could employ the use of ATL ΔHVR mutants, S-to-E and S-to-A phosphomimetic variants, potentially the site-specific phosphoserine incorporation (we would need to use the non-hydrolyzable phosphoserine analog here due to natural turnover of the modification in the cell), and inhibitors of kinases confirmed to phosphorylate ATL. To quantify differences in interactions compared with WT ATL, SILAC (stable isotope labeling using amino acids in cell culture) should be carried out with either WT ATL or one of the conditions mentioned above to determine whether interactions are dependent on the HVR or its modification. Particularly, probing the effects of the AurA inhibitors could yield insights to indicate other key players involved in ATL1-specific signaling pathways important in mitotic progression. Generally, we are very interested in investigation of ATL interactions that are mediated within the HVR because a majority of the known protein interactors occur in a transmembrane-dependent manner (Park and Blackstone, 2010; Hu *et al.,* 2009, Rismanchi *et al*., 2008, Sanderson *et al.,* 2006; Chang *et al.,* 2013; Shibata *et al.,* 2008), and do not appear to impose any regulatory power on ATL activity. HVR- and phosphorylation-dependent binding partners for the other two ATL isoforms will also be important to pursue, especially since based

on our current knowledge, mechanisms for the ATL3 HVR may deviate from those of ATL1 and ATL2.

*Elucidation of ATL cell signaling pathways.*

Evidence of cellular pathways that implicate ATLs are consistently reported, continually expanding our understanding of the extent of ATL's cellular impact. A number of the implicated pathways are directly linked to the maintenance and function of the ER, including regulation of lipid droplet formation and size (Renvoisé *et al*., 2016; Falk *et al*., 2014; Klemm *et al.,* 2013); ER-phagy (Chen *et al*., 2019; Liang *et al*., 2018); targeting of proteins to the inner nuclear membrane (Pawar *et al*., 2017); and ER store-operated calcium entry (SOCE) (Li *et al*., 2017). The elaborate interplay between the structures of the ER and the microtubule cytoskeleton are highly dynamic and dictated by a number of proteins (Terasaki *et al*., 1986) with ATLs among them (Park *et al*., 2010; Sun *et al*., 2020). During mitotic cell progression, both of these structures undergo vast morphological changes (Puhka *et al*., 2007; Lu *et al*., 2009; McCullough and Lucocq, 2005; Wang *et al*., 2013), which we know ATL participates in bringing about (Wang *et al*., 2013). Interestingly, in NIH-3T3 ATL1/2/3 TKO cells, reduced proliferation rates were observed compared to WT cells, with a reduced percentage of cells in mitosis (Zhao *et al*., 2016). ATL's ability to control ER morphology has also made it a key player in the propagation of many viral and bacterial pathogens in the cell (Neufeldt *et al*., 2019; Monel *et al*., 2019; Steiner *et al*., 2018; Steiner *et al*., 2017).

Corresponding with its implications in neuronal health and disease, ATL1 has been shown to function in promoting axonal and dendritic outgrowth (Zhu *et al*., 2006; Liu *et al*., 2019; Shih and Hsueh, 2016), releasing neurotransmitters (Summerville *et al*., 2016), and links have been drawn to its defect in certain epileptic patients (Lu *et al*., 2020). ATL1's role in neuronal health and development is likely also related to its role in regulating BMP signaling (Fassier *et al*., 2010; Summerville *et al*., 2016; Zhao and Hedera, 2013; Zhao *et al*., 2016).

Some of these functions are isoform-specific, while for others it remains unclear or unknown at this time. As the experiments we have proposed begin to elucidate the cellular pathways ATLs participate in, we anticipate that our understanding of these pathways will also deepen.

## REFERENCES


Albanese, S. K., Parton, D. L., Işık, M., Rodríguez-Laureano, L., Hanson, S. M., Behr, J. M., ... & Chodera, J. D. (2018). An open library of human kinase domain constructs for automated bacterial expression. *Biochemistry*, *57*(31), 4675-4689.

Axmann, M., Schütz, G. J., & Huppa, J. B. (2015). Single molecule fluorescence microscopy on planar supported bilayers. *JoVE (Journal of Visualized Experiments)*, (104), e53158.

Beránek, V., Reinkemeier, C. D., Zhang, M. S., Liang, A. D., Kym, G., & Chin, J. W. (2018). Genetically encoded protein phosphorylation in mammalian cells. *Cell chemical biology*, *25*(9), 1067-1074.

Bian, X., Klemm, R. W., Liu, T. Y., Zhang, M., Sun, S., Sui, X., ... & Hu, J. (2011). Structures of the atlastin GTPase provide insight into homotypic fusion of endoplasmic reticulum membranes. *Proceedings of the National Academy of Sciences*, *108*(10), 3976-3981.

Bouhaddou, M., Memon, D., Meyer, B., White, K. M., Rezelj, V. V., Marrero, M. C., ... & Batra, J. (2020). The global phosphorylation landscape of SARS-CoV-2 infection. Cell, 182(3), 685-712.

Brandt, T., Cavellini, L., Kühlbrandt, W., & Cohen, M. M. (2016). A mitofusin-dependent docking ring complex triggers mitochondrial fusion in vitro. *Elife*, *5*, e14618.

Byrnes, L. J., Singh, A., Szeto, K., Benvin, N. M., O'donnell, J. P., Zipfel, W. R., & Sondermann, H. (2013). Structural basis for conformational switching and GTP loading of the large G protein atlastin. *The EMBO journal*, *32*(3), 369-384.

Byrnes, L. J., & Sondermann, H. (2011). Structural basis for the nucleotide-dependent dimerization of the large G protein atlastin-1/SPG3A. *Proceedings of the National Academy of Sciences*, *108*(6), 2216-2221.

Chang, C. R., & Blackstone, C. (2007). Cyclic AMP-dependent protein kinase phosphorylation of Drp1 regulates its GTPase activity and mitochondrial morphology. *Journal of Biological Chemistry*, *282*(30), 21583-21587.

Chang, J., Lee, S., & Blackstone, C. (2013). Protrudin binds atlastins and endoplasmic reticulum-shaping proteins and regulates network formation. *Proceedings of the National Academy of Sciences*, *110*(37), 14954-14959.

Chen, Q., Xiao, Y., Chai, P., Zheng, P., Teng, J., & Chen, J. (2019). ATL3 is a tubular ER-phagy receptor for GABARAP-mediated selective autophagy. *Current Biology*, *29*(5), 846-855.

Deatherage, C. L., Nikolaus, J., Karatekin, E., & Burd, C. G. (2020). Retromer forms low order oligomers on supported lipid bilayers. *bioRxiv*.

Faisal, A., Vaughan, L., Bavetsias, V., Sun, C., Atrash, B., Avery, S., ... & Raynaud, F. I. (2011). The aurora kinase inhibitor CCT137690 downregulates MYCN and sensitizes MYCN-amplified neuroblastoma in vivo. *Molecular cancer therapeutics*, *10*(11), 2115-2123.

Falk, J., Rohde, M., Bekhite, M. M., Neugebauer, S., Hemmerich, P., Kiehntopf, M., ... & Beetz, C. (2014). Functional Mutation Analysis Provides Evidence for a Role of REEP 1 in Lipid Droplet Biology. *Human mutation*, *35*(4), 497-504.

Fassier, C., Hutt, J. A., Scholpp, S., Lumsden, A., Giros, B., Nothias, F., … & Hazan, J. (2010). Zebrafish atlastin controls motility and spinal motor axon architecture via inhibition of the BMP pathway. *Nature neuroscience*, *13*(11), 1380-1387.

Fischer, D., Schabhüttl, M., Wieland, T., Windhager, R., Strom, T. M., & Auer-Grumbach, M. (2014). A novel missense mutation confirms ATL3 as a gene for hereditary sensory neuropathy type 1. *Brain*, *137*(7), e286-e286.

Groves, J. T., Parthasarathy, R., & Forstner, M. B. (2008). Fluorescence imaging of membrane dynamics. *Annual review of biomedical engineering*, *10*.

Guelly, C., Zhu, P. P., Leonardis, L., Papić, L., Zidar, J., Schabhüttl, M., ... & Willems, J. (2011). Targeted high-throughput sequencing identifies mutations in atlastin-1 as a cause of hereditary sensory neuropathy type I. *The American Journal of Human Genetics*, *88*(1), 99-105.

Harrison, S. C. (2015). Viral membrane fusion. *Virology*, *479*, 498-507.

Hornbeck, P.V., Zhang, B., Murray, B., Kornhauser, J.M., Latham, V., Skrzypek, E. (2015). PhosphoSitePlus, 2014: mutations, PTMs and recalibrations. *Nucleic Acids Res*. 43:D512-20.

Hu, J., Shibata, Y., Zhu, P. P., Voss, C., Rismanchi, N., Prinz, W. A., ... & Blackstone, C. (2009). A class of dynamin-like GTPases involved in the generation of the tubular ER network. *Cell*, *138*(3), 549-561.

Hu, X., Wu, F., Sun, S., Yu, W., & Hu, J. (2015). Human atlastin GTPases mediate differentiated fusion of endoplasmic reticulum membranes. Protein & cell, 6(4), 307-311.

Jahn, R., Lang, T., & Südhof, T. C. (2003). Membrane fusion. *Cell*, *112*(4), 519-533.

Kettenbach, A. N., Schweppe, D. K., Faherty, B. K., Pechenick, D., Pletnev, A. A., & Gerber, S. A. (2011). Quantitative phosphoproteomics identifies substrates and functional modules of Aurora and Polo-like kinase activities in mitotic cells. *Science signaling*, *4*(179), rs5-rs5.

Klemm, R. W., Norton, J. P., Cole, R. A., Li, C. S., Park, S. H., Crane, M. M., ... & Shibata, Y. (2013). A conserved role for atlastin GTPases in regulating lipid droplet size. *Cell reports*, *3*(5), 1465-1475.

Krols, M., Detry, S., Asselbergh, B., Almeida-Souza, L., Kremer, A., Lippens, S., ... & McMahon, H. T. (2018). Sensory-neuropathy-causing mutations in ATL3 cause aberrant ER membrane tethering. *Cell reports*, *23*(7), 2026-2038.

Li, J., Yan, B., Si, H., Peng, X., Zhang, S. L., & Hu, J. (2017). Atlastin regulates store-operated calcium entry for nerve growth factor-induced neurite outgrowth. *Scientific reports*, *7*, 43490.

Liang, J. R., Lingeman, E., Ahmed, S., & Corn, J. E. (2018). Atlastins remodel the endoplasmic reticulum for selective autophagy. *Journal of Cell Biology*, *217*(10), 3354-3367.

Liu, T. Y., Bian, X., Romano, F. B., Shemesh, T., Rapoport, T. A., & Hu, J. (2015). Cis and trans interactions between atlastin molecules during membrane fusion. *Proceedings of the National Academy of Sciences*, *112*(15), E1851-E1860.

Liu, X., Guo, X., Niu, L., Li, X., Sun, F., Hu, J., ... & Shen, K. (2019). Atlastin-1 regulates morphology and function of endoplasmic reticulum in dendrites. *Nature communications*, *10*(1), 1-15.

Lu, L., Ladinsky, M. S., & Kirchhausen, T. (2009). Cisternal organization of the endoplasmic reticulum during mitosis. *Molecular biology of the cell*, *20*(15), 3471-3480.

Lu, X., Yang, M., Yang, Y., & Wang, X. F. (2020). Atlastin-1 modulates seizure activity and neuronal excitability. *CNS Neuroscience & Therapeutics*, *26*(3), 385-393.

Mattie, S., Riemer, J., Wideman, J. G., & McBride, H. M. (2018). A new mitofusin topology places the redox-regulated C terminus in the mitochondrial intermembrane space. *Journal of Cell Biology*, *217*(2), 507-515.

McCullough, S., & Lucocq, J. (2005). Endoplasmic reticulum positioning and partitioning in mitotic HeLa cells. *Journal of Anatomy*, *206*(5), 415-425.

McNew, J. A. (2008). Regulation of SNARE-mediated membrane fusion during exocytosis. *Chemical reviews*, *108*(5), 1669-1686.

McNew, J. A., Sondermann, H., Lee, T., Stern, M., & Brandizzi, F. (2013). GTP-dependent membrane fusion. *Annual review of cell and developmental biology*, *29*, 529-550.

Meijer, I. A., Dion, P., Laurent, S., Dupré, N., Brais, B., Levert, A., ... & Soderblom, C. (2007). Characterization of a novel SPG3A deletion in a French-Canadian family. Annals of Neurology:

Official Journal of the American Neurological Association and the Child Neurology Society, 61(6), 599-603.

Monel, B., Rajah, M. M., Hafirassou, M. L., Ahmed, S. S., Burlaud-Gaillard, J., Zhu, P. P., ... & Amraoui, S. (2019). Atlastin Endoplasmic Reticulum-Shaping Proteins Facilitate Zika Virus Replication. *Journal of virology*, *93*(23).

Morin-Leisk, J., Saini, S. G., Meng, X., Makhov, A. M., Zhang, P., & Lee, T. H. (2011). An intramolecular salt bridge drives the soluble domain of GTP-bound atlastin into the postfusion conformation. *Journal of Cell Biology*, *195*(4), 605-615.

Neufeldt, C. J., Cortese, M., Scaturro, P., Cerikan, B., Wideman, J. G., Tabata, K., ... & Bartenschlager, R. (2019). ER-shaping atlastin proteins act as central hubs to promote flavivirus replication and virion assembly. *Nature microbiology*, *4*(12), 2416-2429.

Nikonova, A. S., Astsaturov, I., Serebriiskii, I. G., Dunbrack, R. L., & Golemis, E. A. (2013). Aurora A kinase (AURKA) in normal and pathological cell division. *Cellular and Molecular Life Sciences*, *70*(4), 661-687.

Nye, J. A., & Groves, J. T. (2008). Kinetic control of histidine-tagged protein surface density on supported lipid bilayers. *Langmuir*, *24*(8), 4145-4149.

O'Donnell, J. P., Byrnes, L. J., Cooley, R. B., & Sondermann, H. (2018). A hereditary spastic paraplegia–associated atlastin variant exhibits defective allosteric coupling in the catalytic core. *Journal of Biological Chemistry*, *293*(2), 687-700.

Oslob, J. D., Romanowski, M. J., Allen, D. A., Baskaran, S., Bui, M., Elling, R. A., ... & Heumann, S. A. (2008). Discovery of a potent and selective aurora kinase inhibitor. *Bioorganic & Medicinal Chemistry Letters*, *18*(17), 4880-4884.

Park, S. H., & Blackstone, C. (2010). Further assembly required: construction and dynamics of the endoplasmic reticulum network. *EMBO reports*, *11*(7), 515-521.

Park, S. H., Zhu, P. P., Parker, R. L., & Blackstone, C. (2010). Hereditary spastic paraplegia proteins REEP1, spastin, and atlastin-1 coordinate microtubule interactions with the tubular ER network. *The Journal of clinical investigation*, *120*(4), 1097-1110.

Pawar, S., Ungricht, R., Tiefenboeck, P., Leroux, J. C., & Kutay, U. (2017). Efficient protein targeting to the inner nuclear membrane requires Atlastin-dependent maintenance of ER topology. *Elife*, *6*, e28202.

Polisetty, R. V., Gautam, P., Sharma, R., Harsha, H. C., Nair, S. C., Gupta, M. K., ... & Purohit, A. K. (2012). LC-MS/MS analysis of differentially expressed glioblastoma membrane proteome

reveals altered calcium signaling and other protein groups of regulatory functions. *Molecular & Cellular Proteomics*, *11*(6).

Praefcke, G. J., & McMahon, H. T. (2004). The dynamin superfamily: universal membrane tubulation and fission molecules?. *Nature reviews Molecular cell biology*, *5*(2), 133-147.

Puhka, M., Vihinen, H., Joensuu, M., & Jokitalo, E. (2007). Endoplasmic reticulum remains continuous and undergoes sheet-to-tubule transformation during cell division in mammalian cells. *The Journal of cell biology*, *179*(5), 895-909.

Renvoisé, B., Malone, B., Falgairolle, M., Munasinghe, J., Stadler, J., Sibilla, C., ... & Blackstone, C. (2016). Reep1 null mice reveal a converging role for hereditary spastic paraplegia proteins in lipid droplet regulation. *Human molecular genetics*, *25*(23), 5111-5125.

Rismanchi, N., Soderblom, C., Stadler, J., Zhu, P. P., & Blackstone, C. (2008). Atlastin GTPases are required for Golgi apparatus and ER morphogenesis. *Human molecular genetics*, *17*(11), 1591-1604.

Rogerson, D. T., Sachdeva, A., Wang, K., Haq, T., Kazlauskaite, A., Hancock, S. M., ... & Chin, J. W. (2015). Efficient genetic encoding of phosphoserine and its nonhydrolyzable analog. *Nature chemical biology*, *11*(7), 496-503.

Roy, S., Wyse, B., & Hancock, J. F. (2002). H-Ras signaling and K-Ras signaling are differentially dependent on endocytosis. *Molecular and cellular biology*, *22*(14), 5128-5140.

Rozovsky, S., Forstner, M. B., Sondermann, H., & Groves, J. T. (2012). Single molecule kinetics of ENTH binding to lipid membranes. *The Journal of Physical Chemistry B*, *116*(17), 5122-5131.

Saini, S. G., Liu, C., Zhang, P., & Lee, T. H. (2014). Membrane tethering by the atlastin GTPase depends on GTP hydrolysis but not on forming the cross-over configuration. *Molecular biology of the cell*, *25*(24), 3942-3953.

Sanderson, C. M., Connell, J. W., Edwards, T. L., Bright, N. A., Duley, S., Thompson, A., ... & Reid, E. (2006). Spastin and atlastin, two proteins mutated in autosomal-dominant hereditary spastic paraplegia, are binding partners. *Human molecular genetics*, *15*(2), 307-318.

Shibata, Y., Voss, C., Rist, J. M., Hu, J., Rapoport, T. A., Prinz, W. A., & Voeltz, G. K. (2008). The reticulon and DP1/Yop1p proteins form immobile oligomers in the tubular endoplasmic reticulum. *Journal of Biological Chemistry*, *283*(27), 18892-18904.

Shih, Y. T., & Hsueh, Y. P. (2016). VCP and ATL1 regulate endoplasmic reticulum and protein synthesis for dendritic spine formation. *Nature communications*, *7*(1), 1-16.

Shutt, T., Geoffrion, M., Milne, R., & McBride, H. M. (2012). The intracellular redox state is a core determinant of mitochondrial fusion. *EMBO reports*, *13*(10), 909-915.

Steiner, B., Swart, A. L., Welin, A., Weber, S., Personnic, N., Kaech, A., ... & Hilbi, H. (2017). ER remodeling by the large GTPase atlastin promotes vacuolar growth of Legionella pneumophila. *EMBO reports*, *18*(10), 1817-1836.

Steiner, B., Weber, S., Kaech, A., Ziegler, U., & Hilbi, H. (2018). The large GTPase atlastin controls ER remodeling around a pathogen vacuole. *Communicative & integrative biology*, *11*(2), 1-5.

Summerville, J. B., Faust, J. F., Fan, E., Pendin, D., Daga, A., Formella, J., ... & McNew, J. A. (2016). The effects of ER morphology on synaptic structure and function in Drosophila melanogaster. *Journal of cell science*, *129*(8), 1635-1648.

Sun, J., Zhang, M., Qi, X., Doyle, C., & Zheng, H. (2020). Armadillo-repeat kinesin1 interacts with Arabidopsis atlastin RHD3 to move ER with plus-end of microtubules. *Nature communications*, *11*(1), 1-14.

Terasaki, M., Chen, L. B., & Fujiwara, K. (1986). Microtubules and the endoplasmic reticulum are highly interdependent structures. *The Journal of cell biology*, *103*(4), 1557-1568.

Ueda, H., Yokota, E., Kuwata, K., Kutsuna, N., Mano, S., Shimada, T., ... & Shimmen, T. (2016). Phosphorylation of the C terminus of RHD3 has a critical role in homotypic ER membrane fusion in Arabidopsis. *Plant physiology*, *170*(2), 867-880.

Ulengin, I., Park, J. J., & Lee, T. H. (2015). ER network formation and membrane fusion by atlastin1/SPG3A disease variants. *Molecular biology of the cell*, *26*(9), 1616-1628.

Walsh, A. B., & Bar-Sagi, D. (2001). Differential activation of the Rac pathway by Ha-Ras and K-Ras. *Journal of Biological Chemistry*, *276*(19), 15609-15615.

Wang, S., Romano, F. B., Field, C. M., Mitchison, T. J., & Rapoport, T. A. (2013). Multiple mechanisms determine ER network morphology during the cell cycle in Xenopus egg extracts. *Journal of Cell Biology*, *203*(5), 801-814.

Wang, S., Tukachinsky, H., Romano, F. B., & Rapoport, T. A. (2016). Cooperation of the ER-shaping proteins atlastin, lunapark, and reticulons to generate a tubular membrane network. *Elife*, *5*, e18605.

Zhao, G., Zhu, P. P., Renvoisé, B., Maldonado-Báez, L., Park, S. H., & Blackstone, C. (2016). Mammalian knock out cells reveal prominent roles for atlastin GTPases in ER network morphology. *Experimental cell research*, *349*(1), 32-44.

Zhao, J., & Hedera, P. (2013). Hereditary spastic paraplegia-causing mutations in atlastin-1 interfere with BMPRII trafficking. *Molecular and Cellular Neuroscience*, *52*, 87-96.

Zhao, X., Alvarado, D., Rainier, S., Lemons, R., Hedera, P., Weber, C. H., ... & Bui, M. (2001). Mutations in a newly identified GTPase gene cause autosomal dominant hereditary spastic paraplegia. *Nature genetics*, *29*(3), 326-331.

Zhu, P., Gafken, P. R., Mehl, R. A., & Cooley, R. B. (2019). A highly versatile expression system for the production of multiply phosphorylated proteins. *ACS chemical biology*, *14*(7), 1564-1572.

Zhu, P. P., Patterson, A., Lavoie, B., Stadler, J., Shoeb, M., Patel, R., & Blackstone, C. (2003). Cellular localization, oligomerization, and membrane association of the hereditary spastic paraplegia 3A (SPG3A) protein atlastin. *Journal of Biological Chemistry*, *278*(49), 49063-49071.

Zhu, P. P., Soderblom, C., Tao-Cheng, J. H., Stadler, J., & Blackstone, C. (2006). SPG3A protein atlastin-1 is enriched in growth cones and promotes axon elongation during neuronal development. *Human molecular genetics*, *15*(8), 1343-1353.